

Water nucleation : wave tube experiments and theoretical considerations

Citation for published version (APA):

Holten, V. (2009). *Water nucleation : wave tube experiments and theoretical considerations*. [Phd Thesis 1 (Research TU/e / Graduation TU/e), Applied Physics and Science Education]. Technische Universiteit Eindhoven. <https://doi.org/10.6100/IR654106>

DOI:

[10.6100/IR654106](https://doi.org/10.6100/IR654106)

Document status and date:

Published: 01/01/2009

Document Version:

Publisher's PDF, also known as Version of Record (includes final page, issue and volume numbers)

Please check the document version of this publication:

- A submitted manuscript is the version of the article upon submission and before peer-review. There can be important differences between the submitted version and the official published version of record. People interested in the research are advised to contact the author for the final version of the publication, or visit the DOI to the publisher's website.
- The final author version and the galley proof are versions of the publication after peer review.
- The final published version features the final layout of the paper including the volume, issue and page numbers.

[Link to publication](#)

General rights

Copyright and moral rights for the publications made accessible in the public portal are retained by the authors and/or other copyright owners and it is a condition of accessing publications that users recognise and abide by the legal requirements associated with these rights.

- Users may download and print one copy of any publication from the public portal for the purpose of private study or research.
- You may not further distribute the material or use it for any profit-making activity or commercial gain
- You may freely distribute the URL identifying the publication in the public portal.

If the publication is distributed under the terms of Article 25fa of the Dutch Copyright Act, indicated by the "Taverne" license above, please follow below link for the End User Agreement:

www.tue.nl/taverne

Take down policy

If you believe that this document breaches copyright please contact us at:

openaccess@tue.nl

providing details and we will investigate your claim.

WATER NUCLEATION

WATER NUCLEATION

Wave tube experiments
and theoretical considerations

PROEFSCHRIFT

ter verkrijging van de graad van doctor
aan de Technische Universiteit Eindhoven,
op gezag van de rector magnificus, prof. dr. ir. C.J. van Duijn,
voor een commissie aangewezen door het College voor Promoties
in het openbaar te verdedigen op
maandag 14 december 2009 om 16.00 uur

door

Vincent Holten

geboren te Eindhoven

Dit proefschrift is goedgekeurd door de promotoren:

prof. dr. ir. M.E.H. van Dongen

en

prof. dr. ir. A. Hirschberg

Copromotor:

dr. J. Hrubý

© 2009 Vincent Holten

A catalogue record is available from the
Eindhoven University of Technology Library

ISBN 978-90-386-2094-7

NUR 924

Water today presents a wide array of challenges to the world.

—WILLEM-ALEXANDER, PRINCE OF ORANGE

Preface

This thesis is the latest in a series of studies on condensation and droplet growth performed in our group. Most of these studies have relevance for the handling and conditioning of natural gas, specifically, the removal of condensable substances from it. While natural gas contains mostly methane, it also contains small amounts of condensable substances such as water and nonane, which have to be removed. Currently, this is accomplished by cooling down the gas by an isenthalpic expansion. As a result, the undesired components condense, and the condensate can be removed by filters or coalescers. Additionally, water can be removed by bringing the gas into contact with an absorbing liquid, usually a glycol.

New methods for removal of water and heavy hydrocarbons are based on an isentropic expansion, rather than an isenthalpic one. In the Twister device,¹ for example, a nozzle is used to expand the gas to supersonic velocity, which results in a temperature drop and the formation of small droplets. Static vanes generate a swirling flow, so that the droplets are forced to the wall, where they can be separated from the main flow. Since the residence time of the gas in the device is small, the droplets remain small, and a large centrifugal acceleration is required to separate the droplets.

An isentropic expansion is also used in a novel device for carbon dioxide removal from natural gas.^{2,3} In contrast to the Twister process, the expansion is realized by means of a turbine, which results in a relatively small gas speed and a larger residence time. Therefore, smaller accelerations suffice for droplet removal; in the new device, droplets are separated by a rotating particle separator. For successful design of both this device and the Twister, knowledge on the condensation and droplet growth processes in the device is required.

Since the construction of our expansion wave tube for condensation studies in 1993, several gas–vapour mixtures that are relevant to the natural gas industry have been studied. These include the two-component mixtures water–nitrogen,^{4–6} water–helium,^{6,7} water–methane,⁸ nonane–nitrogen,⁹ nonane–methane,^{4,6,8,10,11} nonane–helium,⁶ and three-component mixtures water–

nonane–methane⁸ and nonane–methane–carbon dioxide,¹⁰ as well as natural gas from the Groningen reservoir.¹² Luijten^{6,13} systematically investigated the effect of carrier gas pressure on the nucleation of water and nonane and found significant effects. Helium is the most ideal carrier gas because it has no effect on the surface tension of water. In contrast, methane strongly affects the nucleation of both nonane and water.

The present research focuses on water nucleation. To simulate the behaviour in natural gas, the nucleation of water is studied experimentally in pure methane and mixtures of methane and carbon dioxide (chapter 6). Carbon dioxide is expected to influence the nucleation significantly, since its solubility in water is relatively high. In addition, the surface tension of water is rather sensitive to the presence of carbon dioxide.

To describe nucleation theoretically, an accurate description of equilibrium is essential, since the rate of nucleation is very sensitive to the deviation from equilibrium. In chapter 1, the vapour–liquid phase equilibrium between water, methane, and carbon dioxide is studied. Experimental data from the literature is reviewed and analysed, and the most appropriate equation of state for the mixture is selected and optimized. After the discussion of phase equilibrium, chapter 2 describes classical nucleation theory and the theory of droplet growth. Besides a derivation of the classical expressions for steady-state nucleation, transient nucleation is included as well.

Besides its relevance for industry, the nucleation of water is also interesting from a scientific point of view. In our experiments, water vapour condenses to a liquid at temperatures from 200 to 240 K, far below the freezing point. While liquid water can be supercooled from ambient temperatures down to about 233 K, freezing prevents the study of liquid water below that temperature. In our setup, liquid water is formed directly from water vapour at temperatures also below 233 K. To study the condensation at a fundamental level, the inert carrier gas helium is used instead of methane. The measurement results are reported in chapter 5.

Our experiments are performed in an expansion wave tube (described in chapter 4), in which a monodisperse droplet cloud is generated with the nucleation pulse principle. With this method, the vapour–gas mixture is first adiabatically expanded to a state of high supersaturation, and kept at that constant thermodynamic state during a short period of time, the nucleation pulse. During this nucleation stage, a large number of droplets are formed. At the end of the nucleation pulse, the gas is slightly recompressed, so that the formation of new droplets stops. A state of supersaturation is maintained, so that the existing small droplets can grow to optically detectable sizes. In this way, nucleation – that is, the birth of droplets – and droplet growth are effectively separated in time.

In chapter 3, the nucleation pulse method is analysed by solving two equations that describe the size distribution of droplets during condensation. The first equation, the kinetic master equation, is fundamental, and is the basis of classical nucleation theory. It describes the growth of molecular clusters of arbitrary size by collisions with monomers. The second equation, the general dynamic equation (GDE), is more simplified and is often used in condensation modelling of industrial devices and in aerosol science.

A word about notation: It is the opinion of the author that every additional subscript, superscript or accent makes a formula more difficult to read. Therefore, it has not always been attempted to create a unique symbol for each quantity. For example, the symbol ρ may denote either mass density, molar density, or number density. Of course, within an equation these meanings are never combined, and the symbol is explained where it is first used.

Acknowledgements

Geen enkel proefschrift komt tot stand zonder hulp van anderen, en dat geldt ook voor dit proefschrift. Allereerst bedank ik mijn promotor, Rini van Dongen, voor zijn begeleiding, steun en inspiratie. Ondanks de verandering van de groep GDY in MTP en zijn pensionering is hij altijd beschikbaar voor hulp en advies. Mico Hirschberg, mijn tweede promotor, wist altijd snel de essentie van mijn werk te vinden en daar nuttige vragen bij te stellen. De kennis uit zijn Shell-verleden kwam daarbij goed van pas.

Ik bedank de andere leden van mijn promotiecommissie – Honza Hrubý, Mike Golombok, Vitaly Kalikmanov, Franz Peters en Rob Hagmeijer – voor het lezen van dit toch wel dikke proefschrift. Mike Golombok in het bijzonder heeft vele nuttige opmerkingen gemaakt. Vitaly Kalikmanov heeft op eigen initiatief een gedetailleerde wiskundige analyse gemaakt naar aanleiding van hoofdstuk 3.

Het experimentele werk van dit proefschrift is financieel gesteund door STW, via het gerelateerde project van Dima Labetski. Ik bedank de medewerkers van de deelnemende bedrijven in de gebruikerscommissie – Nederlandse Gasunie, Twister BV en Shell – voor hun ondersteuning. De experimentele opstelling is door de jaren heen verbeterd dankzij de expertise van onze technici. Jan Willems en Herman Koolmees, bedankt voor jullie werk. Mijn vader, Ad Holten, heeft de optische opstelling meerdere keren verbeterd of opnieuw uitgelijnd. Freek van Uittert heeft bijgedragen op elektronisch gebied. Hopelijk krijgt de opstelling een tweede leven in Delft; mijn dank aan David Smeulders voor de geplande overname ervan. Dima Labetski heeft een gedeelte van de experimenten samen met mij uitgevoerd, waarvoor mijn dank.

De werksfeer in Cascade is goed, wat te danken is aan de medewerkers,

promovendi en studenten; bedankt daarvoor. Ze allemaal opnoemen is niet mogelijk, maar ik wil hier Brigitte en Marjan van de secretariaten bedanken voor hun hulp (ook af en toe een L^AT_EX-probleem voor jullie oplossen was een leuke uitdaging). Ook waardeer ik Ergün Çekli als prettige kamergenoot.

Ik en Rini hebben prettige discussies gehad over nucleatie en druppelgroei met mensen van de groep van Harry Hoeijmakers, namelijk Rob Hagmeijer, Ryan Sidin en Dennis van Putten. Het is leuk om te zien hoe dit heeft geleid tot nieuwe inzichten.

Contacts with people abroad have been very useful to me. I thank Honza Hrubý for his interest in my work and for the invitations to the Institute of Thermomechanics in Prague. Jussi Malila of the University of Kuopio shares my interest in the properties of supercooled water. I thank him for pointing out new measurement data and for making available his preprint. Like Jussi Malila, others have taken the trouble of including my measurement data in their research, including David Brus, Dimo Kashchiev and Tomáš Němec, for which I thank them. I am grateful to Martin Wendland from the Universität für Bodenkultur Wien for making available unpublished data to me. Gerry Wilemski taught me useful things about nucleation and was good company when we were in Prague. Finally, I thank Vitaly Shneidman for pointing out the relevance of his work and for providing the numerical computations, of which the results are in Figure 3.2.

Contents

Introduction 1

- 1 Phase Equilibrium 7**
 - 1.1 Thermodynamics 7
 - 1.2 Equations of state 14
 - 1.3 Software packages 20
 - 1.4 Pure components 23
 - 1.5 Water–methane 30
 - 1.6 Water–carbon dioxide 38
 - 1.7 Methane–carbon dioxide 45
 - 1.8 Ternary system 47
 - 1.9 Surface tension 50
 - 1.10 Conclusion 58

- 2 Nucleation and droplet growth theory 59**
 - 2.1 Capillarity approximation 59
 - 2.2 Energy of cluster formation 60
 - 2.3 Cluster size distributions 63
 - 2.4 Kinetic model 66
 - 2.5 Detailed balance 68
 - 2.6 Steady-state nucleation 72
 - 2.7 Steady-state nucleation rate 76
 - 2.8 Non-steady-state nucleation 79
 - 2.9 Nucleation theorem 84
 - 2.10 Other nucleation theories 89
 - 2.11 Droplet growth 91

- 3 Comparison of the GDE and the kinetic equation 99**
 - 3.1 Introduction 99
 - 3.2 Theory 101
 - 3.3 Numerical approach 106
 - 3.4 Numerical comparison of the models 108
 - 3.5 Conclusion 115

| | | |
|----------|---|------------|
| 4 | Experimental methods | 117 |
| 4.1 | Expansion wave tube | 119 |
| 4.2 | Thermodynamic state | 124 |
| 4.3 | Optical measurements | 128 |
| 4.4 | Mixture preparation | 137 |
| 4.5 | Experimental procedure | 146 |
| 5 | Water nucleation in helium | 147 |
| 5.1 | Experimental supersaturations | 148 |
| 5.2 | Empirical fit of nucleation rates | 149 |
| 5.3 | Nucleation rate results | 150 |
| 5.4 | Empirical correction of classical theory | 153 |
| 5.5 | Critical cluster sizes | 155 |
| 5.6 | Hale's scaled model | 157 |
| 5.7 | Conclusion | 158 |
| 6 | Water nucleation in methane and carbon dioxide | 159 |
| 6.1 | Nucleation rates | 159 |
| 6.2 | Critical cluster composition | 161 |
| 6.3 | Comparison with theory | 164 |
| 6.4 | Possible sources of error | 166 |
| 6.5 | Droplet growth rates | 169 |
| 6.6 | Conclusion | 173 |
| | Conclusion | 175 |
| A | Properties of supercooled water | 179 |
| B | Water–methane composition fits | 187 |
| C | Numerical solution of the kinetic equation | 191 |
| D | Experimental data | 195 |
| | Summary | 203 |
| | References | 207 |
| | Curriculum vitae | 219 |

Introduction

This thesis is about the condensation of water. At first glance, it seems that everything is known about such a simple phase transition – what is left to study? To illustrate some basic concepts, in this chapter we will try to answer a simple question: when does water condense? As an example, we will consider condensation in the air.

It is clear that the occurrence of condensation depends on the amount of moisture in the air. Therefore, it is worthwhile to look at some of the ways the moisture content can be quantified. A straightforward way is to simply specify the mass of water present in a volume of air. Such a specification of absolute humidity does not show whether condensation will occur; for example, does an amount of ten gram of water per cubic metre of air cause condensation? For this reason, it is useful to compare the absolute humidity to a reference value, the saturated state.

What is saturation? The saturated moisture content exists above a pool of water in an enclosed space, in equilibrium (that is, we should wait long enough until the moisture content is stable). The saturated moisture content is the maximum amount of water that can exist in the vapour state, in equilibrium. It is well known that this quantity depends strongly on the temperature, as shown in Figure 1. Usually, the saturated moisture content is expressed as a partial pressure, and is then called the *saturated vapour pressure*. In the figure, the moisture content is also shown as mass of water per m^3 .

We read from Figure 1 that the vapour pressure rises with increasing temperature. This represents the common knowledge that ‘warm air can hold more water vapour than cold air’. However, air does not have a ‘holding capacity’ for water vapour. If that were the case, we would expect the moisture content to double if we doubled the air pressure. In addition, water vapour would then not exist without the presence of air. In reality, the saturated vapour pressure is almost independent of the air pressure.* The rise of the saturated vapour pressure that we see in Figure 1 is therefore not a property

* Only at very high pressures does the saturated vapour pressure deviate from its low-pressure value.

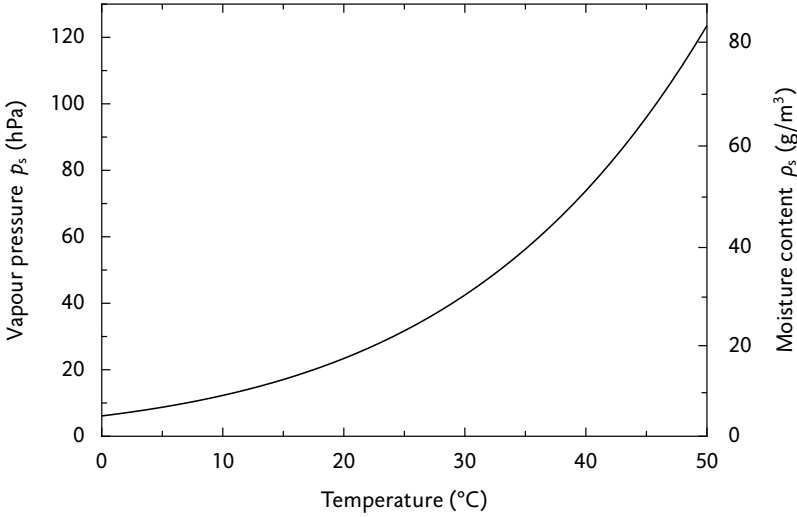


Figure 1: Saturated vapour pressure of water as a function of the temperature.¹⁴ On the right axis, the saturated moisture content is displayed as mass of water per cubic metre.

of the air, but a characteristic of water itself.

Now that we have a definition of a reference state, namely, the saturated state, we can define more common humidity quantities. First, we introduce the *relative humidity* (RH), which is simply the ratio of the actual moisture content and the saturated value, so

$$\text{RH} \equiv \frac{\rho_w}{\rho_s(T)} \quad \text{or} \quad \text{RH} \equiv \frac{p_w}{p_s(T)}, \quad (1)$$

where ρ_w is the mass of water per unit volume, and ρ_s is its value at saturation. Similarly, p_w is the partial water pressure, and p_s is the saturated vapour pressure. The relative humidity is usually expressed as a percentage.

From its definition it is clear that the RH depends both on the amount of moisture and on the temperature. Consider, for example, an atmosphere containing a constant amount of water vapour while it is being cooled down. The RH will increase (because ρ_s or p_s decreases), while the mass of water per unit of volume remains the same. When the RH reaches 100%, mist forms.

The dependence of the RH on the temperature can be inconvenient, since it must always be known whether a change in RH is caused by a change in temperature or by a change in water content. Therefore, an additional quantity exists, which does not depend on the temperature. This is the *dew point*, and it is defined as the temperature to which the atmosphere must be cooled down to reach saturation. Equivalently, it is the temperature at which the RH would be 100%. In the mist formation example, the dew point remains the

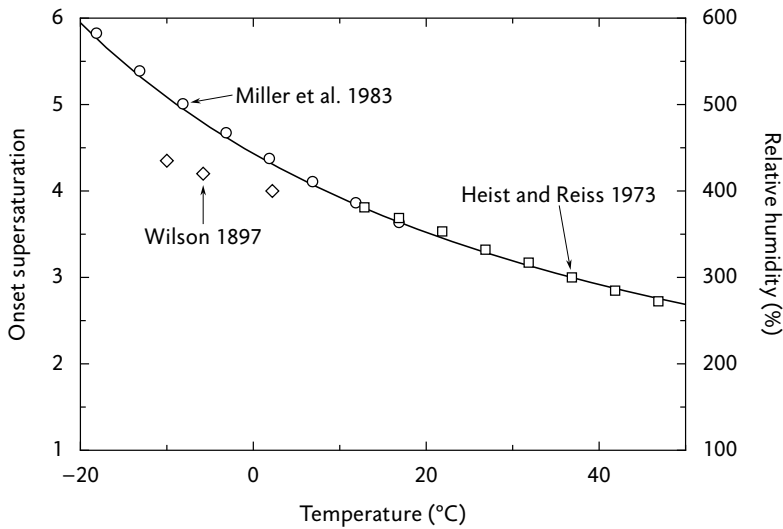


Figure 2: Onset supersaturation (the supersaturation at which condensation is observed) of water as a function of the temperature.^{16–18} The line is an empirical correlation from Wölk and Strey.¹⁹ The results of Wilson¹⁶ are thought to have been influenced by the presence of ions in the air.²⁰

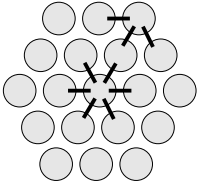
same while the air cools down. When the temperature becomes equal to the dew point, the mist is formed.

At this point it seems that we have accomplished our goal of predicting when water condenses. The apparent answer is: water condenses when the RH reaches 100%, or when the temperature drops below the dew point. Although this statement is plausible and agrees with common experience, it is not true in all cases. Specifically, it fails when the water vapour does not have anything to condense on. Usually, there are surfaces or dust particles that act as starting points for condensation. But what happens when these are absent?

This situation was investigated by researchers such as Wilson¹⁶ at the end of the nineteenth century. Wilson studied the formation of fog in clean moist air that was cooled down by rapidly expanding it. In this way, condensation on the walls was prevented because these remained at room temperature. Wilson found that it was possible to obtain a fog, but it required RH values far above 100%, namely 400% to 800%. He concluded that condensation centres, which he called nuclei, must be present as ‘an essential part of the structure of the moist gas’. He speculated that the nuclei are aggregates of water molecules, which form randomly due to the collisions of the molecules. Remarkably, Wilson was right, as was later proven.

Experiments similar to Wilson’s led to the picture shown in Figure 2. There, the RH is shown at which condensation occurs in clean moist air in

the absence of walls. In the figure, this quantity is referred to as *onset supersaturation*. In condensation research, the term ‘supersaturation ratio’ is used instead of ‘relative humidity’, especially for RH values above 100%. The supersaturation ratio, usually shortened to ‘supersaturation’,* is indicated by the symbol S and is specified as a pure number (not as a percentage), but the definitions of RH and S are identical (Eq. 1). The supersaturation at which the condensation starts is called the onset supersaturation.



It is observed that at any temperature, the water needs to be saturated much more than $S = 1$ to condense. Why is this so? The answer to this question was already given by Gibbs²⁴ in 1876. Condensation requires the formation of a surface, namely, the boundary between liquid and vapour. It turns out that the formation of a surface is energetically unfavourable. This can be understood from a molecular point of view. A molecule deep inside a liquid droplet feels the attractions of neighbouring molecules on all sides. That attraction is the reason that the liquid phase is energetically favoured more than the vapour phase. In contrast, a surface molecule feels less than half of these attractions.

Taking all molecules into account, we can compute W , the energy of formation of an entire droplet or molecular cluster. A positive W means that the formation of a cluster costs energy, whereas a negative W means that energy is released. Whether W is positive or negative depends on the ratio of volume and surface area of a droplet; therefore, W depends on the droplet’s size. It is derived in chapter 2 that W is given by

$$\frac{W}{kT} = -n \ln S + n^{2/3} \Theta, \quad (2)$$

where k is Boltzmann’s constant, T is the temperature, n is the number of molecules in a cluster, S is the supersaturation and Θ is a measure of the surface energy of water. The energy of formation consists of two terms that represent the contributions of the cluster’s volume and surface to the total energy. The first term, $-n \ln S$, is proportional to the number of molecules or to the volume of the cluster. It is negative if $S > 1$, that is, if there is more water vapour than in equilibrium. The surface term $n^{2/3} \Theta$, on the other hand, is always positive.

In Figure 3, the work of formation is plotted as a function of the cluster size, for several values of the supersaturation S . For small clusters, the surface contribution is important, and W is positive at those sizes. The volume term

* The abbreviation of ‘supersaturation ratio’ to ‘supersaturation’ is not adopted by most textbook authors.^{21,22} Some reserve the term ‘supersaturation’ for the quantity $S - 1$.^{20,23} Others call S the ‘saturation ratio’.²³ In this work, ‘supersaturation’ refers to S .

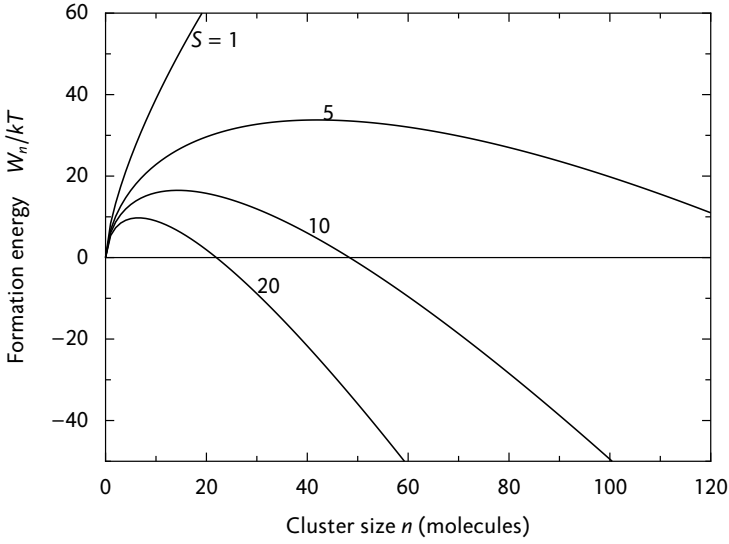


Figure 3: Energy of formation W for water clusters at 20 °C, according to Eq. 2, for several values of the supersaturation S .

contains a higher power of n than the surface term, so there is a size at which the volume term becomes dominant. In the graph, it is seen that for $S > 1$, W reaches a maximum, after which it decreases. The cluster size at which the formation energy W has its maximum value is called the *critical size* and is indicated by n^* . It is easily obtained by solving $dW/dn = 0$, yielding

$$n^* = \left(\frac{2\Theta}{3 \log S} \right)^3. \quad (3)$$

Knowing the size dependence of W does not provide an immediate answer to the question of condensation. It appears from Figure 3 that small clusters are always energetically unfavourable, for any supersaturation. Then how does the phase transition start? The explanation is that clusters with a positive W are rare, but do exist as a result of random molecular collisions, just as Wilson presumed. The number density of clusters follows a Boltzmann distribution,

$$\rho_n \propto \exp(-W/kT) = \exp(n \ln S - n^{2/3}\Theta), \quad (4)$$

where ρ_n is the number of clusters of n molecules per unit of volume. Once a cluster succeeds in growing to a size larger than the critical size, it is likely to grow to macroscopic size. The formation of these small molecular clusters is called *nucleation*. In the absence of particles or walls, nucleation is said to be homogeneous; otherwise, it is heterogeneous.

We can now explain why a supersaturation higher than unity is required for condensation in the absence of dust or walls. The formation of a surface costs energy, and molecular clusters are therefore rare. Only at high supersaturations, there are enough critical clusters to enable a large-scale phase transition. Whether condensation is observable depends on the rate at which clusters grow larger than the critical size, and also on the number density of those clusters. To describe this process more exactly, we define the *nucleation rate* as the frequency at which clusters in a unit volume succeed in surpassing the critical size. In other words, the nucleation rate is the number of energetically stable droplets that are formed per unit time and volume.

The nucleation rate, indicated by the symbol J , can be approximated by the frequency at which critical clusters gain a molecule. This frequency is the product of the number density of critical clusters ρ_{n^*} and the rate C_{n^*} at which molecules hit a critical cluster, so

$$J \approx C_{n^*} \rho_{n^*}. \quad (5)$$

With the expressions for the critical size (Eq. 3) and for the number density (Eq. 4), we obtain

$$J \propto C_{n^*} \exp \left[-\frac{4}{27} \frac{\Theta^3}{(\ln S)^2} \right]. \quad (6)$$

This expression shows that the nucleation rate is very sensitive to the supersaturation. For example, in our experiments it is observed that when S is increased by 10%, the nucleation rate becomes ten times as large. The rate is even more sensitive to the surface energy Θ .

Let us return to the question posed at the beginning: when does water condense? Qualitatively, we can say that in the absence of walls and particles, a sufficiently high supersaturation is required so that nucleation results in an observable amount of droplets. Quantitatively, Eq. 6 specifies the nucleation rate, but since that expression is only an approximation, it is not the ultimate answer. In the end, only experiments can show us the nucleation behaviour of water.

Phase Equilibrium

Nucleation takes place at conditions far from phase equilibrium; indeed, nucleation and droplet growth are the mechanisms that enable the system to reach phase equilibrium. The rate of nucleation depends strongly on the deviation from equilibrium, so knowledge of the exact phase equilibrium conditions is essential. In our experiments, we either examine a binary system (water and methane, or water and helium) or a ternary system (water, methane and carbon dioxide). In the first part of this chapter, the thermodynamics of phase equilibrium is described, and the supersaturation is defined for non-ideal mixtures. In the second part, the liquid–vapour equilibria in our binary and ternary systems are examined in detail, and modelled by an equation of state.

1.1 Thermodynamics

From the first and second laws of thermodynamics, it follows that the energy of a homogeneous, open system in equilibrium is a function of the entropy S , the volume V , and the numbers of molecules of the components n_i :

$$U = U(S, V, n_1, n_2, \dots). \quad (1.1)$$

For a reversible change, the change in energy is given by

$$dU = T dS - p dV + \sum_i \mu_i dn_i, \quad (1.2)$$

with T the temperature, p the pressure, and μ_i the chemical potential of component i . It is usually more convenient to have p and T as independent variables, instead of S and V . This change of variables is performed with a Legendre transform, and the transformed function is called the Gibbs energy G :

$$G = U - TS + pV, \quad (1.3)$$

with a differential of

$$\begin{aligned} dG &= dU - T dS - S dT + p dV + V dp \\ &= V dp - S dT + \sum_i \mu_i dn_i, \end{aligned} \quad (1.4)$$

where Eq. 1.2 was used to eliminate dU . From this equation, it follows that the chemical potential is the partial molecular Gibbs energy:

$$\mu_i = \left(\frac{\partial G}{\partial n_i} \right)_{p, T, n_{j \neq i}}, \quad (1.5)$$

where the subscript means that p , T and all n_j 's except n_i are held constant. The Gibbs energy G and the numbers of molecules n_i are extensive quantities, so that Eq. 1.5 can be integrated at constant p and T with Euler's theorem for homogeneous functions. It then follows that the total Gibbs energy of the mixture is

$$G = \sum_i n_i \mu_i, \quad (1.6)$$

which has a total differential of

$$dG = \sum_i n_i d\mu_i + \sum_i \mu_i dn_i. \quad (1.7)$$

The substitution of Eq. 1.7 in Eq. 1.4 gives the Gibbs–Duhem equation, which relates a change in chemical potential to changes in pressure and temperature.

$$\sum_i n_i d\mu_i = V dp - S dT. \quad (1.8)$$

Chemical potential

The chemical potential of a pure substance is a function of pressure and temperature. As only isothermal processes will be considered here, the temperature dependence will be omitted. For a pure substance at constant T , the Gibbs–Duhem equation reduces to

$$d\mu = (V/n)dp. \quad (1.9)$$

An ideal gas satisfies the relation $pV = nkT$, which allows Eq. 1.9 to be integrated. The difference in chemical potential between two states with equal temperature and pressures p^0 and p is then

$$\mu^{\text{id}}(p) - \mu^{\text{id}}(p^0) = kT \ln \left(\frac{p}{p^0} \right), \quad (1.10)$$

where the superscript 'id' stands for ideal gas. The change in chemical potential resulting from a change in pressure is a function of the ratio of final and initial pressure. Because the chemical potential does not have an absolute reference point, we can only compute differences of potentials.

We now consider a mixture of gases (ideal or non-ideal) at total pressure p , with $n = \sum_i n_i$ the total number of molecules. The partial pressure of a substance is defined as

$$p_i = \frac{n_i}{n} p = y_i p, \quad (1.11)$$

where the molar fraction y_i of substance i was defined as the ratio of the number of molecules of substance i and the total number of molecules. By definition, the sum of partial pressures is equal to the total pressure.

If all the components are ideal gases, the chemical potential of a component is independent of the other components. Therefore, it is the same as the chemical potential of the pure component at a pressure equal to the partial pressure.

$$\bar{\mu}_i^{\text{id}}(p, y_i) = \mu_i^{\text{id}}(p_i) = \mu_i^{\text{id}}(y_i p). \quad (1.12)$$

The overbar on the $\bar{\mu}$ refers to the chemical potential of a component in a mixture, whereas μ retains its meaning of pure-component chemical potential.

The equivalent of Eq. 1.10 for a component in a mixture of ideal gases can be found by applying Eq. 1.12 to two different mixtures, and subtracting the results. In this way, the difference in chemical potential between the two mixtures is found.

$$\bar{\mu}_i^{\text{id}}(p, y_i) - \bar{\mu}_i^{\text{id}}(p^0, y_i^0) = kT \ln \left(\frac{y_i p}{y_i^0 p^0} \right). \quad (1.13)$$

The difference in chemical potential of a component is a function of the ratio of partial pressures.

The chemical potential of a component in the mixture can also be compared with that of the pure component, at a pressure equal to the pressure of the mixture, by taking $y_i^0 = 1$ and $p_0 = p$. The result is

$$\bar{\mu}_i^{\text{id}}(p, y_i) - \mu_i^{\text{id}}(p) = kT \ln(y_i), \quad (1.14)$$

where Eq. 1.12 was used. The term $kT \ln y_i$ represents the decrease in chemical potential that results from the mixing of the pure component with the other components. A mixture that obeys Eq. 1.14 is called an *ideal solution*.

Fugacity

It is desirable to describe chemical potential differences of components in non-ideal gas mixtures in a similar form as in Eq. 1.13. For this purpose, a

quantity called *fugacity* with symbol f is introduced, which has a dimension of pressure. It is defined by the relation²⁵

$$\bar{\mu}_i(p, \mathbf{y}) - \bar{\mu}_i^{\text{id}}(p, y_i) = kT \ln \left(\frac{\bar{f}_i(p, \mathbf{y})}{y_i p} \right). \quad (1.15)$$

The overbar on the \bar{f} again refers to a property of a mixture component. Further, $\bar{\mu}_i$ (without superscript ‘id’) is the real chemical potential of component i , which depends on the total pressure p and the molar fractions of *all* other components, denoted by the vector $\mathbf{y} = (y_1, y_2, \dots)$. In contrast, the ideal chemical potential $\bar{\mu}_i^{\text{id}}$ only depends on p and the molar fraction y_i of component i .

The fugacity describes the deviation from ideal behaviour in a convenient way. For an ideal gas, the left-hand side of Eq. 1.15 vanishes, so the fugacity of an ideal gas is simply equal to the partial pressure.

$$\bar{f}_i^{\text{id}} = y_i p. \quad (1.16)$$

In general, the fugacity and the partial pressure are not equal; their ratio is called the fugacity coefficient ϕ , or

$$\phi_i = \frac{\bar{f}_i}{y_i p}. \quad (1.17)$$

We now apply Eq. 1.15 to two mixtures and subtract the results to find the difference in chemical potential. The terms containing the ideal partial pressures cancel, yielding

$$\bar{\mu}_i - \bar{\mu}_i^0 = kT \ln \left(\frac{\bar{f}_i}{\bar{f}_i^0} \right), \quad (1.18)$$

where the notation has been simplified by omitting the dependencies of $\bar{\mu}$ and \bar{f} . This equation can be seen as an alternative definition of the fugacity; namely, a ratio of fugacities is equivalent to a difference in chemical potential. The ratio of fugacities \bar{f}_i/\bar{f}_i^0 is called the *activity* of component i , and depends on the chosen reference state.²⁵ This definition of the activity is more general than the usual one,^{26,27} where the reference is always the pure component. For that particular pure reference state, Eq. 1.18 can be written in a form similar to the equation for ideal solutions (Eq. 1.14). This results in

$$\bar{\mu}_i(p, T, \mathbf{y}) - \mu_i(p, T) = kT \ln(\gamma_i y_i), \quad (1.19)$$

where the activity coefficient γ_i was introduced as

$$\gamma_i = \frac{\bar{f}_i}{y_i \bar{f}_i^0}, \quad (1.20)$$

and f_i (without bar) is the fugacity of the pure component i . For ideal solutions, the activity coefficient is unity (compare Eq. 1.14).

Binary system

We consider binary systems in which one component is water and the other is a carrier gas. According to the Gibbs phase rule, when two phases are in equilibrium in a binary system, there are two degrees of freedom (e.g. pressure and temperature). Accordingly, the equilibrium vapour fraction of water can be written as a function of the temperature and the pressure.

We will calculate the chemical potential of water in the mixture, both in the vapour phase and in the liquid phase. As a reference chemical potential, we use that of pure water in liquid–vapour equilibrium, at a temperature T with a saturated vapour pressure $p_s(T)$.

The subscript i is omitted; all quantities refer to the condensing component (water, in our case). The symbol x will be used to denote the molar fraction of water in the liquid phase, while y refers to the corresponding molar vapour fraction. Further, superscripts ‘l’ and ‘v’ (used with the chemical potential μ) denote water in the liquid and vapour phase, respectively.

The chemical potential of water in the liquid phase is

$$\begin{aligned}\bar{\mu}^l(p, x) &= \mu^l(p) + kT \ln(\gamma x) \\ &= \mu^l(p_s) + \int_{p_s}^p v^l(p') dp' + kT \ln(\gamma x),\end{aligned}\quad (1.21)$$

where the activity coefficient from Eq. 1.19 was used to express the difference with the chemical potential of pure water. Furthermore, the Gibbs–Duhem equation (Eq. 1.9) with molecular volume v^l was used to account for the pressure difference $p - p_s$.

The chemical potential of the water in the vapour phase can immediately be related to the pure, saturated state with the help of Eq. 1.18, yielding

$$\bar{\mu}^v(p, y) = \mu^v(p_s) + kT \ln\left(\frac{\phi y p}{\phi_s p_s}\right).\quad (1.22)$$

The chemical potential of water vapour is equal to that of liquid water, both in the pure case and in the binary two-phase equilibrium, so

$$\mu^v(p_s) = \mu^l(p_s) \quad \text{and} \quad \bar{\mu}^v(p, y_{\text{eq}}) = \bar{\mu}^l(p, x_{\text{eq}}),\quad (1.23)$$

where the subscript ‘eq’ refers to the binary two-phase equilibrium. With these conditions for phase equilibrium, the combination of Eqs. 1.21 and 1.22 leads to

$$kT \ln\left(\frac{\phi_{\text{eq}} y_{\text{eq}} p}{\phi_s p_s}\right) = \int_{p_s}^p v^l(p') dp' + kT \ln(\gamma_{\text{eq}} x_{\text{eq}}).\quad (1.24)$$

For the vapour fraction of water it follows that

$$y_{\text{eq}} = \frac{p_s}{p} \frac{\phi_s}{\phi_{\text{eq}}} \gamma_{\text{eq}} x_{\text{eq}} \exp \left(\int_{p_s}^p \frac{v^l(p')}{kT} dp' \right). \quad (1.25)$$

This final result contains several factors that influence the vapour fraction. In the simplest approximation, the partial pressure of water yp is equal to the saturated vapour pressure p_s , so that the vapour fraction equals the pressure ratio p_s/p . In addition, the x_{eq} takes into account that the vapour fraction decreases when other substances dissolve into the liquid; together with the pressure ratio it forms *Raoult's law*. Next, the factors ϕ_s and ϕ_{eq} are corrections for the non-ideality of the water vapour, and γ_{eq} corrects for the liquid non-ideality. Finally, the exponential factor is called the *Poynting correction*.^{25,26} It represents the effect on the liquid of the pressure increase from p_s to p , which increases the vapour fraction; it is independent of the type of carrier gas. Even when all substances are ideal, the Poynting effect is present. For water, the Poynting effect is relatively small: for temperatures above 230 K and pressures below 10 bar, the exponential factor lies between 1.00 and 1.01.

The vapour fraction is approximately inversely proportional to the pressure, and also replicates the strong temperature dependence of $p_s(T)$. Therefore, it is often more convenient to use a derived quantity called *enhancement factor* from which these dependencies have been excluded. The enhancement factor f_e is defined as

$$f_e(p, T) = y_{\text{eq}}(p, T) \frac{p}{p_s(T)} = \frac{p_w(p, T)}{p_s(T)}, \quad (1.26)$$

and equals the ratio of the partial water pressure p_w in the vapour phase and the saturated vapour pressure $p_s(T)$ of pure water. The enhancement factor is usually larger than unity, which corresponds to an increase or 'enhancement' of the water vapour fraction. At low pressure ($p = p_s$), the enhancement factor equals unity.

Supersaturation

The supersaturation is a measure of the deviation from equilibrium; it compares the current, possibly metastable, state with the corresponding equilibrium state. Which equilibrium composition corresponds to a certain supersaturated state is not always a trivial question.

The supersaturation S_i of component i in the vapour phase is defined as the activity of that component, where the reference state is a vapour-liquid equilibrium at the same temperature and pressure. Then S_i is given by

$$S_i = \frac{\bar{f}_i(p, T, \mathbf{y})}{\bar{f}_i(p, T, \mathbf{y}_{\text{eq}})} = \exp \left[\frac{\bar{\mu}_i^{\text{y}}(p, T, \mathbf{y}) - \bar{\mu}_i^{\text{y}}(p, T, \mathbf{y}_{\text{eq}})}{kT} \right], \quad (1.27)$$

where the last equality follows from Eq. 1.18. This definition of S_i is incomplete because in systems with three or more components, the equilibrium composition y_{eq} is not uniquely defined by p and T . However, a binary system at vapour–liquid equilibrium has two degrees of freedom, so p and T suffice to determine the equilibrium. In that case, the supersaturation definition can be simplified, using the definition of the fugacity coefficient (Eq. 1.17) and the enhancement factor (Eq. 1.26), resulting in

$$S = \frac{\phi}{\phi_{\text{eq}}} \frac{y}{y_{\text{eq}}} = \frac{yP}{f_e p_s} \frac{\phi}{\phi_{\text{eq}}}. \quad (1.28)$$

In this equation and in the following ones, the subscript i has been omitted; all quantities refer to the condensing component (in our case, water). In Eq. 1.28, the fugacity coefficients ϕ and ϕ_{eq} account for the intermolecular forces between a water molecule and other molecules (both water molecules and carrier gas molecules). Both in the initial state and in the equilibrium state, the vapour fraction of water in our experiments is very small (at most 5×10^{-3}), so that nearly all neighbour molecules are carrier gas molecules. Therefore, ϕ and ϕ_{eq} are approximately equal, and Eq. 1.28 reduces to

$$S \approx \frac{y}{y_{\text{eq}}} = \frac{yP}{f_e p_s}. \quad (1.29)$$

Ternary system

In a system with three components at two-phase equilibrium, there are three degrees of freedom. Considering our ternary system, methane/carbon dioxide/water, the equilibrium vapour fraction of water can be written as a function of temperature, pressure and the vapour fraction of carbon dioxide, for example. Then, the enhancement factor can be defined as

$$f_e(p, T, y_c) = y_{\text{eq}}(p, T, y_c) \frac{P}{p_s(T)}, \quad (1.30)$$

where y_c is the vapour fraction of carbon dioxide.

To define the supersaturation, a reference state is needed. Unlike the binary case, in the ternary system pressure and temperature alone are insufficient to define an equilibrium state; the vapour fraction of one component is needed as well. In our experiments, the amount of water is so small that the vapour fractions of methane and carbon dioxide hardly change during condensation; therefore, either vapour fraction can be taken constant. We arbitrarily choose to take the carbon dioxide fraction constant, so that Eq. 1.27 becomes

$$S = \frac{\phi(p, T, y, y_c)}{\phi_{\text{eq}}(p, T, y_c)} \frac{y}{y_{\text{eq}}(p, T, y_c)} \approx \frac{yP}{f_e(p, T, y_c) p_s(T)}, \quad (1.31)$$

where the same approximation for the fugacity coefficients was made as in the binary case.

1.2 Equations of state

A fundamental thermodynamic equation such as $U = U(S, V, n_1, n_2, \dots)$ or $G = G(p, T, n_1, n_2, \dots)$ provides information about all thermodynamical quantities of a system. For our purposes, an equation of state that relates pressure, temperature, volume and composition (called a thermal equation of state) is sufficient. Such an equation of state (EOS) is usually explicit in the pressure,

$$p = p(T, v, \mathbf{x}), \quad (1.32)$$

and depends on the temperature T , a specific volume v (such as the molar or molecular volume), and the molar fractions $\mathbf{x} = (x_1, x_2, \dots)$. For a pure component, Eq. 1.32 reduces to

$$p = p(T, v). \quad (1.33)$$

Cubic equations of state

An important type of EOS is the cubic EOS, which has the form of Eq. 1.33, and can be converted to a cubic equation in the specific volume (i.e., it contains powers of v of degree three and lower). A cubic EOS is the simplest EOS that can describe both the gaseous and the liquid phase because the equation $p = p(T, v)$ can have multiple solutions of v for a single p and T . The simplest cubic EOS is the van der Waals equation

$$p = \frac{RT}{v - b} - \frac{a}{v^2}, \quad (1.34)$$

where v is the molar volume and R is the molar gas constant. Furthermore, a and b are substance-specific constants that account for the intermolecular forces and the molecular volume, respectively. Two other widely-used equations are the Soave modification²⁸ of the Redlich–Kwong²⁹ EOS, denoted by RKS, and the Peng–Robinson³⁰ (PR) EOS. The RKS EOS has the form

$$p_{\text{RKS}} = \frac{RT}{v - b} - \frac{a(T)}{v(v + b)}, \quad (1.35)$$

and the PR EOS is

$$p_{\text{PR}} = \frac{RT}{v - b} - \frac{a(T)}{v(v + b) + b(v - b)}, \quad (1.36)$$

where a depends on temperature as

$$a(T) = a_0 \cdot [1 + c \cdot (1 - \sqrt{T/T_c})]^2, \quad (1.37)$$

with a_0 and c substance-specific constants, and T_c the critical temperature. The temperature dependence of a was chosen by Soave²⁸ to optimize the calculated saturated vapour pressure.

To describe mixtures, a single EOS is used – the one that is used to model the pure components – but with parameters a and b that depend on the mixture composition. In this so-called one-fluid model, the equations that describe the composition dependence of the parameters are called mixing rules. Usually, a quadratic dependence on molar fraction is taken:²⁵

$$a = \sum_i \sum_j x_i x_j a_{ij}, \quad \text{and} \quad b = \sum_i \sum_j x_i x_j b_{ij}. \quad (1.38)$$

Here $a_{ii} = a_i$ is the value of a for the pure component i . The values a_{ij} and b_{ij} (with $i \neq j$) are binary parameters, which are obtained from the pure-component values with the combining rules

$$a_{ij} = \sqrt{a_i a_j} (1 - k_{ij}), \quad (1.39)$$

and

$$b_{ij} = \frac{b_i + b_j}{2} (1 - l_{ij}). \quad (1.40)$$

In these equations, the binary interaction parameters k_{ij} and l_{ij} have been introduced, which are corrections to the ideal arithmetic-mean and geometric-mean combining rules. The values of k_{ij} and l_{ij} are obtained by fitting the EOS to experimental mixture data. Often, the k_{ij} parameter alone provides an acceptable fit, and l_{ij} is taken zero. The mixing rule for b from Eq. 1.38 then reduces to the linear rule $b = \sum_i x_i b_i$.

CPA equation of state

Cubic equations of state perform well for non-polar substances, such as hydrocarbons, and their mixtures. They are less accurate for substances with strong attractive interactions between molecules, where the formation of molecular clusters can strongly affect the substance behaviour. Water, which is present in the mixtures we consider, has the ability to form hydrogen bonds and is therefore an associative substance.

A well-known description of associating fluids is called ‘chemical theory’, first published by Dolezalek in 1908.³¹ In this theory, each possible cluster

of molecules is considered a chemical species, which is formed and decomposed by chemical reactions. The concentration of each species is determined by the chemical equilibrium constants of the reactions. A disadvantage of chemical theory is that all reactions have to be known, as well as a method to compute or measure their equilibrium constants. An often-cited example of a chemical theory is that of Heidemann and Prausnitz,³² who combined a van der Waals-type EOS with chemical association reactions.

SAFT model

In contrast to chemical theories, physical theories explain non-idealities by interactions between molecules. The foundations for the statistical mechanics of associating fluids were laid by Wertheim³³ in a series of papers published in 1984 and 1986. Based on these papers, a theory called SAFT (statistical associating fluid theory) was developed by Chapman et al.³⁴ and Huang and Radosz.^{35,36} The original derivation of the SAFT theory is 'difficult to read' in the words of Müller and Gubbins,³⁷ who present a simplified overview in their review. Prausnitz et al.³⁸ even mention: 'The literature on SAFT is complex and confusing. The original article by Wertheim, while brilliant, is essentially incomprehensible. Much patience is required to understand what SAFT is, what it can and what it cannot do.'

The SAFT theory is a perturbation theory, in which the Helmholtz energy is a sum of the ideal gas Helmholtz energy and contributions from the molecular structure and interactions. Specifically, the effect of segmented molecules (also called chain molecules), and the effect of association sites on the molecules are taken into account.

In the SAFT model, a molecule can have any number of association sites of one or more types (for example, with a positive or negative charge), but the position of the sites on the molecule cannot be specified. A site on a molecule can bond to exactly one site on another molecule; furthermore, double or higher bonds between two molecules are not allowed. If molecules have more than one site, chain-like or branched clusters can be formed, but ring-like structures are not permitted. Association sites can be used to model hydrogen bonds, for example. In that case, one site type represents the hydrogen atoms that can participate in a hydrogen bond, and another site type represents the lone electron pairs on electronegative atoms.

CPA model

In 1996, Kontogeorgis et al.³⁹ argued that the essential part in any EOS for associating fluids is the association term, while the performance of the EOS is relatively insensitive to the rest of the model. Taking into account the complexity of models like SAFT, they concluded that a simpler EOS for associating fluids could be obtained by combining a simple cubic EOS with the as-

sociation term of SAFT. The resulting EOS is called ‘cubic plus association’ (CPA).^{40,41} In terms of pressures, the CPA EOS can be written as

$$p_{\text{CPA}} = p_{\text{cubic}} + p_{\text{assoc}}, \quad (1.41)$$

where p_{cubic} is p_{RKS} or p_{PR} , for example. The association term is given by^{40,42}

$$p_{\text{assoc}} = -\frac{RT}{2v} \left(1 - v \frac{\partial \ln g}{\partial v} \right) \sum_i x_i \sum_{A_i} (1 - X_{A_i}), \quad (1.42)$$

with v the molar volume, g the radial distribution function evaluated at hard-sphere contact (to be discussed later) and x_i the molar fraction of component i . Further, A_i is the notation for site A on a molecule of component i , and X_{A_i} is the molar fraction of component i that has no bonds with other molecules at site A_i . The first sum in Eq. 1.42 is a summation over all components ($i = 1, 2, \dots$), while the second is a summation over all association sites of a component (e.g., for $i = 1$, the sites $A_1 = \text{I}_1, \text{II}_1, \text{III}_1, \dots$). Equation 1.42 follows from Wertheim’s statistical theory; a simpler heuristic derivation is given in the review of Müller and Gubbins.³⁷

The free-site fractions X_{A_i} are found by solving the set of mass balance equations

$$X_{A_i} = \frac{1}{1 + (1/v) \sum_j x_j \sum_{B_j} X_{B_j} \Delta_{A_i B_j}}, \quad (1.43)$$

where $\Delta_{A_i B_j}$ is the association strength between site A on molecule i and site B on molecule j . It has a dimension of volume and is given by the equation

$$\Delta_{A_i B_j} = \left[\exp \left(\frac{\varepsilon_{A_i B_j}}{kT} \right) - 1 \right] g(v) b_{ij} \beta_{A_i B_j}, \quad (1.44)$$

where $\varepsilon_{A_i B_j}$ is the association energy and $\beta_{A_i B_j}$ is the dimensionless association volume parameter.

Radial distribution function

In Eqs. 1.42 and 1.44, the quantity $g(v)$ appears, which is the radial distribution function (RDF) of a hard-sphere fluid, evaluated at molecular contact. The RDF describes how the local density varies as a function of the distance from the centre of a molecule, and is defined as the ratio of the local density and the average density.⁴³ For a fluid of hard spheres, the RDF is zero for distances smaller than the molecular diameter (because molecules cannot occupy the same space), and unity for large distances. In the SAFT and CPA EOS, only the value of the RDF at a distance equal to the molecular diameter (that is, at molecular contact) is used.

In SAFT, the RDF for mixtures of hard spheres derived by Mansoori et al.⁴⁴ is used. However, when Yakoumis et al.⁴⁵ extended CPA from pure components to mixtures, they retained the pure-component radial distribution function. Later, the RDF was further simplified by Kontogeorgis et al.⁴⁶ for faster computation. In contrast, Pfohl et al.⁴⁷ used the more complicated RDF for mixtures in their modified CPA EOS. The effect of the RDF on the results of CPA is minor, according to Kontogeorgis et al.,⁴⁰ who report that even the simplification $g = 1$ 'results in very similar performance'.

Pure components

Equations 1.43 and 1.44 are very general and allow for different interaction strengths between different sites. For pure-component association, simplifying assumptions are usually made, such as: (a) all site fractions and interaction strengths are equal, or (b) there are two types of sites, with equal interactions between unlike sites and no interactions between like sites. The latter association type, which will be used in this work, is suitable for modelling hydrogen bonds. The two site types then represent the positively charged hydrogen atom and the negative lone electron pair on another atom, respectively.

As an example, consider a molecule with two positive and two negative sites. With assumption (b) and an interaction strength denoted by Δ , the free-site fractions of all sites are equal and given by

$$X = \frac{\sqrt{1 + 8\Delta/v} - 1}{4\Delta/v} = \frac{2}{1 + \sqrt{1 + 8\Delta/v}}, \quad (1.45)$$

which follows from Eq. 1.43.

A pure associating component in the CPA EOS is defined by six parameters, namely, the two association parameters ε and β from Eq. 1.44, and the four cubic-EOS parameters a_0 , b , c and T_c . For components that have no association sites, or only sites with one polarity, the CPA EOS reduces to the cubic EOS that is used in its definition, and four parameters suffice.

Mixtures

When the CPA EOS is used to describe mixtures, the complexity of the EOS depends on the number of associating components. When only one associating component is present, the association term p_{assoc} from Eq. 1.42 for the mixture is the same as for the pure associating component. When, on the other hand, two or more associating components are present, we have to distinguish between self-association (association of the pure component) and cross-association (association between different components). There are also components without self-association that can take part in cross-association, depending on the type of the sites.

In any case with cross-association, the interaction strengths between sites on molecules of different components are needed. These parameters are often expressed in the form of combining rules, the simplest of which is the Elliott rule,⁴⁸

$$\Delta_{A_i B_j} = \sqrt{\Delta_{A_i B_i} \Delta_{A_j B_j}}, \quad (1.46)$$

where $A \neq B$ because only unlike sites associate ($\Delta_{A_i B_j}$ refers to, for example, the interaction between a positive site on a molecule of component i and a negative site on a molecule of component j). Another approach⁴⁹ is to write combining rules for the parameters ε and β , in the form

$$\varepsilon_{A_i B_j} = \sqrt{\varepsilon_{A_i B_i} \varepsilon_{A_j B_j}}, \quad \beta_{A_i B_j} = \sqrt{\beta_{A_i B_i} \beta_{A_j B_j}}. \quad (1.47)$$

All combining rules imply that the interaction A_i-B_j is the same as B_i-A_j , even though completely different site pairs are involved. When one of the cross-associating components does not have self-association, the combining rules lose their physical meaning because the non-self-associating component does not have the parameters Δ , ε , or β . In that case, these quantities are only used as fitting parameters without clear physical meaning.

Versions of CPA

After CPA was developed by Kontogeorgis et al.³⁹ in the group of Tassios, several modifications were made, primarily by Pfohl et al.⁴⁷ Most of those changes have been adopted by the Tassios group in recent publications,⁵⁰⁻⁵² but Kontogeorgis (who has left the Tassios group) and coworkers^{40,53,54} are still using the original version of CPA. In the present work, both versions will be used, so the differences are summarized below.

1. In the original Kontogeorgis version of CPA, the cubic EOS was RKS, while Pfohl et al. used the PR EOS. According to Pfohl et al.,⁴⁷ PR performs better than RKS for systems with carbon dioxide, although Pfohl et al.⁵⁵ showed earlier that the opposite is true when a cubic EOS is fitted to vapour pressure and liquid density.
2. Pfohl et al. reduced the number of parameters for the cubic part from four to three, by using equations that relate the a_0 and b parameters to the critical temperature T'_c and critical pressure p'_c . These critical parameters have prime marks, because they are fitting parameters and do not correspond to the experimental critical conditions; moreover, they do not even correspond to the calculated critical values in the case of an associating component. The ratio T/T_c that appears in Eq. 1.37 was replaced by T/T'_c , so that the experimental T_c disappears from the parameter set. In addition, the parameter c was replaced by the parameter ω' , which resembles

the Pitzer acentric factor.⁵⁶ The parameter c is a quadratic function of ω' ; the prime again indicates that ω' is a fitting parameter and may not be equal to the experimental acentric factor. The result of all these changes is the replacement of the parameter set a_0 , b , c and T_c by the reduced set T'_c , p'_c and ω' .

3. Pfohl et al. used the $a(T)$ function from Mathias⁵⁷ instead of Eq. 1.37 for $T > T'_c$ because the original Soave $a(T)$ shows unphysical behaviour at temperatures much higher than the critical temperature.⁵⁷
4. Pfohl et al. used the true radial distribution for mixtures instead of the pure-component RDF, as described above.

In this work, calculations with the CPA EOS were performed with the program Phase Equilibria (PE2000) by Pfohl et al.^{58,59} The PE2000 program contains several CPA versions, including the original Kontogeorgis formulation and the modified version by Pfohl et al. However, PE2000 uses the radial distribution function by Mansoori et al.⁴⁴ in all CPA versions, so the Kontogeorgis version in this work is not exactly equal to the original formulation. The different versions will be indicated as follows: CPA-RKS-K refers to the Kontogeorgis formulation with the Mansoori RDF, and CPA-RKS and CPA-PR refer to the Pfohl modification with either RKS or PR as the cubic EOS.

1.3 Software packages

The binary and ternary mixtures we consider are common in the natural gas industry, so it is not surprising that modelling tools have been developed for these mixtures. However, the industrial demands on these programs are quite different from our requirements, so an evaluation of the suitability of such a program is required. Two commercially available software packages were tested: NIST SUPERTRAPP and the GERG-2004 EOS.

NIST Supertrapp

The National Institute of Standards and Technology (NIST) of the USA has worked on the SUPERTRAPP (super transport property prediction) program⁶⁰ since 1981. It is also called the 'thermophysical properties of hydrocarbon mixtures database', and contains data for about 200 hydrocarbons and several inorganic substances. The range of validity of the program is 0 to 3000 bar and 10 to 1000 K. Water can only be included in the mixture as an impurity, with a molar fraction of less than five percent. It is therefore to be expected that predictions involving water have a limited accuracy. Phase compositions are computed with the Peng–Robinson EOS. The binary interaction parameters for this EOS are estimated using a correlation with critical molar volumes

and acentric factors. For the calculation of phase properties such as density and heat capacity, SUPERTRAPP offers a choice between Peng–Robinson and a model developed by NIST. Because we only use phase compositions, the choice of property model is not relevant for us.

GERG EOS

The GERG-2004 EOS^{61,62} was chosen by GERG (Groupe Européen de Recherches Gazières) as the reference equation of state for natural gases. The EOS contains data for 18 components, including the linear alkanes from methane to octane, carbon dioxide, nitrogen, helium, and water. The range of validity is 90–450 K and 0–350 bar.

The primary aim of the developers of the GERG EOS was a high accuracy (better than 0.1%) in gas phase properties, such as the density and speed of sound. In contrast, phase composition calculations were allowed to have uncertainties of 3% to 5%.

The GERG equation of state is explicit in the Helmholtz free energy, and consists of three parts: the ideal-gas part, the contribution of the pure substances and a departure function. The pure-component equations contain up to 24 polynomial and exponential terms, with coefficients that are fitted to property data. The departure function describes the non-ideality of the mixture, and is fitted to data of binary mixtures.

In the literature a model called ‘GERG-water’ is cited.^{54,63,64} Confusingly, this model is not the GERG-2004 EOS, but a modified Peng–Robinson EOS.

Evaluation of the packages

Two tests were performed to compare the phase equilibrium programs. First, the enhancement factor of water in methane was computed at 291 K and pressures up to 70 bar. These values are the conditions in the saturators in our setup. Enhancement factors were calculated with Eq. 1.26, using the programs’ predictions of the equilibrium vapour fraction of water in the water–methane system. In both programs, the water fraction is obtained by an algorithm called ‘isothermal flash calculation’. Such a calculation gives the compositions and amounts of the liquid and vapour phases that are in equilibrium at a given pressure, temperature and overall composition. The equilibrium vapour fraction of water should not depend on the overall composition, although the amounts of vapour and liquid do depend on it. Of course, the overall composition should contain enough water to allow the formation of a liquid phase, and enough methane to enable the existence of a vapour phase.

Figure 1.1 shows the enhancement factors predicted by different models, and the experimental value. The uncertainty in the experimental enhancement factor increases from zero near 0 bar to ± 0.05 near 70 bar. Both the

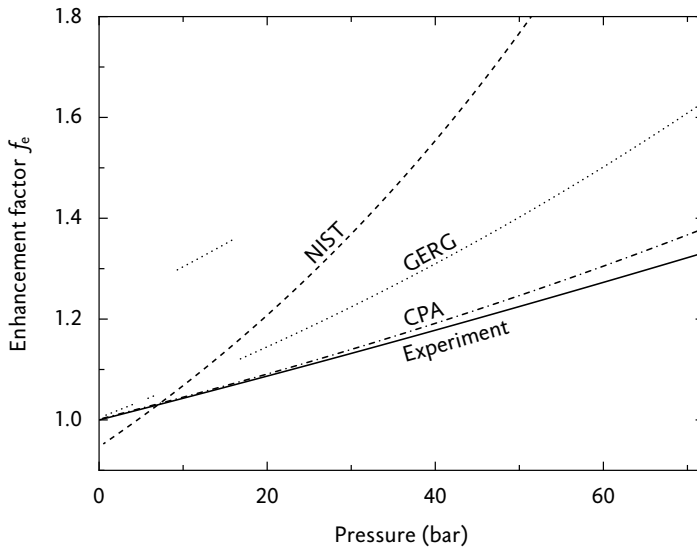


Figure 1.1: Enhancement factor (Eq. 1.26) of water in methane at 291 K. Shown is the experimental correlation of Eq. B.1 and model predictions by NIST-SUPERTRAPP, GERG-2004, and the CPA model from this work. The disconnected part of the GERG result between 9 and 16 bar is caused by an error in the GERG computer program and has no physical meaning.

GERG and the NIST program significantly overpredict the enhancement factor in almost the entire pressure range. As the pressure approaches the equilibrium vapour pressure of water (0.02 bar at 291 K) the enhancement factor should become unity; instead, the NIST enhancement factor becomes 0.95. Moreover, the NIST program gives a pressure dependence that is too strong. These inaccuracies are not surprising because the NIST model was not designed for water calculations.

The GERG program, on the other hand, includes a more accurate EOS for water and gives a better prediction as well. The low-pressure limit is correct, but the pressure dependence is too large. In the range of 9 bar to 16 bar, the flash calculations in the GERG program seem to converge to incorrect solutions, so a reliable value for the enhancement factor cannot be obtained at these conditions. Changing the overall composition did not solve this convergence problem. At 70 bar, the relative error in the GERG enhancement factor (and, therefore, also in the water vapour fraction) is more than 20%, which is much larger than the 5% uncertainty that is stated in the GERG-2004 description.⁶¹

The second test involved the computation of the solubility of carbon dioxide in liquid water. The equilibrium composition of the mixture of CO₂ and water was evaluated at 273.15 K (the lowest temperature where reliable ex-

perimental data exists) and at 2.5 bar (the highest partial pressure of CO₂ that occurs in our experiments). According to the accurate correlation of Diamond and Akinfiev,⁶⁵ at these conditions the molar fraction of CO₂ in water is 3.4×10^{-3} . The GERG model gives a fraction of 2.3×10^{-5} , and the NIST model predicts a fraction of 2.0×10^{-4} . With a respective deviation of one and two orders of magnitude, both the NIST and the GERG program perform poorly in reproducing the carbon dioxide solubility.

On the basis of the tests, it was decided that both software packages were not accurate enough for our purposes, and that a dedicated EOS had to be used. On the basis of the good results published in the literature,^{40,41} we selected the CPA EOS.

1.4 Pure components

The first step in fitting the CPA model is the optimization of the pure-component parameters. In the case of a component without self-association, this amounts to the three RKS or PR parameters; for self-associating substances two additional parameters are determined. A difficulty is that the choice of pure-component models and their parameters has an influence on the predicted composition of the binary mixtures, but this effect cannot be evaluated during the optimization of the pure-component parameters

Two methods exist for obtaining the parameters of a cubic EOS; one is to derive them from the critical conditions, another to fit the model to equilibrium vapour pressure and liquid density. The advantage of the first method is an exact reproduction of the critical temperature and pressure at the expense of accuracy further from the critical point. For our model, accuracy in the critical region is unimportant, whereas the vapour pressure at low temperatures should be predicted as accurately as possible. Therefore, we fitted the cubic EOS and the full CPA EOS to the experimental vapour–liquid equilibrium data.

Usually, an EOS is fitted at temperatures between about $0.5T_c$ and $0.9T_c$. The quality of the fit is given by the *objective function* f_{obj} , which is defined here as

$$f_{\text{obj}} = \frac{1}{2}(\Delta p_s + \Delta v_l), \quad (1.48)$$

with Δp_s and Δv_l the root-mean-square relative deviations of vapour pressure and liquid specific volume,

$$\Delta p_s = \left[\frac{1}{n} \sum_{i=1}^n \left(\frac{p_{s,i}^{\text{calc}} - p_{s,i}^{\text{exp}}}{p_{s,i}^{\text{exp}}} \right)^2 \right]^{1/2}, \quad (1.49)$$

and analogously for Δv_i . The sum runs over n data points (indicated by subscript i) that are selected for the fitting procedure. The fitting program iteratively searches for optimum EOS parameters that minimize the value of the objective function.

Water

It was expected that the prediction of the properties of water would reveal substantial differences between the candidate models CPA-PR, CPA-RKS and CPA-RKS-K. In contrast, it was assumed that the other components (methane and carbon dioxide) could be described well by any CPA version.

Experimental data

When selecting experimental data for fitting, both the source of the data and the temperature range have to be considered. In the case of water, the IAPWS-95 model clearly provides the most accurate description to date. It even reproduces the density of supercooled liquid water down to 234 K (see appendix A.2). Therefore, the IAPWS model was used for experimental vapour pressures and liquid densities. As mentioned before, usually a temperature

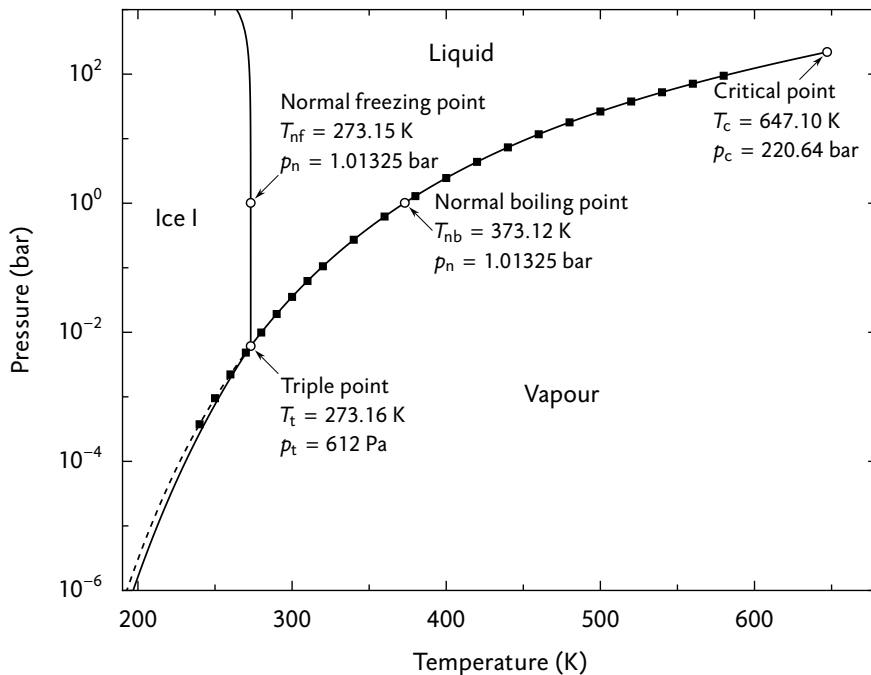


Figure 1.2: Phase diagram of water. Below the triple point, the solid line represents the sublimation pressure of ice, and the dashed line is the vapour pressure of supercooled liquid water. The small squares on the vapour–liquid equilibrium line are the data points used for the CPA fit. Data from Refs. 14, 66, 67.

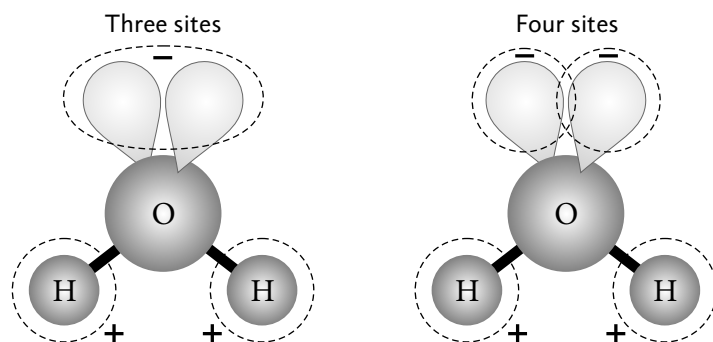


Figure 1.3: The water molecule with three or four association sites. The lobes above the oxygen atom represent the lone electron pairs. The lobes are not in the plane of the drawing; the arrangement of the lone pairs and the H atoms around the O atom is approximately tetrahedral. Adapted from Aparicio-Martínez and Hall.⁶⁸

range of $0.5T_c$ to $0.9T_c$ is chosen, which corresponds to 320–580 K for water. In this work, we are interested in lower temperatures, around 235 K, so we extended the range to 240–580 K. To bias the fit towards higher accuracy at low temperatures, more data points were included below 320 K. Specifically, points in the range of 240–320 K were spaced 10 K apart and points in the range of 320–580 K were given a spacing of 20 K. The points are shown in Figure 1.2, the phase diagram of water.

Association part

The association of the water molecule can be described by a three-site or a four-site model, as shown in Figure 1.3. In the literature both variants are discussed, but there is no agreement on which number of sites is best. Furthermore, the most appropriate number of sites depends on the other components in the mixture. For example, Perakis et al.⁵⁰ successfully used four-site water in a mixture with carbon dioxide and ethanol, but had to use three-site water in a mixture with carbon dioxide and acetic acid.⁵¹ Aparicio-Martínez and Hall⁶⁸ and Perakis⁵¹ mention that the simultaneous existence of four hydrogen bonds per water molecule might be impossible because of steric hindrance. In this case, steric hindrance means that there may not be enough space at the oxygen atom to form two hydrogen bonds at the same time. Despite these molecular considerations, in most studies the four-site model has given the best results, so we choose this model as well.

Fitting

Three versions of the CPA EOS were fitted to the property data, namely CPA-RKS-K, CPA-RKS and CPA-PR. The optimized parameters are shown in Table 1.1 and the deviations from the data in Table 1.2. The CPA-RKS and CPA-PR perform about equally well, and slightly better than CPA-RKS-K. Also shown are

Table 1.1: Optimized parameters of several CPA models for water

| EOS | Reference | T'_c (K) | p'_c (bar) | ω' | ε/k (K) | β | |
|-----------|-------------------------------|---|--------------|-----------|---------------------|----------|--|
| CPA-PR | this work | 401.51 | 167.09 | 0.086979 | 1651.7 | 0.072120 | |
| CPA-PR | Perakis ^{50,51} | 305.40 | 135.62 | 0.1609 | 1811.3 | 0.1062 | |
| CPA-PR | A.-Martínez ⁶⁸ | 547.01 | 214.99 | 0 | 1573.0 | 0.024694 | |
| CPA-RKS | this work | 405.31 | 189.42 | 0.071531 | 1629.8 | 0.083316 | |
| CPA-RKS | A.-Martínez ⁶⁸ | 559.39 | 242.57 | 0 | 1460.2 | 0.032988 | |
| | | a (bar L ² /mol ²) b (L/mol) c | | | | | |
| CPA-RKS-K | this work | 1.36452 | 0.015094 | 1.1161 | 1715.9 | 0.093944 | |
| CPA-RKS-K | Peeters ⁶⁹ | 0.76225 | 0.015240 | 2.0549 | 1721.1 | 0.135340 | |
| CPA-RKS-K | Kontogeorgis ^{46,53} | 1.2277 | 0.014515 | 0.67359 | 2003.1 | 0.0692 | |

The values of T'_c are 647.096 K in this work and 647.3 K in Peeters.⁶⁹ Kontogeorgis et al.^{46,53} did not specify T'_c .

Table 1.2: Deviations of several CPA models for water in the temperature range of 240–580 K.

| EOS | Reference | Δp_s (%) | Δv_l (%) | Δv_v (%) | f_{obj} (%) |
|-----------|-----------------------|------------------|------------------|------------------|----------------------|
| CPA-PR | this work | 0.12 | 1.8 | 3.1 | 1.0 |
| CPA-RKS | this work | 0.11 | 1.9 | 3.3 | 1.0 |
| CPA-RKS-K | this work | 0.35 | 2.0 | 2.2 | 1.2 |
| CPA-RKS-K | Peeters ⁶⁹ | 0.89 | 5.7 | 1.7 | 3.3 |

The quantities Δp_s , Δv_l and Δv_v are root-mean-square relative deviations of the calculated vapour pressure, liquid volume and vapour volume, respectively. The value f_{obj} is the objective function, which is the mean of Δp_s and Δv_l .

the parameters from Peeters.⁶⁹ Peeters fitted the CPA model to data in the temperature range of 220–320 K, using extrapolated density data. As could be expected, the overall deviations of his model in the range of 240–580 K are higher.

When CPA-PR and CPA-RKS were fitted, it was observed that the optimum parameters were close to the region in parameter space where ω' changed sign. Therefore, the optimum values for ω' are close to zero.

Deviations

Because the final EOS will be used to predict equilibrium vapour pressures of water in a mixture, it is essential that pure water vapour pressures are reproduced accurately. The liquid density, on the contrary, will not be used and is allowed to deviate more. Figure 1.4 shows the relative errors of the vapour pressure that different CPA models predict. Similarly, liquid density predictions are plotted in Figure 1.5.

The CPA-PR and the CPA-RKS equations reproduce the vapour pressure

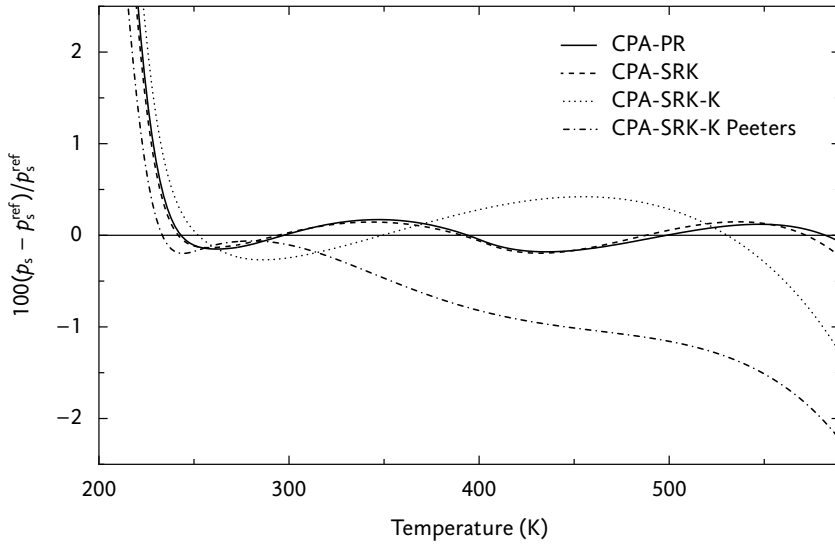


Figure 1.4: Relative deviations of the equilibrium vapour pressure of water calculated by several CPA models. Below 273 K, deviations are shown relative to the Murphy and Koop⁶⁷ vapour pressure equation; above 273 K, the reference is the IAPWS model.

equally well, and perform better than the Kontogeorgis version. The CPA-RKS- κ model from Peeters has a systematic deviation at high temperatures because the model was only fitted between 220 and 320 K. Below 234 K, the models cannot be compared to the IAPWS vapour pressure (see appendix A.1) so they are instead compared to the Murphy and Koop⁶⁷ vapour pressure. Below the temperature range where the models were fitted, the deviations increase rapidly. For example, the Peeters model has an error of 7% at 200 K; the other models have deviations of about 10%. At 235 K, the temperature where we will use the model, the Peeters model is best.

The temperature dependence of the water density cannot be reproduced by any CPA model. In the range of 300 to 600 K, the deviations of all models except Peeters's one are acceptable, but near the critical point and below 250 K, the CPA model performs worse than expected. In particular, even with its association part, CPA cannot reproduce the maximum in the density of water, which was also noted by Lundström et al.⁷⁰ This maximum (and the low density of water at low temperatures) is caused by hydrogen bonds, and it is somewhat surprising that an EOS with association is unable to model this behaviour.

For our purposes, the accuracy of the liquid density is of minor importance because it will not be used in further calculations. At 235 K, the deviations are moderate, namely 5% to 7%. Peeters's model was fitted at low temperature only; consequently, it performs better there than the other models.

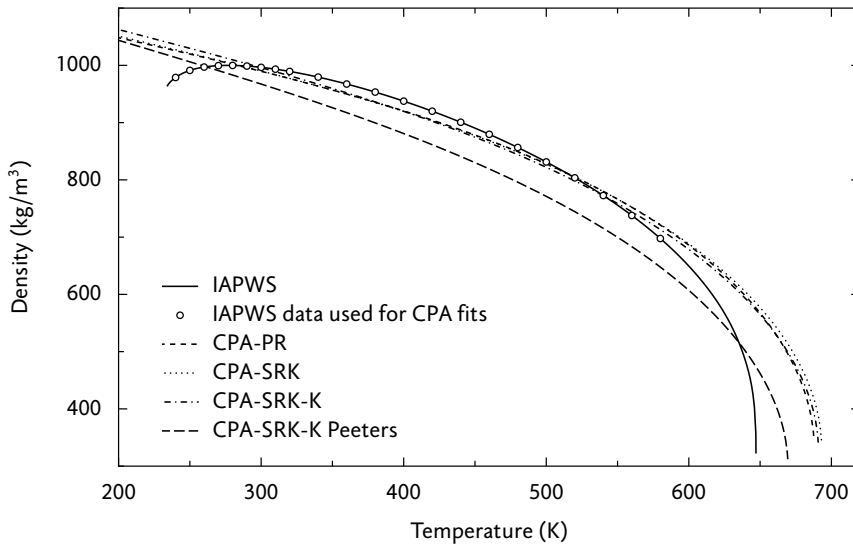


Figure 1.5: Equilibrium liquid densities of water predicted by several CPA models.

To conclude, the CPA-RKS and CPA-PR models describe water with the smallest overall deviations. However, these models cannot satisfactorily reproduce the composition of the water–methane binary system, as will be shown in section 1.5.

Methane and carbon dioxide

Methane and carbon dioxide can be described quite well by a cubic EOS such as PR or RKS. Therefore, the association part of CPA is not required; the parameters ϵ and β are set to zero.

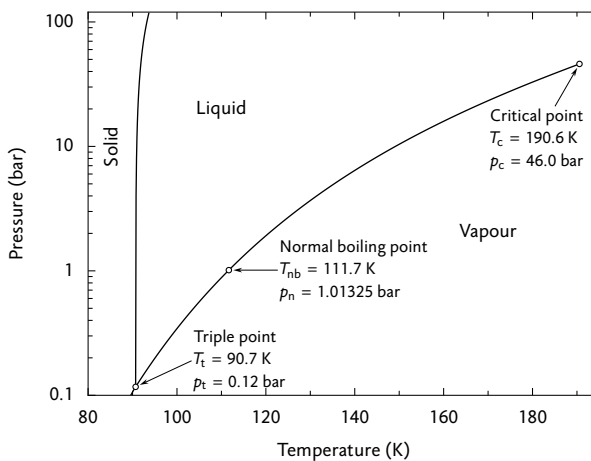


Figure 1.6: Phase diagram of methane.

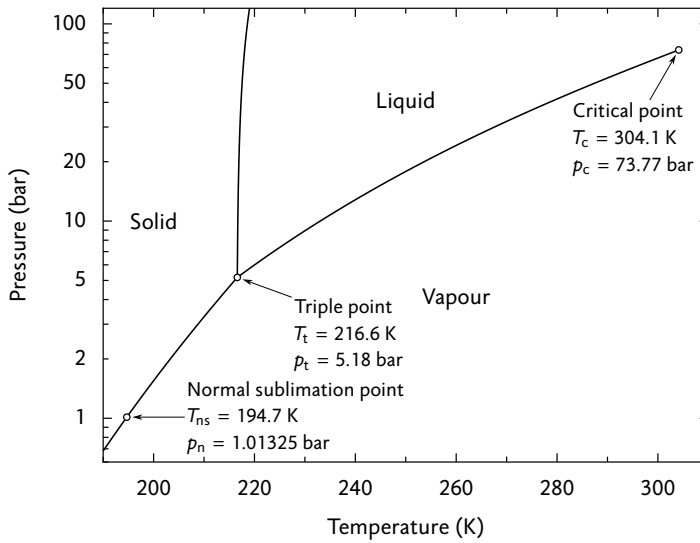


Figure 1.7: Phase diagram of carbon dioxide.

The vapour pressure and liquid density of both components were taken from the reference equations developed in the group of Wagner,^{71,72} available in the NIST webbook.⁷³ Phase diagrams are shown in Figures 1.6 and 1.7.

Carbon dioxide was fitted in the temperature range between the triple point (216.59 K) and 294 K with points spaced 10 K apart. Methane was fitted in the range of 100 to 180 K; again with a spacing of 10 K. The optimized parameters and the deviations are listed in Table 1.3. The Pfohl and the Kontogeorgis CPA model perform equally well, which is caused by the proximity of the fitted T'_c and p'_c to the experimental T_c and p_c . The quality of the CPA fits is illustrated by the pressure–density diagrams of Figure 1.8, in which the two-phase envelope is shown together with several isotherms.

Table 1.3: Parameters of two CPA models for methane and carbon dioxide.

| | Parameters | | | Deviations (%) | | | |
|----------------|---|--------------|-----------|----------------|--------------|--------------|-----------|
| | T'_c (K) | p'_c (bar) | ω' | Δp_s | Δv_l | Δv_v | f_{obj} |
| CPA-RKS | | | | | | | |
| methane | 193.41 | 48.555 | -0.01540 | 0.48 | 3.3 | 2.5 | 1.9 |
| carbon dioxide | 310.11 | 82.819 | 0.19398 | 0.11 | 1.8 | 5.8 | 0.9 |
| CPA-RKS-K | a (bar L ² /mol ²) | b (L/mol) | c | Δp_s | Δv_l | Δv_v | f_{obj} |
| methane | 2.2921 | 0.028694 | 0.45083 | 0.48 | 3.3 | 2.5 | 1.9 |
| carbon dioxide | 3.4835 | 0.026974 | 0.76538 | 0.11 | 1.8 | 5.8 | 0.9 |

Experimental critical values are $T_c = 190.56$ K and $p_c = 45.99$ bar for methane⁷¹ and $T_c = 304.13$ K and $p_c = 73.77$ bar for carbon dioxide.⁷²

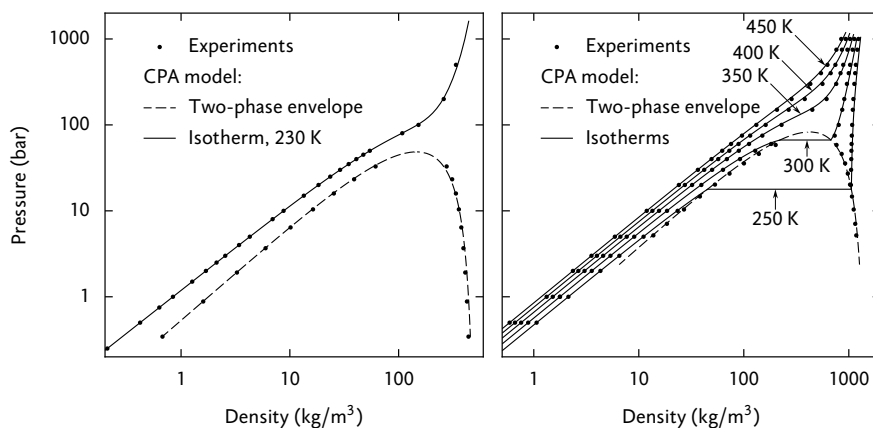


Figure 1.8: Pressure–density diagrams of methane (left) and carbon dioxide (right). The lines are the predictions of the CPA-RKS EOS, with the parameters of Table 1.3. The dots represent experimental data on the two-phase envelope and on isotherms.

1.5 Water–methane

The water–methane system is of interest to the natural gas industry and has therefore been extensively studied. In equilibrium, the liquid phase is rich in water, whereas the gaseous phase contains mostly methane. At low temperature and high pressure, gas hydrate can be formed, an ice-like phase with hydrocarbon molecules that stabilize its crystal structure.⁷⁴ In the liquid–vapour case, the composition is completely given by two quantities: the molar fraction of water in the vapour phase (or, equivalently, the enhancement factor of water in methane), and the molar fraction of methane in the liquid (that is, the solubility of methane in water). The CPA model has been fitted to these two quantities.

Figure 1.9 shows the phase diagram of the methane–water system. In a binary system, three-phase equilibrium states are represented by lines, and a four-phase equilibrium state by a point. The number and type of phases that exist between the equilibrium lines depend on the overall composition of the system. For example, in the diagram of Figure 1.9, at 240 K and 60 bar, the following phase combinations are possible, ordered by increasing water content: (1) methane-rich vapour; (2) methane-rich vapour and hydrate; (3) hydrate; (4) hydrate and ice; (5) ice.

Experimental data

There exists much data on the water vapour fraction in methane, but the accuracy of most measurements is unsatisfactory. Measurements from the literature that were evaluated are summarized in Table 1.4. This list is not exhaustive; more references are given in Mohammadi et al.⁷⁷ and Chapoy.⁷⁸

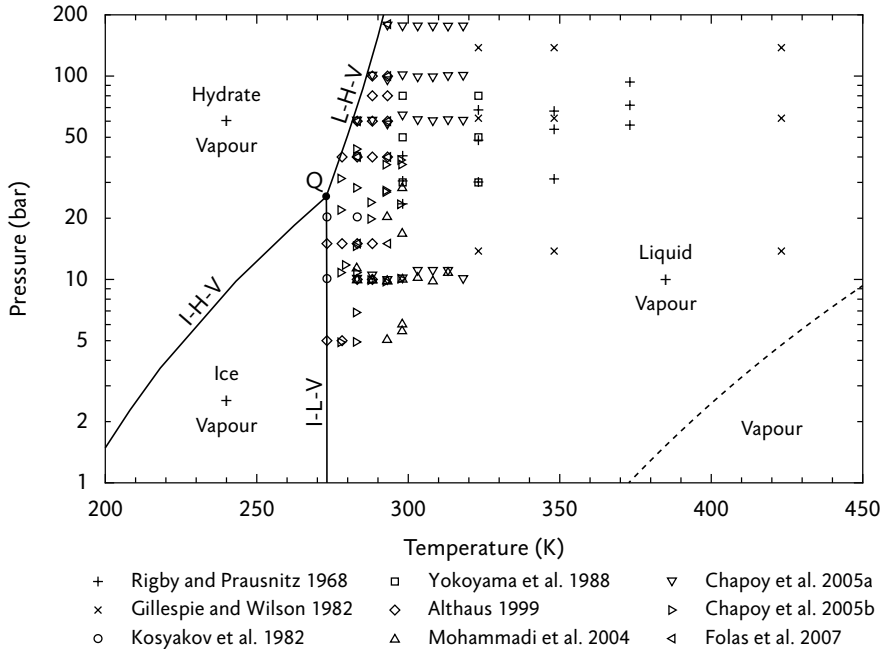


Figure 1.9: Phase diagram of the methane–water system.^{75,76} Solid lines represent equilibrium between three phases, with L denoting liquid rich in water, H hydrate, I ice, and V vapour rich in methane. The dashed line is the vapour pressure of pure water. The point Q is the quadruple point where the four phases L-H-I-V are in equilibrium. The equilibrium line I-L-H above the point Q is not shown, since it is not relevant in the presence of excess methane. The data points mark the conditions at which the equilibrium water vapour fraction has been measured.

Table 1.4: Measurements of the equilibrium water vapour fraction in the methane–water system

| Reference | Year | Note | Reference | Year | Note |
|------------------------------------|------|------|--------------------------------|-------|------|
| Olds ⁷⁹ | 1942 | | Althaus ⁸⁰ | 1999 | |
| Rigby and Prausnitz ⁸² | 1968 | a | Chapoy et al. ⁸³ | 2003 | c |
| Kosyakov et al. ⁸⁴ | 1982 | b | Mohammadi et al. ⁷⁷ | 2004 | |
| Gillespie and Wilson ⁸⁵ | 1982 | | Chapoy et al. ⁸⁶ | 2005a | |
| Yarym-Agaev et al. ⁸⁷ | 1985 | | Chapoy et al. ⁸⁸ | 2005b | |
| Yokoyama et al. ⁸⁹ | 1988 | | Folas et al. ⁵⁴ | 2007 | |

a: good accuracy; b: only two points per isotherm; c: corrected in Chapoy 2005a

The temperature and pressure at which individual measurements were performed are shown in the phase diagram, Figure 1.9. Measurements of the water vapour fraction at conditions where hydrate or ice exists were discarded.

To evaluate the data, the reported vapour fractions were converted to en-

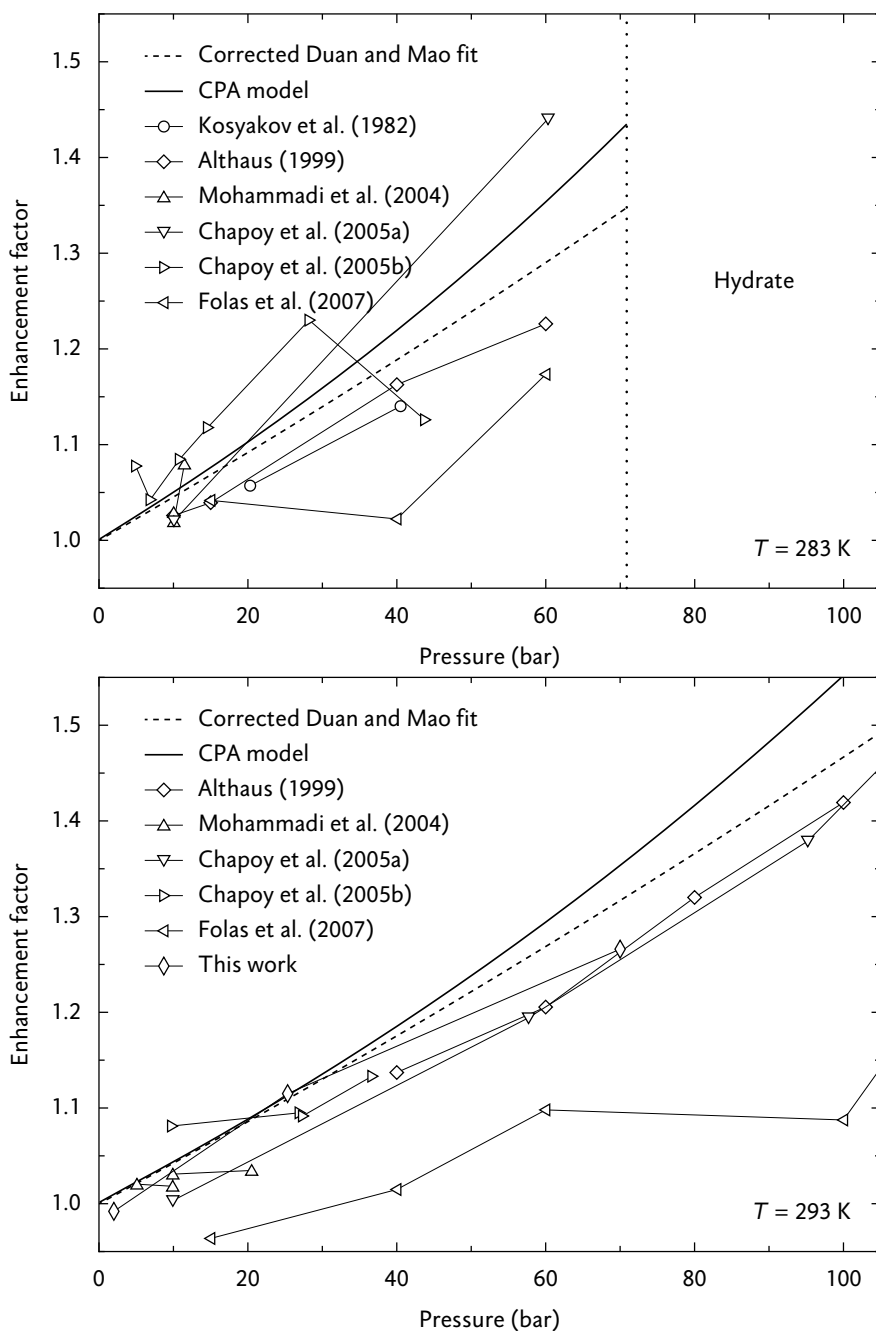
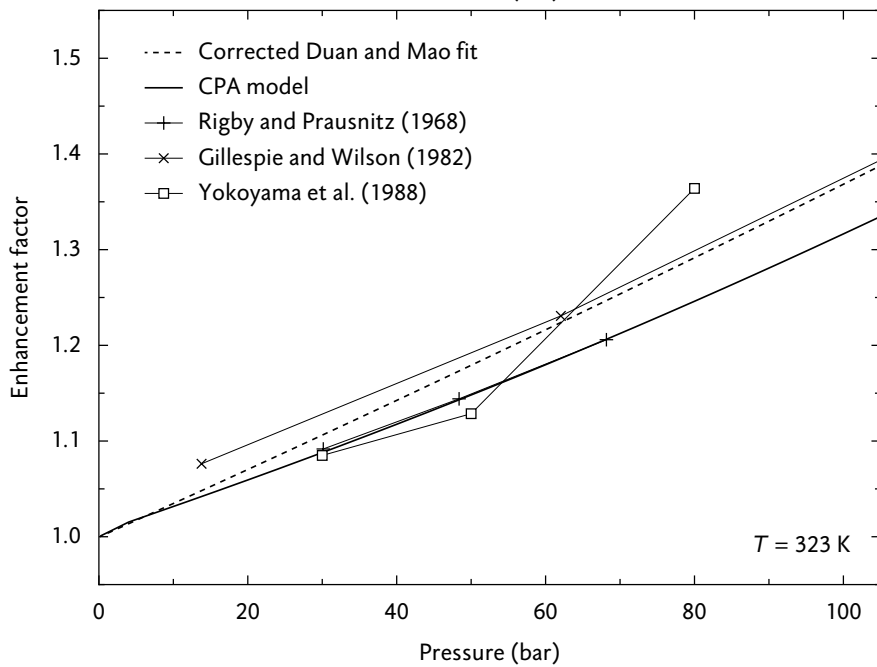
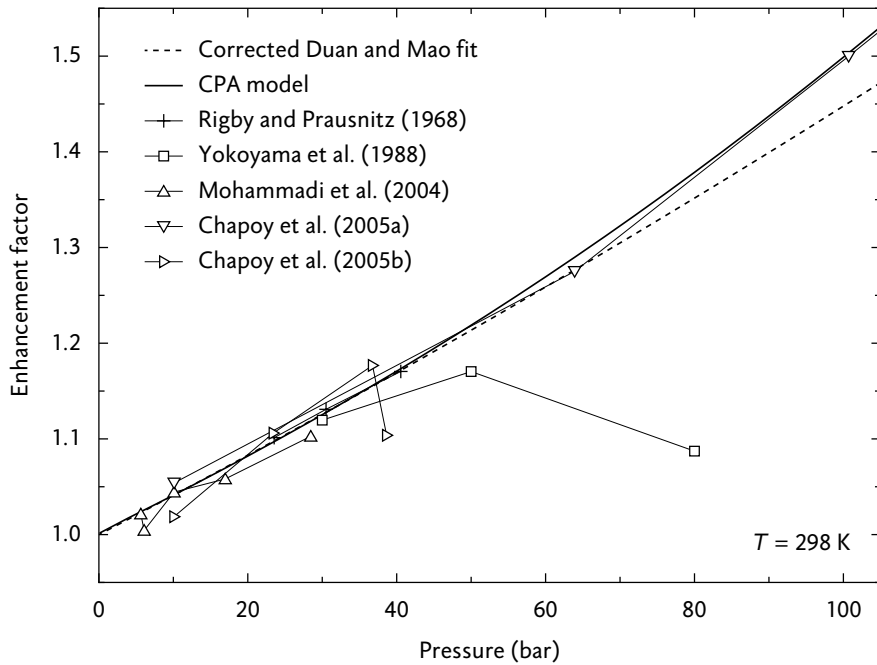


Figure 1.10: This page and next page: enhancement factor of water in methane as a function of pressure, for temperatures of 283, 293, 298 and 323 K. Symbols indicate measurements; references for the experimental data are listed in Table 1.4. Also shown are the corrected fit to the model of Duan and Mao (see appendix B) and the result from the CPA EOS developed in this section.



hancement factors using the definition of Eq. 1.26, and plotted as a function of pressure. Four of these plots are shown in Figure 1.10, each corresponding to a different temperature. There is considerable scatter in the data, particularly at the lowest temperature of 283 K. A reason for the lack of accurate measurements is the small value of the water vapour fraction (about 10^{-4} to 10^{-3}) and, consequently, the large amount of gas that is required for the analysis. In addition, it can take a long time to reach equilibrium. In spite of the inaccuracies, it can be concluded from the plots that the enhancement factor increases approximately linearly with the pressure, and decreases with increasing temperature.

In 2006, Duan and Mao⁹⁰ presented semi-empirical equations for the equilibrium water vapour fraction and the methane liquid fraction in the water–methane system. The result from their equation appeared to represent the measurements reasonably well. At low pressure, however, the Duan and Mao enhancement factor does not approach unity, but a value of about 1.015. This would cause an error of 1.5% in the supersaturation because the equilibrium vapour fraction of water and the enhancement factor appear in its definition, Eq. 1.29. The nucleation rate is quite sensitive to the supersaturation; indeed, an increase in the supersaturation of 1.5% causes an increase in the nucleation rate of about 40%.

To correct the low-pressure behaviour of the enhancement factor, a polynomial function in p and T was fitted to the data of the Duan and Mao model, while constraining it to the low-pressure limit. The fitted function, which is shown in appendix B, has been used in this work as the experimental vapour composition in the methane–water system. It is also shown in Figure 1.10.

Like the vapour composition, the solubility of methane in liquid water has been the subject of many investigations. Duan and Mao⁹⁰ and Chapoy⁷⁸ give extensive lists of references, dating from 1855 to 2004. The Duan and Mao model reproduces most of these measurements accurately. Figure 1.11 compares the model with recent measurements of Chapoy et al.⁹¹ A polynomial fit was also made for this model and is given in appendix B.

Fitting to experimental data

The binary interaction parameters k_{ij} and l_{ij} (defined in Eqs. 1.39 and 1.40) were determined by fitting the CPA models to experimental two-component, two-phase equilibrium compositions. In all cases considered here, one phase is liquid and the other is gaseous. In subscripts of k_{ij} and other parameters, the phases will be identified by the first letters of their name. For example, k_{mw} represents the interaction parameter of the water–methane system.

The equilibrium compositions of the two phases are functions of temperature and pressure. In principle, k_{ij} and l_{ij} therefore depend on both p and

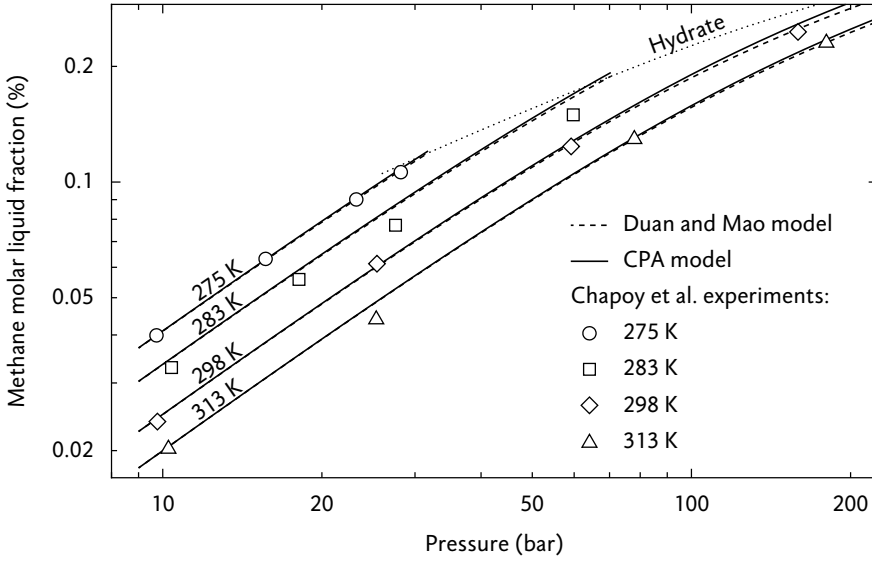


Figure 1.11: Molar liquid fraction of methane in the water–methane system as a function of pressure, for different temperatures. Shown are the model of Duan and Mao,⁹⁰ the experimental data of Chapoy et al.⁹¹ and the CPA model from this work (CPA-RKS-K with Peeters’s parameters). At high pressure and low temperature, the vapour–liquid area is limited by the hydrate–vapour–liquid equilibrium line (dotted).

T . In practice, the parameters are made temperature-dependent only, and sometimes even constant. A weak or zero temperature dependence is preferable because it allows for a reliable extrapolation of the parameter outside the fitted temperature range. In that case, the predictions of the EOS outside the fitted range are more trustworthy. In this work, the l_{ij} parameter was taken equal to zero, to reduce the number of parameters that have to be extrapolated.

The objective function, used for the optimization of the interaction parameters, is defined at a temperature T as

$$f_{\text{obj}}(T) = \frac{1}{4}(\Delta x_1 + \Delta x_2 + \Delta y_1 + \Delta y_2), \quad (1.50)$$

where Δx and Δy are the averages of the relative deviations of, respectively, the liquid and vapour molar fractions at T , with subscripts 1 and 2 referring to the two components. For example, Δx_1 is given by

$$\Delta x_1(T) = \frac{1}{n} \sum_{i=1}^n \left| \frac{x_1^{\text{calc}}(p_i) - x_1^{\text{exp}}(p_i)}{x_1^{\text{exp}}(p_i)} \right|, \quad (1.51)$$

where p_1 to p_n are pressure values that have been selected for the fit at temperature T .

Table 1.5: Deviations of the CPA water–methane equilibrium composition at 298.15 K

| EOS | Water parameters | Maximum deviations (%) | | | |
|-----------|-----------------------|------------------------|--------------|--------------|--------------|
| | | 2–10 bar | | 2–100 bar | |
| | | Δx_m | Δy_w | Δx_m | Δy_w |
| CPA-PR | this work | 0.0 | 3.5 | 0.6 | 47.6 |
| CPA-RKS | this work | 0.2 | 2.8 | 3.0 | 39.3 |
| CPA-RKS-K | this work | 0.1 | 1.2 | 2.1 | 20.5 |
| CPA-RKS-K | Peeters ⁶⁹ | 0.1 | 0.2 | 1.6 | 3.4 |

The deviations of the methane liquid fraction x_m and the water vapour fraction y_w are computed from $\Delta x = |(x_{\text{calc}} - x_{\text{exp}})/x_{\text{exp}}|$, at several pressures in the range shown. Only the maximum deviation (which usually occurs at the highest pressure) is listed. The different pure component parameter sets for water are shown in Table 1.1.

To compare the different CPA versions, the variants CPA-PR, CPA-RKS and CPA-RKS-K were evaluated at a temperature of 298.15 K. Furthermore, the CPA-RKS-K model was fitted both with the water pure component parameters from this work and those obtained by Peeters. All models were fitted to the vapour and liquid compositions, with k_{mw} (the binary interaction parameter for water–methane) as a fitting parameter. Like Peeters,⁶⁹ it was found that the liquid composition was much more sensitive to the k_{mw} value than the vapour composition. Therefore, fitting to only the liquid composition gave nearly the same k_{mw} as fitting to both phase compositions.

The fitting results, presented as maximum relative deviations of the compositions, are listed in Table 1.5. To study the influence of different pressure ranges, the fitting procedure was performed for pressures from 2 to 10 bar and also from 2 to 100 bar. The optimum k_{mw} value is quite insensitive to the pressure range; specifically, the absolute difference in k_{mw} between the two pressure ranges is at most 0.0007, while the value of k_{mw} lies between -0.03 and 0.24 . The composition deviations, on the other hand, strongly depend on the fitted pressure range, as Table 1.5 illustrates. In most cases, the largest deviation occurs at the largest pressure (that is, the end of the pressure range), and the deviation is approximately proportional to the pressure itself. For that reason, the deviations in the last two columns of table Table 1.5 are roughly an order of magnitude larger than those in the two previous columns.

Considering the performance of the different CPA variants, the CPA-RKS-K model is clearly better than the CPA-PR and CPA-RKS models. Furthermore, the use of Peeters's water parameters greatly reduces the deviations. Therefore, the CPA-RKS-K model with Peeters's parameters was chosen as a final model, even though it gives the worst description of pure water, as shown in section 1.4. This is not a serious limitation because the CPA prediction of the

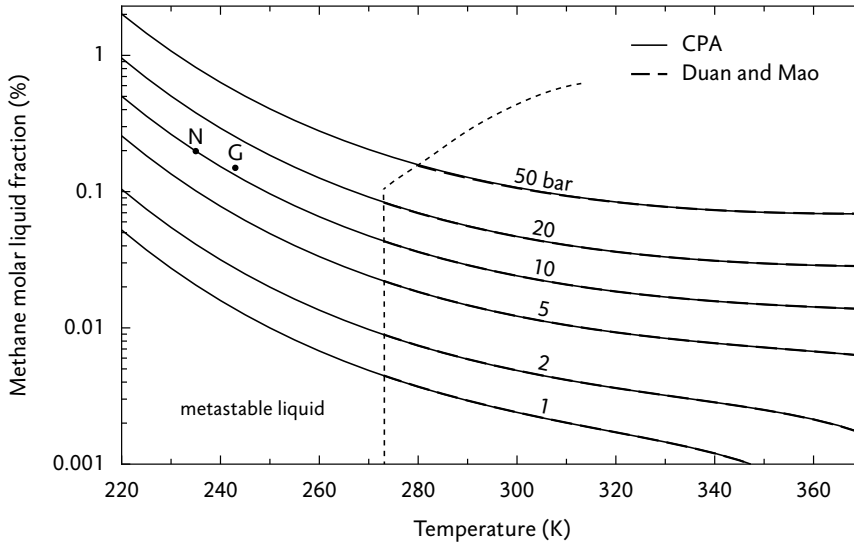


Figure 1.12: Solubility of methane in liquid water, according to the CPA EOS developed in this section and the model of Duan and Mao.⁹⁰ To the left of the dashed line, liquid water is metastable; the stable phase is ice or hydrate (Figure 1.9). The points labelled N and G indicate our experimental nucleation and growth conditions, respectively.

water density will not be used.

Next, the selected model was fitted to binary data at several temperatures in the range of 273 to 375 K, with an optimum k_{mw} determined at each T . Because we intended to use the model primarily at pressures of 10 bar and lower, the pressure range of fitting was chosen to be 2 to 10 bar, although, as mentioned above, the k_{mw} parameter was insensitive to the pressure range. The optimum k_{mw} values varied smoothly with T , and could be reproduced by the parabola

$$k_{mw} = -1.71211 + 2.39605 \tau - 0.638842 \tau^2, \quad \text{with } \tau = T/(320 \text{ K}). \quad (1.52)$$

The largest absolute difference between an optimized k_{mw} and the value given by Eq. 1.52 is only 7×10^{-5} . With these k_{mw} values, the liquid composition is accurately reproduced; for pressures below 10 bar and temperatures between 273 and 375 K, the relative error in the methane liquid fraction is less than 0.7%. Furthermore, as Figure 1.12 shows, the low-temperature prediction looks plausible.

However, the enhancement factor, plotted in Figure 1.13, does not agree with the Duan and Mao model that was used as input. In particular, the CPA predicts a stronger temperature dependence than the Duan and Mao model. Still, the experimental value of the enhancement factor is so uncertain (see Figure 1.10) that it cannot be said that one model fits the experiments better

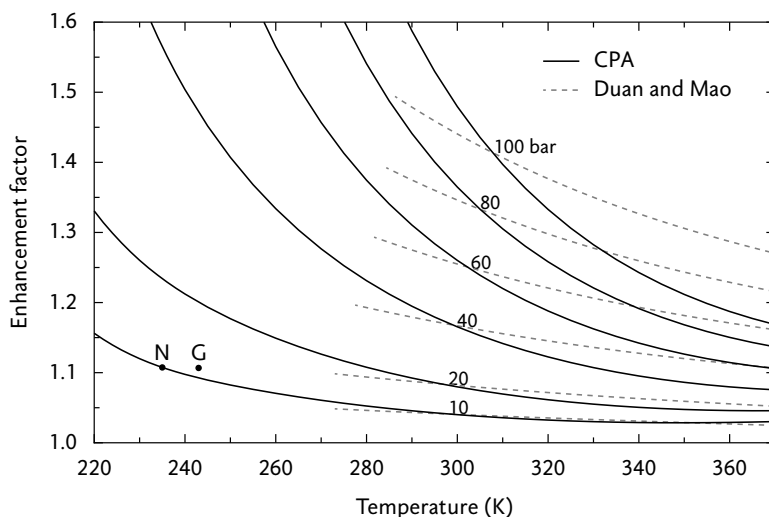


Figure 1.13: Enhancement factor of water in methane, according to the CPA EOS developed in this section and the corrected fit to the model of Duan and Mao (Eq. B.1). The points labelled N and G indicate our experimental nucleation and growth conditions, respectively.

than the other. At our nucleation temperature, 235 K, the uncertainty in the enhancement factor (and vapour fraction) is estimated at 5%.

1.6 Water–carbon dioxide

The phase diagram of the water–carbon dioxide system is similar to that of the water–methane system. However, the critical point of pure carbon dioxide is at a higher temperature (304 K) than the hydrate equilibrium line (283 K), which gives rise to a second quadruple point; see Figure 1.14. Features of the phase diagram are discussed by Wendland et al.,⁹² Longhi⁹³ and Diamond.⁹⁴

When CO_2 dissolves into water, it partially dissociates into the ions HCO_3^- and H^+ . The HCO_3^- ion can dissociate further into CO_3^{2-} and H^+ . These dissociation reactions could potentially lead to inaccuracies in the description, if only the molar fraction of CO_2 in water is included in the model. To estimate the magnitude of the errors, the composition of a solution of carbon dioxide in water was computed with a model of Li and Duan.⁹⁶ As Table 1.6 illustrates, the products of the first dissociation reaction have a concentration that is about 800 times lower than that of CO_2 . All dissociations can therefore be safely ignored in our model. Still, it is worth noting that the dissociation of CO_2 in this example reduces the pH of the solution from 7 to 3.6.

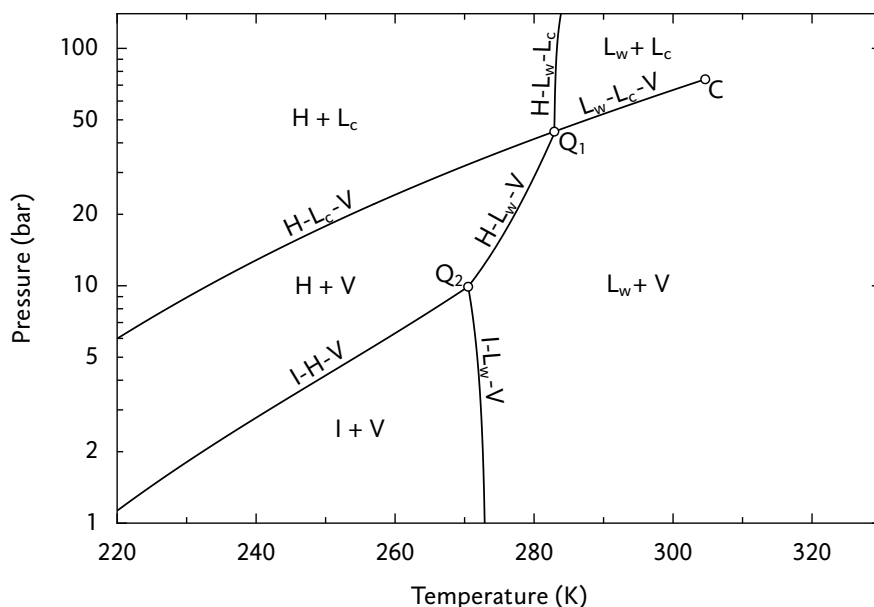


Figure 1.14: Phase diagram of the carbon dioxide–water system.^{74,92,95} Solid lines are three-phase equilibrium lines, with L_w denoting liquid rich in water, L_c liquid rich in carbon dioxide, H hydrate, I ice, and V vapour rich in carbon dioxide. Q_1 and Q_2 are quadruple points, and C is the critical end point at which L_c and V become equal. The equilibrium line $I - H - L_w$ above the point Q_2 is not shown, since it is not relevant in the presence of excess carbon dioxide.

Experimental data

A large number of studies on the solubility of carbon dioxide in water have been evaluated in the reviews by Diamond and Akinfiev⁶⁵ (272 to 373 K and up to 1000 bar) and Spycher et al.⁹⁷ (285 to 373 K and up to 600 bar). Particularly the Diamond and Akinfiev review is useful because the temperature range covered is larger, and the authors provide a computer program that gives an accurate correlation of the solubility data. A model that covers even a larger pressure–temperature area is that of Duan et al.,⁹⁸ valid from 273 to 533 K and up to 2000 bar, albeit with less accuracy. The Diamond and Akinfiev model and the Duan et al. model are compared in Figure 1.15, which shows that there are only minor differences between them.

Table 1.6: Composition of the aqueous solution of carbon dioxide at 273.15 K and 2.5 bar, computed with the model of Li and Duan.⁹⁶

| Molecule | Molality (mol/kg) | Molar fraction |
|--------------------|------------------------|------------------------|
| CO_2 | 0.186 | 3.33×10^{-3} |
| H^+ | 2.29×10^{-4} | 4.11×10^{-6} |
| HCO_3^- | 2.29×10^{-4} | 4.11×10^{-6} |
| CO_3^{2-} | 2.61×10^{-11} | 4.69×10^{-13} |

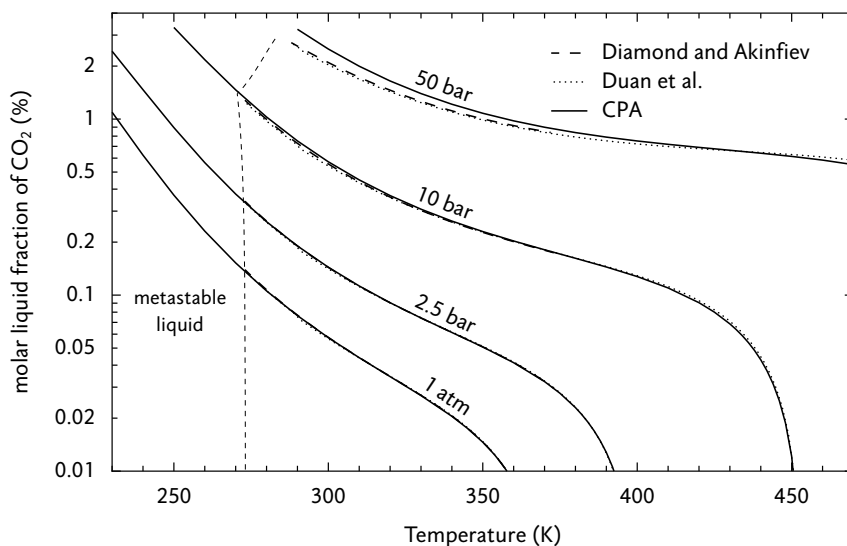


Figure 1.15: Solubility of carbon dioxide in liquid water, according to the models of Diamond and Akinfiev⁶⁵ and Duan et al.,⁹⁸ which can be considered as experimental data. The lines are the results from the CPA EOS developed in this section. To the left of the dashed line, liquid water is metastable; the stable phase is ice or hydrate (Figure 1.14).

The solubility of carbon dioxide in water is much higher than that of methane. For example, at 275 K and 10 bar, the methane solubility is 0.04% (Figure 1.11), whereas the carbon dioxide solubility is about 30 times as high, namely 1.2%. The solubility of carbon dioxide decreases rapidly as the boiling temperature is approached, where it vanishes.

The composition of the vapour phase in the water–carbon dioxide system is not as accurately known as the liquid composition. Most studies were performed at pressures above 50 bar or at temperatures above 373 K, as the literature overview by Mohammadi et al.⁷⁷ shows. There are only a few measurements at lower temperature and pressure, and these mutually disagree. For this work, the studies of Wiebe and Gaddy,⁹⁹ Coan and King,¹⁰⁰ and Gillespie and Wilson⁸⁵ were evaluated. The data of Wiebe and Gaddy was found to be too inaccurate and was discarded. The other two data sets could be reasonably represented by a fit of the enhancement factor (Eq. 1.26) as a function of temperature and pressure,

$$f_e = 1 + \frac{0.216 p_r}{\tau - 0.816}, \quad \text{with} \quad p_r = \frac{p - p_s(T)}{100 \text{ bar}} \quad \text{and} \quad \tau = \frac{T}{320 \text{ K}}. \quad (1.53)$$

Here $p_s(T)$ is the vapour pressure of pure water. In Figure 1.16, the fit is compared with experimental data. The fit is valid between 288 and 533 K,

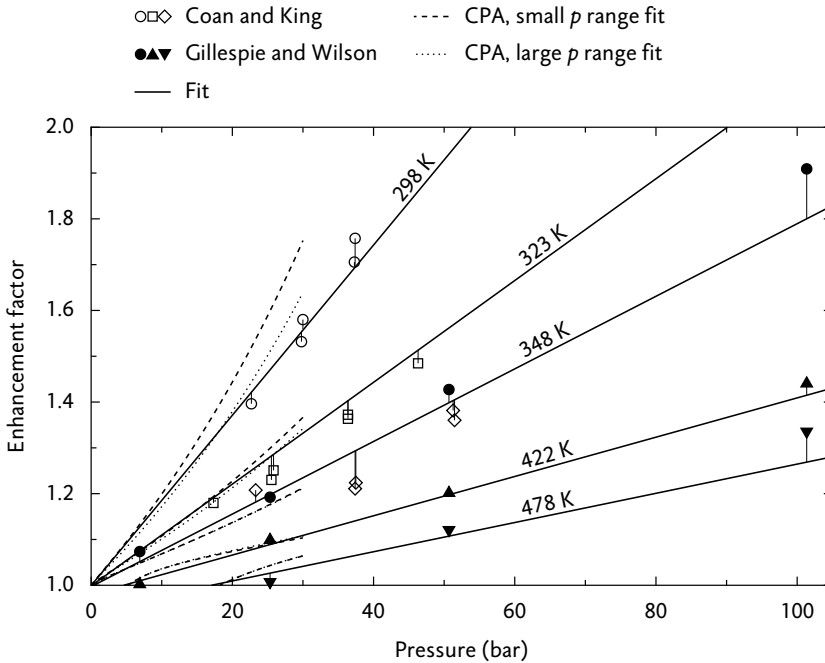


Figure 1.16: Enhancement factor of water in carbon dioxide. Solid lines are calculated from the fit of Eq. 1.53. The points are experimental data from Coan and King¹⁰⁰ and Gillespie and Wilson.⁸⁵ The temperature that belongs to the data points is the same as that of the fitted line to which they are connected by vertical lines. Dashed and dotted lines are the results from the CPA EOS developed in this section.

for pressures from $p_s(T)$ to 50 bar, and has a relative uncertainty $\Delta f_e/f_e$ of about $\pm 5\%$. This relative error is carried over to the vapour fraction of water and to the supersaturation, and the error in the nucleation rate caused by a 5% error in the supersaturation is about a factor of three. Such deviations are undesirable, but more accurate data currently does not exist.

For temperatures higher than 304 K, the graph of the water vapour fraction y_w as function of the pressure shows a minimum around 70 bar, after which y_w anomalously rises as the pressure is increased.⁹⁹ This phenomenon is not reproduced by the simple linear pressure dependence of the enhancement factor in the fit of Eq. 1.53. Therefore, the fit can only reliably be used at moderate pressures, up to about 50 bar.

Pressure range of the CPA fit

Unlike the water-methane case, the CPA model was found to be quite sensitive to the pressure range when fitting it to the water-carbon dioxide experimental data. Choosing a smaller pressure interval generally leads to a higher accuracy in that interval, but the model may then fail to capture physically

important trends outside the interval. Therefore, the CPA fit was performed twice; for a small pressure range of 1.5–7 bar and a larger range of 1.5–30 bar. In both cases, the lowest pressure (1.5 bar) is well above the vapour pressure of pure water at all temperatures considered, and the pressure range also includes the partial pressure of carbon dioxide in our experiments, which is at most 2.5 bar. In the following sections, the results from both pressure ranges will be presented separately.

Cross-association

It was not possible to accurately describe the water–carbon dioxide system composition with k_{cw} as the only fitting parameter. The liquid composition was predicted with sufficient accuracy, but the vapour fraction of water (the value that is needed for in our work) was not. For example, at 300 K and 7 bar, the relative deviation in the water vapour fraction would be 8.8%. However, the performance of the model could be greatly improved by including the cross-association between the carbon dioxide and water molecules.

The carbon dioxide molecule can be taken as having two negative association sites, so that it can associate with a positive site on a water molecule, but not with other carbon dioxide molecules. In this way, adjusting the cross-association of carbon dioxide will not influence the pure-component performance of the carbon dioxide in the model. The cross-association of water and carbon dioxide has been implemented by several authors,^{41,50,101} with Kontogeorgis et al.⁴¹ noting that including cross-association improves the prediction of the water solubility in carbon dioxide, especially if the four-site model for water (Figure 1.3) is used, like in this work. The justification for the two negative sites is that the carbon dioxide is a strong quadrupole^{50,102} without a dipole moment. Two poles with negative charge are located at the two oxygen atoms, and a positive charge is along a ring near the carbon atom.¹⁰³

At several temperatures in the range of 288 to 395 K, the optimum value of the interaction strength Δ_{cw} was determined (Figure 1.17). The temperature-dependent expression for Δ_{cw} , Eq. 1.44, was then fitted to the optimum values, with the association strength ϵ_c and the association volume β_c as fitting parameters, and Eq. 1.47 as mixing rules. The resulting values were

$$\begin{aligned} \epsilon_c/k &= 2817.1 \text{ K}, & \beta_c &= 7.2636 \times 10^{-5}, & \text{for the small } p \text{ range,} \\ \epsilon_c/k &= 2017.8 \text{ K}, & \beta_c &= 5.0354 \times 10^{-4}, & \text{for the large } p \text{ range.} \end{aligned} \quad (1.54)$$

With cross-association, the relative error in the water vapour fraction at 300 K and 7 bar was greatly reduced from 8.8% to 0.5%, whereas the error in the liquid composition remained low at 1.6%. (These values pertain to the small pressure range fit.)

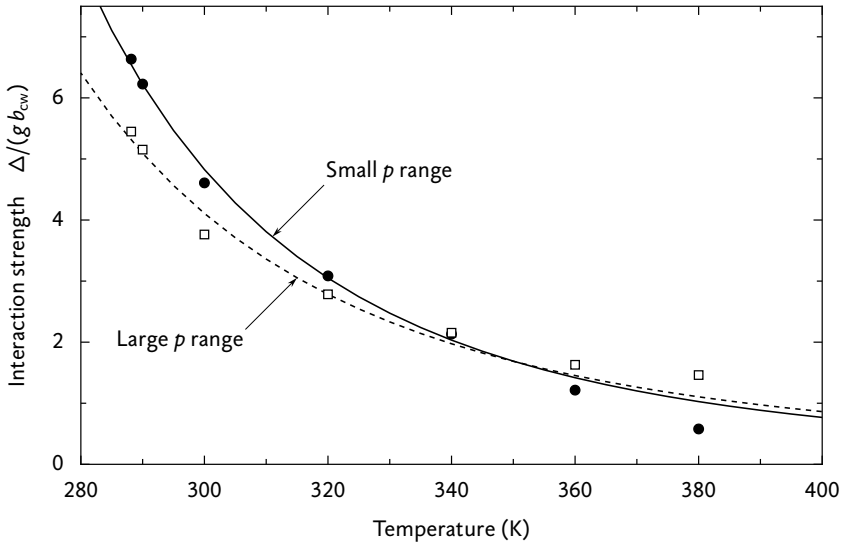


Figure 1.17: The interaction strength between a negative site on carbon dioxide and a positive site on water, as a function of temperature. The interaction strength Δ_{cw} is scaled by the product of the contact value g and the binary volume parameter b_{cw} , see Eq. 1.44. The points are obtained by fitting Δ_{cw} to experimental binary compositions. The lines represent a temperature-dependent Δ_{cw} according to Eq. 1.44, with parameters of Eq. 1.54.

Fitting of interaction parameter

The fitting of the binary parameter k_{cw} was done for temperatures between 288 and 370 K, and for the two selected pressure ranges. It was desirable to include lower temperatures, but no vapour composition data was available below 288 K. The fitted k_{cw} values vary little with temperature, and range between 0.16 and 0.21. The parabolas

$$\begin{aligned} k_{cw} &= -0.07682 + 0.45108 \tau - 0.18217 \tau^2, & \text{small } p \text{ range,} \\ k_{cw} &= -0.33506 + 0.80689 \tau - 0.29043 \tau^2, & \text{large } p \text{ range,} \end{aligned} \quad (1.55)$$

with $\tau = T/(320 \text{ K})$ are the best fits to the values. For the small pressure range fit, the deviations of the predicted compositions are small; over the chosen pressure and temperature range, the water vapour fraction has a relative error of 0.5% or less, and the carbon dioxide liquid fraction is accurate within 1.9%. The exact deviations are shown in Figure 1.18a as a function of temperature. As expected, the deviations of the large pressure range fit (Figure 1.18b) are larger than those of the small pressure range fit, when comparing them at equal pressures. At the low end of the temperature range, the curvatures suggest a rapid increase of all deviations with decreasing temperature. Therefore, an error in the water vapour fraction of several percent can be expected

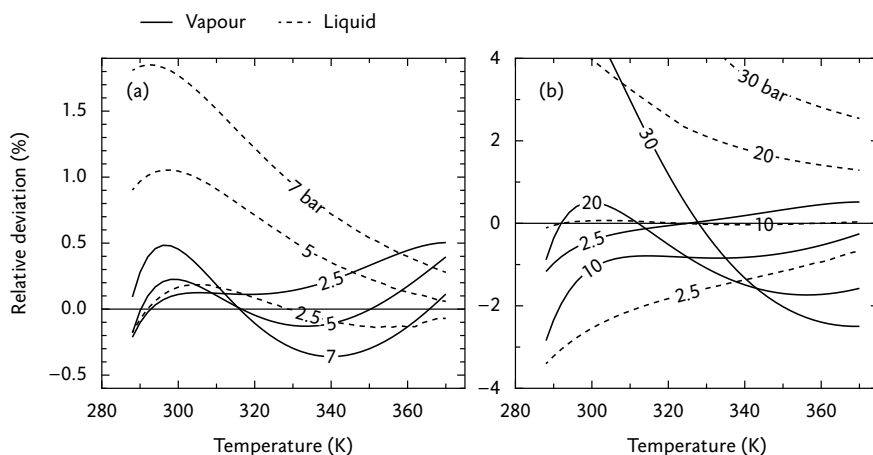


Figure 1.18: Relative deviations of the CPA vapour fraction of water in carbon dioxide, $(y_{\text{calc}} - y_{\text{exp}})/y_{\text{exp}}$, and the liquid fraction of carbon dioxide in water, $(x_{\text{calc}} - x_{\text{exp}})/x_{\text{exp}}$, at several pressures, for the (a) small and (b) large pressure range fit.

at 235 K and 2.5 bar, our experimental partial carbon dioxide pressure.

The results of the CPA EOS are shown in Figures 1.15 and 1.16, together with the experimental data. As mentioned above, the accuracy of the model decreases at pressures above the fitting range, especially at low temperatures. For the small pressure range fit at 290 K and 20 bar, the error in the water vapour fraction is 6%, at 50 bar it becomes 60%. The use of this water–carbon dioxide model is therefore limited to pressures below about 10 bar. The large pressure range fit can be used up to about 20 bar, at 290 K.

Temperature dependence of the enhancement factor

In this work, the CPA model is used to predict the equilibrium vapour fraction of water around 235 K. Therefore, the most important property of the water–carbon dioxide CPA model is the enhancement factor at that temperature. Unfortunately, that quantity cannot be predicted accurately, as Figure 1.19 illustrates. Both the small and large pressure range fits agree fairly well with the experimental correlation (which also has a limited accuracy). At lower temperatures, however, the two predictions diverge, leading to a deviation of a factor 1.14 in f_e at 235 K and 2.5 bar, and a factor 1.5 at 10 bar.

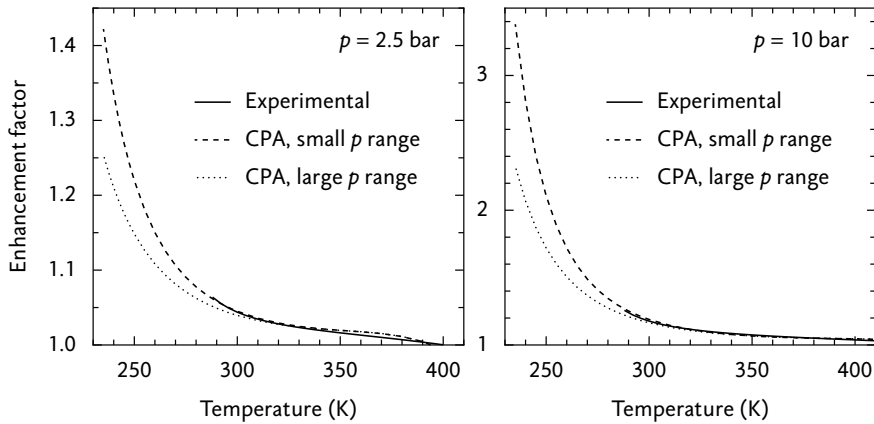


Figure 1.19: The enhancement factor of water in carbon dioxide as a function of temperature, at 2.5 bar (left) and 10 bar (right). Note the different vertical scales. The experimental values are taken from the correlation of Eq. 1.53. The two CPA predictions result from the fits to experimental data in a small or large pressure range.

1.7 Methane–carbon dioxide

The methane–carbon dioxide system can be simply modelled by the CPA EOS without association, which corresponds to the RKS EOS.

The accuracy of the vapour–liquid phase equilibrium of methane and carbon dioxide in our CPA model is not essential because all our experiments take place in the single-phase area of this system (i.e., the pressure is not high enough for liquid carbon dioxide, see Figure 1.7). However, the interaction parameter of this binary system will influence the final ternary model, so it must be determined.

The CPA model was fitted to the phase composition data of Davalos et al.¹⁰⁴ and Wei et al.¹⁰⁵ at temperatures of 230 K, 250 K and 270 K. The measurements could be reasonably well reproduced with a temperature-independent interaction parameter,

$$k_{\text{cm}} = 0.090. \quad (1.56)$$

The experimental data and the CPA result are shown in Figure 1.20. In this plot, the compositions of both the vapour and the liquid phase are shown as a function of pressure. By convention, the compositions are on the horizontal axis. The points on the left vertical axis, where vapour and liquid curves join, represent pure carbon dioxide at vapour–liquid equilibrium. As the pressure rises, the compositions of vapour and liquid phases first diverge, but later they become more alike again. Finally, a critical point is reached, and a single-phase area begins.

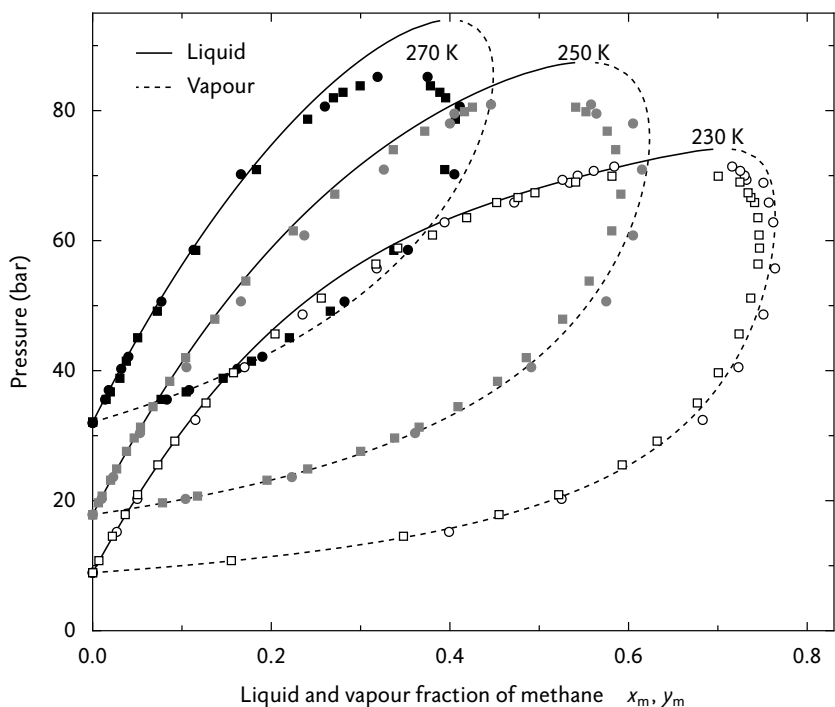


Figure 1.20: Vapour-liquid equilibrium isotherms for methane-carbon dioxide. Solid and dashed lines represent the liquid and vapour composition according to the CPA EOS. Squares are measurements of Wei et al.¹⁰⁵ and circles are from Davalos et al.¹⁰⁴

The RKS EOS cannot describe the compositions at higher pressures and near the critical points, but at lower pressures it fits the experiments quite well. According to Wei et al., the deviations at higher pressure are a common feature of simple cubic EOS, and are worse for this system because the methane and carbon dioxide molecules are chemically dissimilar.

In Figure 1.21, the relative differences between model and experiments at 230 K are shown. In contrast to the previous figure, this plot demonstrates that also at lower pressures, there is some disagreement between the data sets of Wei et al. and Davalos et al. The CPA vapour composition lies between the results of the two experimental studies for pressures up to 60 bar, while there is a larger systematic error in the liquid composition.

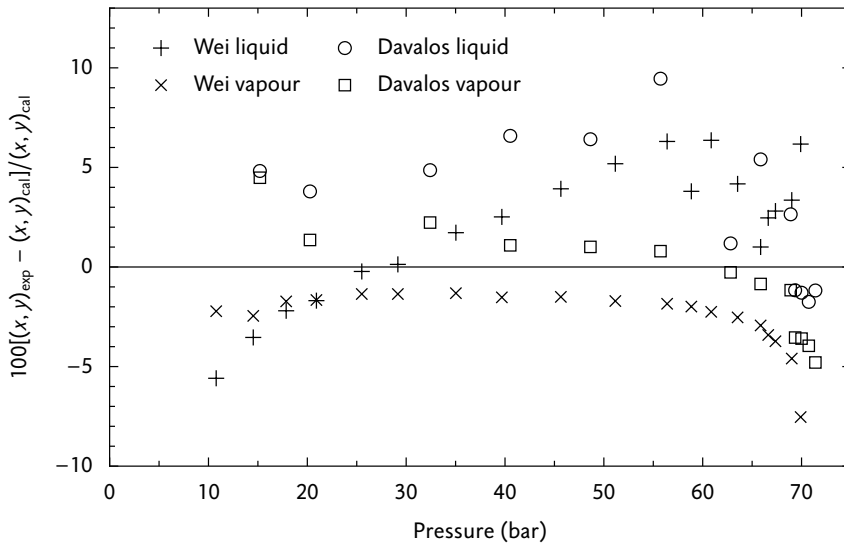


Figure 1.21: Methane–carbon dioxide system: relative differences between the experimental methane fractions x , y and the CPA EOS predictions at 230 K. The measurements are from Wei et al.¹⁰⁵ and Davalos et al.¹⁰⁴

1.8 Ternary system

It is straightforward to combine the models for the three binary systems into a ternary model, since the binary interaction parameters k_{ij} can be used without modification. In this way, the ternary model correctly reduces to one of the binary models if one of the components is not present in the mixture.

To analyse our experiments, the equilibrium fraction of water (or its enhancement factor) is needed at 235 K and 10 bar, as a function of the carbon dioxide fraction. The enhancement factor was computed at these conditions, and is plotted in Figure 1.22.

There is little experimental data on the water–methane–carbon dioxide system to compare our model to. Only one relevant study was found: that of Jarne et al.,⁶³ who measured the dew point temperatures of this system. The dew point temperature is the temperature to which a mixture with a fixed composition must be cooled down, at constant pressure, to form liquid on a surface. It is assumed that the dew point corresponds to saturation, so that it describes the liquid–vapour equilibrium of the system.

The disadvantage of dew point measurements compared to direct equilibrium vapour fraction measurements is that small differences in the equilibrium vapour pressure (or the enhancement factor) are often not detectable in the dew point temperature. For example, a difference of 10% in the vapour pressure leads to a difference of 1 K in the dew point temperature, which can

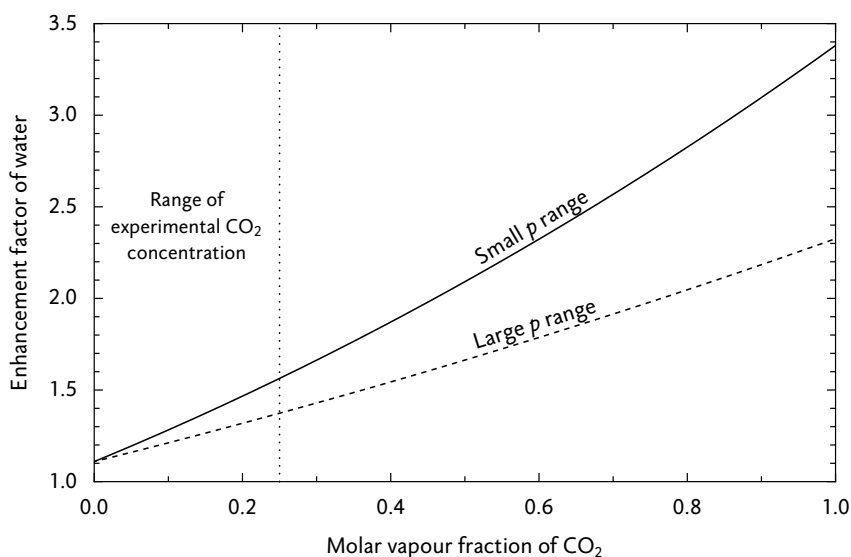


Figure 1.22: Enhancement factor of water in the water–methane–carbon dioxide system at 235 K and 10 bar, as a function of the carbon dioxide concentration, according to the CPA. The leftmost point of the horizontal axis corresponds to water in methane, and the rightmost point to water in carbon dioxide. The two curves represent the results using the different pressure fitting ranges for the water–carbon dioxide model.

be difficult to measure.

Figure 1.23a shows dew point temperatures measured by Jarne et al. in a mixture with a fixed composition of 80% methane, 20% carbon dioxide and 340 ppm water. The pressure of the system was varied, and at several pressures, the dew point temperature was measured. The dew point temperature increases with increasing pressure because at a higher pressure the partial pressure of water is higher as well, and condensation then occurs at a higher temperature.

The predictions of our CPA model are also shown in Figure 1.23a, as are the GERG and NIST models. All models predict nearly the same dew point temperatures for pressures below 10 bar, except for the NIST model. No model reproduces the experimental data of Jarne et al., which lie at temperatures of about 3 K higher. However, the slope dp/dT of experiment and models agrees.

A simple analysis of the experiments of Jarne et al. explains some of the discrepancies. For each dew point, the enhancement factor of water was calculated using Eq. 1.26. For dew points below 273 K, two enhancement factors were computed; one relative to the liquid–vapour equilibrium of water, the other relative to the ice–vapour equilibrium. These values are different be-

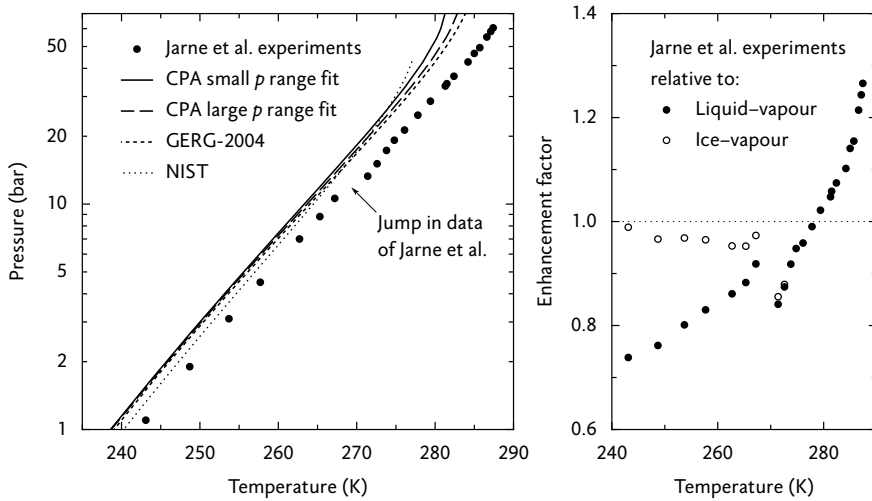


Figure 1.23: *Left:* Dew points of a mixture of methane (80%), carbon dioxide (20%) and water (340 ppm), as measured by Jarne et al.⁶³ and predicted by several models. *Right:* Enhancement factor of water, calculated from the measurements of Jarne et al. For measurements below the freezing temperature of water, enhancement factors corresponding to both liquid water and ice are shown.

cause of the different equilibrium vapour pressures of liquid water and ice (see Figure 1.2). The results are plotted in Figure 1.23b as a function of temperature.

There is an obvious jump in the enhancement factor near 270 K. Probably, below this temperature the dew point of ice was measured, instead of liquid water. This assumption is corroborated by the enhancement factors relative to ice, which converge to unity for low temperature and pressure. It is therefore not surprising that all models in Figure 1.23a deviate from the experimental data below 270 K, as the models predict the metastable liquid–vapour equilibrium, while the experiments represent the ice–vapour equilibrium.

On the other hand, the experiments above 273 K unambiguously represent the equilibrium with liquid water. However, the models do not agree with those experiments either. Figure 1.23b shows that several measurements have enhancement factors below unity. Such values are unlikely, considering the experimental data of the water–methane and water–carbon dioxide systems, where the enhancement factor is always higher than unity. Furthermore, the enhancement factor has to converge to unity for low pressures, but the actual experimental trend is towards much lower enhancement factors. It is therefore likely that there is a systematic error in the measurements of Jarne et al.

After the work on the CPA model of this chapter had been completed, the recent measurements of Qin et al.¹⁰⁶ on the water–methane–carbon dioxide system were found. Their data is at high pressure (100–500 bar), but in future work this data could be used to verify the behaviour of the ternary system.

1.9 Surface tension

Water

The surface tension of pure water above 273 K is accurately known,¹⁰⁷ but in the supercooled regime it is difficult to measure. As listed by Debenedetti,¹⁰⁸ the only three existing data sets are from Hacker,¹⁰⁹ down to 251 K, Floriano and Angell,¹¹⁰ down to 246 K, and Trinh and Ohsaka,¹¹¹ down to 252 K. The Hacker measurements show an inflection point at about 268 K, below which the surface tension has a larger temperature dependence; see Figure 1.24. The data of Floriano and Angell is less accurate, but the authors also noted an inflection. The [Trinh and Ohsaka](#) measurements show a systematic deviation, but the trend agrees with the Hacker data. Furthermore, a molecular dynamics simulation by Lü and Wei¹¹² shows an inflection point as well.

Because of the inflection point, the surface tension of supercooled water

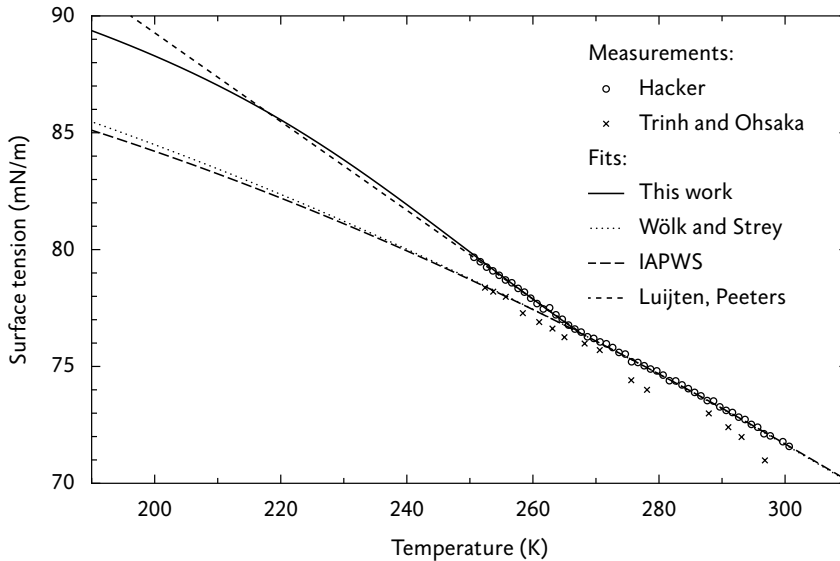


Figure 1.24: Surface tension of pure liquid water; measurements by Hacker¹⁰⁹ and Trinh and Ohsaka¹¹¹ and fits from this work (Eq. 1.57), Wölk and Strey,¹⁹ IAPWS¹⁰⁷ (Eq. 1.58), and Luijten.¹¹³ The IAPWS correlation is valid down to 273.16 K; here it is extrapolated to lower temperatures. No distinction is made between water under its own vapour pressure and water under atmospheric pressure (that is, in air).

cannot be obtained by extrapolation of the values at ambient temperature. Therefore, the fit used by Wölk and Strey,¹⁹ originally developed by Heist and Reiss,¹⁷ is not well suited for use below about 265 K. A better correlation was given by Luijten,⁶ who extrapolated a linear fit to Hacker's low-temperature data; Peeters⁸ adopted this fit. Hruby¹¹⁴ took a different approach, and developed a model that predicts the density of supercooled water, from which the surface tension could be derived. These surface tension values can be reproduced to within 0.2% relative error with the fit¹¹⁵

$$\sigma_w(T) = \sigma_I(T) - \sigma_a \tanh\left(\frac{T - T_a}{T_b}\right) + \sigma_b, \quad 100 \text{ K} < T < 267.5 \text{ K}, \quad (1.57)$$

where $\sigma_a = 2.854 \text{ mN/m}$, $\sigma_b = 1.666 \text{ mN/m}$, $T_a = 243.9 \text{ K}$, $T_b = 35.35 \text{ K}$, and $\sigma_I(T)$ is the IAPWS surface tension^{107,116}

$$\sigma_I(T) = 0.2358 \tau^{1.256} (1 - 0.625 \tau) \text{ N/m}, \quad (1.58)$$

with $\tau = 1 - T/(647.096 \text{ K})$.

Water-carbon dioxide

The influence of carrier gas pressure on the surface tension was studied theoretically by Eriksson,¹¹⁷ his results are summarized by Luijten.¹¹³ The main conclusion is that adsorption of carrier gas molecules onto the surface results in a decrease of the surface tension, as long as the molar fraction of carrier gas molecules is higher on the surface than in the liquid. As we will see, this is the case in the water-carbon dioxide system.

The surface tension in the water-carbon dioxide system has been measured by several researchers in the temperature range of 278 to 383 K, at pressures up to 450 bar. Overviews of publications are given in Hebach et al.¹¹⁸ and Chiquet et al.¹¹⁹ For this work, the data sets of Chun and Wilkinson¹²⁰ and Hebach et al.¹¹⁸ were selected because they span a wide temperature and pressure range and are given in tabular form. It is worth noting that these experimenters determined surface tensions in different ways: Chun and Wilkinson used the capillary rise method, while Hebach et al. used the pendant drop method.

Both methods to measure surface tension require knowledge of the density difference between the two phases. As pointed out by Chiquet et al.,¹¹⁹ most researchers did not measure densities, but used known values of the densities of pure water and pure carbon dioxide. An estimation of the effect of dissolved carbon dioxide on the liquid density (based on the partial molar volume of carbon dioxide in water¹²¹) shows that solubility of the gas cannot be neglected at the conditions where measurements have been made. On the

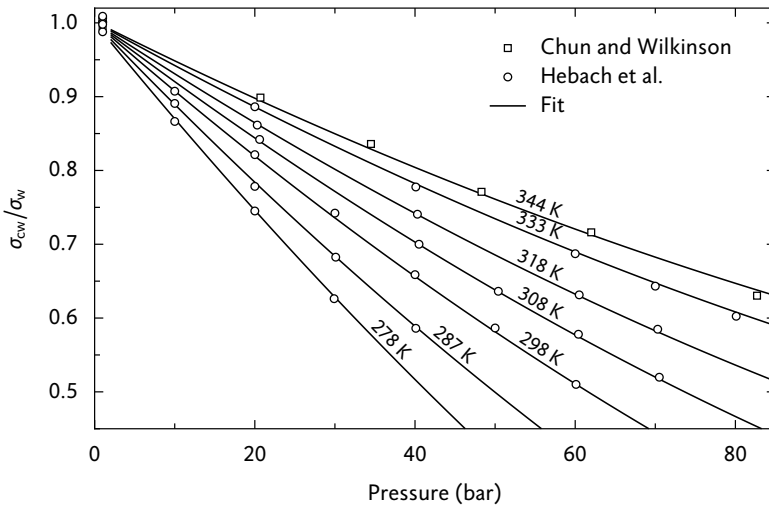


Figure 1.25: Surface tension of the carbon dioxide–water system, relative to the pure water surface tension σ_w . Experimental data from Hebach et al.¹¹⁸ and Chun and Wilkinson.¹²⁰ The solid curves represent the fit from Eq. 1.61.

other hand, the effect of water vapour on the density of the gas phase is so small ($\Delta\rho/\rho < 10^{-3}$) that it can be ignored.

Because Hebach et al. calculated their surface tension data using pure-component densities, a correction was applied to their data. The density of water saturated with carbon dioxide was computed with the model of Duan et al.,¹²² using the solubility data of Diamond and Akinfiev.⁶⁵ For the gas phase, the density of carbon dioxide was taken from the model of Span and Wagner.⁷² The maximum relative change in surface tension due to the correction was 2%. Chun and Wilkinson¹²⁰ did not specify which liquid density they used, so their data cannot be corrected and must be regarded as less accurate.

To test the internal consistency of each data set, the surface tension was plotted as a function of the pressure. In such a plot (Figure 1.25) the isotherms should smoothly converge to the pure water surface tension, for decreasing pressure. The Hebach et al. measurements satisfy this criterion, but most Chun and Wilkinson isotherms show bends at 20 bar; these isotherms are not shown in Figure 1.25. Only the isotherm at the highest temperature (344 K) is smooth and was retained.

The set of measurements was further reduced by discarding the high-pressure data for which carbon dioxide was present in the liquid form. These measurements are not relevant for us, since carbon dioxide is never liquid in our experiments. Above the critical temperature (304 K), only measurements below 80 bar were included. The selected measurements are shown in

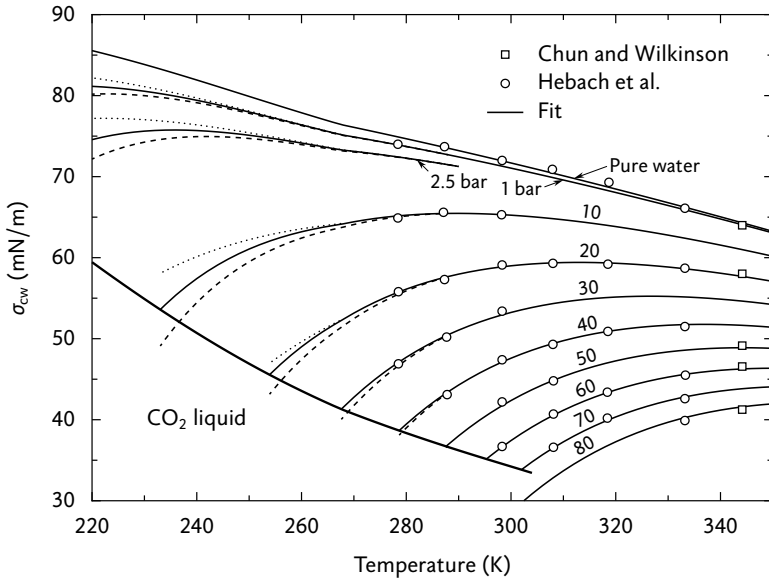


Figure 1.26: Surface tension of the carbon dioxide–water system; experimental data from Hebach et al.¹¹⁸ and Chun and Wilkinson.¹²⁰ The solid curves represent the fit from Eq. 1.61; the dashed and dotted curves show other possible extrapolations, and indicate the uncertainty at low temperature. At low temperature and high pressure, the carbon dioxide-rich phase becomes a liquid and the fits are not applicable there.

Figures 1.25 and 1.26.

For the analysis of our nucleation experiments, we need surface tension values for supercooled water at 235 K, far below the lowest-temperature measurements at 278 K. Therefore, the surface tension must be extrapolated using a suitable fit. Luijten^{13,113} developed a fit function based on the Langmuir adsorption model, which neglects the dissolution of the carrier gas into the liquid. In our case, the solubility of carbon dioxide in water cannot be neglected, so the Luijten fit cannot be used. Instead, the fit function

$$\frac{\sigma_{cw}(p, T)}{\sigma_w(T)} = 1 - g(p) \exp[h(T)] \quad (1.59)$$

was used, where $\sigma_{cw}(p, T)$ is the surface tension in the water–carbon dioxide system, $\sigma_w(T)$ is the surface tension of pure water, and g and h are functions to be determined. The pressure will not be extrapolated beyond the range of measurements, so the form of the $g(p)$ function (polynomial, exponential or otherwise) is not too important; it should just interpolate the measurements well. In contrast, the extrapolation to low temperature is sensitive to the form

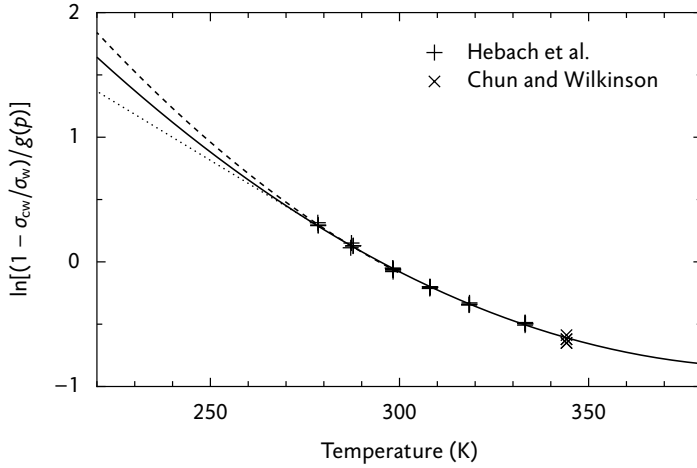


Figure 1.27: Surface tension of the carbon dioxide–water system, scaled to eliminate the pressure dependence according to Eq. 1.60. Experimental data from Hebach et al.¹¹⁸ (10 to 80 bar) and Chun and Wilkinson¹²⁰ (21 to 83 bar). The solid curve indicates the temperature dependence from Eq. 1.61; the dashed and dotted curves show other possible extrapolations, and indicate the uncertainty at low temperature.

of $h(T)$. Equation 1.59 can be written as

$$h(T) = \ln \left[\frac{1 - \sigma_{cw}(p, T)/\sigma_w(T)}{g(p)} \right]. \quad (1.60)$$

Therefore, a plot of the right-hand side of Eq. 1.60 versus T shows the shape of $h(T)$. In such a plot, Figure 1.27, all experimental isobars coincide because the $g(p)$ scaling successfully compensates for the pressure dependency. From the figure, it appears that a quadratic function of T reproduces the temperature dependence well. A quadratic function was chosen for $g(p)$ as well, which resulted in the surface tension fit

$$\frac{\sigma_{cw}}{\sigma_w} = 1 - (p_r - 0.233p_r^2) \exp[-0.848 + 7.87(1.25 - \tau)^2], \quad (1.61)$$

with

$$\tau = \frac{T}{320 \text{ K}} \quad \text{and} \quad p_r = \frac{p - p_s(T)}{100 \text{ bar}}. \quad (1.62)$$

The fit is shown in Figures 1.25 and 1.26. In the range of 275 to 345 K and 0 to 80 bar, the relative accuracy is 0.5%. When the fit is extrapolated to lower temperatures, the uncertainty increases, as the dashed and dotted lines in the figures illustrate.

Water–methane

There are only a few reliable measurements of the surface tension in the water–methane system. In 1995, Sachs and Meyn¹²³ concluded: ‘Nearly all of the published surface tension data in the system methane/water seem to be extremely inaccurate or even wrong.’ For this reason, Sachs and Meyn performed precise measurements in a wide range, 3–660 bar and 298–398 K. Since then, other experimental data has been published (see the review in Schmidt et al.¹²⁴), but the data of Sachs and Meyn remains the most accurate. Unfortunately, only their data at 298 K is tabulated,¹²⁵ while the higher-temperature data is only given in a graph in a rarely-cited paper.¹²³ For this work, the high-temperature measurements were digitized from a scan of the graph, which limits the accuracy of the pressure to 1 bar, whereas the stated experimental pressure accuracy is 0.05 bar. After digitizing, the data was found to agree with the 298 K data¹²⁵ and earlier measurements by Jho et al.¹²⁶ Figures 1.28 and 1.29 show the surface tension as a function of pressure and temperature.

Several functions to fit the data were evaluated. First, a fit based on Luijten’s approach was found to be difficult to extrapolate to low temperature, where the methane surface coverage becomes higher than the validity limit of the Langmuir model. Second, a fit of the form of Eq. 1.59 failed to satisfactorily reproduce the experimental data. Finally, a polynomial function of

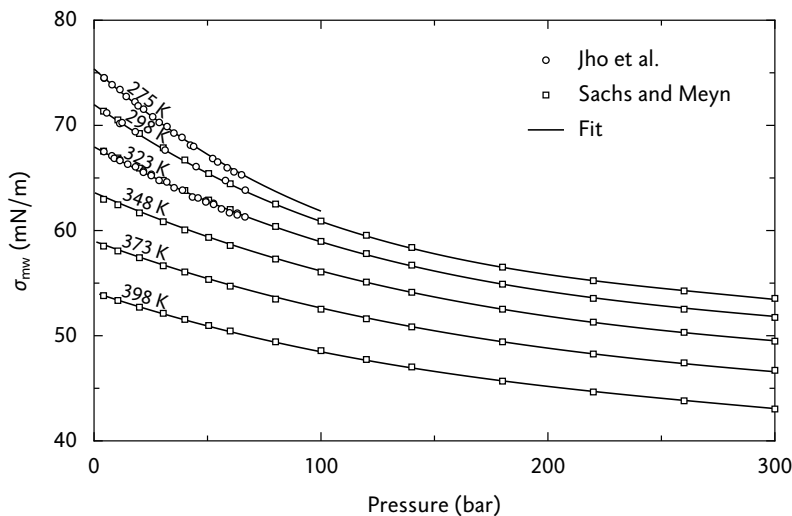


Figure 1.28: Surface tension of the methane–water system; experimental data from Jho et al.¹²⁶ and Sachs and Meyn.¹²³ The solid curves represent the fit from Eq. 1.63.

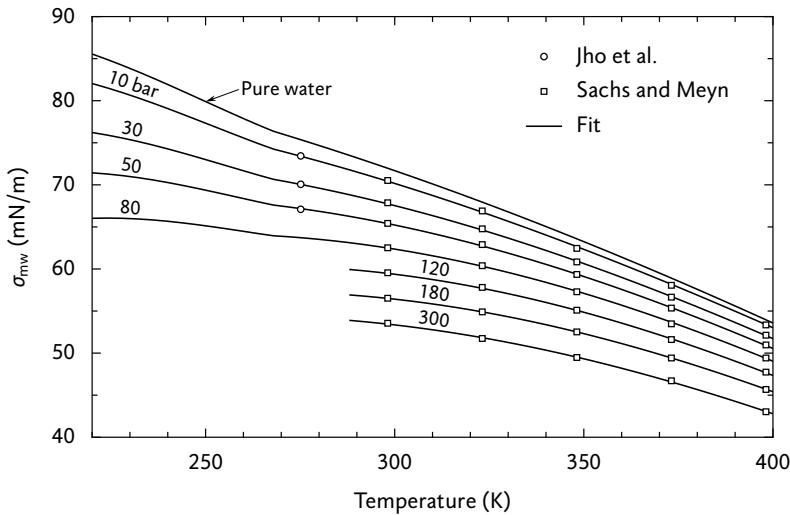


Figure 1.29: Surface tension of the methane–water system; selected experimental data from Jho et al.¹²⁶ and Sachs and Meyn.¹²³ The solid curves represent the fit from Eq. 1.63.

pressure and temperature was fitted to the data, yielding

$$\frac{\sigma_{mw}}{\sigma_w} = 1 + (-1.5921 + 2.3987 \tau - 0.98497 \tau^2) p_r + (0.87224 - 1.4345 \tau + 0.61051 \tau^2) p_r^2 + (-0.14474 + 0.24687 \tau - 0.10727 \tau^2) p_r^3, \quad (1.63)$$

with τ and p_r defined as in Eq. 1.62. In the range of 275–400 K and 0–300 bar, the relative accuracy of the fit is better than 0.5%. The extrapolation of polynomials can be problematic; in this case, the extrapolation to temperatures of about 235 K seems reasonable for pressures lower than about 100 bar, as Figure 1.29 illustrates. At that temperature, however, the relative uncertainty is several percent.

Ternary system

Only one set of measurements exists of the surface tension in the water–methane–carbon dioxide system, that of Ren et al.¹²⁷ Their data suffers from a number of inconsistencies. First, the data in their table does not match their graph. Second, the measurements do not agree with the surface tensions of the binary systems water–methane and water–carbon dioxide. Third, the surface tension is not a smooth function of the gas composition, at constant temperature and pressure. Finally, Ren et al. computed surface tensions using inaccurate density difference values. To correct for the last problem, we recomputed the surface tensions using accurate density values.^{14,62,73} The re-

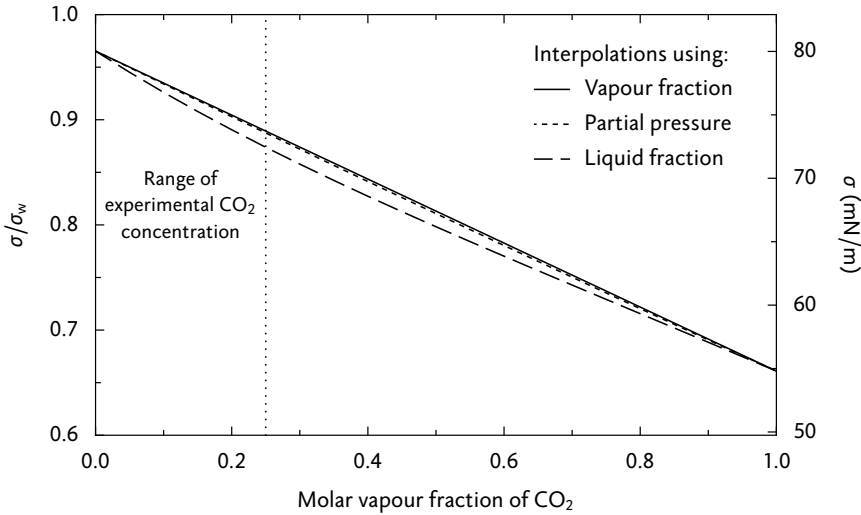


Figure 1.30: Surface tension of the water–methane–carbon dioxide system at 235 K and 10 bar, as a function of the carbon dioxide concentration in the vapour phase. *Left axis:* as fraction of the pure water surface tension; *right axis:* as value in mN/m.

calculated data, however, still suffers from the other inaccuracies. Therefore, the Ren et al. data was completely discarded.

Without experimental data, the surface tension in the ternary system must be derived from the binary systems, for example by interpolation. The simplest interpolation is a linear one, using the vapour fraction of carbon dioxide y_c ,

$$\sigma_t(p, y_c) = y_c \sigma_{cw}(p) + (1 - y_c) \sigma_{mw}(p), \quad (1.64)$$

where σ_t is the surface tension in the ternary system. Alternatively, the partial pressures of methane and carbon dioxide can be used to determine the contributions of the binary systems. Then, each binary surface tension is evaluated at the corresponding partial pressure, and the surface tension reductions are added,

$$\sigma_t(p, y_c) - \sigma_w = \{ \sigma_{cw}(y_c p) - \sigma_w \} + \{ \sigma_{mw}[(1 - y_c)p] - \sigma_w \}. \quad (1.65)$$

Another option is to assume that the reduction of surface tension is proportional to the molar liquid fractions x_m and x_c of methane and carbon dioxide in the ternary system. In that case, a suitable interpolation is

$$\sigma_t(p, y_c) - \sigma_w = [\sigma_{cw}(p) - \sigma_w] \frac{x_c(p, y_c)}{x_c(p, 1)} + [\sigma_{mw}(p) - \sigma_w] \frac{x_m(p, y_c)}{x_m(p, 0)}. \quad (1.66)$$

The liquid fractions are computed with the CPA equation of state.

Figure 1.30 shows the surface tension obtained by the three interpolation methods. The results differ little because the binary-system surface tensions are approximately linear functions of the pressure, and the liquid fractions are nearly proportional to the partial pressures. In the rest of this work, the surface tension of the ternary system is computed with the liquid-fraction interpolation.

1.10 Conclusion

Each of the pure components water, methane, and carbon dioxide can be adequately described by the CPA model. The greatest difficulty lies in reproducing water's density maximum at 277 K and the vapour pressure of supercooled water below 240 K. That these properties are difficult to model is not surprising, as both are influenced by water's anomalous low-temperature behaviour. Hence, a specialized EOS would be required to improve the agreement for those quantities. For our use at 235 K, the CPA performance for the pure components is acceptable.

Several difficulties were encountered during the modelling of the binary systems. First, the performance of the binary EOS depends strongly on the pure-component parameters. To obtain an acceptable water–methane model, it was necessary to choose parameters that resulted in a suboptimal reproduction of water's density and vapour pressure. A second difficulty is the lack of accurate experimental data on enhancement factors in the water–methane and water–carbon dioxide systems. The many inconsistencies of existing literature data seem to have been noted only by [Koglbauer and Wendland](#).¹²⁸

Because of the inaccurate data, the uncertainty of the CPA prediction is relatively large, especially at 235 K. For the water–methane system, the relative uncertainty of the enhancement factor at 235 K and 10 bar is estimated at 5%. For the ternary system with 25% carbon dioxide at the same pressure and temperature, the relative uncertainty is about 15%. Since the supersaturation is proportional to the enhancement factor (Eq. 1.29), the uncertainty in the supersaturation is equally large. Furthermore, the strong supersaturation dependence of the nucleation rate results in quite large errors in the nucleation rate; relative errors of 5% and 15% in the supersaturation cause errors of a factor of 3 and 25 in the nucleation rate, respectively.

In the analysis of the surface tension in our experimental systems, the same problems were encountered as in the enhancement factor modelling: the lack of accurate data and the uncertain extrapolation down to 235 K. The resulting relative uncertainty of the water–methane surface tension is about 4%, and that of the surface tension in the ternary system with 25% carbon dioxide is about 6%. These relative errors of 4% and 6% cause theoretical nucleation rate errors of a factor of 60 and 500, respectively.

Nucleation and droplet growth theory

2

2.1 Capillarity approximation

Before quantities such as the nucleation rate can be derived, a model for the cluster has to be adopted. Most theories are based on a simplified model called the ‘capillarity approximation’. In this model, it is assumed that the cluster is spherical and that it has a uniform density equal to that of the bulk liquid. The interface between the liquid and the vapour is taken infinitely thin and the surface tension there is equal to that of the interface between the bulk phases at equilibrium. A real cluster has different properties, and it seems likely that not a single assumption of the capillarity approximation is satisfied. Nevertheless, it is frequently used, at least in all theories we will encounter in this chapter.

The volume v_n of a cluster is proportional to the number of molecules n that it consists of, so

$$v_n = n v_1, \quad (2.1)$$

where v_1 is the average volume available for one molecule in the bulk liquid. That is, $v_1 = M/(\rho_l N_A)$, with ρ_l the bulk liquid mass density, M the molar mass and N_A the Avogadro constant. Using the geometry of a sphere, the radius r_n of the cluster is related to its volume according to

$$(4\pi/3)r_n^3 = v_n, \quad (2.2)$$

from which it follows that

$$r_n = (3v_1/4\pi)^{1/3} n^{1/3} \equiv r_1 n^{1/3}. \quad (2.3)$$

Analogously, the surface area a_n of the cluster is

$$a_n = (36\pi)^{1/3} v_1^{2/3} n^{2/3} \equiv a_1 n^{2/3}. \quad (2.4)$$

2.2 Energy of cluster formation

Consider a system in which a cluster is formed. Initially, the system contains a mixture of a vapour and one or more carrier gases at temperature T and pressure p^g . In the final state, the system contains a liquid cluster of the same temperature, which is surrounded by the vapour-carrier gas mixture. We will now derive the change in free energy between the initial and final state. It is assumed that the system is so large that the formation of a cluster does not significantly change the state of the vapour-gas mixture. With this assumption, it can be shown²³ that all free energies – Helmholtz and Gibbs free energies and the grand potential – change by the same amount. Any of these three quantities can be chosen for the evaluation; here, the Gibbs free energy is selected. This implies that the temperature, the pressure of the vapour-gas mixture, and the total amount of molecules remain constant.

It was already derived in chapter 1 that the Gibbs energy G_0 of the initial state, the homogeneous mixture, is given by (Eq. 1.6)

$$G_0 = \sum_i n_i \bar{\mu}_i^g, \quad (2.5)$$

where n_i are the numbers of molecules of component i and $\bar{\mu}_i^g$ is the chemical potential of component i in the gas phase; the bar on the $\bar{\mu}$ indicates that the chemical potential refers to a component in a mixture.

The next task is the evaluation of the Gibbs free energy G of the final state. It is not valid to simply take the sum of Gibbs energies of the liquid and gas phases (because the liquid phase is isolated), so G must be calculated from the energy U , which can be legitimately written as the sum of liquid, gas and surface contributions,²³

$$U = U^l + U^g + \sigma a, \quad (2.6)$$

where σ is the surface energy per unit area and a is the cluster's area. For a homogenous part of the system, the energy U^{hom} is

$$U^{\text{hom}} = TS - pV + \sum_i \bar{\mu}_i n_i. \quad (2.7)$$

Therefore, the energy of the liquid cluster is

$$U^l = TS^l - p^l V^l + \sum_i \bar{\mu}_i^l n_i^l. \quad (2.8)$$

The energy of the remaining $n - n^l$ molecules in the gas phase is

$$U^g = TS^g - p^g V^g + \sum_i \bar{\mu}_i^g (n_i - n_i^l), \quad (2.9)$$

where the chemical potential $\bar{\mu}_i^g$ is the same as in the initial state (Eq. 2.5) because the pressure, temperature and composition of the gas phase are constant. The total energy is then

$$U = TS - p^l V^l - p^g V^g + \sum_i \bar{\mu}_i^l n_i^l + \sum_i \bar{\mu}_i^g (n_i - n_i^l) + \sigma a, \quad (2.10)$$

where it was used that $S \equiv S^l + S^g$. The Gibbs free energy G now follows from the energy U according to Eq. 1.3, $G = U - TS + p^g(V^l + V^g)$, which leads to

$$G = V^l(p^g - p^l) + \sum_i \bar{\mu}_i^l n_i^l + \sum_i \bar{\mu}_i^g (n_i - n_i^l) + \sigma a. \quad (2.11)$$

The change in Gibbs energy $\Delta G \equiv G - G_0$ is then

$$\Delta G = V^l(p^g - p^l) + \sum_i (\bar{\mu}_i^l - \bar{\mu}_i^g) n_i^l + \sigma a. \quad (2.12)$$

Now, the chemical potential difference $\Delta\bar{\mu} \equiv \bar{\mu}^l - \bar{\mu}^g$ of the vapour component will be evaluated. For notational simplicity, the subscript indicating the component will be omitted. When the conditions at which the chemical potential is evaluated are explicitly given, $\Delta\bar{\mu}$ is written as

$$\Delta\bar{\mu} = \bar{\mu}^l(p^l, x) - \bar{\mu}^g(p^g, y), \quad (2.13)$$

where x is the fraction of vapour molecules in the cluster and y is the vapour fraction in the gas phase. (For three or more components, the chemical potentials depend on two or more fractions, but this dependency is omitted.) We now add and subtract the two-phase equilibrium potential $\bar{\mu}^g(p^g, y_{\text{eq}})$, yielding

$$\begin{aligned} \Delta\bar{\mu} &= \bar{\mu}^l(p^l, x) - \bar{\mu}^g(p^g, y_{\text{eq}}) + \underbrace{\bar{\mu}^g(p^g, y_{\text{eq}}) - \bar{\mu}^g(p^g, y)}_{-kT \ln S} \\ &= \bar{\mu}^l(p^l, x) - \bar{\mu}^l(p^g, x_{\text{eq}}) - kT \ln S. \end{aligned} \quad (2.14)$$

Here, the definition of S was used (Eq. 1.27), and the equality of chemical potentials in equilibrium allows replacing the gas-phase by the liquid-phase potential (that is, the second term on the right-hand side). Considering the liquid phase as an ideal solution (Eq. 1.14) results in the simplification

$$\Delta\bar{\mu} = v_1(p^l - p^g) + kT \ln(x/x_{\text{eq}}) - kT \ln S, \quad (2.15)$$

where the Gibbs–Duhem equation (Eq. 1.9) was used with molecular liquid volume v_1 . In nucleation theories where the cluster composition is taken into account (such as quasi-unary theory), this $\Delta\bar{\mu}$ expression is used in further derivations. Instead, it is assumed from here on that the liquid consists solely

of the vapour component, so that $x = x_{\text{eq}} = 1$. The expression for $\Delta\bar{\mu}$ then finally becomes

$$\Delta\bar{\mu} = v_1(p^l - p^g) - kT \ln S. \quad (2.16)$$

When this result is substituted in the equation for ΔG , Eq. 2.12, the pressure-volume terms cancel (because $V^l \equiv n^l v_1$), and the end result is

$$\Delta G = -n^l kT \ln S + \sigma a. \quad (2.17)$$

In a recent derivation of the energy of formation by Wedekind et al.¹²⁹ for an inert and ideal carrier gas, the pressure-volume terms do not cancel, leaving a term $V^l(p^g - p_s)$, with p_s the pure-component saturated vapour pressure. The authors claim that this additional pressure-volume work should be included in the work of formation and in the derivation of the nucleation rate. However, Wedekind et al. did not include the Poynting correction in their definition of the supersaturation, although the Poynting effect is present even in the case of ideal substances. When the supersaturation definition is corrected for the Poynting effect, the spurious pressure-volume term disappears.

In the rest of this work, the energy of formation is denoted by the symbol W_n , not ΔG , as it is independent of the kind of free energy that is used. The number of molecules in the cluster is indicated by n . With the assumptions of the capillarity approximation (Eq. 2.4), the energy of formation is written as

$$\begin{aligned} W_n &= -n kT \ln S + \sigma a_n \\ &= -n kT \ln S + \sigma a_1 n^{2/3}. \end{aligned} \quad (2.18)$$

To simplify this expression, we introduce the dimensionless surface energy Θ , defined as

$$\Theta \equiv \frac{a_1 \sigma}{kT}. \quad (2.19)$$

Equation 2.18 then becomes

$$\frac{W_n}{kT} = -n \ln S + \Theta n^{2/3}. \quad (2.20)$$

The work of formation can thus be described by two terms: one is proportional to the surface area and represents the energy needed to form a new phase interface; the other one is proportional to the volume and represents the energy gained by forming an amount of the new phase (if $S > 1$).

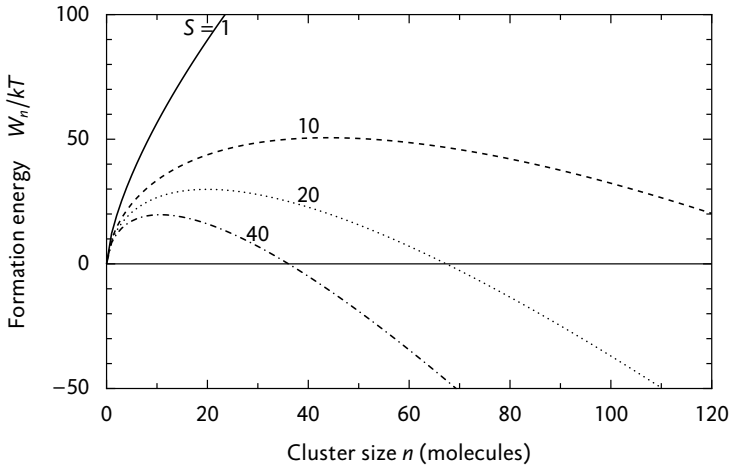


Figure 2.1: Energy of formation W_n for water at 235 K, according to Eq. 2.20, for several supersaturations.

The work of formation reaches its maximum value at the critical size n^* , given by

$$n^* = \left(\frac{2\Theta}{3 \ln S} \right)^3. \quad (2.21)$$

The critical size is therefore determined by two independent variables: the supersaturation and the dimensionless surface energy.

2.3 Cluster size distributions

In equilibrium, the distribution of cluster sizes is given by a Boltzmann distribution,

$$\rho_n \propto \exp(-W_n/kT), \quad (2.22)$$

where ρ_n is the equilibrium number density of clusters of n molecules. Several expressions for the distributions have been in use; Wilemski¹³⁰ describes the most common ones. In this chapter, three distributions will be studied, and we will adopt Wilemski's names for the distributions.

Frenkel distribution

The oldest distribution, given by Frenkel,^{131,132} has the number of monomers as a prefactor in the Boltzmann distribution, which gives

$$\rho_n^F = \rho_1 \exp(-W_n/kT), \quad n \geq 2, \quad (2.23)$$

or, with substitution of W_n from Eq. 2.20,

$$\rho_n^F = \rho_1 \exp(n \ln S - \Theta n^{2/3}), \quad n \geq 2. \quad (2.24)$$

As indicated, these expressions cannot be applied at $n = 1$ because they do not reduce to the identity $\rho_1^F = \rho_1$ for that value of n . This limitation is sometimes seen as a problem, but Wilemski¹³⁰ points out that there is no reason why a distribution should have a simple form that can be applied to every cluster size. Instead, the distribution can simply be redefined to equal the monomer density at $n = 1$. This approach will be adopted here.

Courtney distribution

Whereas the monomer concentration could be redefined easily, the Frenkel distribution suffers from a more fundamental problem: the failure to satisfy the law of mass action. According to that law, the relation

$$\rho_n = \rho_n^{\text{sat}} S^n \quad (2.25)$$

must hold, while the Frenkel distribution yields $\rho_n^F = \rho_n^{\text{sat}} S^{n+1}$. This inconsistency is avoided by the Courtney¹³³ distribution, the second distribution to be considered here. As a prefactor, it uses the monomer density at saturation ρ_1^{sat} instead of ρ_1 , leading to

$$\rho_n^C = \rho_1^{\text{sat}} \exp(n \ln S - \Theta n^{2/3}), \quad n \geq 2. \quad (2.26)$$

The Courtney distribution differs by a factor of $1/S$ from Frenkel's expression, and satisfies the law of mass action. Like the Frenkel distribution, it must be redefined at $n = 1$ to yield $\rho_1^C = \rho_1$.

Self-consistent distribution

It has been noted by several authors (e.g. Girshick and Chiu¹³⁴) that the monomer density 'inconsistency' of the Courtney distribution can be removed by changing $n^{2/3}$ to $n^{2/3} - 1$. The resulting distribution, called the self-consistent classical (scc) distribution, is given by

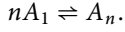
$$\rho_n^{\text{scc}} = \rho_1^{\text{sat}} \exp[n \ln S - \Theta(n^{2/3} - 1)], \quad n \geq 1. \quad (2.27)$$

The justification for this form (as presented by Girshick and Chiu¹³⁴ and Kashchiev²²) is that according to Eq. 2.20, the formation energy of a monomer W_1 is not zero, and the distribution should be taken from

$$\rho_n = \rho_1 \exp[-(W_n - W_1)/kT], \quad (2.28)$$

Law of mass action

The equilibrium between monomers and a cluster A_n containing n molecules can be represented as the reversible ‘reaction’



According to the law of mass action,⁴³ the concentrations ρ_1 and ρ_n of components A_1 and A_n are related by

$$\rho_n = (\rho_1)^n K_n(T), \quad (1)$$

where the equilibrium constant $K_n(T)$ may not depend on p , S or ρ_1 .¹³⁰ Evaluating Eq. 1 at saturation, we obtain

$$K_n(T) = \rho_n^{\text{sat}} / (\rho_1^{\text{sat}})^n.$$

Since K does not depend on S , this result is valid for all S . Substituting it back into Eq. 1 gives

$$\rho_n = \rho_n^{\text{sat}} (\rho_1 / \rho_1^{\text{sat}})^n = \rho_n^{\text{sat}} S^n,$$

which proves Eq. 2.25 for $S \leq 1$. For $S > 1$, the law of mass action must be applied to a constrained equilibrium. Since such an equilibrium is unattainable in reality, the validity of the law of mass action for this state is questionable, but in the nucleation literature the law is applied without reservation.^{22,130}

which results in Eq. 2.27. Quantitatively, the scc distribution is related to the other distributions by

$$\frac{\rho_n^{\text{scc}}}{\rho_n^{\text{c}}} = e^{\Theta} \quad \text{and} \quad \frac{\rho_n^{\text{scc}}}{\rho_n^{\text{f}}} = \frac{e^{\Theta}}{S}, \quad n \geq 2. \quad (2.29)$$

Because Θ is of the order of ten, the difference between the scc distribution and the other ones is considerable. The e^{Θ} factor, however, does not affect the supersaturation dependence of the distribution, so the scc distribution also satisfies the law of mass action.

Size and supersaturation dependence

For convenience, the three distributions are repeated here.

$$\begin{aligned} \rho_n^{\text{f}} &= \rho_1 \exp(n \ln S - \Theta n^{2/3}), & n \geq 2. \\ \rho_n^{\text{c}} &= \rho_1^{\text{sat}} \exp(n \ln S - \Theta n^{2/3}), & n \geq 2. \\ \rho_n^{\text{scc}} &= \rho_1^{\text{sat}} \exp[n \ln S - \Theta(n^{2/3} - 1)], & n \geq 1. \end{aligned} \quad (2.30)$$

The size dependence of the three distributions is illustrated in Figure 2.2 for a subsaturated state (with $S = 0.5$) and for a supersaturated state ($S = 20$). In

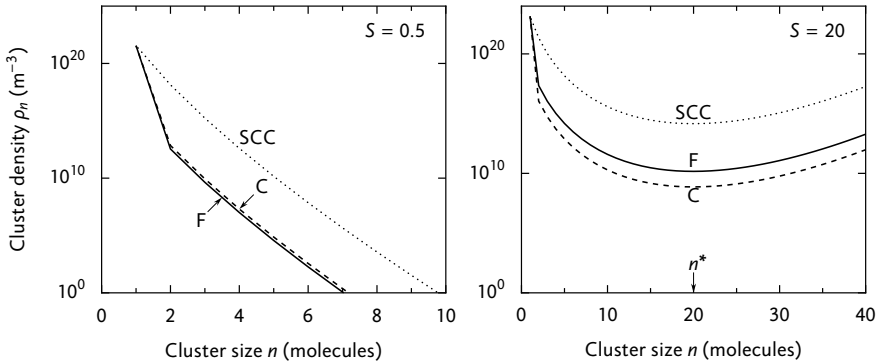


Figure 2.2: Cluster size distributions for water at 235 K, according to the Frenkel (F), Courtney (C), and self-consistent (SCC) distributions of Eq. 2.30. *Left:* subsaturated state, *right:* supersaturated state.

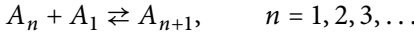
the subsaturated state, the cluster density rapidly falls off with increasing n . The Frenkel and Courtney distributions have a kink at $n = 2$ which results from the redefinition of the monomer density.

In the supersaturated state, the cluster density also decreases with increasing n , but it flattens at the critical size n^* , and then starts increasing without limit. This behaviour cannot represent the initial stage of condensation, since, as Frenkel¹³² notes, the main mass of the system would be found in the liquid state if ρ_n rises without bounds. This discrepancy is a consequence of treating the supersaturated system as if it were in stable equilibrium; in reality, a supersaturated vapour can be at most metastable. But even the distribution in a metastable supersaturated vapour will not increase as it does in Figure 2.2; such an increasing distribution cannot exist. In contrast, the descending part of the supersaturated distribution will prove to be a reasonable approximation of the distribution during steady-state nucleation (section 2.6).²² To completely analyse the problem of stationary nucleation, thermodynamics alone is insufficient; in addition, the kinetics of cluster formation must be taken into account, which will be done in the next section.

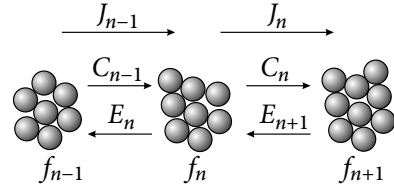
2.4 Kinetic model

The derivation of classical nucleation theory is based on a kinetic model known as the Szilard model.¹³⁵ In this model, clusters can gain or lose only single molecules, and cluster–cluster interactions are neglected. Ignoring collisions between clusters is justified by the scarcity of these clusters; monomers (i.e., single molecules) are much more abundant. If A_n represents a cluster containing n molecules, the size change of that cluster by attachment or de-

tachment of a monomer can be represented by the reversible ‘reaction’



The rates at which these reactions take place are specified by the condensation coefficients C_n and evaporation coefficients E_n . Specifically, C_n is the rate at which monomers condense on a cluster of n molecules, and E_n is the rate at which molecules evaporate from such a cluster. Denoting the number density of n -clusters by f_n , we find that the rate of change of the n -cluster concentration is



$$\frac{df_n}{dt} = C_{n-1}f_{n-1} - (C_n + E_n)f_n + E_{n+1}f_{n+1}. \quad (2.31)$$

The net number of clusters per unit time and volume that grow from size n to $n + 1$ is denoted by J_n . This quantity can be thought of as a flux, or current, in size space.

$$J_n = C_n f_n - E_{n+1} f_{n+1}. \quad (2.32)$$

With the definition of J_n , the kinetic equations can also be expressed as

$$\frac{df_n}{dt} = J_{n-1} - J_n. \quad (2.33)$$

The condensation coefficient C_n is the frequency at which monomers condense on a single cluster with n molecules. In the literature, this quantity is known by several different names, such as ‘condensation rate’,²¹ ‘forward rate’,¹³⁶ ‘forward rate coefficient’,¹³⁰ and ‘monomer attachment frequency’.²² Of course, also the symbols used for the condensation coefficient are diverse; the notation that is used here comes from Abraham. In any case, there is agreement on the dimension of C_n ; it is a pure frequency, with a dimension of inverse time.

Obviously, C_n depends on the concentration of monomers in the vapour and the size of the cluster. Also, C_n only counts monomers that stay attached to the cluster, instead of reflecting off the surface. This effect is accounted for by the parameter α_n , which is the fraction of monomers hitting the cluster that stick. Like C_n , the quantity α_n has different names in the literature, for example ‘sticking probability’,¹³⁰ ‘accommodation coefficient’,¹³⁷ ‘condensation coefficient’,^{21,136} and ‘sticking coefficient’.²² It is usually taken equal to unity, and we will do the same. If, conversely, α_n is not assumed unity but

taken n -independent, the nucleation rate becomes proportional to α_n . Recent simulations¹³⁸ of clusters of water molecules suggest that α_n is strongly size-dependent up to about $n = 20$; for small clusters, α_n is smaller than 0.1, and it rises to values in the range of 0.7 to 1 for n larger than about 20. Such a behaviour of α_n is expected to have a large effect on the nucleation rate.

The condensation coefficient is the product of the sticking probability α_n , the collision frequency per unit area β and the cluster surface area a_n . It follows from kinetic gas theory¹³⁹ that β is equal to one quarter of the product of monomer number density ρ_1 and the mean molecular speed \bar{u} :

$$\beta = \frac{1}{4}\rho_1\bar{u} \quad (2.34)$$

From the Maxwell–Boltzmann velocity distribution it follows that¹³⁹ $\bar{u} = (8kT/\pi m)^{1/2}$, with $m = M/N_A$ the molecular mass. Therefore,

$$C_n = \alpha\beta a_n = \left(\frac{kT}{2\pi m}\right)^{1/2} \rho_1 a_1 n^{2/3}. \quad (2.35)$$

This expression is not accurate for very small clusters because these are not spherical. It is not accurate either for clusters that are much larger than the mean free molecular path; in that case, the monomer concentration near the cluster surface is lower than the monomer concentration far away. The growth then becomes controlled by diffusion, which has been discussed in section 2.11.

For dilute vapours which consist mainly of monomers, the monomer density is proportional to the partial pressure of the vapour and, accordingly, to its supersaturation. The condensation coefficient is then also proportional to the supersaturation,

$$C_n = S C_n^{\text{sat}} = S C_1^{\text{sat}} n^{2/3}, \quad (2.36)$$

where the superscript ‘sat’ refers to the saturated state with $S = 1$.

2.5 Detailed balance

The condensation coefficient can be derived from straightforward kinetic considerations. It is difficult to derive an expression for the evaporation coefficient from first principles, but it is possible to relate it to other known properties, using a method called ‘detailed balancing’. The detailed balance method can be applied in two ways, depending on the condition at which it is evaluated. Both ways will be presented.

Constrained equilibrium

The balance at ‘constrained equilibrium’ is the classical way of finding the evaporation coefficient. This method is now obsolete, but will be treated here because it was for some time the only existing method, and many derivations are therefore based on it. In this method, it is hypothesized that for any supersaturation S , a stable equilibrium distribution ρ_n exists, for which the nucleation rate is zero. (That is, $J_n = 0$ for all n .) However, as described in section 2.3, the distribution ρ_n is unstable and cannot exist for a supersaturated state. The only way to maintain the distribution is to constrain it in some way that prevents its collapse; for this reason, the equilibrium is said to be *constrained*. Hypothetically, such a state could be realized with the help of a Maxwell demon; see page 70 for details. Accepting its existence, hypothetical as it may be, it follows from Eq. 2.32 that

$$C_n \rho_n = E_{n+1} \rho_{n+1}, \quad \text{or} \quad E_{n+1} = \frac{\rho_n}{\rho_{n+1}} C_n. \quad (2.37)$$

This method to determine E_n is called ‘detailed balancing’; in statistical mechanics, detailed balance requires that the transition rates between any pair of states are equal in either direction.

When Eq. 2.30 is substituted into Eq. 2.37, it follows that all cluster size distributions yield the same result for E_n for $n \geq 3$, namely

$$E_n = C_{n-1}^{\text{sat}} \exp\{\Theta[n^{2/3} - (n-1)^{2/3}]\}, \quad n \geq 3, \quad (2.38)$$

For large n , a useful approximation is

$$E_n \approx C_{n-1}^{\text{sat}} \exp\left(\frac{2}{3}\Theta n^{-1/3}\right), \quad n \text{ large}, \quad (2.39)$$

which has a relative error of less than 4% for n higher than about 20, for usual values of Θ in the range of 10 to 20.

All E_n except E_2 are independent of the choice of cluster distribution. The reason for the difference in E_2 values is that the ρ_n^{F} and ρ_n^{C} formulas of Eq. 2.30 are not valid for $n = 1$, which was pointed out by Wilemski.¹³⁰ In those cases, E_2 must be evaluated from $E_2 = (\rho_1/\rho_2)C_1$, where ρ_2 (but not ρ_1) is calculated from Eq. 2.30. Remarkably, solely the E_2 coefficient is responsible for the dependence of the nucleation rate on the cluster distribution, since the kinetic model of Eq. 2.31 is fully determined by the C_n and E_n coefficients. All these coefficients are independent of the cluster distribution, except for E_2 .

Phase equilibrium

The physical vapour–liquid equilibrium is the saturated state ($S = 1$). Unlike the constrained equilibrium, the saturated state is stable, and the cluster distribution could be measured. (Of course, stable undersaturated states with

Maxwell's demon

Many nucleation theoreticians have mentioned that the constrained equilibrium distribution is artificial and cannot be realized in reality. Hypothetically, it could be maintained if it were constrained in some way that prevents its collapse. The constraint has been described with the help of a Maxwell demon, which is a hypothetical entity that is able to observe and act upon individual molecules. In 1867, Maxwell¹⁴⁰ invented a 'finite being' to illustrate limitations of the second law of thermodynamics. Later, William Thomson¹⁴¹ used the word 'demon', a term of which Maxwell did not approve. Thomson defined the demon as an intelligent being capable of observing and manipulating individual molecules.

So how does the demon attain constrained equilibrium? In most descriptions^{20,142} the demon takes clusters that succeed in growing to a certain size M , breaks them apart into their constituent molecules, and returns these as monomers to the system. This corresponds to the boundary condition $f_M = 0$, which Abraham²¹ and McDonald¹⁴³ attribute to Szilard. Instead of maintaining the constrained equilibrium, this condition leads to steady-state nucleation. This led Katz¹³⁶ to conclude, 'The attainment of a constrained equilibrium distribution is beyond even the powers of Maxwell's demon.'

However, when given the right instructions, Maxwell's demon *can* create the desired distribution. McDonald¹⁴³ explained how: the demon simply has to reflect away each molecule that is about to condense on a cluster of a certain size $M - 1$, thus preventing it from growing to size M . Now, the boundary condition is $C_{M-1} = 0$, and consequently also $f_M = 0$. Recalling the definition of J_n (Eq. 2.32), then

$$J_{M-1} = \underbrace{C_{M-1}}_0 f_{M-1} - E_M \underbrace{f_M}_0 = 0,$$

which represents the cut-off in the distribution: there is no flux between sizes $M - 1$ and M . But at steady state, $df_n/dt = 0$ for all n , so

$$J_{n-1} = J_n \quad \text{for all } n.$$

Because $J_M = 0$,

$$J_n = 0 \quad \text{for all } n.$$

which is the condition for constrained equilibrium.

In conclusion, the Szilard boundary condition can be viewed as a sink in size space¹⁴⁴ leading to steady-state nucleation. In contrast, the Maxwell demon can be seen as a barrier in size space, which leads to a pile-up of clusters – the constrained-equilibrium distribution.

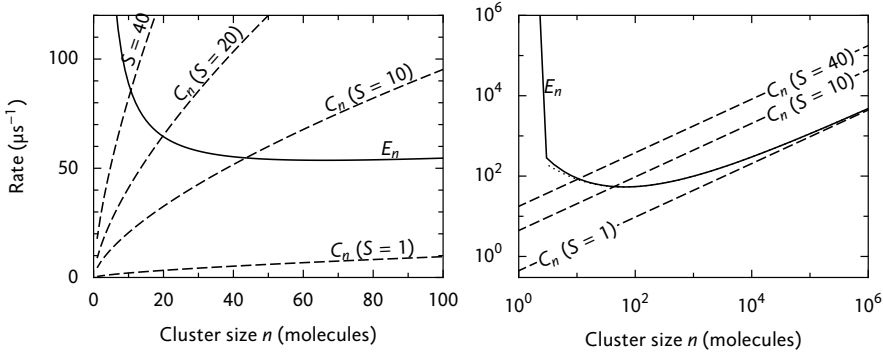


Figure 2.3: Condensation and evaporation coefficients C_n and E_n as a function of the cluster size for water at 235 K. *Left:* linear scale, *right:* logarithmic scale. The Courtney distribution was chosen for evaluation; this only affects E_2 . For large cluster sizes, $E_n \approx C_n^{\text{sat}}$. In the right-hand figure, the approximate E_n of Eq. 2.39 is also plotted (dotted).

$S < 1$ also exist and are measurable, but are not needed in this derivation.) Because the constrained equilibrium state is avoided, this approach is a more physical and also more elegant way of deriving the classical nucleation theory. As in the constrained equilibrium, $J_n = 0$ for all n , so the detailed balance condition reads

$$C_n^{\text{sat}} \rho_n^{\text{sat}} = E_{n+1}^{\text{sat}} \rho_{n+1}^{\text{sat}}, \quad (2.40)$$

where superscript ‘sat’ indicates that the balance holds only at the saturated state. We adopt the usual assumption that the evaporation coefficient depends only on the cluster size, and is independent of the density of the vapour. This is so, because it is the thermal motion of the cluster molecules that determines the probability of evaporation. As long as thermal equilibrium is maintained, the thermal motion of the cluster molecules is not affected by the vapour density. Therefore, for any supersaturation, the evaporation coefficient is given by

$$E_{n+1} = \frac{\rho_n^{\text{sat}}}{\rho_{n+1}^{\text{sat}}} C_n^{\text{sat}}. \quad (2.41)$$

To obtain values for E_n , the cluster distributions ρ_n of Eq. 2.30 are evaluated at $S = 1$ and substituted into Eq. 2.41. It is then found that E_n for $n \geq 3$ is the same for all cluster size distributions, and equal to the result of the constrained equilibrium, Eq. 2.38. Conversely, the E_2 values depend on the cluster distribution, but the F and C distributions have the same E_2 since they agree on the value of ρ_2^{sat} .

The evaporation and condensation coefficients C and E are equal for a critical cluster. With the expression of Eq. 2.21 for the critical size, $n^* = [2\Theta/(3 \ln S)]^3$, it immediately follows from the approximate Eq. 2.39 that

$$E_{n^*} \approx C_{n^*-1}. \quad (2.42)$$

The size dependence of the coefficients is shown in Figure 2.3 for water.

2.6 Steady-state nucleation

With the condensation and evaporation coefficients known, we proceed to finding solutions of the kinetic equations, Eq. 2.31. During steady-state nucleation, all J_n are the same and equal to the steady-state nucleation rate J . This condition may also be derived by setting $df_n/dt = 0$ in Eq. 2.33. The steady-state concentrations will be denoted by f_n^s .

As boundary condition, the concentration of a certain subcritical cluster of size i is held constant,

$$f_i^s = \rho_i. \quad (2.43)$$

where ρ_i is given by Eq. 2.30. When $i = 1$, this corresponds to a constant monomer concentration.

Condition 2.43 implies that there is no depletion; there is either an unlimited supply of i -sized clusters, or the amount of matter in newly formed clusters is negligible compared to the clusters of size i . Numerical simulations¹⁴⁵ have demonstrated that at very high supersaturations (e.g., $S > 300$ for $\Theta = 12$), depletion of monomers becomes important so soon that the steady state is never reached. However, also at lower supersaturations the experimental conditions (such as pressure and temperature) may change so rapidly that a steady state cannot be established. The current treatment is therefore limited to moderate supersaturations and relatively slow changes of conditions.

The derivation of the nucleation rate expression depends on the state at which the detailed balance is evaluated (either at constrained equilibrium or at phase equilibrium). Both approaches will be described.

Constrained equilibrium

Substitution of $J_n = J$ in Eq. 2.32, together with the constrained-equilibrium condition of Eq. 2.37 yields

$$\frac{J}{C_n \rho_n} = \frac{f_n^s}{\rho_n} - \frac{f_{n+1}^s}{\rho_{n+1}} \quad (2.44)$$

When this equation is summed from $n = i$ to $n = N$, successive terms on the right-hand side cancel; only the $n = i$ and $n = N$ terms remain, leading to

$$J \sum_{n=i}^N \frac{1}{C_n \rho_n} = 1 - \frac{f_{N+1}^s}{\rho_{N+1}}. \quad (2.45)$$

The last term vanishes for large N , so

$$J = \left(\sum_{n=i}^N \frac{1}{C_n \rho_n} \right)^{-1}. \quad (2.46)$$

This is the constrained-equilibrium expression for J . To evaluate it, a model for the equilibrium distribution ρ_n must be selected. However, without a complete derivation, we can evaluate the dependence of J on the distribution, as shown by Wilemski.¹³⁰ According to Eqs. 2.26 and 2.29,

$$\frac{\rho_n^c}{\rho_n^f} = \frac{1}{S} \quad \text{and} \quad \frac{\rho_n^{\text{SCC}}}{\rho_n^f} = \frac{e^\Theta}{S}, \quad n \geq 2. \quad (2.47)$$

These relations are not valid for $n = 1$, but in the sum of Eq. 2.46, the $n = 1$ term is usually negligible (and if $i > 1$ is chosen, this term is not present at all). Because the ratio of distribution functions in Eq. 2.47 is independent of n ,

$$\frac{J^c}{J^{\text{cl}}} = \frac{1}{S} \quad \text{and} \quad \frac{J^{\text{SCC}}}{J^{\text{cl}}} = \frac{e^\Theta}{S}. \quad (2.48)$$

For the purpose of defining a reference rate that can be used later on, J^f is here denoted by J^{cl} . This is the classical rate expression as obtained by Frenkel,¹³² which results from a constrained-equilibrium approach with the Frenkel distribution.

Kinetic approach

The derivation of the nucleation rate using a detailed balance at saturation was introduced by Katz and Wiedersich¹⁴² and summarized by Katz and Donohue.¹³⁶ In their derivations, they stressed that all quantities could be expressed in terms of kinetic coefficients (such as the condensation coefficient), and that the thermodynamic supersaturation did not appear. This led them to call their method the ‘kinetic approach’; this name is still used today. It must be realized, however, that the constrained-equilibrium approach also depends on kinetic arguments.

In the kinetic approach, the steady-state condition $J_n = J$ is again substituted in Eq. 2.32, but now the equilibrium expression of Eq. 2.41 is used

instead of Eq. 2.37, yielding

$$\frac{J}{C_n \rho_n^{\text{sat}}} = \frac{f_n^s}{\rho_n^{\text{sat}}} - \frac{C_n^{\text{sat}}}{C_n} \frac{f_{n+1}^s}{\rho_{n+1}^{\text{sat}}}. \quad (2.49)$$

According to Eq. 2.36, the ratio C_n^{sat}/C_n , which appears above, is equal to $1/S$. If we would not substitute this result, S would not appear in the derivation, as mentioned above. Katz and Donohue¹³⁶ remark that for non-ideal systems the ratio C_n^{sat}/C_n may not be equal to $1/S$, but Luijten (appendix D of Ref. 113) has shown that for our experimental conditions the equality holds.

After elimination of the ratio C_n^{sat}/C_n in favour of S , we divide both sides of Eq. 2.49 by S^n and obtain

$$\frac{J}{C_n \rho_n^{\text{sat}} S^n} = \frac{f_n^s}{\rho_n^{\text{sat}} S^n} - \frac{f_{n+1}^s}{\rho_{n+1}^{\text{sat}} S^{n+1}}, \quad (2.50)$$

which is a form suitable for summation. Summing from $n = i$ to $n = N$ gives

$$J \sum_{n=i}^N \frac{1}{C_n \rho_n^{\text{sat}} S^n} = \underbrace{\frac{f_i^s}{\rho_i^{\text{sat}} S^i}}_A - \frac{f_{N+1}^s}{\rho_{N+1}^{\text{sat}} S^{N+1}}. \quad (2.51)$$

The last term on the right-hand side again vanishes for large enough N . The value of the other term, A , depends on the choice of i and the distribution. First, consider the case $i = 1$. Then $A = 1$, since $f_1^s \equiv \rho_1 = S \rho_1^{\text{sat}}$. For $i > 1$, however, the value of A depends on the cluster size distribution formula in Eq. 2.30. For the F distribution, with Eq. 2.43, $f_i^s \equiv \rho_i = S^{i+1} \rho_i^{\text{sat}}$, so $A = S$. For the C and SCC distributions, $f_i^s \equiv \rho_i = S^i \rho_i^{\text{sat}}$, and therefore $A = 1$.

Using the same reasoning as in the previous section and the distribution expressions from Eq. 2.30, the result for J can be compared to the classical nucleation rate expression, which gives

$$\frac{J^c}{J^{\text{cl}}} = \frac{1}{S}, \quad \frac{J^{\text{SCC}}}{J^{\text{cl}}} = \frac{e^\Theta}{S}, \quad \text{and} \quad \frac{J^F}{J^{\text{cl}}} = \begin{cases} 1/S & i = 1 \\ 1 & i > 1. \end{cases} \quad (2.52)$$

To clarify, J^{cl} still represents the classical rate that Frenkel¹³² obtained using the constrained-equilibrium approach. In the current kinetic approach, the Frenkel rate depends on i ; if $i = 1$, the Frenkel rate is equal to the Courtney rate, and if $i > 1$, the Frenkel rate is equal to the classical rate. For the C and SCC distributions, the result for J is the same as in the constrained equilibrium case. In fact, this is so for any distribution that satisfies the law of mass action. For such a distribution, the relation

$$\rho_n = \rho_n^{\text{sat}} S^n \quad (2.53)$$

holds, which results in $A = 1$. Equation 2.51 then gives

$$J = \left(\sum_{n=i}^N \frac{1}{C_n \rho_n^{\text{sat}} S^n} \right)^{-1} = \left(\sum_{n=i}^N \frac{1}{C_n \rho_n} \right)^{-1}, \quad (2.54)$$

which is equal to the constrained-equilibrium result (Eq. 2.46). In the rest of this chapter, we will assume that the distribution ρ_n satisfies the law of mass action.

Steady-state distribution

The steady-state distribution f^s can be obtained by summing Eq. 2.50 from $n = k$ to $n = N$, which results in

$$f_k^s = \rho_k^{\text{sat}} S^k J \sum_{n=k}^N \frac{1}{C_n \rho_n^{\text{sat}} S^n}, \quad (2.55)$$

or by summing from $n = i$ to $n = k$, which gives

$$f_k^s = \rho_k^{\text{sat}} S^k \left(1 - J \sum_{n=i}^{k-1} \frac{1}{C_n \rho_n^{\text{sat}} S^n} \right). \quad (2.56)$$

Both equations are equivalent, but only the last equation can be evaluated for $S < 1$, an undersaturated equilibrium state. From Eq. 2.54 it follows that $J = 0$ for $S < 1$. In Eq. 2.56, the zero J is multiplied by a finite sum, and the result for f_k^s is then

$$f_k^s = \rho_k^{\text{sat}} S^k = \rho_k, \quad S < 1. \quad (2.57)$$

This is the expected result: the steady-state distribution reduces to the equilibrium distribution for $S < 1$.

For large cluster sizes, the steady-state distribution can be approximated by substituting one of the ρ_n distributions from Eq. 2.30. It is found that

$$\begin{aligned} f_n^s &= J \sum_{k=n}^N \frac{1}{C_k} \frac{\rho_n^{\text{sat}} S^n}{\rho_k^{\text{sat}} S^k} \approx \sum_{p=0}^{\infty} \frac{J}{C_{n+p}} S^p \exp\{\Theta[(n+p)^{2/3} - n^{2/3}]\} \\ &\approx \frac{J}{C_n} \sum_{p=0}^{\infty} \frac{\exp(\frac{2}{3} p \Theta n^{-1/3})}{S^p} = \frac{J}{C_n} \frac{S}{S - \exp(\frac{2}{3} \Theta n^{-1/3})}. \end{aligned} \quad (2.58)$$

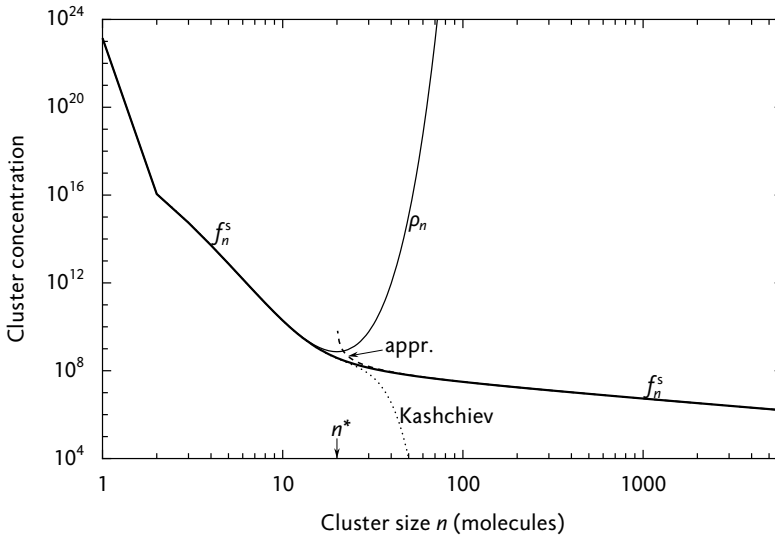


Figure 2.4: Cluster concentration f_n^s during steady-state nucleation as a function of the cluster size for water at 235 K and $S = 20$. The Courtney distribution was chosen for evaluation. For comparison, the constrained-equilibrium distribution ρ_n is also shown, together with the approximate f_n^s from Eq. 2.58, and Kashchiev's approximation (Eq. 13.20 in Ref. 22).

This approximation and the exact result are shown in Figure 2.4. For large enough n , the approximation of Eq. 2.58 can be further simplified by replacing the exponential by unity. Then, f_n^s becomes proportional to $n^{-2/3}$, which results in a line with slope $-2/3$ in the double-logarithmic plot of Figure 2.4.

Another approximation to the steady-state distribution was described by Kashchiev.²² In contrast to the approximate Eq. 2.58, Kashchiev's approximate form is valid for sizes up to the critical size. At larger sizes, it rapidly falls to zero, as Figure 2.4 shows.

2.7 Steady-state nucleation rate

We now return to the expression for the nucleation rate, Eq. 2.54, to evaluate it further. It is possible to obtain a simpler but approximate result with a series of approximations given by Zeldovich¹⁴⁶ and adopted by Frenkel.¹³² First, the summation is replaced by an integration to infinity,

$$J = \left(\sum_{n=i}^N \frac{1}{C_n \rho_n} \right)^{-1} \approx \left(\int_1^{\infty} \frac{1}{C_n \rho_n} dn \right)^{-1}, \quad (2.59)$$

where n is now regarded as a continuous variable. Because ρ_n has a sharp minimum near n^* (see Figure 2.4), the integrand has a sharp peak near that

cluster size. Therefore, only the region near n^* significantly contributes to the integral, and a simplification is possible if the integrand is approximated in that region. For that purpose, the integral is written as

$$J = \left(\int_1^{\infty} \exp[-H(n)] dn \right)^{-1}, \quad (2.60)$$

where $H(n) \equiv \ln(C_n \rho_n)$. Then, the function $H(n)$ is expanded in a Taylor series around the critical size n^* , where the derivative of $H(n)$ is zero:

$$H(n) \approx H(n^*) + \frac{1}{2}(n - n^*)^2 H''(n^*), \quad (2.61)$$

where the double prime denotes the second derivative. Note that the critical size is redefined here as the n for which $H(n)$ has a minimum; this value may be different from the n^* of Eq. 2.21. When the expansion of H of Eq. 2.61 is substituted back in Eq. 2.60 and the lower integration limit is shifted to $-\infty$, the result is a standard integral, with solution

$$J = \left[\frac{H''(n^*)}{2\pi} \right]^{1/2} \exp[H(n^*)] = \zeta C_{n^*} \rho_{n^*}. \quad (2.62)$$

where the Zeldovich factor ζ has been defined as

$$\zeta = [H''(n^*)/(2\pi)]^{1/2}. \quad (2.63)$$

The next step is to evaluate H . To keep the derivation general, the cluster distribution is written as $\rho_n = \rho_0 \exp(-W_n/kT)$, with ρ_0 a prefactor which depends on the choice of equilibrium distribution from Eq. 2.30. We can then write H as

$$\begin{aligned} H(n) &\equiv \ln(C_n \rho_n) \\ &= \ln C_1 + \ln n^{2/3} - \ln \rho_0 - W_n/kT \\ &= \ln C_1 + \ln n^{2/3} - \ln \rho_0 - \Theta n^{2/3} + n \ln S. \end{aligned} \quad (2.64)$$

To find the critical size, we use that $H'(n^*) = 0$, which leads to

$$\frac{\Theta n^{*2/3} - 1}{n^*} = \frac{3}{2} \ln S. \quad (2.65)$$

In most cases $\Theta n^{*2/3} \gg 1$, so the critical size becomes

$$n^* = \left(\frac{2\Theta}{3 \ln S} \right)^3, \quad (2.66)$$

which is the same result as obtained before (Eq. 2.21). Using a similar approximation $\Theta n^{*2/3} \gg 3$, we find for the Zeldovich factor

$$\zeta = \frac{1}{3} \left(\frac{\Theta}{\pi} \right)^{1/2} (n^*)^{-2/3}. \quad (2.67)$$

Typically, ζ is about 0.05 to 0.10. Let us analyse what this value means. Consider the general nucleation rate expression (Eq. 2.62)

$$J = \zeta C_{n^*} \rho_{n^*}, \quad (2.68)$$

which states that the nucleation rate equals the product of the Zeldovich factor, the rate at which monomers condense on a critical cluster, and the constrained-equilibrium number density of critical clusters. If most supercritical clusters became macroscopic droplets, ζ would be of the order of unity. The smallness of ζ as obtained from Eq. 2.67 has several causes. First, the actual number density of critical clusters $f_{n^*}^s$ is smaller than in constrained equilibrium; see Figure 2.4. Indeed, in most cases, the steady-state concentration $f_{n^*}^s$ is about half of ρ_{n^*} . A larger effect, however, results from the evaporation of supercritical clusters. At the critical size, C_n and E_n are approximately equal, so Eq. 2.32 becomes

$$J = C_{n^*} f_{n^*}^s - E_{n^*+1} f_{n^*+1}^s \approx C_{n^*} (f_{n^*}^s - f_{n^*+1}^s). \quad (2.69)$$

A comparison with Eq. 2.68 shows that the Zeldovich factor is approximately given by

$$\zeta \approx \frac{f_{n^*}^s - f_{n^*+1}^s}{\rho_{n^*}} \approx \frac{1}{2} \frac{f_{n^*}^s - f_{n^*+1}^s}{f_{n^*}^s}, \quad (2.70)$$

where it was used that $f_{n^*}^s / \rho_{n^*} \approx 1/2$. This expression illustrates that it is the relative difference of $f_{n^*}^s$ and $f_{n^*+1}^s$ that determines the nucleation rate, not the value of $f_{n^*}^s$ itself. In other words, the derivative of f^s matters, not its value. That is the reason why the Zeldovich factor is much smaller than 1/2. Coincidentally, Eq. 2.69 tells something else about nucleation. Dropping the steady-state requirement, and taking n a continuous variable, we can write Eq. 2.69 as $J \propto \partial f / \partial n$. When we additionally write Eq. 2.33 as $\partial f / \partial t = \partial J / \partial n$, it follows that

$$\frac{\partial f}{\partial t} \propto \frac{\partial^2 f}{\partial n^2}, \quad (2.71)$$

which shows that the distribution near the critical size is essentially determined by diffusion in size space.

We now return to our main task of evaluating the nucleation rate J . From Eqs. 2.62, 2.64 and 2.67 we find that

$$J = \frac{1}{3} C_1 \rho_0 \left(\frac{\Theta}{\pi} \right)^{1/2} \exp \left(-\frac{W_{n^*}}{kT} \right). \quad (2.72)$$

Using the definitions of C_1 (Eq. 2.35) and Θ (Eq. 2.19) it is finally found that

$$J = \rho_0 \rho_1 v_1 \left(\frac{2\sigma}{\pi m} \right)^{1/2} \exp \left[-\frac{4}{27} \frac{\Theta^3}{(\ln S)^2} \right]. \quad (2.73)$$

The Courtney (1/ S -corrected) version of the nucleation rate is obtained with $\rho_0 = \rho_1^{\text{sat}}$ and the SCC version with $\rho_0 = \rho_1^{\text{sat}} \exp(\Theta)$.

Nucleation with carrier gas

The nucleation rate has been derived without referring to a carrier gas that may be present. The non-ideality of the gas–vapour mixture can be easily taken into account in the surface tension σ and the supersaturation S , by including the dependence on the carrier gas pressure and composition, as described in detail in chapter 1. Another parameter that must be corrected for carrier gas effects is the monomer density ρ_1 , which must be evaluated using the compressibility factor Z of the vapour–gas mixture. This factor is defined as $Z = p/(\rho kT)$, with ρ the number density of the mixture. Because of the low vapour fraction, the compressibility factor of the mixture can be taken equal to the compressibility factor Z_g of the pure carrier gas. With the additional assumption that the vapour consists mainly of monomers, the monomer density is approximated by

$$\rho_1 \approx \frac{y p}{Z_g kT} = S \frac{f_e p_s}{Z_g kT}. \quad (2.74)$$

The last equality follows from the definition of supersaturation, Eq. 1.29.

With the definitions of v_1 and Θ from section 2.1, the nucleation rate can now be written as a function of macroscopic quantities as

$$J = \left(\frac{f_e p_s}{Z_g kT} \right)^2 \left(\frac{2\sigma M}{\pi N_A} \right)^{1/2} \frac{S}{\rho_1} \exp \left[-\frac{16\pi}{3} \left(\frac{M}{N_A \rho_1 \ln S} \right)^2 \left(\frac{\sigma}{kT} \right)^3 \right]. \quad (2.75)$$

Here, the Courtney distribution was used. The SCC version is obtained by multiplying this result by e^Θ .

2.8 Non-steady-state nucleation

In the previous sections, the kinetic equation was solved to obtain the steady-state distribution and nucleation rate. In this section, the equation will be

solved for time-dependent solutions. To refresh our memory, the equation describing the kinetics of cluster formation is (Eq. 2.31)

$$\frac{df_n}{dt} = C_{n-1}f_{n-1} - (C_n + E_n)f_n + E_{n+1}f_{n+1}, \quad (2.76)$$

where $f_n(t)$ is the number density of clusters containing n molecules, C_n is the rate at which molecules condense on an n -cluster, and E_n is the rate at which molecules evaporate from such a cluster. The coefficients C_n and E_n will be taken time-independent, which corresponds to a system with constant temperature and supersaturation. Depletion of monomers is therefore excluded, like in the previous section.

A boundary condition similar to the steady-state case (Eq. 2.43) is chosen;

$$f_i(t) = \rho_i, \quad (2.77)$$

where ρ_i is the constrained-equilibrium distribution, and i is a subcritical number of molecules (typically, i lies in the range of five to ten). To complete the model, an initial condition is required. In this chapter, we assume that at time $t = 0$ the supersaturation is instantaneously increased and that no clusters were present before that time. Therefore, the initial condition is

$$f_n(0) = 0, \quad n > i. \quad (2.78)$$

It is possible to find an analytical solution of the set of kinetic equations, as long as n is not too large (that is, several hundred molecules). Because the number of included cluster sizes is finite, a boundary condition at the end of the cluster size range is also needed. Traditionally, the condition

$$f_M(t) = 0 \quad (2.79)$$

is adopted; this is known as the Szilard boundary condition.^{21,143}

To solve Eq. 2.76 with boundary condition Eq. 2.77, we rewrite it in matrix notation:

$$\mathbf{f}'(t) = \mathbf{A}\mathbf{f}(t) + \mathbf{g} \quad (2.80)$$

where

$$\mathbf{f} = \begin{pmatrix} f_{i+1} \\ f_{i+2} \\ \vdots \\ f_{M-1} \end{pmatrix}, \quad \mathbf{g} = \begin{pmatrix} \rho_i C_i \\ 0 \\ \vdots \\ 0 \end{pmatrix}, \quad (2.81)$$

and A is the tridiagonal matrix

$$A = \begin{pmatrix} D_{i+1} & E_{i+2} & & & 0 \\ C_{i+1} & D_{i+2} & E_{i+3} & & \\ & \ddots & \ddots & \ddots & \\ & & C_{M-3} & D_{M-2} & E_{M-1} \\ 0 & & & C_{M-2} & D_{M-1} \end{pmatrix} \quad (2.82)$$

where $D_n = -(C_n + E_n)$ was introduced as a shorthand notation.

Because Eq. 2.80 is inhomogeneous, the solution is equal to the solution of the homogeneous system f^h , plus a particular solution. A natural choice for a particular solution is the steady-state distribution f^s , which is time-independent. The full solution is therefore defined as

$$f(t) = f^h(t) + f^s. \quad (2.83)$$

For the current system, the steady-state distribution is already known from Eq. 2.55. In general, f^s can be found by using its time independence; when $f^{s'} = \mathbf{0}$ is substituted in Eq. 2.80, we obtain

$$A f^s = -g. \quad (2.84)$$

This is a tridiagonal system, so it can be efficiently solved. With f^s known, a particular solution has been found. Next, we turn to the homogenous system,

$$f^{h'}(t) = A f^h(t). \quad (2.85)$$

The solution of such a system is well known^{22,147,148} and consists of exponentials of the form

$$f^h(t) = v e^{\lambda t}, \quad (2.86)$$

with unknown $\lambda < 0$ and v . Substituting this solution in the homogeneous Eq. 2.85 leads to the eigenvalue equation

$$\lambda v = A v, \quad (2.87)$$

where λ is an eigenvalue and v is a corresponding eigenvector of matrix A . Each eigenvalue leads to a solution that has the form of Eq. 2.86; the general solution is a linear combination of these solutions.

$$\begin{aligned} f^h(t) &= c_i v_i e^{\lambda_i t} + \dots + c_M v_M e^{\lambda_M t} \\ &= \underbrace{(v_i \quad \dots \quad v_M)}_V \begin{pmatrix} c_i e^{\lambda_i t} \\ \vdots \\ c_M e^{\lambda_M t} \end{pmatrix} \end{aligned} \quad (2.88)$$

Here V is a matrix which has the eigenvectors v as columns, and c_i to c_M are constants that are determined by the initial condition, that is, $f(0) = \mathbf{0}$. Consequently, $f^h(0) + f^s = \mathbf{0}$, and therefore

$$Vc = -f^s. \quad (2.89)$$

Here c is a vector that has the constants c_i to c_M as elements. Equation 2.89 is a set of linear equations that can be easily solved numerically.

Because of the eigenvalue computation time, which is proportional to $(M-i-1)^3$, the parameter M cannot be very large. Moreover, the f_n near the end of the n range are perturbed by the boundary condition $f_M(t) = 0$ and must be discarded. This problem can be alleviated by adopting the alternative boundary condition

$$f_M(t) = f_{M-1}(t), \quad (2.90)$$

which can be easily implemented by changing the bottom-right element of the matrix A in Eq. 2.82 from D_{M-1} to $D_{M-1} + E_M$.

From an experimental point of view, it is useful to know the concentration of detectable clusters; that is, clusters larger than a certain size. The symbol \hat{f}_n will denote the total concentration of clusters larger than n molecules,

$$\hat{f}_n \equiv \sum_{m=n+1}^{\infty} f_m. \quad (2.91)$$

The time dependence of \hat{f}_n can be found by taking the time derivative, exchanging the summation and derivative, and using Eq. 2.76, yielding

$$\frac{d\hat{f}_n}{dt} = \sum_{m=n+1}^{\infty} \frac{df_m}{dt} = C_n f_n - E_{n+1} f_{n+1} \equiv J_n, \quad (2.92)$$

from which it follows that

$$\hat{f}_n(t) = \int_0^t J_n(t') dt'. \quad (2.93)$$

Because J_n (like f_n) consists of exponentials, the integration is trivial.

Solutions have been obtained for water at 228 K and $S = 20.6$, with $i = 5$ and $M = 150$. The results agree qualitatively with those of Abraham,¹⁴⁹ who solved the kinetic equations using numerical integration in 1969. Figure 2.5 shows the time dependence of the cluster concentrations f_n . At small times, the slopes in the double-logarithmic plot are constant, pointing to power-law behaviour. Indeed, Kashchiev²² and Shneidman¹⁵⁰ have shown that $f_n(t) \propto t^{n-1}$ for small t . Further, it is seen that concentrations of larger clusters need a

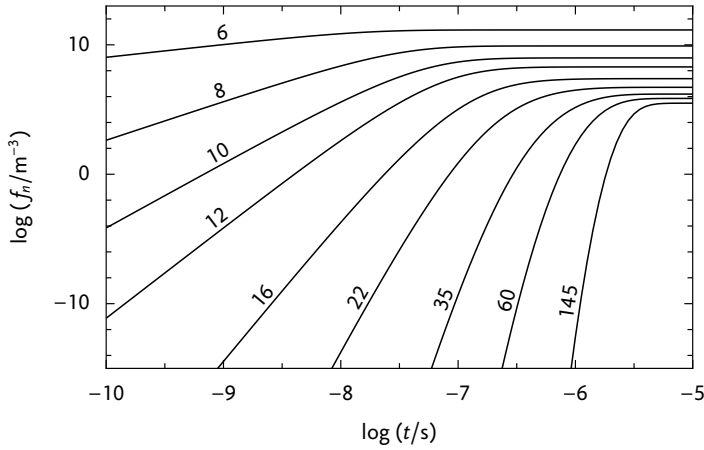


Figure 2.5: Number density of clusters f_n versus time, at 228 K and $S = 20.6$. At $t = 10^{-5}$ s, all cluster concentrations have reached their steady-state values corresponding to a steady-state nucleation rate of $2.85 \times 10^{13} \text{ m}^{-3} \text{ s}^{-1}$. The critical size is 22 molecules.

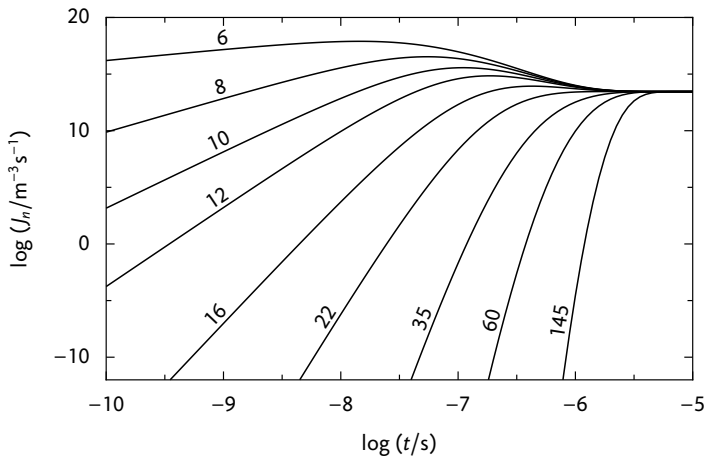


Figure 2.6: Nucleation rates J_n as a function of time, at 228 K and $S = 20.6$.

longer time to reach the steady-state values. After about $6 \mu\text{s}$, all f_n included in this simulation have reached steady-state. In Figure 2.6, the nucleation rates J_n are plotted versus time. It is observed that for clusters smaller than critical (22 molecules), the J_n overshoot their steady-state values, whereas supercritical J_n remain below it.

The total density of clusters larger than 140 molecules is displayed in Figure 2.7, where it is compared with a simple model that assumes an instantaneous steady-state nucleation rate. In agreement with Figures 2.5 and 2.6, the steady state is reached after about $6 \mu\text{s}$; from then on, the slope matches

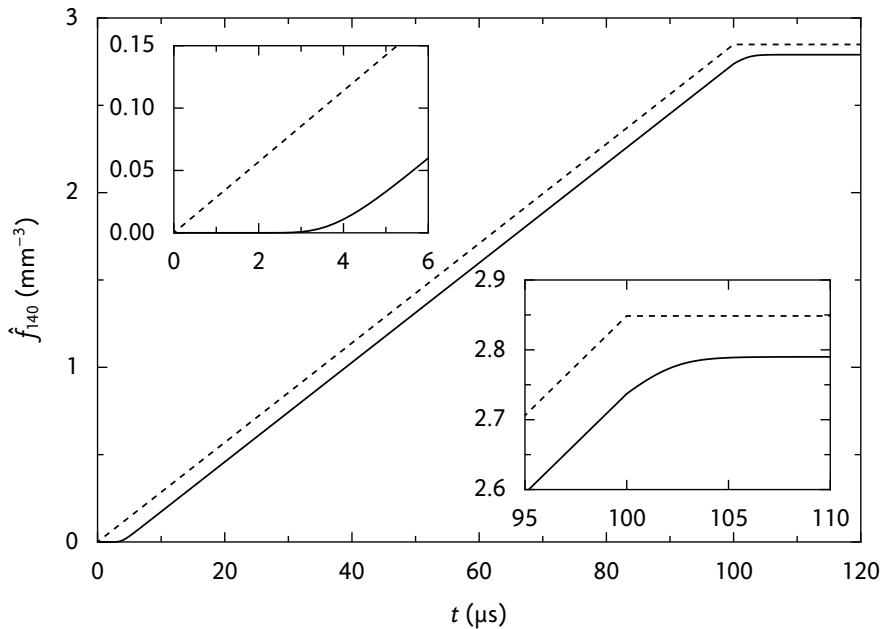


Figure 2.7: Total number density of clusters larger than 140 molecules. From $t = 0$ to $t = 100 \mu\text{s}$, the temperature is 228 K and $S = 20.6$. At $t = 100 \mu\text{s}$, the temperature and supersaturation are instantaneously changed to 236 K and $S = 10$, respectively. The dashed line is the number density when it is assumed that the nucleation rate equals its steady-state value, without taking into account transient behaviour.

the constant- J line.

For this example, the above-mentioned conditions hold between 0 and $100 \mu\text{s}$. After that, the temperature is increased to 236 K and the supersaturation drops to 10. As a result, the steady-state nucleation rate decreases by more than six orders of magnitude. Effectively, the amount of new clusters that are produced after the state change is negligible to the amount that was formed before. In Figure 2.7, it is seen that it takes about $6 \mu\text{s}$ for the cluster concentration to stabilize after the change. Although in both cases the delay to reach steady-state is $6 \mu\text{s}$, the transient effects at the start and stop of the nucleation are not mutually compensating. Specifically, the total cluster density remains lower than the simple model (dashed) predicts.

2.9 Nucleation theorem

The nucleation theorem provides a relation between a measurable quantity – the nucleation rate – and an otherwise hardly obtainable quantity: the number of molecules in a critical cluster. It was derived by Kashchiev¹⁵¹ and Ox-

toby and Kashchiev¹⁵² that

$$\left(\frac{\partial W^*}{\partial \mu_i}\right)_{\mu_{j \neq i}, T} = -\Delta n_i^*, \quad (2.94)$$

where W^* is the work of formation of the critical cluster, μ_i is the chemical potential of component i in the vapour phase, and Δn_i^* is the excess number of molecules of component i in the critical cluster. The excess number is the number of molecules in the cluster minus the number of molecules in one critical cluster volume in the gas phase. In other words, the excess number is the difference between the actual number of molecules in the cluster and the number of molecules in the gas phase that initially occupied the cluster's volume.

The nucleation theorem does not require the capillarity approximation to be valid. In fact, it makes no assumptions about the mechanism of nucleation or the size and shape of the critical cluster. Therefore, the excess number of molecules should not depend on the cluster radius, whose definition is ambiguous for arbitrary cluster shapes. For example, in the framework where the density is a function of the distance r from the cluster centre, the excess number of molecules is defined as¹⁵³

$$\Delta n_i^* = 4\pi \int_0^\infty [\rho_i(r) - \rho_i^{\text{gas}}] r^2 dr. \quad (2.95)$$

Here $\rho_i(r)$ is the number density of component i and ρ_i^{gas} is the density of that component in the gas phase far away from the cluster. This definition is clearly independent of any definition of the cluster radius.

In this section, the nucleation theorem will be applied to a binary mixture of a vapour and a carrier gas, indicated with subscripts 'v' and 'g', respectively. To begin, the nucleation rate is written in a general form

$$J = K \exp\left(-\frac{W^*}{kT}\right), \quad (2.96)$$

which follows from Eq. 2.72, with W^* the work of formation of a critical cluster. Using the chain rule, the derivative of J with respect to S can be written as

$$\begin{aligned} \left(\frac{\partial \ln J}{\partial \ln S}\right)_{p,T} &= -\frac{1}{kT} \left(\frac{\partial W^*}{\partial \mu_v}\right)_{\mu_g, T} \left(\frac{\partial \mu_v}{\partial \ln S}\right)_{p,T} - \frac{1}{kT} \left(\frac{\partial W^*}{\partial \mu_g}\right)_{\mu_v, T} \left(\frac{\partial \mu_g}{\partial \ln S}\right)_{p,T} \\ &\quad + \left(\frac{\partial \ln K}{\partial \ln S}\right)_{p,T}. \end{aligned} \quad (2.97)$$

The derivatives involving W^* can immediately be related to the excess numbers of molecules using Eq. 2.94. Furthermore, from the definition of the supersaturation (Eq. 1.27) it follows that

$$\left(\frac{\partial \mu_v}{\partial \ln S}\right)_{p,T} = kT. \quad (2.98)$$

For a dilute vapour, the chemical potential of the carrier gas μ_g depends only weakly on the concentration of the vapour, so

$$\left(\frac{\partial \mu_g}{\partial \ln S}\right)_{p,T} \approx 0. \quad (2.99)$$

The prefactor K of the nucleation rate depends on the kinetic model. Considering only distributions that obey the law of mass action, and neglecting the pressure dependence of the surface tension and compressibility factor, we can write that $K \propto f_c^2 S$. Therefore

$$\left(\frac{\partial \ln K}{\partial \ln S}\right)_{p,T} = 1. \quad (2.100)$$

Substituting the derivatives into Eq. 2.97, we obtain

$$\left(\frac{\partial \ln J}{\partial \ln S}\right)_{p,T} = \Delta n_v^* + 1. \quad (2.101)$$

In this form, the nucleation theorem can be used to obtain the number of vapour molecules from $J(S)$ measurements. It is equal to the nucleation theorem of a pure vapour.¹⁵² For usual conditions of vapour–liquid nucleation, the excess number of vapour molecules can be taken equal to the actual number of vapour molecules in the cluster. This approximation is justified because the density of the gas phase is much smaller than the liquid density, and the fraction of vapour in the gas phase is also very small.

Pressure nucleation theorem

The pressure nucleation theorem is obtained by taking the derivative of J with respect to p , instead of S . This derivative can be taken either at constant S and T or at constant vapour fraction y and T ; each approach leads to a different result.

We start with the derivation at constant supersaturation, which was pioneered by Oxtoby and Laaksonen¹⁵⁴ and modified by Luijten et al.⁶ The derivation shown here follows Luijten et al. Analogously to Eq. 2.97 we obtain

$$\left(\frac{\partial \ln J}{\partial \ln p}\right)_{S,T} = \frac{\Delta n_v^*}{kT} \left(\frac{\partial \mu_v}{\partial \ln p}\right)_{S,T} + \frac{\Delta n_g^*}{kT} \left(\frac{\partial \mu_g}{\partial \ln p}\right)_{S,T} + \left(\frac{\partial \ln K}{\partial \ln p}\right)_{S,T}, \quad (2.102)$$

where the general nucleation theorem (Eq. 2.94) was used. From the definition of the supersaturation (Eq. 1.27) and the binary two-phase equilibrium (Eq. 1.23) it follows that

$$\left(\frac{\partial\mu_v}{\partial p}\right)_{S,T} = \left(\frac{\partial\mu_v^{\text{eq}}}{\partial p}\right)_T = \left(\frac{\partial\mu_v^{\text{l,eq}}}{\partial p}\right)_T, \quad (2.103)$$

where $\mu_v^{\text{l,eq}}$ denotes the chemical potential of vapour molecules in the liquid phase, in equilibrium. Its pressure dependence can be evaluated with Eq. 1.21, yielding

$$\left(\frac{\partial\mu_v^{\text{l,eq}}}{\partial p}\right)_T = v_v^{\text{l}} + \frac{kT}{\gamma_v^{\text{eq}}x_v^{\text{eq}}} \left(\frac{\partial\gamma_v^{\text{eq}}x_v^{\text{eq}}}{\partial p}\right)_T, \quad (2.104)$$

where v_v^{l} is the molecular volume of pure liquid of the condensing component and x_v^{eq} is the equilibrium molar fraction of the condensing component in the liquid. We assume that the liquid is an ideal solution (see Eq. 1.14), for which the activity coefficient of the vapour component in the liquid phase γ_v^{eq} is unity. For small fractions of dissolved gas, the gas fraction in the liquid $x_g^{\text{eq}} = 1 - x_v^{\text{eq}}$ is proportional to pressure, so that

$$\left(\frac{\partial x_v^{\text{eq}}}{\partial p}\right)_T = -\left(\frac{\partial x_g^{\text{eq}}}{\partial p}\right)_T = -\frac{x_g^{\text{eq}}}{p}. \quad (2.105)$$

With this result, the value of the derivative $(\partial\mu_v/\partial p)_{S,T}$ from Eq. 2.103 is known.

We now continue with the pressure derivative of μ_g , the chemical potential of the carrier gas. It is assumed that μ_g is not significantly influenced by the small amount of vapour. The pressure dependence can then be taken equal to that of a pure component, given by the Gibbs–Duhem equation (Eq. 1.9)

$$\left(\frac{\partial\mu_g}{\partial p}\right)_{S,T} = v_g, \quad (2.106)$$

where v_g is the molecular volume of the gas.

The last derivative which has to be evaluated is the pressure derivative of K . Taking $K \propto f_e^2 S$ and adopting Luitjen's correlation⁶ $f_e \approx \exp[b(T)p]$, we obtain

$$\left(\frac{\partial \ln K}{\partial \ln p}\right)_{S,T} = 2 \left(\frac{\partial \ln f_e}{\partial \ln p}\right)_T \approx 2 \ln f_e. \quad (2.107)$$

With these derivatives, Eq. 2.102 yields the Luijten or S form of the pressure nucleation theorem,

$$\left(\frac{\partial \ln J}{\partial \ln p}\right)_{S,T} = \left(\frac{pv_v^l}{kT} - x_g^{\text{eq}}\right) \Delta n_v^* + Z_g \Delta n_g^* + 2 \ln f_e, \quad (2.108)$$

where the compressibility factor of the gas $Z_g = pv_g/(kT)$ was used to simplify the equation.

Pressure nucleation theorem at constant fraction

An alternative form of the pressure nucleation theorem was derived by Labetski¹⁰ and Kalikmanov and Labetski.¹¹ In their approach, the derivative of J is taken at constant vapour fraction y :

$$\left(\frac{\partial \ln J}{\partial \ln p}\right)_{y,T} = \frac{\Delta n_v^*}{kT} \left(\frac{\partial \mu_v}{\partial \ln p}\right)_{y,T} + \frac{\Delta n_g^*}{kT} \left(\frac{\partial \mu_g}{\partial \ln p}\right)_{y,T} + \left(\frac{\partial \ln K}{\partial \ln p}\right)_{y,T}. \quad (2.109)$$

In this case, the derivatives of μ_v and μ_g can be simplified with the Maxwell relation²⁶

$$\left(\frac{\partial \mu_i}{\partial p}\right)_{y,T} = \bar{v}_i, \quad (2.110)$$

where \bar{v}_i is the partial molecular volume of component i . To evaluate the rightmost derivative in Eq. 2.109, K must be rewritten as a function of y , that is, $K \propto S f_e^2 = y p f_e / p_s$, which results in

$$\left(\frac{\partial \ln K}{\partial \ln p}\right)_{y,T} = 1 + \left(\frac{\partial \ln f_e}{\partial \ln p}\right)_T \approx 1 + \ln f_e. \quad (2.111)$$

With these derivatives, Eq. 2.109 yields the y form of the pressure nucleation theorem,

$$\left(\frac{\partial \ln J}{\partial \ln p}\right)_{y,T} = \frac{p \bar{v}_v^{\text{gas}}}{kT} \Delta n_v^* + Z_g \Delta n_g^* + \ln f_e + 1, \quad (2.112)$$

where the partial molecular volume of the carrier gas in the gas phase was approximated by the molecular volume of the pure carrier gas, and the compressibility factor of the gas was substituted to simplify the result. Furthermore, \bar{v}_v^{gas} refers to the partial molecular volume of the vapour in the gas phase.

Equation 2.112 is the y form of the pressure nucleation theorem (compare the S form of Eq. 2.108), but is hard to use in practice because of the constant

y requirement. When p is changed in the experiment, y must be changed much to keep the nucleation rate J in the observable range. Therefore, at any value of y , only data at a single pressure is available, or even no data at all. As a result, it is not possible to determine the derivative $(\partial \ln J / \partial \ln p)_{y,T}$.

However, at constant temperature, J can be considered as a function of p and y , and Euler's chain relation gives

$$\left(\frac{\partial \ln J}{\partial \ln p}\right)_{y,T} = -\left(\frac{\partial \ln y}{\partial \ln p}\right)_{J,T} \left(\frac{\partial \ln J}{\partial \ln y}\right)_{p,T}. \quad (2.113)$$

Furthermore, at constant p and T , the supersaturation S is proportional to the vapour fraction y . Therefore, the derivative $(\partial \ln J / \partial \ln y)_{p,T}$ in Eq. 2.113 can be replaced by $(\partial \ln J / \partial \ln S)_{p,T}$, which is equal to $\Delta n_v^* + 1$ according to the nucleation theorem (Eq. 2.101). Finally, the pressure nucleation theorem takes the form

$$\left(\frac{\partial \ln y}{\partial \ln p}\right)_{J,T} = -\frac{1}{\Delta n_v^* + 1} \left(\frac{p \bar{v}_v^{\text{gas}}}{kT} \Delta n_v^* + Z_g \Delta n_g^* + \ln f_e + 1\right). \quad (2.114)$$

This expression differs from the result in Labetski's thesis,¹⁰ but agrees with Kalikmanov and Labetski.¹¹

2.10 Other nucleation theories

Since the development of classical nucleation theory, there have been continuous efforts to improve the theory. Remarkably, no alternative theory has become universally accepted. Even a simple change like the $1/S$ correction remains controversial.¹⁵⁵ In this section, several recent developments will be highlighted.

In 2003, Kashchiev¹⁵⁶ proposed an expression for the work of formation of a critical cluster that solves two problems of the classical approach. The first problem is that the capillarity approximation uses the equilibrium surface tension, even for very small clusters. The new theory is constructed in such a way that for all cluster sizes, the surface energy is equal to its equilibrium value by definition. A second problem that is solved is that the classical theory does not take into account the influence of the spinodal, the stability limit of a phase. Kashchiev's expression is defined such that the work of formation vanished at the spinodal. Shortly after its publication, Kashchiev's theory was heavily criticized by Schmelzer and Baidakov,¹⁵⁷ who argued that the theory is not generally applicable, as Kashchiev claims.

Another theory that takes the spinodal into account was developed by Kalikmanov.¹⁵⁸ He proposed the existence of a 'kinetic spinodal', which marks

the transition between metastable and unstable states. At this spinodal, the critical cluster size is minimal; with increasing supersaturation, it would increase, contrary to the classical behaviour. As indicated by Kalikmanov, the theory is only applicable to systems with sufficiently long interparticle interactions, for which a spinodal can be defined. According to Wilemski and Li,¹⁵⁹ 'real gas-liquid systems are characterized by short-range interactions'. They conclude that for vapour-liquid nucleation, an increase of the critical size near the spinodal is theoretically unlikely and has not been found experimentally.

In 2006, Kalikmanov¹⁶⁰ proposed the mean-field kinetic nucleation theory (MKNT), which is valid for clusters of any size. The theory interpolates between very small and very large clusters, and is exact in these limiting cases. Clusters are divided into core molecules and surface molecules; for small clusters, all molecules are surface molecules. For a cluster with a certain number of molecules, the number of core and surface molecules fluctuate; in MKNT, a mean-field approximation is applied by considering only the most probable number of surface molecules for a cluster of given size. The density profile of a cluster is then constructed by assigning the bulk density to the core and a lower but constant density to the surface layer. The resulting density profile is a two-step function of the radial coordinate. The MKNT nucleation rate expression agrees with classical theory for large clusters, but otherwise the difference is several orders of magnitude. It was recently shown¹⁶¹ that the MKNT provides significantly better predictions for argon nucleation rates than classical theory.

The theory of Reguera and Reiss,¹⁶²⁻¹⁶⁴ called 'extended modified liquid drop-dynamical nucleation theory' (EMLD-DNT), is a combination of two theories. The EMLD model accounts for translation and fluctuations of the cluster. It models the cluster as a system of molecules confined to a spherical container. For certain volumes of this container, a liquid droplet can be formed inside; this droplet is modelled by the capillarity approximation. The droplet does not fill the entire container; the remaining volume is filled by gas. In this theory, the spherical system as a whole is considered as the cluster for nucleation. Then, DNT is used to define the volume of the cluster/container as the volume which minimizes the pressure inside the container. The EMLD-DNT theory predicts the existence of a spinodal, where the energy of formation of a critical cluster vanishes.

The so-called gradient theory¹⁶⁵ adopts a more realistic cluster model than the capillarity approximation. In this theory, the density of the cluster varies smoothly from the centre of the cluster to the surrounding vapour phase. Besides the diffuse interface, another difference with the capillarity approximation is the possibility that the liquid density in the centre of the

cluster may not be equal to the bulk liquid density. Gradient theory predicts a surface tension that depends on the cluster size, which results in a work of formation that differs from the classical value. Recently, Hrubý et al.¹⁶⁶ applied gradient theory to clusters of nonane, and computed the work of formation and nucleation rate.

There are also nucleation theories that take the effect of the carrier gas into account in different way than presented in this chapter. Quasi-unary theory¹⁰ treats nucleation of a vapour in a carrier gas as binary nucleation, where clusters with any composition of vapour and carrier gas molecules can be formed. The cluster distribution is then defined in two-dimensional size space. Because there are much more carrier gas molecules than vapour molecules, it can be assumed that detailed balance holds in the gas molecules direction of size space, for each number of vapour molecules in the cluster. This allows expressing the nucleation rate in the form of unary theory, with effective unary condensation coefficients and cluster distributions. In the expression for the work of formation, mixing entropy terms are added to account for the composition of the cluster. To evaluate the quasi-unary theory, the equilibrium liquid fraction of the carrier gas in the condensed vapour should be known.

Previously, the effect of the carrier gas was explained by its influence on the vapour–liquid equilibrium, which leads to vapour fraction enhancement and surface tension reduction. Furthermore, the carrier gas may enter the cluster or be adsorbed on its surface, leading to a change of the surface tension. In addition to these effects, the carrier gas absorbs the latent heat that is released by the growing clusters. Wedekind et al.¹²⁹ tried to account for the thermalization of the cluster by the carrier gas molecules.

2.11 Droplet growth

The mechanism of droplet growth depends on the Knudsen number Kn , defined as

$$Kn \equiv \frac{\lambda}{2r}, \quad (2.115)$$

where r is the droplet radius and λ is the mean free path of vapour molecules. Here, the mean free path is defined as the average distance a vapour molecule travels before its direction becomes randomized by collisions with carrier gas molecules. Peeters et al.¹⁶⁷ showed that this length can be approximated by the mean free path of carrier gas molecules, if the masses of vapour and gas molecules are similar.

Initially, the droplet is small and the Knudsen number is high; for these conditions, the growth can be described by the kinetic processes of conden-

sation and evaporation of vapour molecules. Because of the smallness of the droplet, it can be assumed that the composition of the gas phase in the vicinity of the droplet is the same as the composition far from it. Furthermore, the droplet growth is independent of the carrier gas pressure.

For large droplets and small Knudsen numbers, the continuum formulation of fluid dynamics is applicable. The concentration of vapour molecules near the droplet is decreased because of condensation, and the growth is limited by the diffusion of vapour towards the droplet. The diffusion is strongly influenced by the pressure and type of carrier gas; the higher the carrier gas pressure, the slower the diffusion and droplet growth.

For our nucleation experiments in methane at 10 bar, the molecular mean free path is about 5 nm, according to gas kinetic theory.²⁷ In our setup, droplets can be observed when their diameter becomes larger than about 320 nm. Therefore, all observable growth takes place at $Kn \ll 1$, where the growth is diffusion-controlled. The transition between the two growth mechanisms takes place when the droplet radius becomes about 5 nm; a droplet of that size contains approximately 2000 water molecules.

Free molecular regime

In the regime of large Knudsen numbers, the free molecular regime, the net growth rate of a droplet is given by the difference of the condensation and evaporation coefficients. Using the approximate E_n from Eq. 3.8, the growth rate is

$$\begin{aligned} \frac{dn}{dt} &= C_n - E_n \approx SC_n^{\text{sat}} - C_n^{\text{sat}} \exp\left(\frac{2}{3}\Theta n^{-1/3}\right) \\ &= C_n^{\text{sat}} \left[S - \exp\left(\frac{2}{3}\Theta n^{-1/3}\right) \right] \\ &= C_n^{\text{sat}} (S - e^{Ke}), \end{aligned} \quad (2.116)$$

where the Kelvin number is defined as

$$Ke(r) \equiv \frac{2}{3}\Theta n^{-1/3} = (n^*/n)^{1/3} \ln S. \quad (2.117)$$

The e^{Ke} term represents the Kelvin effect, which corrects for the droplet curvature. At the critical size $n^* = (2\Theta/3 \ln S)^3$, the Kelvin number is equal to $\ln S$ and Eq. 2.116 correctly gives a zero growth rate of a critical cluster.

To find the growth rate of the droplet radius, we convert the number of molecules to the radius with the help of $r = r_1 n^{1/3}$, leading to

$$\frac{dr}{dt} = \frac{dr}{dn} \frac{dn}{dt} = \frac{1}{3} r_1 n^{-2/3} \times (S - e^{Ke}) C_1^{\text{sat}} n^{2/3} = \frac{1}{3} r_1 (S - e^{Ke}) C_1^{\text{sat}}. \quad (2.118)$$

For large droplets, $Ke \rightarrow 0$ and the growth rate dr/dt becomes radius independent.

The result that was just obtained can also be derived with the assumptions of Hertz¹⁶⁸ and Knudsen.¹⁶⁹ They reasoned that the evaporation rate is equal to the impingement rate in the saturated state. With the collision frequency from Eq. 2.34, the molar flow \dot{M}_e that condenses on the droplet is

$$\dot{M}_c = 4\pi r^2 \rho \left(\frac{RT}{2\pi M} \right)^{1/2}, \quad (2.119)$$

where ρ is the molar vapour density, T is the temperature of the vapour, and M is its molar mass. The flow that evaporates from the droplet is

$$\dot{M}_e = 4\pi r^2 \rho^{\text{sat}}(T_d) \left(\frac{RT_d}{2\pi M} \right)^{1/2}, \quad (2.120)$$

where T_d is the droplet temperature and ρ^{sat} is the vapour density at saturation. Condensation causes the molar mass of the droplet to increase at the rate of

$$\dot{M}_d = 4\pi r^2 \rho^l \frac{dr}{dt}, \quad (2.121)$$

where a constant and uniform molar liquid density ρ^l is assumed. From the equality $\dot{M}_d = \dot{M}_c - \dot{M}_e$ it follows that

$$\frac{dr}{dt} = \frac{1}{\rho^l} \left(\frac{R}{2\pi M} \right)^{1/2} \left[\rho T^{1/2} - \rho^{\text{sat}}(T_d) T_d^{1/2} \right]. \quad (2.122)$$

It can be shown that in the case of $T_d = T$, this result is equal to Eq. 2.118, except for the Kelvin effect. That effect can also be included in Eq. 2.122 by correcting ρ^{sat} for the droplet curvature; the result is an additional factor of e^{Ke} in front of ρ^{sat} .

Diffusion-controlled growth

For larger droplets, with small Knudsen numbers, the growth is limited by diffusion of the vapour in the carrier gas. There is a mass flow of vapour molecules towards the droplet; in addition, the release of latent heat results in a heat flow away from the droplet. The carrier gas accounts for most of the heat flow; indeed, it can be considered as an infinite heat bath. For steady-state growth, the difference between the droplet temperature T_d and the gas temperature T can be estimated by¹⁰

$$T_d - T \approx \frac{\rho^l L}{2k_g} \frac{dr^2}{dt}, \quad (2.123)$$

where ρ^l is the molar liquid density, L is the molar latent heat of condensation, k_g is the thermal conductivity of the carrier gas, and dr^2/dt is the growth rate of the squared droplet radius. For our experiments in methane at 235 K and 10 bar, the temperature difference is about 0.3 K and will be neglected. Models that take into account temperature differences have to include equations for the heat flow; such models have been presented by Peeters et al.¹⁷⁰ and Luo et al.¹⁷¹ In our case, it is possible to derive the expression for the growth rate solely from mass flows. The derivation that follows is based on Labetski's¹⁰ description.

The droplet with radius r is centred at the origin in a radially symmetric system; the distance from the origin is denoted by R . The mixture of vapour and carrier gases around the droplet moves with an average radial speed u , defined as

$$u \equiv \sum_i y_i w_i, \quad (2.124)$$

where y_i is the molar fraction of component i and w_i is its radial speed. The diffusive speed v_i of a component is defined as the speed deviation from the average speed, that is,

$$v_i \equiv w_i - u. \quad (2.125)$$

From the definitions of u and v_i it immediately follows that the average of the diffusive speeds $\sum_i y_i v_i$ is zero.

Because of condensation, the radius of the droplet grows at a rate of dr/dt . The molar amount that condenses on the surface per unit of time is

$$\Phi = 4\pi r^2 \rho_s^g \left(\frac{dr}{dt} - u_s \right), \quad (2.126)$$

where ρ^g is the total molar density of the gas phase, and subscript 's' denotes a condition at the droplet surface. For quasi-steady droplet growth, the molar flow in the gas phase is radius independent, so

$$r^2 \rho_s^g u_s = R^2 \rho^g u. \quad (2.127)$$

Condensation causes the molar mass of the droplet to increase at the rate of

$$\dot{M} = 4\pi r^2 \rho^l \frac{dr}{dt}, \quad (2.128)$$

where a constant and uniform molar liquid density ρ^l is assumed. From the equality $\Phi = \dot{M}$ and Eq. 2.127 it follows that

$$-R^2 \rho^g u = r^2 \frac{dr}{dt} (\rho^l - \rho_s^g) \equiv F, \quad (2.129)$$

where F is defined to equal both sides of the equality. The analysis carried out for the total molar flow can also be done for the vapour component only. In that case, similar equations are obtained; using subscript 'v' to denote the vapour component, we have

$$\Phi_v = 4\pi r^2 \rho_{v,s}^g \left(\frac{dr}{dt} - u_s - u_{v,s} \right), \quad (2.130)$$

and

$$\dot{M}_v = 4\pi r^2 \rho_v^l \frac{dr}{dt}. \quad (2.131)$$

The equality $\Phi_v = \dot{M}_v$ gives

$$-R^2 \rho_v^g (u + u_v) = r^2 \frac{dr}{dt} (\rho_v^l - \rho_{v,s}^g) \equiv F_v, \quad (2.132)$$

where F_v is defined analogously to F . Because the total density and the vapour density are related by the vapour fraction according to $\rho_v^g = y_v \rho^g$, the left-hand side of Eq. 2.132 can be written as

$$F_v = y_v F - R^2 \rho_v^g u_v, \quad (2.133)$$

where Eq. 2.129 was also used. The vapour fraction is very small, so Fick's law is used to find the diffusive flow of the vapour,

$$\rho_v^g u_v = -\rho^g D_v \frac{dy_v}{dR}. \quad (2.134)$$

Here D_v is the diffusion coefficient of the vapour component in the gas mixture. In the case of a single carrier gas, D_v is a binary diffusion coefficient; in the case of a mixture of several carrier gases, D_v can be taken as an effective binary diffusion coefficient (e.g., by using Blanc's law²⁵).

The diffusion coefficient is inversely proportional to the total molar density, so the product $\rho^g D_v$ is independent of R . After substitution of Eq. 2.134 into Eq. 2.133, the latter is integrated from r to infinity, with $y_v = y_{v,s}$ at $R = r$ and $y_v = y_{v,\infty}$ at $R \rightarrow \infty$. The result of the integration is

$$-\frac{1}{F} \ln \left(\frac{1 - y_{v,\infty} F / F_v}{1 - y_{v,s} F / F_v} \right) = \frac{1}{r \rho^g D_v}. \quad (2.135)$$

For small vapour fractions, the logarithm can be linearized, which leads to

$$y_{v,\infty} - y_{v,s} = \frac{F_v}{r \rho^g D_v}. \quad (2.136)$$

The definition of F_V (Eq. 2.132) is now inserted, resulting in the growth rate expression

$$\frac{dr}{dt} = \frac{\rho_v^g D_v}{(\rho_v^l - \rho_{v,s}^g) r} (y_{v,\infty} - y_{v,s}). \quad (2.137)$$

The density of the vapour component in the gas phase $\rho_{v,s}^g$ can be neglected because $\rho_{v,s}^g \ll \rho_v^l$. Furthermore, the liquid density of the vapour component is related to the total liquid density by $\rho_v^l = x_v \rho^l$, with x_v the molar fraction of the vapour component in the liquid. Finally, it is assumed that the vapour fraction near the droplet surface is equal to the equilibrium fraction y_v^{eq} . With these simplifications, we obtain

$$\frac{dr}{dt} = \frac{\rho_v^g D_v}{\rho^l x_v r} (y_{v,\infty} - y_v^{eq}), \quad (2.138)$$

which can be written as the growth rate of the squared radius,

$$\frac{dr^2}{dt} = 2 \frac{\rho_v^g D_v}{\rho^l x_v} (y_{v,\infty} - y_v^{eq}). \quad (2.139)$$

This final form is sometimes convenient because its right-hand side does not depend on r . The growth rate of the squared radius is therefore initially independent of time. As the droplet grows, the vapour may be depleted, which leads to a decreasing $y_{v,\infty}$ and growth rate. The coupling between growth and depletion will be discussed next.

Depletion

A simplified diffusion-controlled growth model was described by Muijtjens et al.¹⁷² It takes vapour depletion into account, but assumes constant temperature and pressure.

Consider a system that initially contains nuclei with a number density n , and the water vapour fraction is y_0 . The other subscripts on y will be omitted; here, y refers to the water vapour fraction far from the droplets. During the growth of the droplets, the water vapour fraction is given by

$$y = \frac{y_0 \rho_g - n v x \rho_l}{\rho_g - n v \rho_l}, \quad (2.140)$$

where ρ_g is the molar density of the gas phase, ρ_l is the molar density of the liquid, v is the volume of a droplet, and x is the molar fraction of water in the liquid. During the growth, ρ_g is assumed to remain constant. In Eq. 2.140, the numerator equals the amount of water that remains in the gas phase, and the denominator equals the total amount (water and other components) in

the gas phase. Writing $v = (4\pi/3)r^3$ with r the drop radius, and assuming x to be unity, we obtain

$$n\rho_l \frac{4\pi}{3} r^3 (1 - y) = \rho_g (y_0 - y). \quad (2.141)$$

The vapour fraction y is smaller than 4×10^{-4} in our experiments, so the factor $(1 - y)$ will be approximated as unity. If the Kelvin effect is neglected, the droplet growth stops when the vapour fraction becomes equal to its equilibrium value y_{eq} . It follows from Eq. 2.141 that the maximum droplet radius r_m is

$$r_m = \left[\frac{3}{4\pi} \frac{1}{n} \frac{\rho_g}{\rho_l} (y_0 - y_{\text{eq}}) \right]^{1/3}. \quad (2.142)$$

According to Eq. 2.138, the droplet growth rate is

$$\frac{dr}{dt} = \frac{D}{r} \frac{\rho_g}{\rho_l} (y - y_{\text{eq}}), \quad (2.143)$$

where D is the diffusion coefficient of water vapour in the gas phase. When the difference $(y - y_{\text{eq}})$ is expressed as $(y - y_0 + y_0 - y_{\text{eq}})$, Eqs. 2.141 and 2.142 can be substituted, leading to

$$\frac{dr}{dt} = \frac{4\pi}{3r} D n (r_m^3 - r^3). \quad (2.144)$$

The growth law, which gives the time t at which a droplet reaches a radius r , is now obtained by integration from time t_0 to t , resulting in

$$t - t_0 = \frac{3}{4\pi D n r_m} G\left(\frac{r}{r_m}\right), \quad (2.145)$$

where G is given by^{10,172}

$$\begin{aligned} G(x) &= \int_0^x \frac{x'}{1 - x'^3} dx' \\ &= \frac{1}{\sqrt{3}} \left[\frac{\pi}{6} - \arctan\left(\frac{1+2x}{\sqrt{3}}\right) \right] + \frac{1}{6} \ln \left[\frac{1+x+x^2}{(1-x)^2} \right]. \end{aligned} \quad (2.146)$$

For the experimental analysis of growth curves, it is convenient to express the growth law with the initial growth rate of the squared radius as an independent variable. This variable is called c and is given by

$$c \equiv \left. \frac{dr^2}{dt} \right|_{t=t_0} = \frac{8\pi}{3} D n r_m^3, \quad (2.147)$$

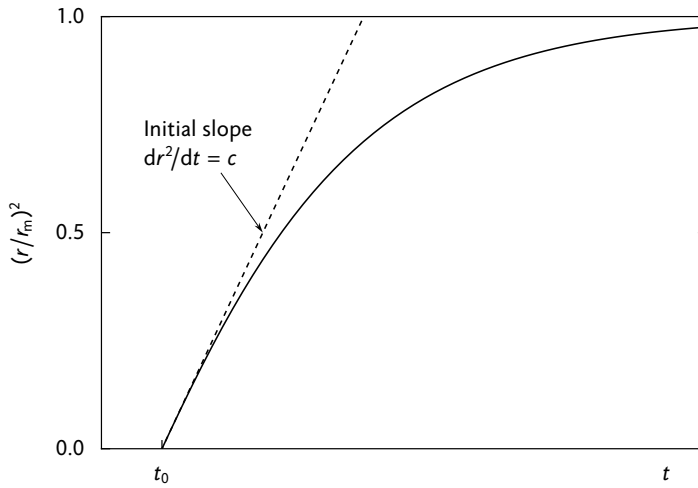


Figure 2.8: Growth curve described by the growth equations of Muijtens et al.,¹⁷² Eqs. 2.146 and 2.148.

which follows from Eq. 2.144. The growth law can then be written as

$$t - t_0 = \frac{2r_m^2}{c} G\left(\frac{r}{r_m}\right). \quad (2.148)$$

The shape of the growth curve is illustrated in Figure 2.8.

Comparison of the GDE and the kinetic equation

3

Abstract

A comparison is made between two models of homogeneous nucleation and droplet growth. The first is a kinetic model yielding the master equations for the concentrations of molecular clusters. Such a model does not make an explicit distinction between nucleation and droplet growth. The second model treats nucleation and growth separately, fully ignoring stochastic effects, and leads to the continuous general dynamic equation (GDE). Problems in applying the GDE model are discussed. A numerical solution of the kinetic equation is compared with an analytic solution of the GDE for two different cases: (1) the onset of nucleation and (2) the nucleation pulse. The kinetic model yields the thickness of the condensation front in size space as a function of supersaturation and dimensionless surface tension. If the GDE is applied properly, solutions of the GDE and the kinetic equation agree, with the exception of very small clusters, near-critical clusters, and the condensation front.

3.1 Introduction

Condensation models play an important role in the simulation of devices such as steam turbines, gas–vapour separators, and combustion engines. At the heart of a condensation model lies the general dynamic equation (GDE), which describes the evolution of the droplet size distribution.^{174–176}

Usually, the GDE consists of independent nucleation and growth terms (and possibly coagulation terms, which are not considered here). The nucleation term describes nucleation as the addition of new droplets to the system at the smallest size considered, generally the critical size. A separate droplet growth model describes the evolution of the droplet population.

However, in reality, a single process – the stochastic size change of mo-

This chapter contains the text of an article by V. Holten and M.E.H. van Dongen, published in the *Journal of Chemical Physics*.¹⁷³ The text has been slightly modified as a result of correspondence with V.A. Shneidman.

lecular clusters – is responsible for both formation and growth. The kinetic model, based on this notion, consists of the kinetic master equations, which describe the concentration of clusters with discrete sizes. This model can be regarded as the most rigorous representation of a system with nucleation, and has been in use^{145,177} since the ground-breaking work of Courtney¹³⁷ and Abraham.¹⁴⁹

The GDE differs from the kinetic equation in three ways. First, in the GDE new droplets are inserted into the system at the critical size. There is no information on concentrations of droplets smaller than the critical size. Second, growth in the GDE is fully deterministic; stochastic effects are ignored. Third, the size distribution in the GDE is continuous, whereas in the kinetic equation it is discrete.

At present, little is known about the effects of the GDE approximations on the predicted droplet distributions. Gelbard and Seinfeld¹⁷⁸ compared a discrete-continuous GDE with a fully continuous GDE and reported agreement. However, the boundary condition of the continuous GDE was chosen such that it matched the solution of the discrete-continuous GDE. Chesnokov and Krasnoperov¹⁴⁵ recently compared an extensive kinetic model with a more limited kinetic model, and did not make a comparison with a continuous GDE.

Hagmeijer et al.¹⁷⁹ applied the GDE to a condensing flow through a nozzle. In this study, the GDE was also used for droplets smaller than critical, while new droplets were still inserted at the critical size. It is unclear how accurate the GDE is below the critical size.

In this paper we compare the GDE and the kinetic equation, both theoretically and numerically. The kinetic model is summarized and its relationship with the Fokker–Planck equation is shown. From that equation, the GDE is derived and an analytical solution of the GDE is given in the case of constant temperature and supersaturation. We then numerically evaluate the kinetic equation and the GDE in two test cases, focusing on the differences at both small and large droplet sizes.

Analytical expressions for nucleation fluxes and size distributions during nucleation have been developed by Shneidman.^{150,180,181} Recently, he analysed the shape of distributions resulting from a nucleation pulse.¹⁸² We will compare our size distribution predicted by the kinetic equation with the result of one of Shneidman's expressions.

3.2 Theory

For the evaluation of the models, we consider a supersaturated vapour at temperature T with monomer number density ρ_1 . Both quantities are taken constant for simplicity. This approximation is reasonable when a dense carrier gas is present (for thermal equilibration) and the amount of molecules in droplets is much smaller than the amount of monomers.

The supersaturation S is defined as $S \equiv \rho_1/\rho_1^{\text{sat}}$, with ρ_1^{sat} the monomer density of a saturated vapour. The work of formation W_n of a cluster with n molecules is²¹

$$W_n/kT = -n \ln S + \Theta n^{2/3}, \quad (3.1)$$

with k Boltzmann's constant, and $\Theta \equiv (a_1\sigma)/(kT)$ with σ the surface tension, $a_1 = (36\pi)^{1/3}v_1^{2/3}$ the molecular surface area and v_1 the molecular volume. The work of formation reaches its maximum value at the critical size $n^* = [2\Theta/(3 \ln S)]^3$.

Kinetic model

The kinetic model used here is the Szilard model, on which the derivation of classical nucleation theory is based. In this model, clusters can gain or lose only single molecules, and cluster–cluster interactions are neglected. The rate of change of the n -cluster concentration is then^{21,22}

$$\frac{df_n}{dt} = C_{n-1}f_{n-1} - (C_n + E_n)f_n + E_{n+1}f_{n+1} = J_{n-1} - J_n, \quad (3.2)$$

where f_n is the number density of clusters with n molecules, C_n is the rate at which molecules condense on an n -cluster and E_n is the rate at which molecules evaporate from such a cluster. The current or flux J_n , the net number of clusters per unit time and volume which grow from size n to $n + 1$, is²¹

$$J_n \equiv C_n f_n - E_{n+1} f_{n+1}. \quad (3.3)$$

The condensation coefficient is the product of the sticking probability (assumed to be unity), the collision frequency per unit area and the cluster surface area,²¹

$$C_n = \rho_1 \left(\frac{kT}{2\pi m} \right)^{1/2} \times a_1 n^{2/3}, \quad (3.4)$$

where m is the mass of a molecule. The evaporation coefficient E_n is found by the detailed balance equation: at saturation ($S = 1$, denoted by superscript 'sat') all J_n equal zero, so Eq. 3.3 becomes

$$E_{n+1} = C_n^{\text{sat}} (\rho_n^{\text{sat}} / \rho_{n+1}^{\text{sat}}). \quad (3.5)$$

The evaporation coefficient is assumed to be supersaturation independent. For the size distribution at saturation ρ_n^{sat} we take the Courtney form,^{130,133}

$$\rho_n^{\text{sat}} = \rho_1^{\text{sat}} \exp(-\Theta n^{2/3}), \quad n \geq 2. \quad (3.6)$$

The combination of Eqs. 3.5 and 3.6 allows writing E_n as

$$E_n = C_{n-1}^{\text{sat}} \exp\{\Theta[n^{2/3} - (n-1)^{2/3}]\} \quad (3.7)$$

$$\approx C_{n-1}^{\text{sat}} \exp\left(\frac{2}{3}\Theta n^{-1/3}\right). \quad (3.8)$$

For constant temperature and supersaturation, all fluxes J_n eventually converge to the same steady-state value denoted by J , given by¹⁴²

$$J = \left(\sum_{n=1}^{\infty} \frac{1}{C_n S^n \rho_n^{\text{sat}}} \right)^{-1}. \quad (3.9)$$

Fokker–Planck equation

The set of equations of Eq. 3.2 can be transformed into a single equation in which n is a continuous variable. The quantities $f_n(t)$, C_n and E_n become the functions $f(n, t)$, $C(n)$ and $E(n)$; the arguments n and t will usually be omitted. Following Kashchiev,²² quantities evaluated at $n-1$ and $n+1$ are approximated by second-order expansions around n :

$$C_{n-1}f_{n-1} \approx Cf - \frac{\partial}{\partial n}(Cf) + \frac{1}{2} \frac{\partial^2}{\partial n^2}(Cf), \quad (3.10)$$

$$E_{n+1}f_{n+1} \approx Ef + \frac{\partial}{\partial n}(Ef) + \frac{1}{2} \frac{\partial^2}{\partial n^2}(Ef). \quad (3.11)$$

Equation 3.2 then becomes a Fokker–Planck equation,¹⁸³

$$\frac{\partial f}{\partial t} = \frac{1}{2} \frac{\partial^2}{\partial n^2} [(C+E)f] - \frac{\partial}{\partial n} [(C-E)f]. \quad (3.12)$$

The first term on the right-hand side of Eq. 3.12 corresponds to diffusion in n -space caused by stochastic fluctuations of the cluster size, with a diffusion coefficient of $\frac{1}{2}(C+E)$. The second term represents the deterministic cluster growth or shrinkage caused by the difference between condensation and evaporation, yielding a drift coefficient of $(C-E)$.

It is advantageous to replace the number of molecules n in the cluster by its radius $r = r_1 n^{1/3}$, where $r_1 = (3v_1/4\pi)^{1/3}$ is the molecular radius. The radius distribution function $F(r, t)$ replaces the earlier distribution $f(n, t)$, according to $f dn = F dr$. The Fokker–Planck equation in r space then becomes

$$\frac{\partial F}{\partial t} = \frac{\partial}{\partial r} \left(D \frac{\partial F}{\partial r} \right) - \frac{\partial(\dot{r}F)}{\partial r}, \quad (3.13)$$

with diffusion coefficient

$$D(r) = \frac{1}{2} \left(\frac{dr}{dn} \right)^2 (C + E) \approx \frac{r_1^4}{18r^2} C_1^{\text{sat}} [S + e^{Ke(r)}], \quad (3.14)$$

and growth rate

$$\dot{r}(r) = \frac{dr}{dn} (C - E) - \frac{1}{2} \frac{dr}{dn} \frac{\partial}{\partial r} \left[(C + E) \frac{dr}{dn} \right] \quad (3.15)$$

$$\approx \frac{1}{3} r_1 C_1^{\text{sat}} \left[S - \left(1 - \frac{\Theta}{9} \frac{r_1^4}{r^4} \right) e^{Ke(r)} \right], \quad (3.16)$$

where the Kelvin number is defined by

$$Ke(r) \equiv \frac{2}{3} \Theta (r_1/r) = (r^*/r) \ln S. \quad (3.17)$$

The approximate results of Eqs. 3.14 and 3.16 were obtained by using Eq. 3.8 and the approximation $C_{n-1}^{\text{sat}} \approx C_n^{\text{sat}}$. From here on, we also discard the term with $(r_1/r)^4$ in the expression for \dot{r} , leading to a simplified growth rate known as the Hertz–Knudsen growth law,

$$\dot{r}(r) = \frac{1}{3} r_1 C_1^{\text{sat}} [S - e^{Ke(r)}]. \quad (3.18)$$

For large droplets, $Ke \rightarrow 0$ and the growth rate \dot{r} becomes radius independent. The e^{Ke} term in Eq. 3.18 represents the Kelvin effect, which corrects for the droplet curvature. At the critical radius, $e^{Ke} = S$ and the growth rate is zero. An important consequence is that at the critical radius, the drift flux $\dot{r}F$ in Eq. 3.13 equals zero, so that the passage of the critical radius in size space is always dominated by diffusion.

General dynamic equation

The first step in deriving the GDE from the Fokker–Plank equation is neglecting the diffusion term. This is justified because the diffusion coefficient D of Eq. 3.14 rapidly approaches zero for clusters with radii $r \gg r_1$. We shall ignore here the dominance of the diffusion term near the critical radius. The GDE thus becomes^{22,175}

$$\frac{\partial F}{\partial t} = - \frac{\partial(\dot{r}F)}{\partial r}. \quad (3.19)$$

Equation 3.19 is sometimes called the ‘condensation equation’.¹⁷⁵ It can be solved by the method of characteristics, and for time-independent \dot{r} the solution is¹⁸⁴

$$F(r, t) = \frac{1}{\dot{r}(r)} g[\bar{t}(r) - t], \quad (3.20)$$

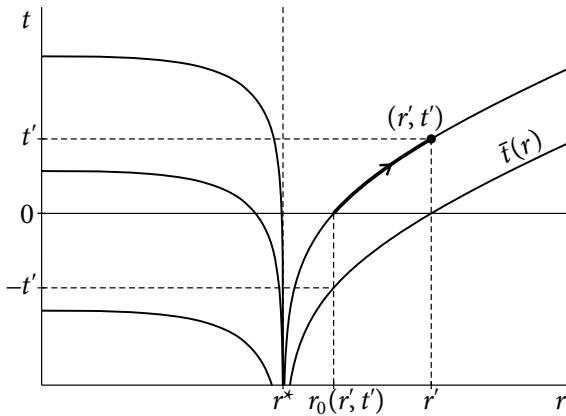


Figure 3.1: Schematic r - t diagram with several characteristics of the general dynamic equation, $\partial F/\partial t = -\partial(\dot{r}F)/\partial r$. At the critical radius r^* , which is taken time-independent, the growth rate is zero and the characteristics are asymptotically vertical. The dot is a droplet with radius r' at time t' , with initial radius $r_0(r', t')$ and radius history shown by a thick line.

with

$$\bar{t}(r) \equiv \int_{r_{\text{ref}}}^r \frac{1}{\dot{r}(r')} dr'. \quad (3.21)$$

Here the lower integration limit r_{ref} can be chosen arbitrarily, as long as r^* is not in the integration interval (the integrand is singular there). The function $g(t)$ is determined by the initial conditions and the choice of r_{ref} , so that the function $F(r, t)$ is independent of r_{ref} .

The function $\bar{t}(r)$ of Eq. 3.21 describes the characteristic curve in the r - t plane that crosses the t axis at $r = r_{\text{ref}}$. Other characteristics can easily be found by shifting the curve in the t direction, and Figure 3.1 shows several of these. Later, we will also require the inverse function of $\bar{t}(r)$, denoted by $\bar{r}(t)$. The $\bar{r}(t)$ function gives the radius of the droplet formed at $t = 0$ and $r = r_{\text{ref}}$ as a function of time.

The absence of the diffusion term means that the GDE of Eq. 3.19 cannot describe the nucleation process, the growth of clusters from monomers to the critical size. The growth rate \dot{r} is negative for clusters that are smaller than the critical size, so that supercritical droplets cannot appear. To include nucleation in the GDE, usually a source term is added to Eq. 3.19 in the form of a delta function,^{175,185} so that the GDE becomes

$$\frac{\partial F}{\partial t} = -\frac{\partial(\dot{r}F)}{\partial r} + \delta(r - r^*)J, \quad (3.22)$$

where J is the steady-state nucleation rate. The nucleated clusters are usually inserted at the critical size, because a cluster of size r^* is regarded as the

smallest stable cluster.¹⁷⁵ However, from a thermodynamical point of view, a critical cluster is in unstable equilibrium. Therefore, in most growth models, the growth rate of a critical cluster equals zero. The solution of Eq. 3.22 then becomes problematic, because the nucleation term can lead to an unlimited droplet concentration at r^* . Still, Eq. 3.22 is commonly used. In those cases the problem at r^* does not occur, due to a time-dependent critical radius,¹⁷⁹ for example.

If the critical radius is constant, the GDE therefore cannot be used with the above delta function. A straightforward way to avoid problems is to introduce nucleated droplets at a radius r_n that is slightly larger than r^* , thus forcing the growth rate of the droplets to be positive. Such a modification leads to a GDE in the form

$$\frac{\partial F}{\partial t} = -\frac{\partial(\dot{r}F)}{\partial r} + \delta(r - r_n)J, \quad r_n > r^*. \quad (3.23)$$

We will now solve this GDE with the initial condition

$$F(r, 0) = F_0(r). \quad (3.24)$$

Hagmeijer¹⁸⁵ has presented the general solution of such a GDE in which J , \dot{r} and r^* may be time-dependent. If these parameters are constant in time, as they are here, a solution can be obtained in a more straightforward way, as we will now show.

The general solution of the GDE is equal to the general solution of the homogeneous equation, Eq. 3.19, with condition (3.24), plus a particular solution of Eq. 3.23 with condition $F(r, 0) = 0$. We start with the homogeneous problem of Eq. 3.19, which represents the evolution of an existing distribution with negligible nucleation. The solution has already been given in a general form in Eq. 3.20. Evaluation at $t = 0$ and substitution of Eq. 3.24 results in an expression for the function g ,

$$g[\bar{t}(r)] = F_0(r) \dot{r}(r). \quad (3.25)$$

For times $t \geq 0$ we can write Eq. 3.20 as

$$F(r, t) = \frac{g[\bar{t}(r) - t]}{\dot{r}(r)} = \frac{g[\bar{t}(r_0)]}{\dot{r}(r)}, \quad (3.26)$$

with

$$r_0(r, t) \equiv \bar{r}[\bar{t}(r) - t]. \quad (3.27)$$

The function $r_0(r, t)$ gives the starting radius of a droplet; that is, the radius the droplet had at $t = 0$. Using the value of g from Eq. 3.25, the solution of the homogeneous problem becomes

$$F(r, t) = F_0[r_0(r, t)] \frac{\dot{r}[r_0(r, t)]}{\dot{r}(r)}, \quad (3.28)$$

which corresponds to the solutions obtained by Loyalka and Park¹⁸⁶ and Hagmeijer.¹⁸⁵ The expression for r_0 in Eq. 3.27 can be simplified by choosing $r_{\text{ref}} = r$, resulting in $r_0(r, t) = \bar{r}(-t)$. This relation is illustrated in Figure 3.1.

Next, we consider the particular solution of Eq. 3.23 with initial condition $F(r, 0) = 0$. This problem corresponds to nucleation at constant temperature and supersaturation, with no droplets present initially. In this case, nucleation can also be represented in the homogeneous equation (Eq. 3.19) by the condition of constant flux $F\dot{r}$ at the radius r_n ,²²

$$F(r_n, t) \dot{r}(r_n) = J, \quad t > 0. \quad (3.29)$$

This boundary condition replaces the delta function in Eq. 3.23. When substituted in Eq. 3.20, the initial and boundary conditions completely determine the function g ; it is a step function, whose value changes from J to 0 at an argument of $\bar{t}(r_n)$. When $r_{\text{ref}} = r_n$ is chosen for simplicity, the solution for the distribution becomes

$$F(r, t) = \begin{cases} J/\dot{r}(r), & r_n \leq r < \bar{r}(t), \\ 0, & \text{otherwise,} \end{cases} \quad (3.30)$$

which is a special case of the solution presented by Kashchiev.²² The function $\bar{r}(t)$ with $r_{\text{ref}} = r_n$ gives the radius history of the first droplet, the one formed at $r = r_n$ and $t = 0$. Since this droplet is the largest one at any moment in time, the function $\bar{r}(t)$ also represents the radius at the front of the distribution.

For our computations, we will not need the general solution of the inhomogeneous GDE of Eq. 3.23. It can, however, be easily obtained by adding the right-hand sides of Eqs. 3.28 and 3.30.

3.3 Numerical approach

Kinetic model

The system of differential equations in the kinetic model, Eq. 3.2, was reduced by the discrete section method,¹⁸⁷ where size space is divided into sections or bins. This method is most often used to solve large systems of kinetic differential equations, and is accurate if the number of bins is large enough.¹⁴⁵

When the division into bins is made, the average cluster concentration f in a bin depends only on the fluxes J_n at the bin edges. These fluxes are estimated using a linear interpolation of average f between two adjacent bins. After sectioning, a reduced system is obtained with one differential equation for each bin. The structure of the system is the same as Eq. 3.2, but with different coefficients in the place of C_n and E_n , and bin averages of f instead of pure f_n . If a bin has unit length, its differential equation reduces to the original equation from Eq. 3.2. For details about the sectioning method, see appendix C.

Usually, the length of a bin is taken proportional to n ,^{145,187,188} leading to a constant number of bins per order of magnitude of the cluster radius r . Instead, we chose the bin lengths such that the bin edges are equidistant in r space, and the bin length is then approximately proportional to $n^{2/3}$. Our choice is better suited to the problem we are solving, for two reasons. First, we convert the computed distribution to r space, and the density of data points along the r axis is then constant. Second, because the growth rate \dot{r} converges to a constant, the growth rate of the number of bins also becomes constant.

We used a bin length of $0.005 \eta_1$ in r space. In n space, the bin size is discrete and rounded to the nearest integer (or to 1 if it is less than 1). The first 1000 bins then have unit length. Comparisons were made with a bin length of $0.0011 \eta_1$ (for which the first 10000 bins have unit length) and no significant differences in the cluster size distribution were found.

The equations were made dimensionless by scaling the cluster concentrations with the monomer concentration ρ_1 , and by introducing a dimensionless time $\tau \equiv C_1 t$. The reduced system was solved by numerical integration using the Crank–Nicolson method¹⁸⁹ (described in appendix C) with dimensionless time steps in the range of 0.02 to 0.04. The lower limit of the solution was taken at $n = 2$ instead of $n = 1$, by keeping the concentration of dimers at the constant value $f_2 = \rho_1^{\text{sat}} \exp(-W_2/kT)$, consistent with the Courtney distribution.¹³³ This limit was chosen because starting at $n = 2$ allowed the use of larger time steps, while the solution is relatively insensitive to the lower limit. As a test, several solutions with lower limits at $n = 1$ and $n = 2$ were compared, and negligible difference was found.

General dynamic equation

The GDE was made dimensionless in the same way as the kinetic equations. In addition, the r coordinate was made dimensionless by scaling it with η_1 .

In the case of nucleation without an existing distribution, the solution was directly computed from Eq. 3.30. In the case of an existing distribution without nucleation, a different approach was taken. Before calculating the solution, the time-independent values of the $\bar{f}(r)$ function were computed in the

size range of interest, as follows. The r range was divided into the parts below and above r^* . Different fixed values of r_{ref} were taken for each part; namely, $r_{\text{ref}} = 0$ for $r < r^*$ and the arbitrary value of $r_{\text{ref}} = 1.001 r^*$ for $r > r^*$. To maintain accuracy in the range around r^* , where $\bar{t}(r)$ is very steep, a coordinate transformation was applied which made \bar{t} an approximately linear function of the transformed coordinate. Equation 3.21 was then used to compute and store a table of values of the \bar{t} function. Interpolation between table values yielded \bar{t} values with a relative accuracy better than 10^{-4} . The $\bar{r}(t)$ function was not precomputed, but implemented as the numerical solution of r in the equation $t = \bar{t}(r)$. Equations 3.27 and 3.28 were finally used to obtain the solution at several times, using the same precomputed $\bar{t}(r)$ for each time.

3.4 Numerical comparison of the models

Transient nucleation at constant temperature and supersaturation

Both the kinetic equation and the GDE were evaluated for conditions corresponding to water vapour at 228 K with a supersaturation of 20.6 (shown in Table 3.1, line A0), with no clusters present initially. The resulting distributions are compared on a logarithmic scale in Figure 3.2a and on a linear scale in Figure 3.2b. While the logarithmic plot shows the differences between the distributions well, a linear plot is necessary to assess the predicted total droplet concentrations (the area under the distribution).

A major difference is the absence of clusters below the critical size in the GDE result, in contrast to the high subcritical concentrations in the result from the kinetic model. This is, of course, caused by the introduction of new droplets at r_n in the GDE. On the other hand, the GDE overpredicts the concentration of clusters that are slightly larger than critical, because the growth rate is small there and the concentration is inversely proportional to it. The peak

Table 3.1: Conditions of the numerical simulations

| State | T (K) | p (Pa) | S | Θ | r^*/r_1 | ρ_1 (m^{-3}) | C_1 (μs^{-1}) | J ($\text{m}^{-3}\text{s}^{-1}$) |
|-------|---------|----------|-------|----------|-----------|------------------------------|------------------------------|--------------------------------------|
| A0 | 228.0 | 225.0 | 20.57 | 12.74 | 2.81 | 7.148×10^{22} | 4.406 | 2.849×10^{13} |
| A1 | 253.2 | 292.5 | 2.319 | 10.61 | 8.41 | 8.366×10^{22} | 5.342 | 2.642×10^{-80} |
| B0 | 217.8 | 116.2 | 34.2 | 13.7 | 2.59 | 3.863×10^{22} | 2.348 | 8.509×10^{13} |
| B1 | 226.7 | 128.4 | 13.5 | 12.9 | 3.29 | 4.102×10^{22} | 2.524 | 3.390×10^7 |
| C0 | 239.6 | 407.3 | 11.3 | 11.7 | 3.22 | 1.231×10^{23} | 7.711 | 1.507×10^{11} |
| C1 | 244.3 | 427.7 | 7.55 | 11.3 | 3.73 | 1.268×10^{23} | 7.992 | 1.491×10^6 |

All conditions represent water vapour. Liquid density and saturated vapour pressure were computed with correlations from Wölk and Strey,¹⁹ and the surface tension was taken from Holten et al.¹¹⁵ In the State column, numbers 0 and 1 denote conditions during and after the pulse, respectively, and B and C refer to the two cases in Figure 3.6.

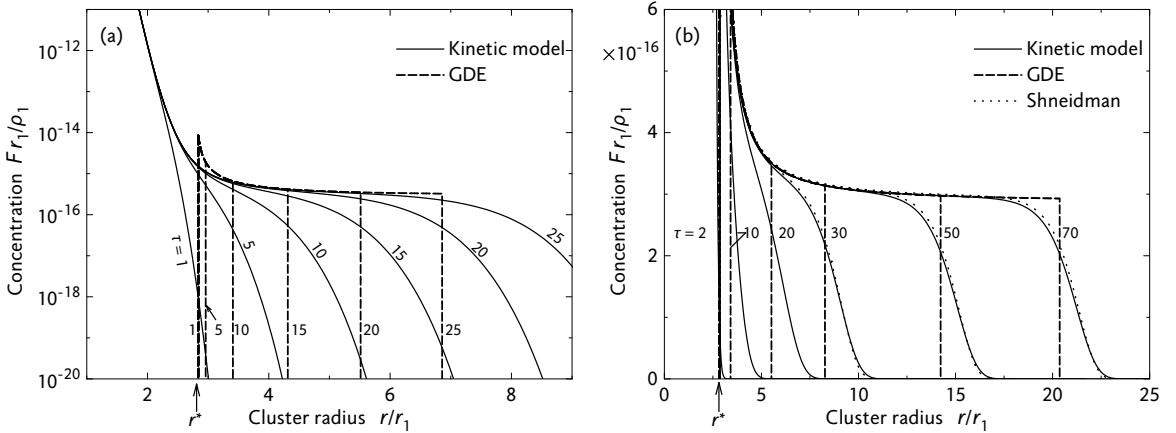


Figure 3.2: Radius distribution function during nucleation, according to the kinetic equation and the GDE, on a logarithmic scale (a) and a linear scale (b). Conditions are given in Table 3.1, line A0. Distributions are shown for several dimensionless times $\tau = tC_1$. The GDE distributions at $\tau = 1$ and $\tau = 2$ are so narrow that the beginning is indistinguishable from the end. The initial radius in the GDE was taken equal to $r_n = 1.01r^*$. In (b) the distribution obtained by Shneidman¹⁸¹ (Eq. 3.31) is also shown.

in the GDE result near r^* thus reflects the singular behaviour of the original GDE, Eq. 3.22, at the critical size. In the distribution from the kinetic equation, however, there is no singularity or discontinuity at the critical size. On the contrary, the concentration decreases smoothly with increasing radius.

In 1988, Shneidman¹⁸¹ derived analytical expressions for the size distribution during nucleation. For the current problem, the expression becomes¹⁹⁰

$$F(r, t) = J\tau_S \frac{\ln S \exp[-\exp(-x)]}{1 - \exp[\ln S(r^*/r - 1)]}, \quad x = \frac{t - t_i(r)}{\tau_S}. \quad (3.31)$$

Here τ_S is Shneidman's time unit and $t_i(r)$ is the 'incubation time'.¹⁸¹ Values for $t_i(r)$ for the current problem were provided by Shneidman;¹⁹⁰ the distribution resulting from Eq. 3.31 is plotted in Figure 3.2b. The analytical result agrees very well with the distribution from the kinetic equation.

In 1976, Ramabhadran et al.¹⁹¹ have derived a condition for which the diffusion term in the Fokker–Planck equation can be neglected with respect to the drift term. They stated that for most distributions, this condition is satisfied, and the simplification is justified. However, it is clear that for sizes near the critical size and in the front region, the diffusion term remains important.

It appears from Figure 3.2 that the distribution eventually becomes independent of r for large droplets. In fact, the steady-state distributions from both models are radius-independent for large radii, because the growth rate \dot{r} is also radius-independent there.

The front of the distribution is also a region with notable differences be-

tween the distributions. The front of the GDE distribution is always sharp, unlike the smooth front from the kinetic equation, because there is no diffusion in the GDE. However, diffusion is not the only cause of the flattening of the front in the kinetic model. For small radii, the growth rate is strongly size-dependent (large droplets grow faster than small ones) and this stretches the front over a larger radius region as it moves in radius space. Another reason for the smooth front is the initial time dependence of the nucleation rate in the kinetic model, whereas the nucleation rate in the GDE is taken constant in time. Including the time dependence of the nucleation rate in the GDE, like in Ref. 22, will probably improve the agreement with the kinetic equation in the front region.

The thickness of the front from the kinetic equation depends on the nucleation conditions. To quantify the dependence, we define the front thickness Δr as

$$\Delta r \equiv \frac{F^s(r_m)}{|\partial F/\partial r|_{\max}}, \quad (3.32)$$

where $|\partial F/\partial r|_{\max}$ is the maximum of the absolute value of $\partial F/\partial r$, and r_m is the radius at which the maximum occurs. Further, $F^s(r) = J/\dot{r}(r)$ is the steady-state radius distribution. (F^s is the steady-state value from the GDE, but for $r \gg r^*$ the kinetic model has the same steady-state value.) The thickness increases as the distribution grows to larger radii, but eventually becomes constant as the diffusion becomes negligible and the growth rate becomes constant. The asymptotic thickness, therefore, depends only on S and Θ .

The asymptotic thickness of the front was calculated for $S \geq 3$ and Θ between 5 and 25, while keeping the critical size n^* above 5 molecules, and the dimensionless nucleation rate $J/(C_1\rho_1)$ between 10^{-100} and 10^{-5} . Figure 3.3 demonstrates that the thickness is largest for low S values, and seems to converge to r_1 for large S . The value $(\Delta r/r_1) - 1$ is approximately proportional to Θ , as the lower part of Figure 3.3 shows.

The GDE front position is to some extent arbitrary, because it depends on r_n , which is a free parameter. We can therefore choose an r_n value such that the GDE matches the kinetic equation best. Specifically, r_n can be chosen such that the number density of clusters in the front region is equal for both models. This condition implies that the integral $\int F(r) dr$ over the front should be equal. We have computed the asymptotic value of r_n that satisfies this requirement, for the same S, Θ values as above. As Figure 3.4 displays, the r_n needs to be several percent higher than the critical size. A higher r_n is needed for higher S and lower Θ values.

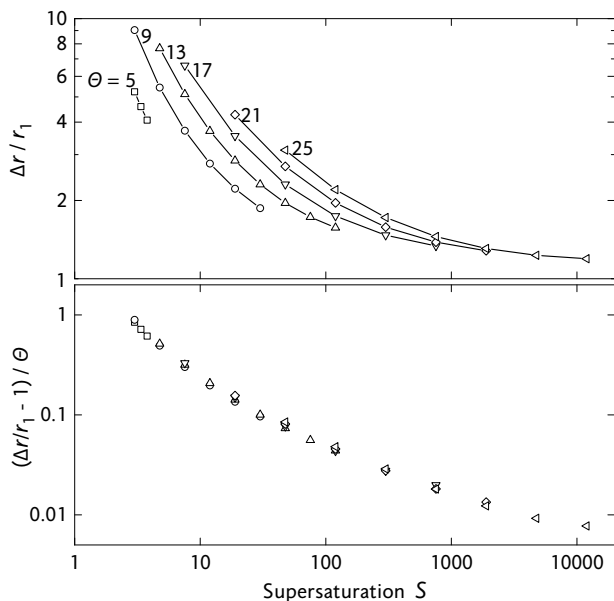


Figure 3.3: Top: Thickness Δr of the front from the kinetic equation, scaled with r_1 , as a function of the supersaturation. Bottom: Subtracting unity and dividing by the dimensionless surface tension Θ collapses all curves onto a single curve.

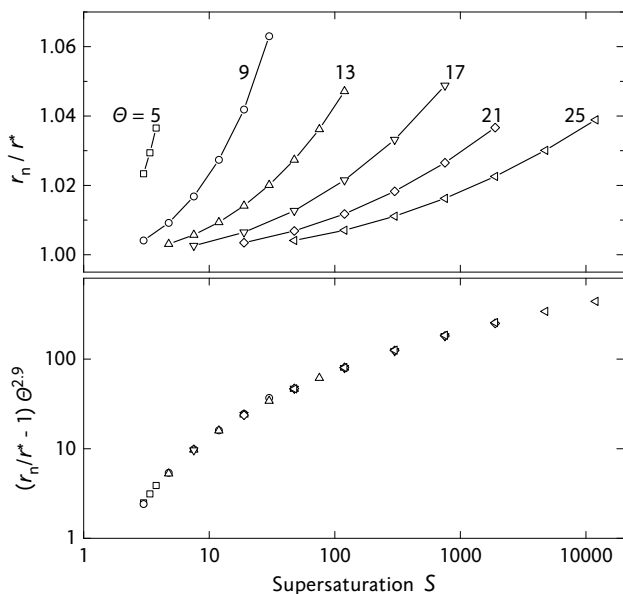


Figure 3.4: Top: Initial radius r_n in the GDE that is required to match the number of droplets predicted by the kinetic equation. Bottom: Subtracting unity and multiplying by $\Theta^{2.9}$ collapses all curves onto a single curve.

Nucleation pulse

An important experimental technique for determining nucleation rates is the nucleation pulse method.^{19,115,192} In this method, a gas–vapour mixture is first rapidly expanded and then recompressed. The expansion causes a temperature drop and a consequent supersaturation increase. Nucleation takes place during the pulse, a short (0.1 to 1 ms) period between the expansion and recompression, when the pressure, temperature and supersaturation are held constant. The recompression of the mixture reduces the supersaturation and stops nucleation. However, the supersaturation after the pulse remains larger than unity, so the droplets that were formed during the pulse grow until they can be detected.

We have evaluated both models in an idealized nucleation pulse. The expansion stage was neglected, and the computation was started at the pulse conditions. The pulse stage then corresponds to the case of constant temperature and supersaturation that has already been covered in the previous section. We also ignored the recompression time at the end of the pulse, and reduced the supersaturation instantaneously. Furthermore, in the GDE we neglected the small nucleation rate after the pulse, so that the homogeneous solution (Eq. 3.28) applies.

Figure 3.5 shows the evolution of the distribution after a pulse of dimensionless duration $C_1\Delta t = 220$. This corresponds to a duration of 0.05 ms, which is quite short and has a pronounced effect on the shape of the distribution function. The pulse conditions are taken the same as the conditions of Figure 3.2, and the conditions after the pulse represent water vapour at 253 K with a supersaturation of 2.3 (Table 3.1, line A1).

The increase of r^* causes a rapid collapse of the distribution function at small sizes. In the deterministic GDE, all droplets that become subcritical after the pulse (droplets sized between r_0^* and r_1^* in Figure 3.5) will eventually evaporate. The sharp lower boundary of the GDE distribution moves to smaller sizes (at $\tau = 0.45$ it can be seen as a vertical straight line) until it reaches $r = 0$ and the part of the GDE distribution below r_0^* becomes smooth. The kinetic distribution shows a similar collapse but does not decrease toward zero at small sizes. Instead, the distribution converges to the new steady-state distribution, which is lower than the old one, but still high at small sizes. Interestingly, the GDE prediction is accurate down to about $r = 2r_1$, which is an even smaller radius than the original minimum radius of the distribution near r_0^* .

As before, the two models also differ in the front region. In our example, the change in conditions at the end of the pulse does not have an effect on the thickness of the front, because the front is located at radii much larger than the critical size. Only the propagation speed of the front decreases.

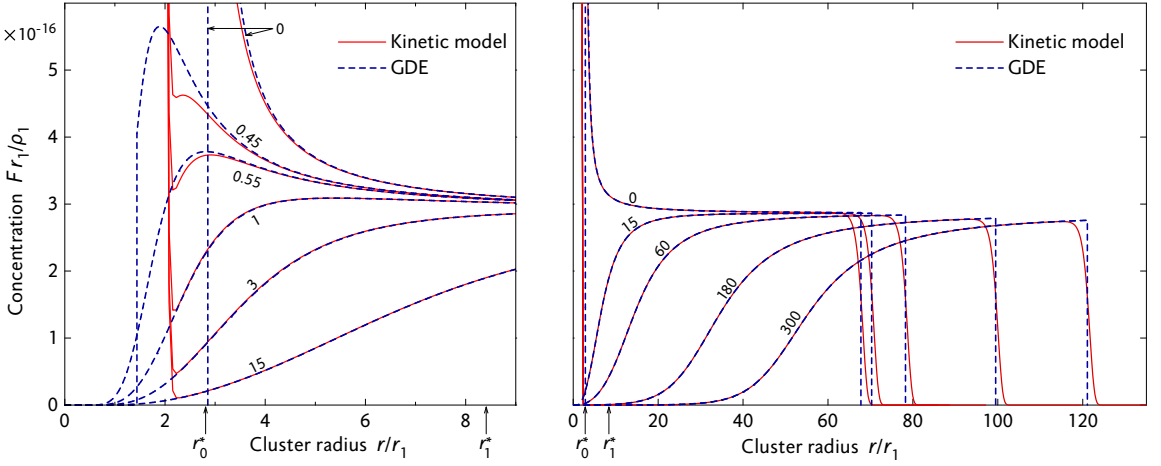


Figure 3.5: Radius distribution function at the end of and after the nucleation pulse, according to the kinetic equation and the GDE. The left part of the figure is a magnification of the distributions at small sizes. Numbers near the curves are the dimensionless times $\tau = tC_1$ since the end of the pulse. The value of the critical size during the pulse, r_0^* , and after the pulse, r_1^* , is indicated. Near r_0^* , the dashed vertical line is the minimum radius of the GDE distribution at the end of the pulse. The solid near-vertical curves near $r/r_1 = 2$ approximate the steady-state distribution for the conditions after the pulse.

At intermediate droplet sizes, the agreement between both models is excellent. Apparently, the changing shape of the collapsing distribution at those sizes is primarily caused by the size dependence of the growth rate, not by diffusion in size space. This is somewhat surprising for droplets near the critical radius r_1^* , where the drift flux $\dot{r}F$ in the Fokker–Planck equation (Eq. 3.13) is small and the diffusion flux is dominant. Let us analyse the behaviour at the critical size in detail, assuming that the Fokker–Planck equation is a good approximation of the kinetic equation. The drift flux is zero, but the GDE agrees with the kinetic equation, so the diffusion term must be negligible. From the Fokker–Planck equation, we find that the diffusion term is negligible compared to the drift term if

$$\left| \frac{\partial D}{\partial r} \frac{\partial F}{\partial r} + D \frac{\partial^2 F}{\partial r^2} \right| \ll \left| F \frac{\partial \dot{r}}{\partial r} \right|. \quad (3.33)$$

This condition is satisfied for relatively large values of F with small enough first and second derivatives. Therefore, although the drift flux $\dot{r}F$ is zero at the critical radius, the drift term $\partial(\dot{r}F)/\partial r$ can be dominant compared to the diffusion term.

In nucleation pulse experiments, the number of droplets that are larger than a certain radius is detected. This smallest detectable radius is usually much larger than the critical size. Therefore, the large difference between the

GDE and the kinetic equation at small sizes has no influence on the predicted number of detected droplets. The only remaining difference is that of the front of the distribution. As we have shown in the previous section, this difference can be minimized if a suitable initial radius is chosen in the GDE. The predicted number of detectable droplets is then the same in both models.

Let us consider how the nucleation pulse is used experimentally to determine nucleation rates. It is assumed that the nucleation rate is constant in time and all nuclei are eventually detected, and the experimental nucleation rate is computed from¹⁹²

$$J_{\text{exp}} = \frac{\rho_{\text{exp}}}{\Delta t}, \quad (3.34)$$

where ρ_{exp} is the number density of detected droplets and Δt is the pulse duration. The underlying assumption is that

$$\rho_{\text{exp}} \approx J\Delta t, \quad (3.35)$$

which is not exactly true because it takes a certain time to establish the steady-state J , and to stop the nucleation after the end of the pulse. Furthermore, at the end of the pulse r^* increases, so some droplets become subcritical, then evaporate, and are not detected. The kinetic model allows us to test the accuracy of approximation (3.35), by computing the ratio of detected droplets, defined here as

$$d \equiv \frac{\rho_{\text{kin}}}{J\Delta t}, \quad (3.36)$$

where ρ_{kin} is the number density of droplets that reach a detectable size in the kinetic model. As long as the detectable size is much larger than the critical size, d does not depend on the detectable size. The ratio d then depends on five parameters: the pulse conditions S_0 and Θ_0 , the conditions after the pulse S_1 and Θ_1 , and the dimensionless pulse duration $\Delta\tau$. The number of parameters is too large to compute the ratio d for all possible conditions. Therefore, we have evaluated it for two sets of S and Θ values, as a function of $\Delta\tau$, shown in Figure 3.6.

For short pulses the detected ratio is small, because most droplets become subcritical after the pulse and evaporate. For long pulses, the number of evaporating droplets and the transient behaviour of J become relatively unimportant. However, care must be taken that the pulse is not made too long, because depletion cannot be ignored for long pulses. The effects of depletion are not included in our current model, so Figure 3.6 does not show the errors made for long pulse durations. Conversely, depletion is negligible for short pulses, so Figure 3.6 can be used to obtain a lower limit for the pulse duration.

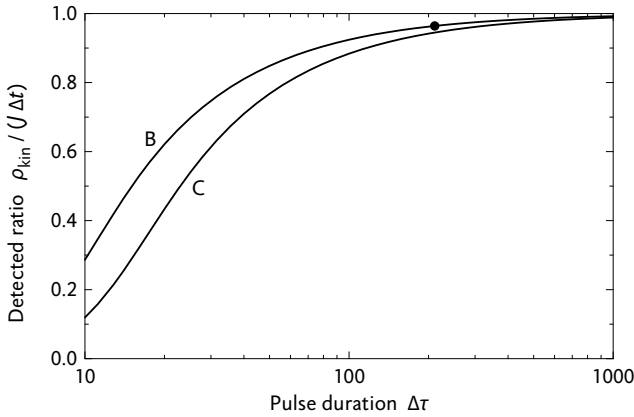


Figure 3.6: Ratio of the detected number density of droplets and the assumed number density in the nucleation pulse method $J\Delta t$, as a function of the dimensionless pulse duration. Line B corresponds to typical pulse conditions from experiments in our group.¹¹⁵ The dot represents the pulse duration $\Delta\tau = 211$ that was experimentally used for these conditions. Line C represents a typical pulse condition from the experiments of Wölk and Strey,¹⁹ with experimental pulse duration $\Delta\tau \approx 1.4 \times 10^4$. Conditions are listed in Table 3.1.

3.5 Conclusion

We have addressed the problem of the formation of droplets in a supersaturated vapour, both with a discrete kinetic equation and a continuous general dynamic equation. The relationship between the equations can be easily understood by writing the kinetic equation as a Fokker–Planck equation in continuous radius coordinates. Neglecting the diffusion term in this equation immediately leads to the GDE.

The advantage of the kinetic equation is that it correctly describes nucleation and growth simultaneously. This is not trivial for the GDE, since it shows a singular behaviour near the critical radius. It is therefore necessary to change the GDE such that new droplets are introduced at a radius that is slightly larger than the critical radius. By adjusting this initial radius, selected differences between the GDE and the kinetic equation can be minimized. As an example, we have shown the initial radius that is required for agreement of the total number density of large droplets.

We have compared the kinetic equation and the GDE for constant temperature and supersaturation, and in a nucleation pulse. Three radius ranges can be distinguished. First, the shape of the front is sharp in the GDE size distribution and smooth in the kinetic one, illustrating the absence in the GDE of diffusion in size space. Second, for droplet sizes between the critical region and the front region, the GDE agrees well with the kinetic equation. If nu-

cleation is unimportant compared to the existing droplet concentration, the GDE is also accurate in the critical region. Finally, at the lower end of the size range, between monomers and the critical size, large differences between the models are inevitable. The kinetic distribution is high in this size range, because of the high concentration of monomers, whereas the GDE distribution approaches zero for small radii.

The application of the kinetic model to a nucleation pulse enabled us to assess the accuracy of the nucleation pulse method as it is experimentally used. It was found that short pulses lead to an evaporation of a considerable part of the droplets that are formed, which decreases the accuracy of the determined nucleation rate.

A limitation of this study is that the models have not been evaluated for continuously changing conditions, such as the flow in a nozzle. In such a situation, the agreement between the models could be different.

Experimental methods

One of the most successful methods to measure nucleation rates is the nucleation pulse method, which separates the processes of nucleation and droplet growth. With this method, nucleation is confined to a short time period called the pulse, a state of high supersaturation that has a duration of the order of a millisecond. After the pulse, the supersaturation is reduced, so that the nucleation rate decreases significantly. The supersaturation remains higher than unity, to enable the droplets to grow to detectable sizes. It is assumed that all the droplets that are formed during the pulse are eventually detected, so that the nucleation rate J follows from

$$J = n_{\text{exp}}/\Delta t, \quad (4.1)$$

where n_{exp} is the observed droplet number density and Δt is the duration of the pulse.

A supersaturation pulse is most easily created with a pressure pulse, as illustrated in Figure 4.1. A fast adiabatic expansion causes pressure and temperature to decrease to the nucleation pulse level. As a result, the vapour be-

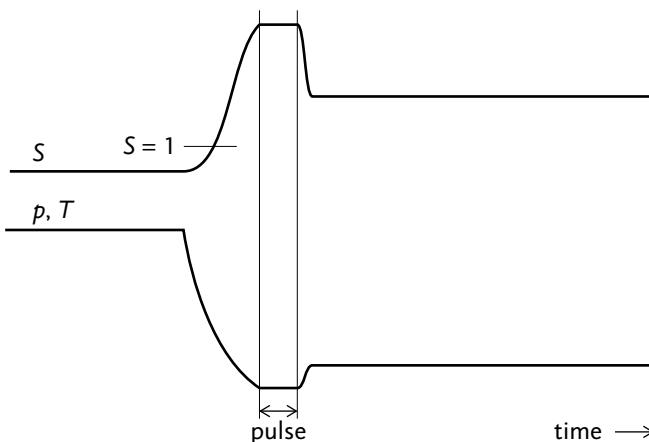


Figure 4.1: Schematic pressure, temperature and supersaturation history during a nucleation experiment.

comes supersaturated and nucleation starts. The pulse is ended by a small recompression, which reduces the supersaturation significantly. The reason that the supersaturation is so strongly affected by a relatively small change in temperature is that the equilibrium vapour pressure depends approximately exponentially on the temperature (for water, a temperature increase of 10 K roughly doubles the vapour pressure). After the recompression, the supersaturation remains higher than unity, which causes the droplets to grow further. The nucleation rate after the pulse is typically several orders of magnitude lower than during the pulse, so the amount of droplets that are formed after the pulse is negligible.

In 1965, Allard and Kassner¹⁹³ were the first to apply the nucleation pulse method for their measurements of the nucleation rate of water; their setup was later used by Miller et al.¹⁸ The setup is an expansion chamber with a single piston that creates the pressure profile. Because of the time it takes to reverse the piston motion, pulses could not be made shorter than 10 ms. In 1981, Wagner and Strey¹⁹⁴ developed a two-piston expansion chamber, where one piston was used for the expansion and the other for the recompression. This setup was able to generate shorter nucleation pulses than the single-piston chamber.

A disadvantage of the earlier expansion chambers was that the pulse supersaturation and temperature could not be varied independently. The reason was that the setup contained a saturated vapour at the beginning of an experiment. The only way to change the pulse supersaturation was to vary the expansion depth, but this also changed the pulse temperature. This limitation was overcome by the group of Strey,¹⁹² by premixing the gas–vapour mixture before transferring it to the expansion chamber. Additionally, the new setup contained valves instead of pistons, to generate smoother and better reproducible pressure pulses. The new chamber was used by Viisanen et al.¹⁹⁵ and Wölk and Strey¹⁹ for precise measurements of water nucleation rates.

An alternative way to realize the nucleation pulse method was presented by Peters¹⁹⁶ in 1983. He argued that the performance of the expansion chambers was inherently limited by their moving parts. Therefore, the pulse could be more accurately created in a device without moving parts: the shock tube. Such a tube consists of a high-pressure section (HPS) and a low-pressure section (LPS), initially separated by a diaphragm (or membrane). Rupture of the diaphragm causes an isentropic expansion of the test gas mixture in the HPS. The pressure pulse is created by a recompression wave that originates from a constriction in the LPS.

Taking Peters's ideas as a starting point, a modified expansion wave tube was built at the Eindhoven University of Technology, with a design that was described by Looijmans et al.¹⁹⁷ in 1993. The main difference with Peters's

setup is the use of a widening in the LPS instead of a constriction, which improves the pressure history after the pulse. The first experimental results were presented by Looijmans et al.¹⁹⁸ in 1995. Later, the tube was used to study the nucleation of water^{6,8} and nonane^{6,8,10} at high pressure (10–40 bar). This setup has also been used for the present work, and will be described in this chapter. Between the helium and methane experiments of this work, the setup was slightly changed. In this chapter, the most recent state of the setup is given, and all examples pertain to the methane experiments. Where relevant, differences with the helium experiments are indicated.

4.1 Expansion wave tube

The expansion wave tube is basically a shock tube. The test gas mixture, which consists of a vapour and one or more carrier gases, is placed in the HPS; the LPS contains carrier gas only. When the diaphragm is broken, an expansion wave (indicated by A in Figure 4.2) travels into the HPS and a compression wave or shock wave (B) travels into the LPS. Our shock tube has a locally widened LPS; the interaction of the shock wave with this geometry results in a weak expansion wave (C) and an equally weak compression wave (D) which are sent in the direction of the HPS. When the shock wave reaches the end of the LPS, it reflects back (not shown).

Near the end wall of the HPS, a pressure history shown in the centre of Figure 4.2 is realized. When the expansion wave arrives, the pressure decreases rapidly (a–b). A short time after the pressure drop ends, the weak expan-

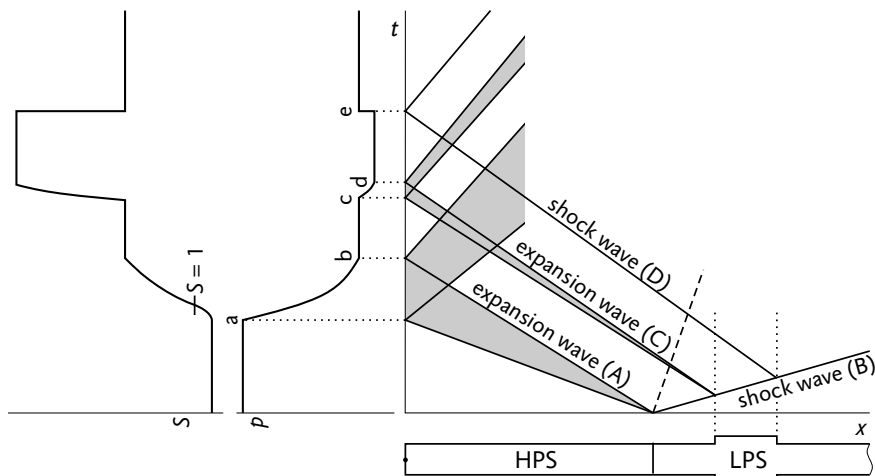


Figure 4.2: Right: schematic x - t plot of the waves in the expansion tube. Centre: pressure at the end wall of the HPS. Left: supersaturation at the end wall.

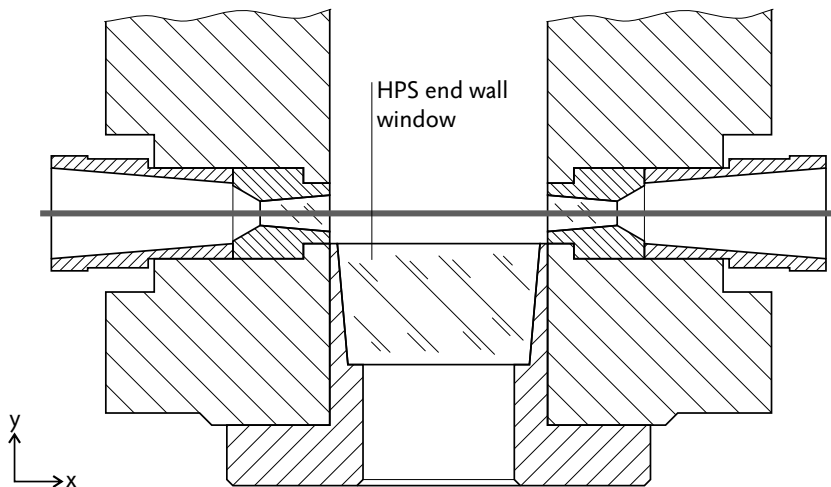
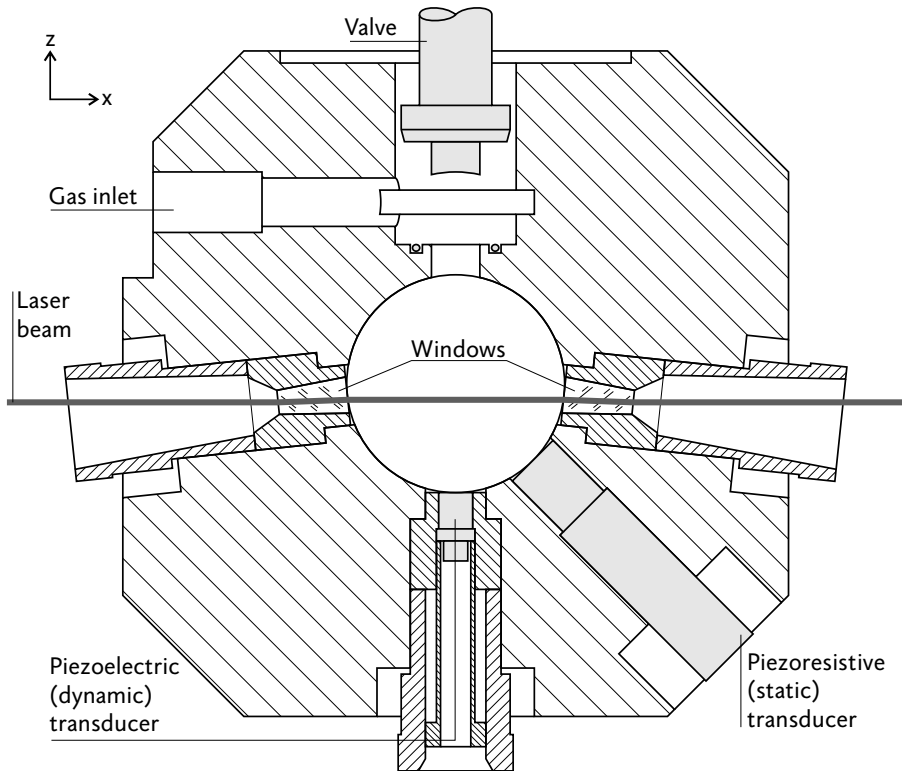
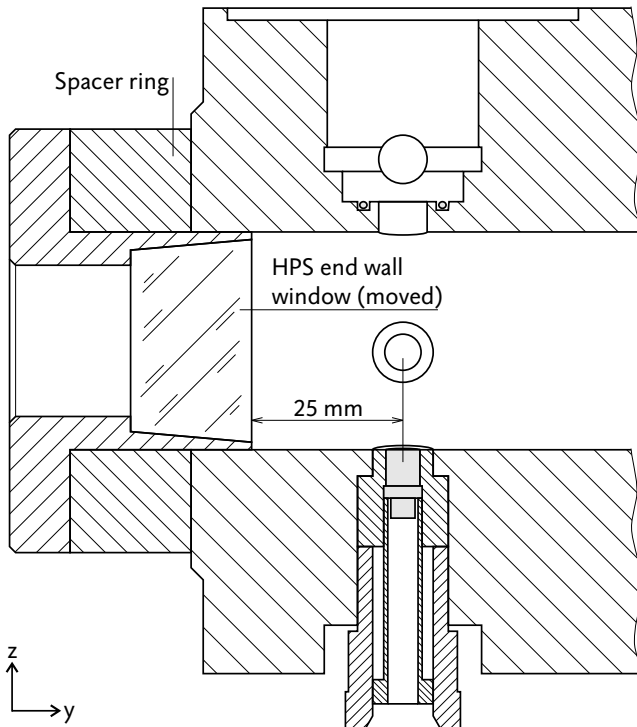
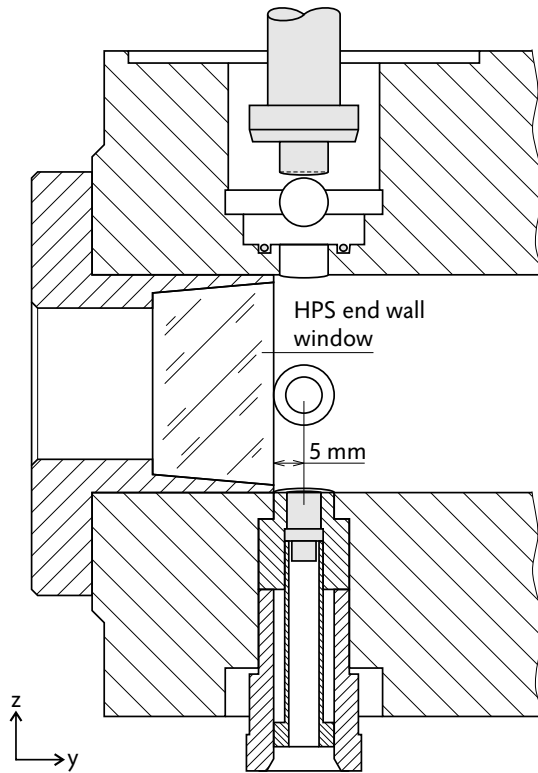


Figure 4.3: This page and next page: cross-sections of the measurement section in the HPS shown at 80% of the true size. The actual internal diameter of the measurement section is 36 mm. The HPS tube runs along the y direction, and z points upward in the laboratory frame. The end wall of the HPS can be moved further from the measurement plane by inserting an intermediate spacer ring.



sion and compression wave cause a small dip in the pressure (c–d–e); this is the pulse. After that, the pressure remains approximately constant, until the shock wave reflected from the LPS end wall arrives. This ends the measurement time, since the temperature increases and the droplets evaporate.

To ensure a long measurement time, the LPS should be as long as possible; in our setup, it is 9.23 m long. For the HPS, a short length is preferable; in that case, the cooling rate of the gas at the end wall is large, and the amount of test gas needed to fill the HPS is small. On the other hand, the HPS cannot be too short because the expansion time should be significantly longer than the time it takes to rupture the diaphragm. Looijmans⁹ estimated the minimum length of the HPS at 0.66 m. Currently, the HPS length is 1.25 m. The other dimensions of the tube are as follows: inner diameter 36 mm, inner diameter of widening 41 mm, length of widening 0.15 m, distance from diaphragm to widening 0.14 m.

The LPS and HPS are separated by a diaphragm, a 150 μm thick membrane made of polyester. The diaphragm is pressed against a ribbon that is heated to 600 °C by means of an electrical current at the start of an experiment. The subsequent rupture and opening of the diaphragm is estimated to occur in 0.15 ms.⁹ More details and a schematic are given by Looijmans and van Dongen.⁴

The measurement plane (i.e., the plane in which pressure measurements and optical detection are performed) is located at a distance of 5 mm from the HPS end wall (Figure 4.3). For high-pressure experiments, this is far enough from the wall to prevent the influence of boundary layers. For low-pressure experiments, the end wall can be moved so that the measuring plane is at 25 mm from the end wall.

Pressure measurement

The pressure changes at the end wall of the HPS are recorded by a piezoelectric pressure transducer (Kistler type 603B). Transducers of this type measure relative pressure changes, that is, the output voltage difference is proportional to the pressure difference. Their fast response is a prerequisite for our experiments, but they also have a number of disadvantages. The proportionality constant can only be determined by calibration to a known pressure change, and such a calibration must be done regularly. In addition, the head of the piezoelectric transducer is sensitive to thermal gradients and must be coated with silicone rubber; also, the tension which results from mounting influences the characteristics.

To increase the reliability of the pressure measurement, the setup was modified in 2004 to allow an *in situ* calibration of the piezoelectric transducer during the experiment. This was achieved by installing an additional

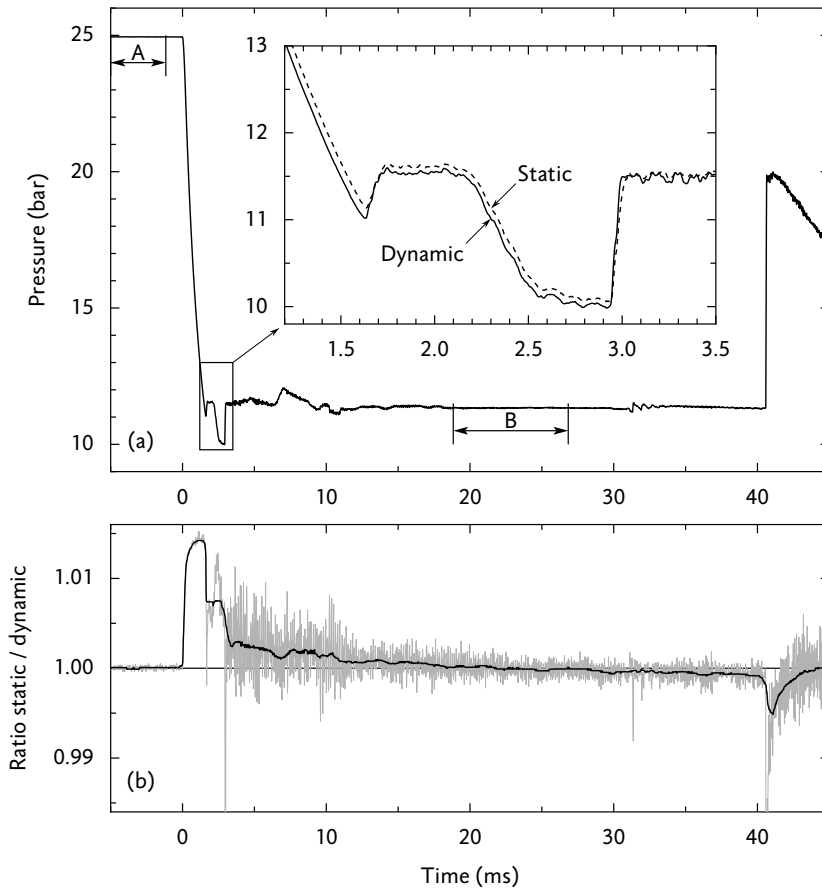


Figure 4.4: Pressure measured by the static and dynamic transducers at the end of the high-pressure section. (a): In the overview of the entire signal, the difference between the transducers is too small to be seen. The signal from the dynamic transducer is scaled such that it matches the static transducer in intervals A and B. Inset: difference between the transducers in the pulse region. (b): Ratio of the pressures measured by the static and dynamic transducers. Grey line: raw signals, black line: smoothed with a median filter, width 1 ms.

transducer at the end wall, capable of measuring absolute pressures. The new piezoresistive transducer (Kistler type 4073A50) can be calibrated statically (at constant pressure) and is less sensitive to thermal gradients and mounting tension. The piezoresistive transducer is not designed to accurately measure fast pressure changes, but it can be used to calibrate the piezoelectric one. In Figure 4.4a, the measured signals from the dynamic (piezoelectric) and the static (piezoresistive) transducer are shown together. The piezoelectric signal is scaled such that it agrees with the piezoresistive signal during a time interval A just before the expansion and during an interval B about 15 ms after the

pulse. It is assumed that at the beginning of interval B, the static transducer has had enough time to stabilize so that its value is reliable.

As noted by Labetski,¹⁰ after the scaling there is a difference between the pressures measured by the two transducers; specifically, the static transducer gives a higher pressure during the pulse than the dynamic transducer. To see the difference better, the ratio between the two pressure signals is plotted in Figure 4.4b. The deviation of the transducers increases rapidly at the beginning of the expansion and reaches a maximum value of 1.4% at the end of the expansion. During the pulse, the deviation is about 0.7%. After the pulse, the deviation slowly decreases; when the reflected shock wave arrives at 40.6 ms, it changes direction.

The variation of the deviation means that the position of interval B influences the calibration of the dynamic transducer. However, the difference is rather small. Specifically, moving the interval from the position in Figure 4.4 to the latest possible time (just before the reflected shock wave) would decrease the obtained pulse pressure by less than 0.01 bar, which is negligible compared to the pressure fluctuations that occur during the pulse.

4.2 Thermodynamic state

Temperature

The initial temperature of the gas mixture determines the temperature during the nucleation pulse, and must be accurately known. It is assumed that gas mixture has the same temperature as the HPS walls, which have laboratory temperature (about 295 K). The temperature is measured at several locations in the HPS walls with resistance thermometers (Tempcontrol PT-8316) connected to a digital indicator (Dostmann T955). The accuracy of each thermometer is ± 0.03 K, and the temperatures measured at two locations near the HPS end wall differed less than 0.04 K. The temperature of the tube wall was also measured at a distance of 0.15 m from the end wall; it differed at most 0.10 K from the end wall temperature. Because our nucleation observation position is close to the end wall, the value from the thermometer closest to the end wall was taken. The accuracy of that initial temperature measurement is believed to be ± 0.04 K.

During the expansion and the nucleation pulse, the temperature changes so rapidly that it cannot be measured. However, the time between the start of the expansion and the nucleation pulse is so small that the heat flow from the tube walls (which remain at laboratory temperature) to the colder gas mixture at the observation position can be neglected. In that case, all reversible state changes of the gas mixture are isentropic, and the temperature can be

computed from the pressure signal and the initial temperature. For the helium experiments, the ideal-gas relation¹³⁹

$$T = T_0(p/p_0)^{(\gamma-1)/\gamma}, \quad (4.2)$$

was used, where $\gamma = c_p/c_v$ is the ratio of the specific heats, and p_0 and T_0 are the initial pressure and temperature, respectively. The γ value was corrected for the presence of water vapour in the mixture according to^{195,199}

$$\gamma = 1 + \left(\frac{y}{\gamma_w - 1} + \frac{1 - y}{\gamma_h - 1} \right)^{-1}, \quad (4.3)$$

where γ_w and γ_h are the specific heat ratios of water vapour and helium, respectively, and y is the water vapour fraction. For helium, the ideal value $\gamma_h = 5/3$ was taken. The γ value of water depends on the temperature, and therefore changes during the expansion. However, the effect of the water vapour on the γ value of the mixture is quite small (in our experiment with the highest amount of water vapour, the γ changed only by 0.2%), so that an average value of $\gamma_w = 1.33$ could be used. The final temperature correction due to the γ correction of Eq. 4.3 was at most 0.15 K, compared to a temperature calculated with the pure-helium γ .

In the case of experiments in methane or methane with carbon dioxide, the non-ideality of the carrier gas prevents the use of Eq. 4.2. For these experiments, the temperature was computed using the GERG-2004 equation of state,⁶² again assuming isentropic behaviour. Because of the high carrier gas pressure and the corresponding low water vapour fraction, the presence of water in the mixture was not taken into account. In previous works of our group^{198,200} where methane was used as carrier gas, the equation of state by Sychev et al.²⁰¹ was employed. To test the accuracy of both EOS, the temperatures for our water–methane experiments were calculated both with the GERG-2004 and the Sychev et al. equations of state; they agreed within 0.01 K.

As an additional test, the GERG EOS was compared to the NIST SUPERTRAPP⁶⁰ program, for expansions of carbon dioxide–methane mixtures with carbon dioxide fractions from 0 to 1. The NIST program was found to give temperatures of about 1.5 K higher than the GERG model. Apart from this large systematic offset, both models agree on the trend of temperature with increasing carbon dioxide fraction. This trend is therefore plausible. Considering the offset, the NIST values also deviate by 1.5 K from the accurate pure-methane predictions by the Sychev and GERG equations of state; therefore, the NIST values are likely incorrect. In summary, the GERG-2004 EOS is the most reliable model to compute the temperatures, both for pure methane and for mixtures of methane and carbon dioxide.

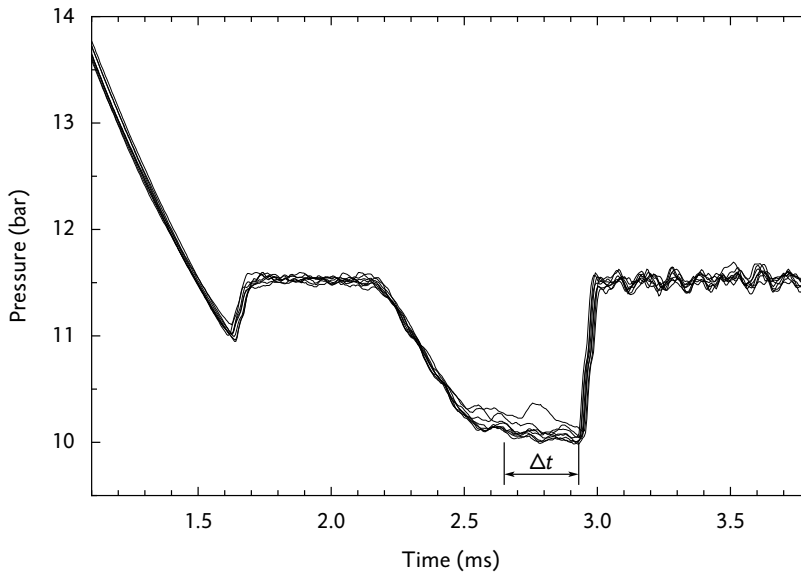


Figure 4.5: Pressure pulse measured by the dynamic transducer. The pressure signals from eight experiments are superimposed, showing that the pressure at the bottom of the pulse cannot be reproduced as well as the pressure before and after the pulse. The duration Δt of the pulse is determined visually for each experiment; here an average duration is displayed. The time origin is the same as in Figure 4.4, that is, $t = 0$ is the time at which the expansion wave arrives at the measuring position.

Pulse conditions

The pressure during the pulse determines the temperature and the supersaturation of a nucleation experiment. In addition, the duration of the pulse determines the computed nucleation rate. As Figure 4.5 shows, neither of these quantities can be easily defined. First, the beginning of the pulse (at a time of 2.2–2.5 ms in Figure 4.5) is created by a small expansion wave, so it takes some time for the pressure to decrease to the desired level. In the deepest part of the pulse (2.5–2.95 ms), where nucleation takes place, the pressure also decreases somewhat, which makes it difficult to accurately assign the nucleation pressure. Furthermore, this part of the pulse cannot be reproduced accurately from experiment to experiment, although the pressures before and after the pulse can be matched. The pulse is ended by a shock wave at 3 ms, which accurately defines the end of the pulse.

Because of the strong dependence of the nucleation rate on the supersaturation, only the deepest portion of the bottom of the pulse contributes significantly to the amount of formed droplets. When the pulse boundaries are visually determined from a figure such as Figure 4.5, this is taken into account, resulting in an average pulse duration of 0.27 ms. The pulse pressure

is then defined as the average of the pressure between the pulse boundaries, and the pulse temperature and supersaturation follow from the pressure.

Because the pulse boundaries are determined by visual inspection of the pressure signal, the uncertainty in the pulse duration can be as large as 30%. Through Eq. 4.1, this inaccuracy also affects the computed nucleation rate. In addition, the uncertainty in the position of the pulse edges also introduces errors in the pulse pressure and temperature. To alleviate this problem, Wölk²⁰² fitted a trapezoidal construction to the pressure around the pulse, illustrated earlier by Viisanen et al.¹⁹⁵ Our more irregular pulses cannot be easily reproduced by such a shape. Instead, it is possible to determine the nucleation rate without the subjective definition of the pulse duration, by integration over the entire pressure history. This technique was used by Miller et al.¹⁸ and (in a modified form) by Schmitt and coworkers.²⁰³ In our case, we integrate an empirical nucleation rate function $J_m(t) \equiv J_m[T(t), S(t)]$ over the entire pressure history, resulting in a modelled droplet number density n_m ,

$$n_m = \int J_m(t) dt. \quad (4.4)$$

Because the value of J_m outside the pulse is orders of magnitude lower than it is during the pulse, n_m does not depend on the integration limits as long as the pulse is included in the integration interval. By a similar integration, the pulse conditions p_p and T_p can be found. For that purpose we define the pulse pressure as a weighted average over the entire pressure history, where the weight factor is proportional to the number of droplets that were formed at a certain pressure. Using this definition, the weighted pressure average is computed by taking the nucleation rate as a weight factor,

$$p_p = \frac{\int p(t)J_m(t) dt}{\int J_m(t) dt} = \frac{1}{n_m} \int p(t)J_m(t) dt. \quad (4.5)$$

The corresponding pulse temperature T_p is calculated from p_p by the isentropic relation of Eq. 4.2 or a suitable equation of state. Alternatively, the temperature could be calculated as the weighted average $T_p = n_m^{-1} \int T(t)J_m(t) dt$. In practice, the difference between the two methods is small (1 mK) so either method can be used. The pulse supersaturation S_p is found from Eq. 1.29.

To obtain the experimental nucleation rate that corresponds to the pulse parameters T_p and S_p , the theoretical nucleation rate is corrected with the ratio of experimental and modelled droplet densities,

$$J_{\text{exp}} = \frac{n_{\text{exp}}}{n_m} \times J_m(T_p, S_p). \quad (4.6)$$

The values T_p , S_p and J_{exp} constitute the result of the integration method.

As mentioned before, the method requires an empirical nucleation rate expression. Such an expression can only be obtained if nucleation measurements are available in a wide enough temperature and supersaturation range. This is the case for our experiments in helium, but not for our measurements in methane and carbon dioxide, which were performed at 235 K only. In this work, the pulse integration method was therefore only applied to the measurements in helium; the data of the methane experiments was obtained by visually choosing the pulse boundaries.

4.3 Optical measurements

When the droplets have become large enough, they can be detected optically. To determine the number density of droplets in our setup, two quantities are measured: the extinction of a laser beam that passes through the droplet cloud, and irradiance of the light that is scattered by the droplets at an angle of 90° . The irradiance of the scattered light shows a characteristic pattern as a function of the droplet size, so that the size of the growing droplets can be obtained as a function of time when this irradiance is continuously measured. The smallest droplets of which the size can be measured have a diameter of the same order as the wavelength of the light. Together with the extinction measurement, the number density of droplets can be determined.

Optical setup

The optical setup that is employed is drawn in Figure 4.6. The light source is a diode-pumped solid-state laser (Lasos LasNova GL 3220 T01) with a wavelength of 532 nm, a power of 20 mW and a beam diameter of 0.7 mm. Within the time of our measurements (40 ms), the stability of the irradiance is better than $\pm 0.1\%$. The light is vertically polarized.

The beam enters and exits the tube through windows in the sides. These windows are inclined at an angle of 6° to prevent interference with the reflected beams. The windows are made of BK7 optical glass, which has a high homogeneity. Inside the tube, the beam passes at a distance of 5 mm from the end wall, and lies in the same vertical plane as the pressure transducers. After it leaves the tube, the beam is focused by lens L1 with a focal length of 0.10 m. Diaphragm D1 (with an aperture diameter of 1.5 mm) is located at the focal point of L1, to remove forward-scattered light. The beam finally enters the detector housing through an aperture with a diameter of 6 mm, in which it illuminates a stack of three semitransparent plastic screens, each screen having a thickness of 0.15 mm. The photodiode with an area of $3 \text{ mm} \times 3 \text{ mm}$ is placed behind the screens, at a distance of about 7 mm.

A potential problem of the optical setup after the tube is the dependence

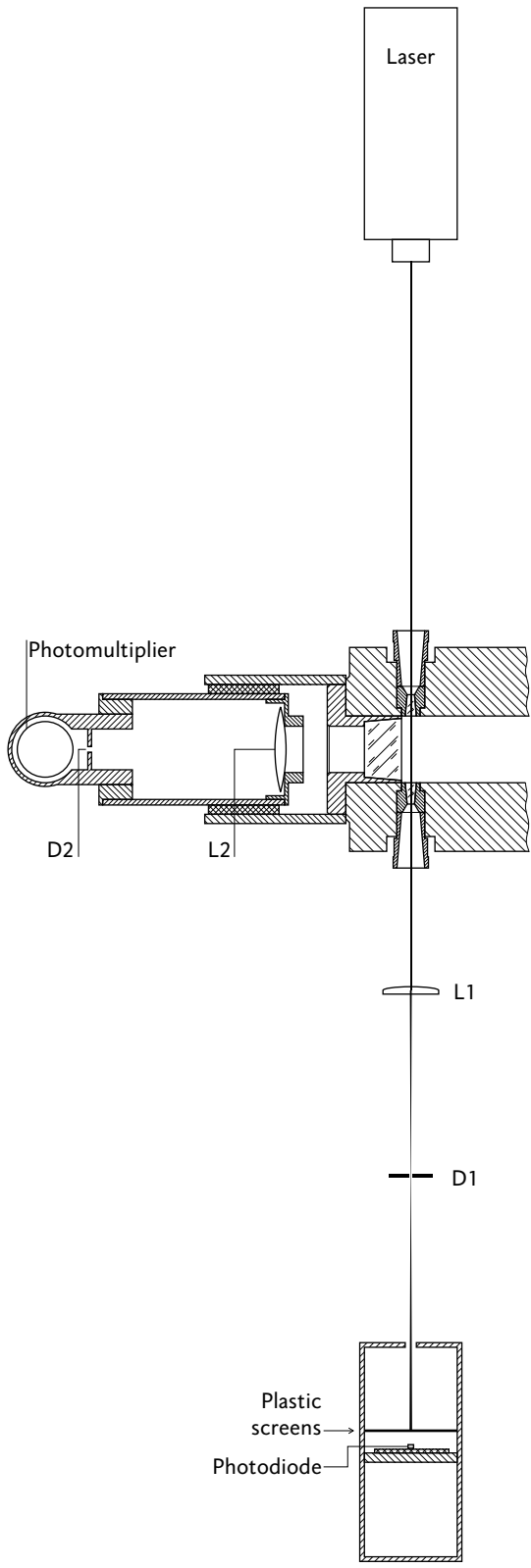


Figure 4.6: Optical setup on scale 1:4.

of the exit angle of the beam on the pressure in the tube. This dependence is caused by the variation of the refractive index of the gas in the tube, and results in an angular deviation of the beam during the expansion.⁹ When the laser beam directly illuminated the photodiode, the recorded signal would show a deviation during the expansion. For that reason, the beam is imaged on semitransparent screens which are placed some distance away from the photodiode. After careful calibration, the measured irradiance change during the expansion could be limited to 0.2%, and irradiance variations after the expansion were within $\pm 0.15\%$.

The light that is scattered by the droplet cloud leaves the tube through a window that covers nearly the entire end wall of the tube; it has a diameter of 30 mm. The combination of the positive lens L2 (with a focal length of 0.10 m) and the slit D2 (with a width of 4 mm and a height of 22 mm) ensures that only light with a scattering angle close to 90° reaches the detector. Specifically, the angle between the incident beam and the scattered beam is limited to $90^\circ \pm 1.1^\circ$, and the angle with the horizontal plane is limited to $0^\circ \pm 6^\circ$. The detector is a photomultiplier tube (Hamamatsu 1P28A) powered by a high-voltage power supply (Hamamatsu C956-04).

The description given above concerns the setup after April 2007, which was used for the water nucleation experiments in methane and carbon dioxide. The most recent experiments of Labetski¹⁰ were done with the lens and diaphragm exchanged; the beam first passed through the diaphragm and was then focused by the lens. During the earlier experiments of Labetski and the water–helium experiments of this work, an argon-ion laser was used as a light source. This laser was less stable, which required a more complicated optical setup that is described by Labetski.¹⁰

Scattering theory

To infer the droplet size and concentration from the optical measurements, the theoretical scattering and extinction of a light beam by a droplet cloud must be known. These properties can be derived from the scattering of light by a single droplet, for which the basic theory will now be given.

Consider the scattering of arbitrarily polarized light by a particle in the origin, shown in Figure 4.7. The irradiance of the incident light is I_0 (with a dimension of energy per time and area), the irradiance of the scattered light at a distance R from the particle is called I . The incident light is a plane wave travelling in the positive z direction. To account for the angular dependence of the scattered light irradiance, it is customary to define a reference plane called the scattering plane, which is the plane through the incident beam (on the z -axis) and the scattered beam of interest. The amplitude E_0 of the incident wave can then be resolved into a component E_{0l} parallel with the scat-

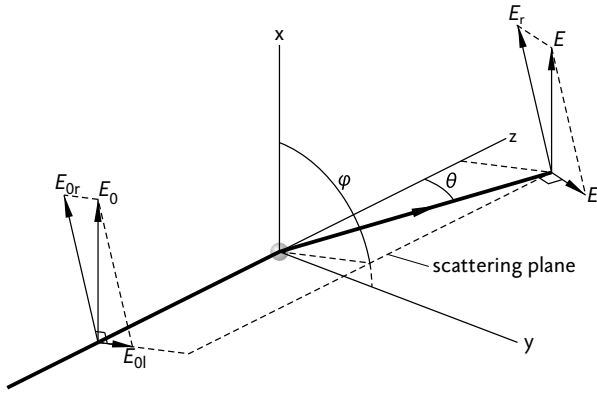


Figure 4.7: Scattering of light by a particle. Light travels in the positive z direction and is scattered by a particle in the origin. The angle of the scattering plane with the x - z plane is ϕ ; the angle of the scattered light with the z -axis is θ .

tering plane and a component E_{0r} perpendicular to it. The scattered beam amplitude E is analogously resolved into components E_l and E_r . The scattering by the object is described by the relation²⁰⁴

$$\begin{pmatrix} E_l \\ E_r \end{pmatrix} = \begin{pmatrix} S_2 & S_3 \\ S_4 & S_1 \end{pmatrix} \frac{e^{-ikr+ikz}}{ikr} \begin{pmatrix} E_{0l} \\ E_{0r} \end{pmatrix}, \quad (4.7)$$

where i is the imaginary unit and $k = 2\pi/\lambda$ is the wave number, with λ the wavelength of the light. The quantities S_1 to S_4 generally depend on the scattering angles θ and ϕ that are defined in Figure 4.7. For a spherical particle, however, S_3 and S_4 are zero, so that the amplitudes are given by

$$E_r = S_1(\theta) \frac{e^{-ikr+ikz}}{ikr} E_{0r} \quad \text{and} \quad E_l = S_2(\theta) \frac{e^{-ikr+ikz}}{ikr} E_{0l}. \quad (4.8)$$

For a spherical particle, S_1 and S_2 are independent of ϕ because the geometry is axially symmetric around the z -axis. The irradiance of the scattered light is the square of the absolute value of the amplitude,

$$\begin{aligned} I &= |E_r|^2 + |E_l|^2 \\ &= \frac{|S_1(\theta)|^2}{k^2 R^2} |E_{0r}|^2 + \frac{|S_2(\theta)|^2}{k^2 R^2} |E_{0l}|^2. \end{aligned} \quad (4.9)$$

In our experiments, the incident light is linearly polarized in the x direction, that is, at an angle of ϕ with the plane of scattering. In that case, $E_{0l} = E_0 \cos \phi$ and $E_{0r} = E_0 \sin \phi$, so that

$$I = \frac{i_1(\theta) \sin^2 \phi + i_2(\theta) \cos^2 \phi}{k^2 R^2} I_0 \equiv \frac{F(\theta, \phi)}{k^2 R^2} I_0, \quad (4.10)$$

where $i_1(\theta) \equiv |S_1(\theta)|^2$ and $i_2(\theta) \equiv |S_2(\theta)|^2$. In the last equality, the dimensionless function F is defined as

$$F(\theta, \phi) \equiv i_1(\theta) \sin^2 \phi + i_2(\theta) \cos^2 \phi. \quad (4.11)$$

The total energy flux P in a solid angle given by $\theta_1 < \theta < \theta_2$ and $\phi_1 < \phi < \phi_2$ is found by integrating the irradiance, resulting in

$$\begin{aligned} P &= \int_{\theta_1}^{\theta_2} \int_{\phi_1}^{\phi_2} I(\theta, \phi) R^2 \sin \theta \, d\theta \, d\phi \\ &= \frac{I_0}{k^2} \int_{\theta_1}^{\theta_2} \int_{\phi_1}^{\phi_2} F(\theta, \phi) \sin \theta \, d\theta \, d\phi \\ &= \frac{I_0}{k^2} \int_{\theta_1}^{\theta_2} [i_1(\theta) f_1 + i_2(\theta) f_2] \sin \theta \, d\theta. \end{aligned} \quad (4.12)$$

with $f_1 \equiv \int_{\phi_1}^{\phi_2} \sin^2 \phi \, d\phi$ and $f_2 \equiv \int_{\phi_1}^{\phi_2} \cos^2 \phi \, d\phi$.

The expressions for $i_1(\theta)$ and $i_2(\theta)$ follow from the solution of the Maxwell equations, as derived by Mie²⁰⁵ in 1908. For an exposition of Mie theory, the reader is referred to the books of van de Hulst²⁰⁴ and Bohren and Huffman.²⁰⁶

Mie theory gives the exact result of the far-field irradiance of light scattered by a single particle. In the case of scattering by multiple particles, the scattered light irradiances of the particles may be added without regard for phase effects, provided that the particles scatter independently. Independent scattering is achieved if the particles are so far apart that there is no systematic relation between the phases of the scattered waves from several particles. Van de Hulst²⁰⁴ estimates that an interparticle distance of three times the particle radius ensures independent scattering; in our setup, this condition is satisfied.¹⁰

In dense particle clouds, a particle may not be illuminated directly by the light source, but instead by light that has already been scattered by another particle. This phenomenon is called *multiple scattering*. When this effect is negligible, the attenuated light irradiance of light travelling through a cloud of identical particles is given by the law of Lambert–Beer:

$$I = I_0 \exp(-\beta d), \quad (4.13)$$

where d is the extinction length and β is the extinction coefficient. For spherical particles, β is given by²⁰⁴

$$\beta = n\pi r^2 Q_{\text{ext}}, \quad (4.14)$$

where r is the radius of a particle and n is the droplet number density. The parameter Q_{ext} , called the extinction efficiency, is

$$Q_{\text{ext}} = \frac{4}{\alpha^2} \text{Re}[S(0)], \quad (4.15)$$

where $S(0) = S_1(\theta = 0) = S_2(\theta = 0)$; the functions S_1 and S_2 are those from Eq. 4.8. Furthermore, α is the so-called size parameter, a dimensionless quantity defined as

$$\alpha = \frac{2\pi r}{\lambda} = kr. \quad (4.16)$$

According to van de Hulst,²⁰⁴ a correction for multiple scattering may be required when the optical depth βd of Eq. 4.13 exceeds 0.1, which corresponds to an attenuation of about 10%. In contrast, Swanson et al.²⁰⁷ have shown that the Lambert–Beer law may hold up to optical depths of 10, provided that the detector does not capture too much forward-scattered light. In practice, the input aperture of the detector should be small enough. Since the maximum optical depth that occurs in our experiments is 0.6, the use of the Lambert–Beer law seems justified.

Analysis of optical signals

Scattered light

The size of the growing droplets is derived from the irradiance of the scattered light. This is possible because that irradiance shows a characteristic pattern of maxima and minima as a function of the droplet size (Figure 4.8).

In our experiments, the observed irradiance of the scattered light does not exactly follow the values predicted by Mie theory. In addition to the light that originates from the droplets, a time-dependent (or droplet radius-dependent) background irradiance is observed; this background irradiance increases as the droplets grow (Figure 4.9). To be able to fit a theoretical scattering signal to the experimental signal, the background irradiance must be taken into account. It is assumed that the observed irradiance I_{sca} consists of a term proportional to the Mie theory F value, given by Eq. 4.11, and the background irradiance I_{b} ,

$$I_{\text{sca}}(r) = a F(\theta, r) + I_{\text{b}}(r), \quad (4.17)$$

with a a positive constant and r the time-dependent droplet radius. The background irradiance is caused by scattered light that reaches the detector indirectly, for instance via the tube walls. We assume that the background irradiance is proportional to the amount of light that is scattered by the droplet

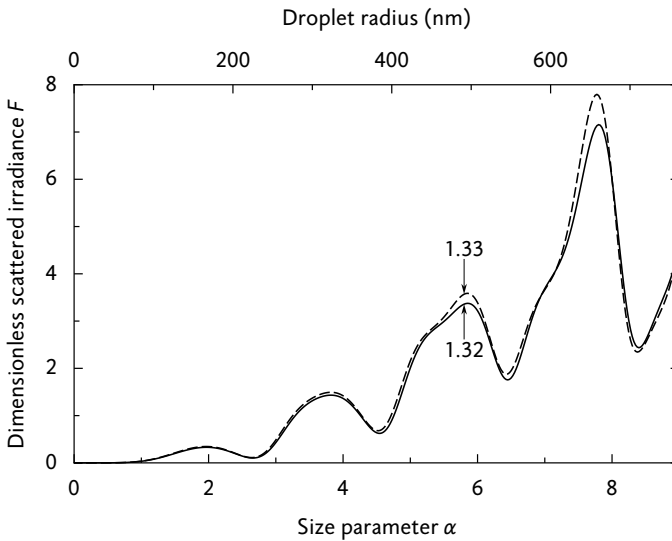


Figure 4.8: Dimensionless irradiance F of the scattered light (Eq. 4.10) as a function of the size parameter α (Eq. 4.16), for water, according to Mie theory. The scattering angles θ and ϕ (Figure 4.7) are both 90° . The scattered irradiance is shown for refractive indexes of 1.32 and 1.33, which correspond to water at different temperatures (see appendix A.3). The droplet radius scale is valid for our laser beam wavelength of 532 nm; the size parameter scale is valid for any wavelength.

cloud in all directions. Since absorption is negligible, the total amount of scattered light is equal to the extinction of the incident beam (Eq. 4.13), so that the background irradiance can be written as

$$I_b(r) = b\{1 - \exp[-\beta(r) d]\}, \quad (4.18)$$

where d is the extinction length, β is the extinction coefficient defined in Eq. 4.14, and b is a positive constant.

In about a quarter of the experiments, the background model of Eq. 4.18 did not result in an acceptable fit of the experimental scattered irradiance. These experiments all have a high nucleation rate, and depletion plays a significant role. The combination of a high droplet density and a strongly size-dependent growth rate results in a background irradiance that cannot be adequately described by the simple model of Eq. 4.18. In those cases, the background was represented by a quadratic function of time, with three fitting parameters.

By fitting the radius-dependent expression for I_{sca} to the experimental time-dependent signal, the droplet growth curve $r(t)$ can be obtained. The accuracy of that method depends on how the fit is performed. In practice, the shape of the growth curve $r(t)$ is optimized so that the scattering irradiance

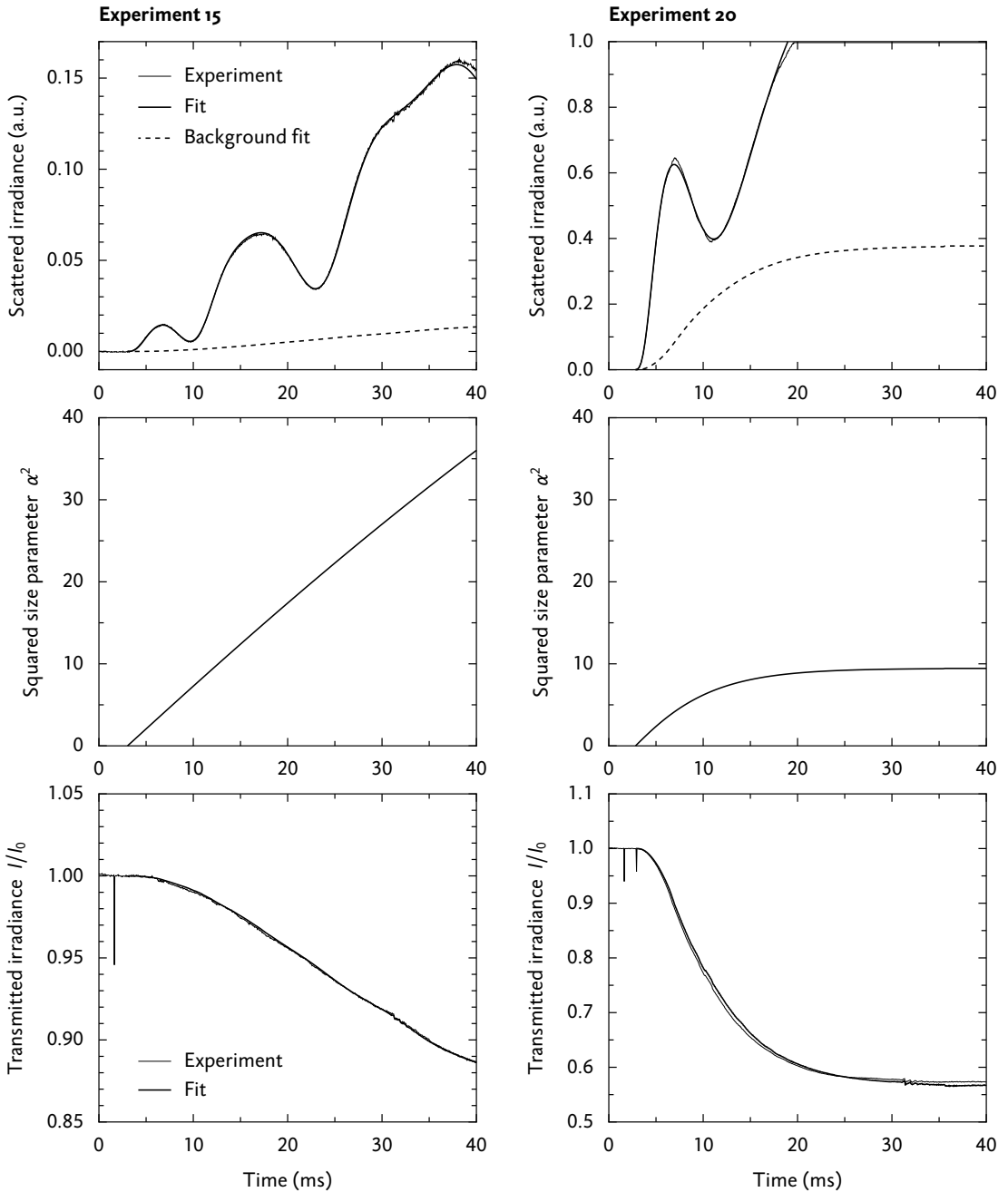


Figure 4.9: Examples of optical signals and fits. *Top:* irradiance of the 90° -scattered light, experimental signal and fit according to Eq. 4.17. The background irradiance fit (Eq. 4.18) is shown dashed. *Centre:* Squared size parameter of the droplets according to Eq. 4.19. This growth curve follows from the fit of the scattered irradiance (top). *Bottom:* Extinction of the main beam, indicated by the relative irradiance of the transmitted light; experimental signal and fit according to Eq. 4.13. The fit is performed with the droplet number density as the only free parameter; the growth curve is known from the scattered irradiance fit (centre). The spikes before 5 ms are caused by the passing shock wave (D in Figure 4.2), which disturbs the laser beam.

is best reproduced. To limit the computations, it is desirable to describe the shape of the growth curve by as few parameters as possible. These parameters assume the role of fitting parameters in the optimization. It was found that the droplet growth curves from our experiments could be reproduced well with a simple growth model with three parameters, which is described in the following section. The total number of fitting parameters (including a and b from Eqs. 4.17 and 4.18) is then five.

It is experimentally difficult to achieve a scattering angle θ of exactly 90° . Because the scattered irradiance is quite sensitive to θ , a possible deviation of the angle must be taken into account.²⁰⁸ Values of the scattering function F were computed for several angles deviating up to 0.2° from the ideal value. The fitting procedure described above was repeated for these angles, and the angle with the best matching scattered-light irradiance curve was selected.

Growth model

The growth model is the simplified diffusion-controlled growth model with depletion, described in section 2.11. The growth law expression (Eq. 2.148) gives the time t at which a droplet reaches a radius r ,

$$t - t_0 = \frac{2r_m^2}{c} G\left(\frac{r}{r_m}\right), \quad (4.19)$$

where t_0 is the time at which the droplet growth starts, $c = dr^2/dt|_{t=t_0}$ is the initial growth rate of the squared radius, r_m is the maximum droplet radius (which is reached when the supersaturation has decreased to unity) and G is given by Eq. 2.146. The model has three parameters: t_0 , c and r_m . If depletion can be neglected, as is the case in some experiments, the model reduces to $r^2 = c(t - t_0)$, which has only two parameters.

Extinction

After the growth curve $r(t)$ has been obtained, the only remaining unknown in the expression of the light extinction, Eq. 4.13, is the droplet number density n . Therefore, n can be determined by fitting the theoretical extinction curve to the experimental one. The extinction length d from Eq. 4.13 is approximated by the inner diameter of the high-pressure section. Because of thermal boundary layers the droplet cloud does not fill the entire diameter, but for the purpose of determining the droplet density, the current approximation is accurate enough.

The number density of droplets that is detected is higher than the number density at the end of the pulse, since the recompression that ends the pulse also compresses the droplet cloud. In addition, the number density of droplets varies slightly after the pulse due to fluctuations in the pressure. Both deviations are taken into account by assuming that the droplet number density

is proportional to the gas density. Changes in the gas density are computed from the pressure signal. The final result for the droplet density that is computed corresponds to the pressure at the bottom of the pulse, and is usually accurate to within 5%.

4.4 Mixture preparation

The accurate preparation of a mixture of vapour and carrier gases is essential for our measurements, and a separate section, called the mixture preparation device (MPD), has been built for that purpose. It was designed by Hrubý, and a detailed description is found in his report.²⁰⁹ The MPD, schematically shown in Figure 4.10, allows saturating a carrier gas flow with vapour and mixing it with one or more dry carrier gas flows to obtain the desired mixture composition. The MPD does not produce a limited amount of the mixture; instead, it continuously generates a flow with the wanted composition. After evacuating the high-pressure section, it is filled with the mixture produced by the MPD. When the desired pressure is reached, an upstream pressure controller (UPC) opens a valve and leads the flow to waste, while maintaining the pressure. After that, the flow from the MPD is led through the high-pressure section for about one hour, to saturate the walls of the setup and to attain adsorption equilibrium. This flushing process ensures that the mixture inside the HPS has the same composition as the mixture leaving the MPD.

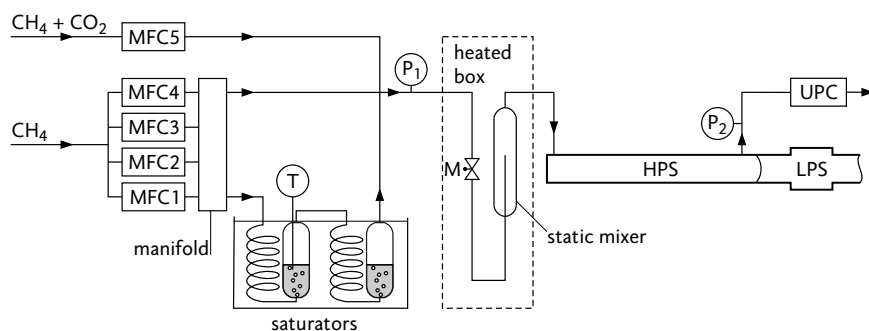


Figure 4.10: Scheme of the mixture preparation device (MPD) and its connection to the high-pressure section (HPS) of the expansion tube. Dry carrier gases are supplied at the left-hand side; a manifold allows the selection of mass flow controllers (MFC) that control the flow rates of saturation and dilution flows. In the saturators, the dry gas bubbles through liquid water. The pressure reduction from the saturation pressure P_1 to the HPS pressure P_2 takes place at the metering valve M that is located in a heated box. The HPS pressure is maintained by an upstream pressure controller (UPC).

Saturators

The device that saturates a gas with water vapour at controlled total pressure and temperature is called a saturator. Saturation of the gas can be achieved, for example, by leading the gas over a liquid surface or by bubbling the gas through a volume of liquid. The bubbling method was chosen for our setup because it saturates the gas faster and more completely. A potential disadvantage of the bubbling method is that the breaking of bubbles at the liquid surface might produce small liquid droplets which could be dragged along with the flow and possibly lead to composition inaccuracies. Furthermore, bubbling may introduce condensation nuclei that enable heterogeneous nucleation, as was experimentally proven by Wilson¹⁶ in 1897.

To improve the saturation performance of a bubble saturator, the bubble residence time has to be as long as possible and the bubble size has to be small. The design of our saturators is based on the descriptions of Wylie and Fisher²¹⁰ and Hyland and Wexler,²¹¹ and takes both factors into account. A detailed cross-section on a scale of 1:2 is shown in Figure 4.11. At the bottom of the vessel, where the gas enters, the flow is split up into eight parts to improve the spreading of gas through the vessel and to decrease the bubble size. The bottom half of a cylinder is filled with three layers of glass beads; from bottom to top a 7 cm high layer of 5 mm diameter beads, a 3 cm layer of 3 mm beads, and a 3 cm layer of 2 mm beads. The beads serve two purposes: below the water surface, they increase the time it takes for a bubble to reach the water surface, and above the surface they catch the remains of broken bubbles. Smaller beads lead to smaller bubbles and a better distribution of carrier gas; however, using solely the smallest beads could lead to a high resistance for the gas flow. It is essential that the water level in the saturator is such that the free surface is within the volume filled with beads, so that the bubble remains will be caught.

To be certain of complete saturation of the carrier gas, our setup contains two saturators connected in series. To check the performance of a single saturator, it is possible to temporarily use only one saturator, and compare the water content with the double-saturator situation.

The temperature control of the saturators is realized by immersing them in a thermostatic bath. It contains a relatively large volume of water (56 L) and its temperature variations are within 0.01 K. The temperature of the water inside the saturators is measured by a platinum resistance thermometer that has an accuracy of 0.02 K. Before the dry gas enters the saturator, it is cooled down to the saturator temperature by leading it through a tube that is helically coiled around the saturator.

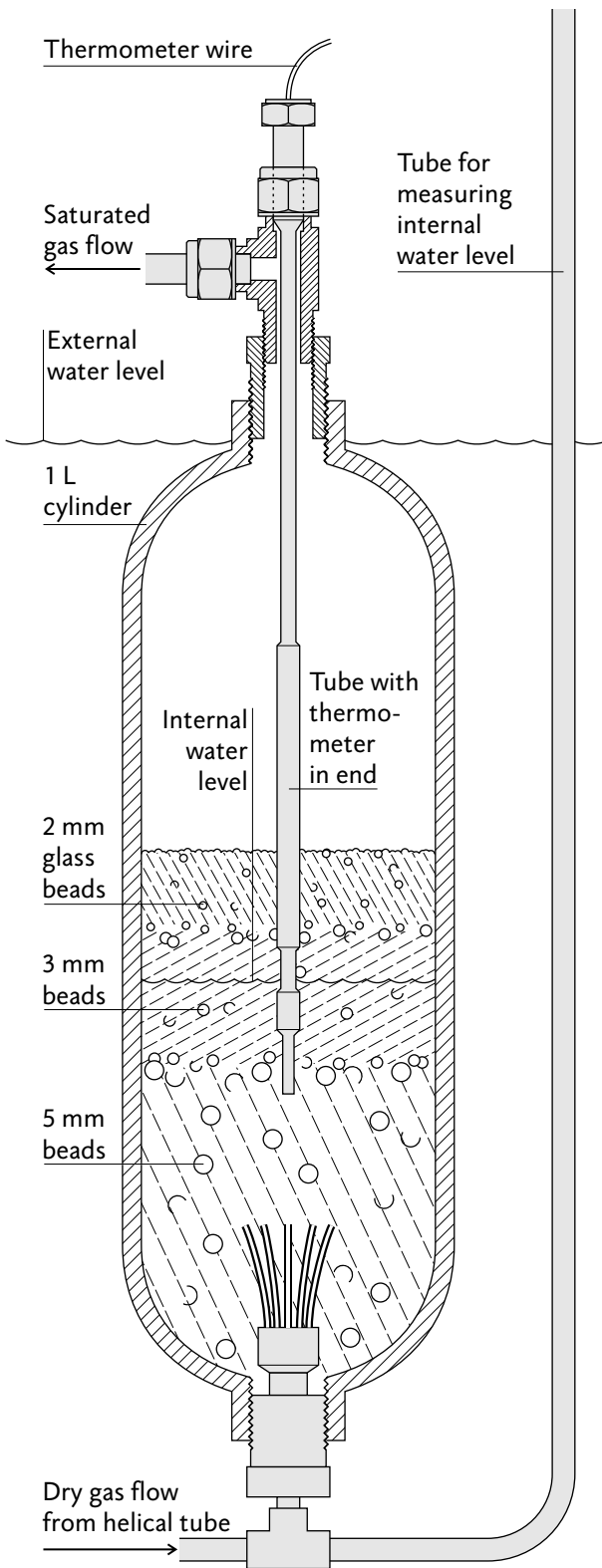


Figure 4.11: Saturator on scale 1:2. The dry gas mixture from the helically coiled tube enters at the bottom and is split by eight thin tubes, after which it bubbles through the water in the volume filled with beads. The saturated flow leaves the saturator at the top left. The vertical tube on the right is used to measure the water level inside the saturator when it is not pressurized; the water level in the tube is then the same as in the saturator. The tube is also used for refilling. When the saturator is pressurized, the tube is closed by a valve at the top (not shown).

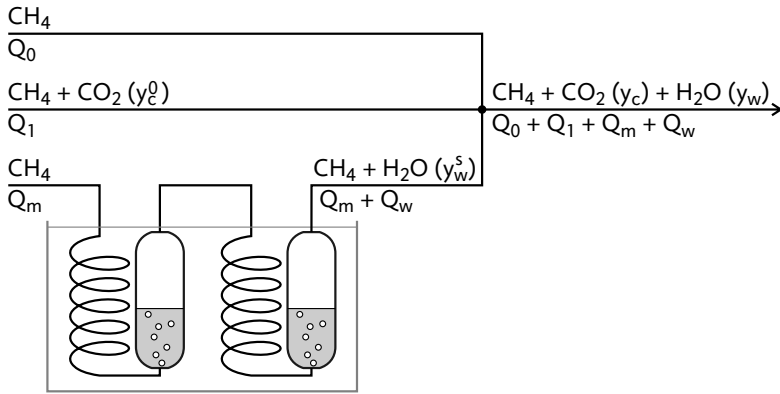


Figure 4.12: Mixing of saturated vapour and carrier gas flows. Above each line, the components in the mixture are specified; a quantity in parentheses is the molar fraction of a component. Below each line, the molar flow rates are given; Q_0 is a pure methane flow rate for dilution, Q_1 is a flow rate of a methane–carbon dioxide mixture (or, with $y_c^0 = 1$, a pure carbon dioxide flow rate). Furthermore, Q_m is the flow rate of pure methane that is saturated with water vapour; the flow Q_w after the saturators represents the flow rate of the added water vapour.

Flow control and mixing

To obtain the desired composition of the gas–vapour mixture, several flows are mixed with a controlled flow rate, as illustrated in Figure 4.12. During an experimental series, the pressure and temperature in the saturators are kept constant, which means that the molar water fraction y_w^s in the flow from the saturators is also constant. To vary the water fraction across experiments, the saturator flow is diluted with a pure methane flow. Alternatively, the pressure in the saturators could be adjusted to obtain the desired water fraction directly from the saturators, but this introduces additional uncertainties because of the limited amount of data on high-pressure equilibria. For that reason, the dilution method was chosen.

The choice of saturator temperature and pressure is based on several factors. The temperature of a saturator must be lower than laboratory temperature to prevent condensation in the saturated gas flow that leaves the saturators. In our experiments, the temperature was 291 K. The saturated water fraction is determined by the pressure p and the temperature T in the saturator according to Eq. 1.26,

$$y_w^s = f_e(p, T) \frac{p_s(T)}{p}. \quad (4.20)$$

When selecting a pressure, it is taken into account that it is not possible to increase the water fraction that leaves the saturators – it can only be decreased

by dilution. Therefore, the saturator pressure must be so low that the saturated water fraction y_w^s is higher than the highest water fraction y_w that is needed in the experiments. Another consideration is that the more the saturated flow is diluted, the higher is the uncertainty in the final water fraction y_w . For this reason, the saturated water fraction y_w^s should not be too high, so the saturator pressure should not be too low. It follows that the pressure should optimally be such that y_w^s is just above the highest fraction that is required in the experimental series. In practice, a pressure lower than optimal is chosen because phase equilibrium data is scarce for high pressures.

For experiments in which carbon dioxide is present in the mixture, another flow is added to the flow that leaves the saturators. For experiments with a low carbon dioxide fraction (several percent), a mixture of methane and carbon dioxide is added; for higher carbon dioxide fractions, pure carbon dioxide is added.

The water and carbon dioxide fractions of the final mixture are determined by ratios of molar flow rates that are shown in Figure 4.12. If there is no accumulation of methane in the saturators, methane leaves the saturator at the same rate Q_m as it enters it. In the saturators, water is added to the gas, and the water flow rate after the saturators is denoted by Q_w . Since the water fraction after the saturator y_w^s is by definition equal to $Q_w/(Q_m + Q_w)$, the flow rate of water is

$$Q_w = \frac{y_w^s}{1 - y_w^s} Q_m. \quad (4.21)$$

The total flow Q_{tot} is defined as

$$Q_{\text{tot}} = Q_0 + Q_1 + Q_m + Q_w, \quad (4.22)$$

where Q_0 is the dilution flow rate of pure methane, and Q_1 is the flow rate of a methane–carbon dioxide mixture with a carbon dioxide fraction of y_c^0 . The fraction of water in the final mixture becomes

$$y_w = \frac{Q_w}{Q_{\text{tot}}} = \frac{y_w^s}{1 - y_w^s} \frac{Q_m}{Q_{\text{tot}}}, \quad (4.23)$$

which can also be written as a function of the three input flows, yielding

$$y_w = \frac{y_w^s}{1 + (1 - y_w^s)(Q_0 + Q_1)/Q_m}. \quad (4.24)$$

The fraction of carbon dioxide in the final mixture is given by

$$y_c = y_c^0 \frac{Q_1}{Q_{\text{tot}}}. \quad (4.25)$$

The molar fractions depend on ratios of flow rates, so multiplying all flow rates by a certain factor does not change the composition. This feature is used to control the pressure of the mixture preparation device. For example, when the pressure is too low, a controller increases all flows by the same factor, until the pressure reaches the preset value.

The pressure in the mixture preparation device is measured by a transducer (Druck PMP 4070) with an accuracy of 0.1 bar. The transducer is located after the saturators, near the point where all flows are mixed, but the pressure in the saturators is assumed to be equal to the pressure at the transducer.

Each of the three initial flow rates is measured and controlled by a mass flow controller (MFC, Brooks 5850S). Such a device determines the gas flow by temperature measurement of the gas at the upstream and downstream sides of a small heater. The temperature difference is proportional to the mass flow. The flow is controlled with a solenoid valve that chokes the flow on the downstream side of the flow meter.

Before the experimental series, the MFCs were calibrated according to the Brooks Instrument calibration specifications.²¹² During the calibration, the output tube of the MPD (which is normally connected to the HPS flushing tube) is connected to a gas flow calibrator (Brooks Vol-U-Meter 1067), which is a precision-bore glass cylinder with a frictionless piston. By collecting the gas in the cylinder and measuring the piston speed, the volume flow can be determined. This volume flow is converted to a molar flow using the ideal gas equation. The ideal-gas assumption introduces a relative error in the molar flow of 0.2% for methane and 0.5% for carbon dioxide. This should be compared to the intrinsic relative accuracy of an MFC, which is about 1%.

The characteristics of an MFC slightly depend on the inlet pressure. Therefore, during calibration, the inlet pressure is set to the value that is used during the experiments. The outlet pressure, however, is atmospheric during the calibration – a value that differs strongly from the experimental pressure in the MPD. It is believed that this difference does not affect the calibration, since the flow rate meter in the MFC is located at the upstream side of the pressure drop.

For the saturation flow (Q_m) and the dilution flow (Q_1), three MFCs with different flow rate ranges are available; their maximum normal volume flow rates are 2.4, 1.2, and 0.24 litres per minute for methane. The selection of an MFC depends on the flow rates that are required to produce a mixture with the desired composition. It must also be taken into account that the uncertainty of the flow rate is higher when an MFC is used at a low fraction of its maximum flow rate. For example, at 20% of maximum flow, the relative uncertainty is 1.7%, and at 10% it is 2.7%. In our experiments, the flow rates

were always more than 30% of the maximum value, and the relative error is less than 1.4%. The total flow rate (Q_{tot}), which is the flow rate at which the HPS was flushed, corresponded to a normal volume flow rate of 1.7 to 2 litres per minute.

Using an MFC with carbon dioxide causes difficulties that were also encountered by Labetski.¹⁰ At the pressure drop in the MFC, the carbon dioxide cools down due to the Joule–Thomson effect. Without precautions, the temperature in the MFC can become so low that the device stops functioning. To prevent this, the tube on the upstream side of the MFC and the MFC itself were heated to about 47 °C. This temperature is safely within the operating range of the MFC, which is 0–70 °C. The heating was applied both during calibration and during experiments.

Pressure reduction and static mixing

The pressure in the HPS, which increases during filling from zero to the initial pressure for the nucleation experiment, is lower than the pressure in the saturation section. The pressure reduction takes place at a metering valve marked by M in Figure 4.10, which is used to manually set the total flow through the MPD. Because of Joule–Thomson cooling, the temperature of mixture the mixture decreases during the pressure reduction. To prevent condensation of the vapour, the metering valve and the tubing close to it are placed inside a box that is heated to 70 °C.

The heated box also contains a static mixer, which smoothes temporal fluctuations in the mixture composition. The mixer is called static because it has no moving parts. The mixture enters the vessel of 0.3 L through a tube with small holes (0.2 mm diameter). The static mixer is heated to reduce adsorption.

Flushing

The flushing section is depicted in more detail in Figure 4.13. The pressure in the flushing circuit is measured by a transducer (Druck PMP 4070) with an accuracy of 0.03 bar. During flushing, the pressure is controlled by an upstream pressure controller (Brooks 5866), which receives the signal of the Druck transducer. After the filling of the HPS, the flushing pressure is equal to the initial HPS pressure in the nucleation experiment. The reading of the Druck transducer is used as initial pressure, not the reading of the less accurate piezoresistive transducer in the HPS. During flushing, the humidity at the end of the flushing section is monitored using a relative humidity sensor (Vaisala Humicap HMP 234), a data acquisition device and a plotting program.

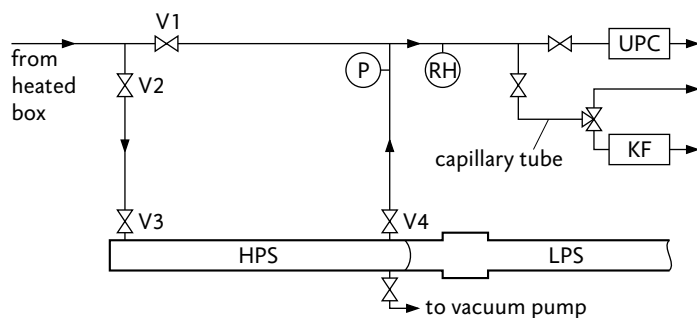
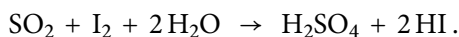


Figure 4.13: Scheme of the flushing section. During normal flushing, valve V1 is closed and the gas flows through the HPS, past the pressure transducer P and the relative humidity sensor RH, and finally through the upstream pressure controller UPC. For water content measurements, valve V1 is open and V2 is closed, so that the gas is led directly to the RH sensor and the Karl Fischer coulometer KF.

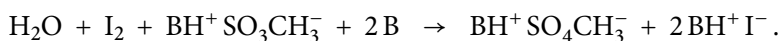
Karl Fischer titration

A relatively new addition to the setup is a Karl Fischer coulometer (Metrohm 831 KF), capable of determining the water fraction with a relative accuracy of about 1%. This device is used only to check the water content of the mixture; for the analysis of the experiments, the mixture composition is computed from the MFC flow rates.

The Karl Fischer titration method is based on the oxidation of sulphur dioxide by iodine,²¹³



To determine the amount of water, sulphur dioxide should be present in excess, and the acids that are produced should be neutralized by a base. These requirements have led to the Karl Fischer reagent, which is a solution of iodine, sulphur dioxide, and a base in methanol. The full reaction with water that takes place in the reagent is²¹³



where B is the base and SO_3CH_3^- is an ion that is formed from sulphur dioxide and methanol.

The amount of water in a sample can be determined from the amount of iodine that is consumed, as one molecule of H_2O consumes one molecule of I_2 . In a coulometer, the I_2 is produced by electrolysis from a reagent that contains iodide (I^-). The amount of I_2 that is generated is known exactly from the integration of the applied electrolysis current strength as a function of time. The end of the reaction and the consumption of all the water in the sample

is marked by the appearance of excess I_2 . This event is detected by measuring the voltage between two electrodes, between which a constant current is applied.

Before the coulometer is used in our setup, it is prepared for use. The flow that comes from the mixture preparation device is led directly to the coulometer and the UPC, and bypasses the expansion tube (see Figure 4.13). The UPC is set to maintain a pressure that is slightly higher than atmospheric. The coulometer is connected via a capillary tube, and the pressure difference results in a small flow towards the coulometer. Using the three-way valve in Figure 4.13, the flow from the capillary tube bypasses the coulometer just before it reaches the device. The flow is set up in this way to flush as much of the tubing as possible before the coulometer is used.

The KF method yields an absolute water content, for example, in micrograms of water. Since we are interested in the relative amount (the molar fraction) of water in our gas mixture, the amount of gas mixture that is supplied to the coulometer must be known precisely. Therefore, the setup is used as follows. After flushing, the flow rate is reduced and the UPC is closed. All the gas produced by the mixture preparation device then flows to the coulometer. Steady state is verified by confirming that the pressures in the MPD and in the flushing section remain constant. In that case, the molar flow of carrier gas to the coulometer is equal to the known molar flow through the mass flow controller. For successful titration, the gas flow to the coulometer should be between 0.05 and 0.25 L/min.²¹³ For this work, a flow rate of about 0.1 L/min was used.

A measurement starts by turning the three-way valve so that the flow is directed to the coulometer. The gas mixture then flows through a tube whose end is immersed in the Karl Fischer reagent, so that the gas mixture bubbles through the liquid. The measurement is ended by turning the three-way valve. The product of the measurement time and the molar flow rate yields the molar amount of gas whose water content has been determined. To minimize the influence of transient effects that occur when the flow is started and stopped, the measurement time should be at least ten minutes.

Currently, the tube leading into the titration cell is made of plastic. According to Metrohm,²¹⁴ the absorption of water by the plastic affects the measurement of the water content, so metal tubing should be used in the future. In addition, the setup should be changed so that it complies with the ISO standard²¹⁵ for this type of measurement.

4.5 Experimental procedure

The experimental procedure starts by inserting a new membrane between the HPS and the LPS. The LPS and the HPS are then evacuated for about 30 minutes; the evacuation is started in the LPS first to ensure that the membrane bends in the right direction. Not just the HPS, but also the flushing tubing and the static mixer are evacuated. The final pressure in the HPS is less than 10 Pa.

With the saturators disconnected from the rest of the MPD, the pressure in the MPD is set to the desired value by manually controlling the MFCs. Then, the PID controller that operates the MFCs is activated. Next, the pressure in the saturators is equalized to the MPD pressure through a needle valve that is located in the tube leading to the saturators. When the pressure is constant, the needle valve is opened fully and the saturators are connected to the MPD.

With the MPD fully operational, the filling of the HPS is started by opening the heated metering valve (M in Figure 4.10) slightly. As a result, the gas mixture starts flowing from the MPD into the flushing tube and the HPS. Consequently, the pressure in the MPD decreases and the MFCs open to let gas into the MPD. Gas starts to bubble through the saturators. Slowly, the metering valve is opened more until the MFC flows reach the desired values.

While the HPS is being filled, the pressure in the LPS must periodically be equalized to the HPS pressure to prevent a large pressure difference over the membrane, which may cause a premature rupture. As the pressure in the HPS rises, the pressure difference over the metering valve decreases, and the valve must be opened more to maintain a constant flow rate. After about 30 minutes, the pressure in the HPS reaches the desired value, and the UPC opens, which starts the flushing of the gas mixture through the HPS.

The flushing process takes about one hour. When the relative humidity indicated by the Humicap sensor no longer changes, valve V1 in Figure 4.13 is opened and V2 is closed, so that the gas flow bypasses the HPS and flows directly to waste. The HPS is isolated by closing valves V3 and V4. The amplifier of the dynamic pressure transducer is set to the 'operate' mode. Finally, the trigger of the data acquisition system is armed and the diaphragm is broken.

The signals from the static and dynamic pressure transducers, the photomultiplier and the photodiode are recorded by a data acquisition device (LeCroy 6810 Waveform Recorder). Its sampling rate is 200 kHz and the resolution is 12 bits.

Water nucleation in helium

The homogeneous nucleation rate of water is an important quantity. Before effects of carrier gases are considered, the water nucleation rate should be known under conditions as ideal as possible – the carrier gas should be inert and the pressure should be low. In that case, the water nucleation rate should be almost independent of the kind of carrier gas and of its pressure. The Poynting effect (Eq. 1.25) is negligible at low pressures, so vapour fraction enhancement can be neglected. Furthermore, noble gases like helium and argon do not significantly influence the surface tension of water at atmospheric pressure.²¹⁶ It is not desirable to remove the carrier gas altogether, since the thermal equilibration between water clusters and the gas results in isothermal nucleation, which is one of the assumptions of classical nucleation theory. For that reason, the carrier pressure should not be too low.

Many experiments to measure the water nucleation rates under these conditions have been performed in the last 30 years; overviews of experiments are given by Wölk et al.²¹⁷ and Brus et al.²¹⁸ In 1993, Viisanen et al.¹⁹⁵ compared water nucleation rates in each of the five stable noble gases at pressures below 1 bar, and found that the rate was independent of the kind of carrier gas. At high pressures, however, an influence is expected; argon, for example, is known to affect the surface tension of water.²¹⁶ A recent example of accurate rate measurements are the experiments by Wölk and Strey,¹⁹ performed between 220 and 260 K in argon in a nucleation pulse chamber. Their data will be compared to our results.

In 2002, Peeters et al.²¹⁹ published nucleation rates obtained in our pulse-expansion wave tube, down to 200 K. A striking feature of these data was a jump in nucleation rates at 207 K, which was interpreted as a transition from vapour–liquid to vapour–solid nucleation. To confirm this transition, we repeated Peeters’s measurements in 2003. Our new data did not show any transition, so we reanalysed the results of Peeters et al. It was found that an inaccuracy in vapour fraction calculations had caused the apparent jump; the corrected data⁷ show no evidence of a transition in the nucleation process.

It is usually assumed that the supersaturation dependence of the nuclea-

tion rate is accurately predicted by classical nucleation theory (CNT). Equivalently, it is assumed that CNT correctly predicts the number of molecules in the critical cluster. It will be shown that these assumptions do not hold for our experiments and those of Wölk and Strey.

5.1 Experimental supersaturations

Experiments were performed at pulse temperatures between 200 and 240 K at constant nucleation pressures of about 1 bar. Figure 5.1 shows the supersaturation S during the nucleation pulse, obtained with Eq. 1.29, for our experiments and those of Wölk and Strey.^{19,202} In the calculation of the supersaturation, the Poynting effect (Eq. 1.25) is ignored, because for our nucleation pressure and temperature it results in a relative change in S of about 0.1%, which is much smaller than the experimental uncertainty in S . In addition, helium is considered as an ideal gas, which results in an enhancement factor (Eq. 1.26) of unity. Equation 1.29 then reduces to the familiar relation

$$S = \gamma p / p_s = p_v / p_s, \quad (5.1)$$

where γ is the water vapour fraction, p is the total pressure, p_s is the equilibrium vapour pressure of water, and p_v is the partial pressure of water in the gas phase.

With decreasing temperature, the supersaturation must be increased to keep nucleation rates within the experimental measurement range, in our

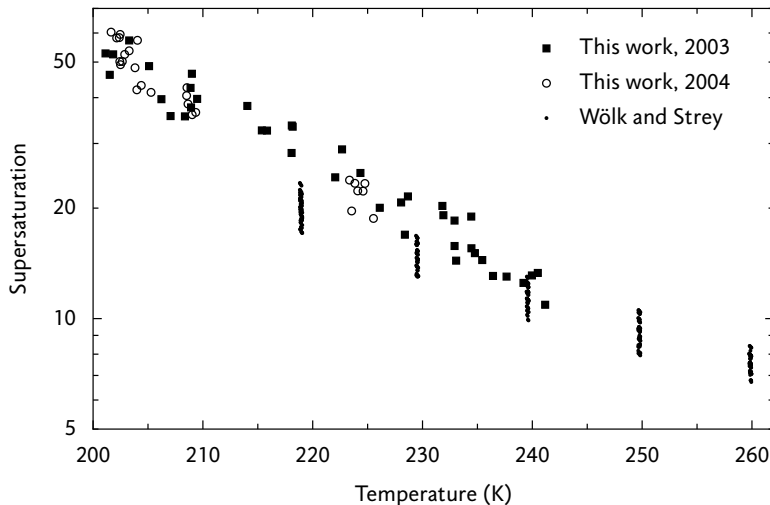


Figure 5.1: Supersaturation in the nucleation pulse as a function of the nucleation temperature. Shown are our 2003 and 2004 data sets, and the data of Wölk and Strey^{19,202} obtained in a nucleation pulse chamber.

case 3×10^{13} to $3 \times 10^{17} \text{ m}^{-3}\text{s}^{-1}$. At equal temperature, the supersaturations of Wölk and Strey are lower than ours, reflecting the lower nucleation rate range of 10^{11} – $10^{15} \text{ m}^{-3}\text{s}^{-1}$ of their nucleation pulse chamber. Wölk and Strey's data consists of five isothermal sets spaced roughly 10 K apart, while our 2003 dataset is more evenly spread across the 200–240 K range. In 2004, we also performed isothermal measurements at 203, 209 and 224 K. Compared to the isotherms of Wölk and Strey, our isotherms have more scatter in the temperature; at most, a 1 K deviation from the mean isotherm temperature. These deviations occur because pressure pulses can not always be accurately reproduced with our setup.

5.2 Empirical fit of nucleation rates

We proceed now to the way our nucleation rates were obtained. Lacking a nucleation rate model, the first step was to analyse experiments with the traditional method, by manually defining the pulse duration and using Eq. 4.1 to obtain J . This procedure yielded a set of preliminary nucleation rates. To obtain an empirical expression for the nucleation rate, the function

$$J_{\text{fit}}(T, S) = J_0 S \exp \left[a_0 + a_1 T - \frac{b_0 + b_1 T}{(\ln S)^2} \right], \quad (5.2)$$

was then fitted to the preliminary 2003 nucleation rate data, where a_0 , a_1 , b_0 , and b_1 are fitting parameters and $J_0 \equiv 1 \text{ m}^{-3}\text{s}^{-1}$ is included for dimensional consistency. This function is based on the empirical formula of Miller et al.,¹⁸ but has fewer fitting parameters and a pre-exponential factor of S instead of S^2 . When the logarithm of Eq. 5.2 is taken, the model becomes linear in the parameters, so that they can be determined by a least-squares linear fitting procedure.

After the nucleation rate model had been obtained, the next step was an analysis using the pulse integration method of Eqs. 4.4–4.6. The maximum differences of the integration results with the preliminary dataset were 40% in J , 0.3 K in T , and 0.4% in p . The fact that these differences are not too large indicates that the accuracy of the traditional method is acceptable. However, because the pulse integration method eliminates human subjectiveness, it decreases the scatter in the results.

To improve the accuracy even further, Eq. 5.2 was again fitted to the newly obtained data, after which the pulse integration method was reapplied to update nucleation rates, temperatures and pressures. This procedure was repeated several times until the fitting parameters changed by less than 0.2%.

The result was

$$\begin{aligned} a_0 &= -1.9, & a_1 &= 0.2737 \text{ K}^{-1}, \\ b_0 &= 901.7, & b_1 &= -2.878 \text{ K}^{-1}. \end{aligned} \tag{5.3}$$

The fitted model is valid for temperatures between 200 and 240 K and nucleation rates in the range 3×10^{13} to $1 \times 10^{17} \text{ m}^{-3} \text{ s}^{-1}$. For temperatures lower than about 224 K, the validity range is smaller, namely 5×10^{14} to $1 \times 10^{17} \text{ m}^{-3} \text{ s}^{-1}$. The fit function J_{fit} reproduces all but five of our 2003 nucleation rates within a factor of two, which is an acceptable error when the uncertainties of the experimental rates, temperatures and supersaturations are taken into account. Of the remaining five experiments, three have rates that differ from the fitted rate by a factor of five to six, and can be considered as outliers. Refitting the function to the data without the outliers did not change the fit significantly, so the original fit was retained.

Finally, to examine the sensitivity of the integration method on the specific model used, all experiments were reanalysed using the classical nucleation rate (Eq. 2.75) as the model instead of Eq. 5.2. Although the predictions of classical theory differ by several orders of magnitude from J_{fit} , the resulting J_{exp} changes only a few percent. It is therefore concluded that the integration method is relatively insensitive to the rate model and the resulting nucleation rates are reliable.

5.3 Nucleation rate results

In Figure 5.2, the nucleation rates of the three isotherms in our 2004 series and those of Wölk and Strey are plotted as functions of the supersaturation. For comparison, the fit of the 2003 rates has been evaluated at the mean temperatures of our 2004 isotherms and three isotherms of Wölk and Strey that are in our temperature range. The fit agrees well with those Wölk and Strey isotherms, both in value and in slope, and provides a plausible extension of their nucleation rates to lower temperatures and higher supersaturations.

The nucleation rates of our 203 K isotherm of the 2004 series systematically deviate about one order of magnitude from the 2003 rates, as can be seen in Figure 5.2. The data at 209 K are also somewhat lower than the 2003 fit. Possibly, the 2004 results were influenced by a change in measurement position – in 2004, the distance between the laser beam and the end wall was increased from 5 to 25 mm (see Figure 4.3 on p. 121). The reason to investigate the effect of different end wall distances was the possible influence of thermal boundary layers, which are formed as a consequence of the temperature difference between the cold expanded gas and the tube walls.

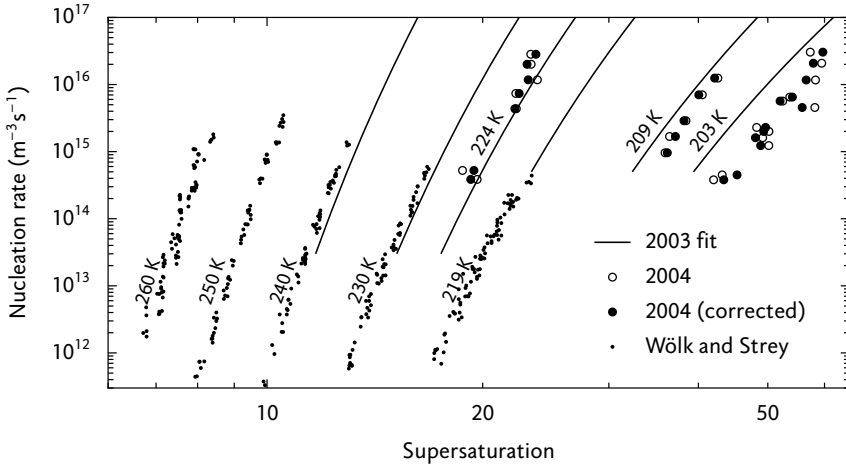


Figure 5.2: Nucleation rates as a function of the supersaturation. The open circles show the original 2004 results; the filled circles are the results after the supersaturation is corrected for temperature deviations, as in Eq. 5.4, which decreases the scatter. The isotherms of Wölk and Strey are also shown. The solid curves are isotherms of the 2003 fit of Eq. 5.2 calculated at the mean temperatures of the 2004 isotherms and the Wölk and Strey isotherms.

However, according to numerical simulations by Luo et al.,²²⁰ this change should not influence the nucleation conditions. Even at a distance as close as 5 mm from the wall, the thermal boundary layer has a significant influence only after 7 ms after the end of the nucleation pulse. The issue is therefore still unresolved.

Correction for scatter

The points of the 2004 isotherms, indicated by open circles, show the scatter that is partially caused by deviations of the nucleation temperature. It is possible to correct for the scatter in temperatures in a model-independent way, as follows. For each experiment, we estimate the supersaturation S_{corr} that is obtained when the temperature is made equal to the mean isotherm temperature \bar{T} , while keeping the nucleation rate constant. In a first-order approximation, S_{corr} is then

$$S_{\text{corr}} = S + \left(\frac{\partial S}{\partial T} \right)_J (\bar{T} - T). \quad (5.4)$$

To use this expression, the derivative $(\partial S / \partial T)_J$ is required. Looijmans et al.⁴ and Luijten et al.,⁶ who also used Eq. 5.4, calculated it from CNT. Instead, to analyse our results in a more theory-independent way, we derived it from our experimental data, as follows. First, Eq. 5.2 was solved for S to obtain S as a function of J and T ; then, partial differentiation with respect to T gave

the required derivative. The corrected results, indicated by the filled circles in Figure 5.2, indeed show that the correction succeeds in reducing the scatter.

Comparison with classical nucleation theory

Let us now compare the experimental nucleation rates with the classical nucleation theory predictions of Eq. 2.75. This is conveniently done by plotting the ratio of the experimental rates and the CNT rates as a function of temperature, as in Figure 5.3a. Only at 260 K, there is agreement between experiment and theory; at lower temperatures, the deviation increases – at 200 K, the experimental rates are a factor 10^4 to 10^6 higher than predicted. This deviation, which is caused by the incorrect temperature dependence of the CNT nucleation rate, is well known and observed in almost all water nucleation experiments²¹⁷ and also in the nucleation of other substances such as nonane²²¹ and the *n*-alcohols.²²²

Apart from the incorrect temperature dependence, the vertical scatter of the scaled rates is higher than expected, exceeding an order of magnitude for

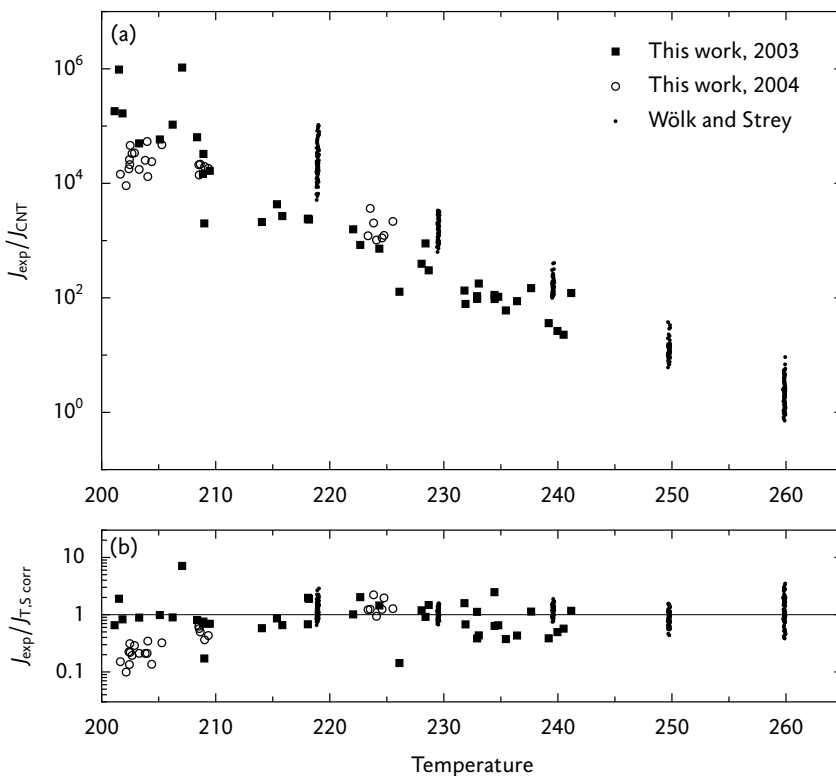


Figure 5.3: Ratio of the experimental and theoretical nucleation rates as a function of the temperature. (a) Ratio to classical nucleation theory, Eq. 2.75; (b) Ratio to temperature- and supersaturation-corrected theory, Eq. 5.8.

several Wölk and Strey isotherms. The Wölk and Strey scaled rates also show a systematic positive deviation from our 2003 rates, at equal temperature. This seems to contradict the agreement found earlier in Figure 5.2, but the difference is actually caused by the incorrect supersaturation dependence of the CNT nucleation rate, as will be shown in section 5.4.

As the temperature dependence of the experimental rates is smooth, we assume that down to 200 K water condenses as supercooled liquid drops, which remain liquid during our measurement time (15 ms). Supercooled water does not normally exist below 233 K, because a liquid sample that is cooled down will inevitably freeze at that temperature, due to homogeneous ice nucleation.²²³ Since conventional measurements on supercooled water are thus impossible below 233 K, its properties there can only be estimated by extrapolations of higher-temperature data (see appendix A). Therefore, the theoretical predictions of the nucleation rate below 233 K are more uncertain than those above that temperature.

5.4 Empirical correction of classical theory

The classical nucleation rate expression predicts an incorrect temperature dependence, as illustrated in Figure 5.3. On theoretical and experimental grounds, Wölk et al.²¹⁷ suggested that the discrepancy could be described by

$$\ln\left(\frac{J_{\text{exp}}}{J_{\text{CNT}}}\right) = A_1 + \frac{B_1}{T}, \quad (5.5)$$

where A_1 and B_1 are constants. An appropriate empirical correction of the theoretical rate is then

$$J_{\text{corr}}^T = \exp(A_1 + B_1/T) \times J_{\text{CNT}}. \quad (5.6)$$

Wölk et al. determined the constants A_1 and B_1 from their water nucleation rate measurements. They then compared the predictions of Eq. 5.6 to a large amount of data by other experimenters, and found that their new expression worked well in a large temperature range.

Because of several differences, the A_1 and B_1 values from Wölk et al. cannot be adopted. First, in this work, the $1/S$ correction in the nucleation rate expression is used, whereas Wölk et al. did not; second, different correlations are used for water's density, vapour pressure, and surface tension. It was found that the density correlation from this work resulted in a temperature dependence of $\ln(J_{\text{exp}}/J_{\text{CNT}})$ that could not be reproduced by a simple function as in Eq. 5.5; even a cubic function of T was insufficient. Therefore, for

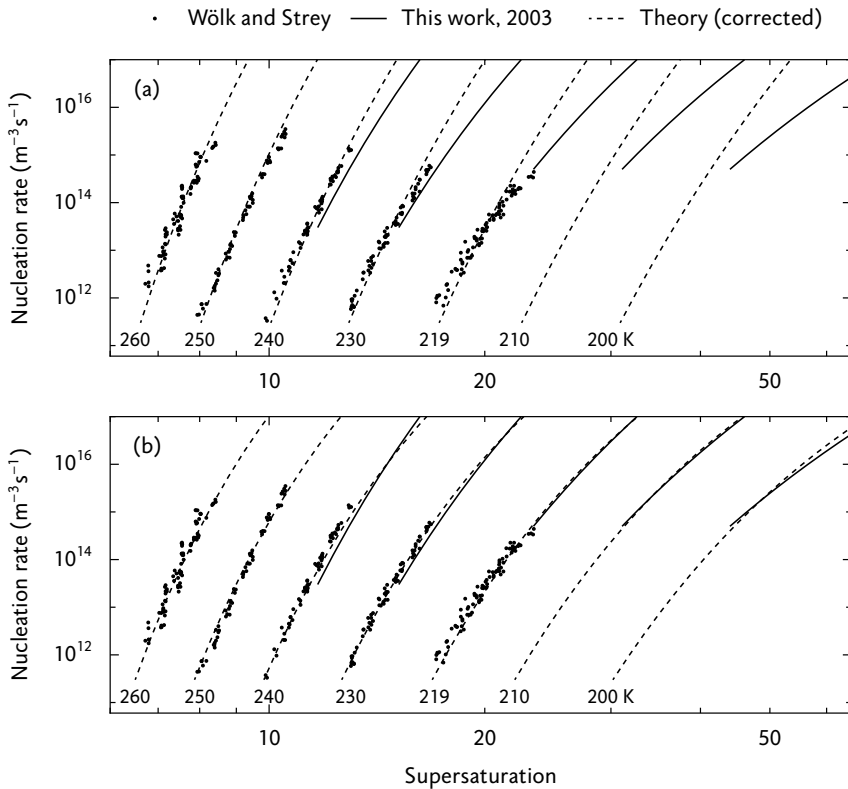


Figure 5.4: Comparison of experimental nucleation rates and empirically-corrected classical theory. (a) Temperature-corrected theory (Eq. 5.6); (b) Temperature- and supersaturation-corrected theory (Eq. 5.8).

the corrections in this section, the Wölk density correlation is used. When the J_{corr}^T function is fitted to the [Wölk and Strey](#) data, the result is

$$A_1 = -50.0 \pm 0.5 \quad \text{and} \quad B_1 = (1.32 \pm 0.01) \times 10^4 \text{ K}. \quad (5.7)$$

However, when the corrected rates are compared to our results in the J - S plot of Figure 5.4a, it is seen that the slopes do not agree. That is, the supersaturation dependence of the theory is incorrect. This is an important observation. In nucleation literature, it has always been assumed that the supersaturation dependence of the rate is well predicted by classical theory.¹⁹ A temperature-dependent correction is then sufficient. However, it is seen in Figure 5.4 that for high nucleation rates and low temperatures, the slope of the theoretical lines differs significantly from the experiments. Therefore, to obtain an accurate empirical correction, a supersaturation-dependent correction must be included. The following expression was found to be adequate:

$$J_{\text{corr}}^{T,S} = \exp(A_2 + B_2/T + C_2 \ln S) \times J_{\text{CNT}}, \quad (5.8)$$

where A_2 , B_2 and C_2 are constants. The $J_{\text{corr}}^{T,S}$ function was fitted to the [Wölk and Strey](#) data and the 2003 data from this work, which resulted in

$$A_2 = -68 \pm 2, \quad B_2 = (2.11 \pm 0.06) \times 10^4 \text{ K}, \quad \text{and } C_2 = -6.0 \pm 0.3. \quad (5.9)$$

The resulting nucleation rates are displayed in [Figure 5.4b](#). In addition, the ratio of the experimental rates to $J_{\text{corr}}^{T,S}$ is shown in [Figure 5.3b](#).

5.5 Critical cluster sizes

To determine the critical size with the nucleation theorem of [Eq. 2.101](#), the slope of the isotherms must be determined. In most cases the isotherms are slightly curved, but when a straight line is fitted to the isotherm, the slope of the line is found to be a good approximation of the slope at the centre of the isotherm. In the case of isotherms that have much scatter or consist of a small number of points, another consideration should be made. The scaled error in $\ln S$ (the error in $\ln S$ times the slope of the line) is higher than the error in $\ln J$, so we fitted the lines by applying the least squares method in the $\ln S$ direction. That is, in the $\ln J$ - $\ln S$ plot of [Figure 5.2](#), we minimized the sum of squared *horizontal* residuals. In the case of the isotherms of [Wölk and Strey](#) that have little scatter it is not necessary to specify the direction of minimization, because it has only a small (2%) influence on the slope. (Only for the 260 K isotherm, which has more scatter, the difference is 9%.)

For comparison with theory we want to assign a single theoretical n^* value to the isotherm, which is not straightforward since n_{cl}^* varies along the isotherm. One could evaluate n_{cl}^* at each isotherm point and then take the mean, as [Wölk and Strey](#) did, but we will specify a single reference temperature and supersaturation at which n_{cl}^* is evaluated. It is reasonable to take as a reference supersaturation value the mean of $\ln S$ of the points, because the lines are fitted in a plot with $\ln S$ as abscissa, and fitting a straight line to a curved isotherm gives the slope in the centre of this isotherm. As a reference temperature we will take the mean of the temperatures of the isotherm points.

The empirical fit of the 2003 data of [Eq. 5.2](#) also allows us to obtain an estimate of the critical cluster size. In particular, from [Eqs. 2.101](#) and [5.2](#) we derive that

$$n_{\text{fit}}^* = \left(\frac{\partial \ln J_{\text{fit}}}{\partial \ln S} \right)_T - 1 = \frac{2(b_0 + b_1 T)}{(\ln S)^3}. \quad (5.10)$$

Using the experimental temperature and supersaturation values, an n_{fit}^* value can be calculated for each experiment of the 2003 series.

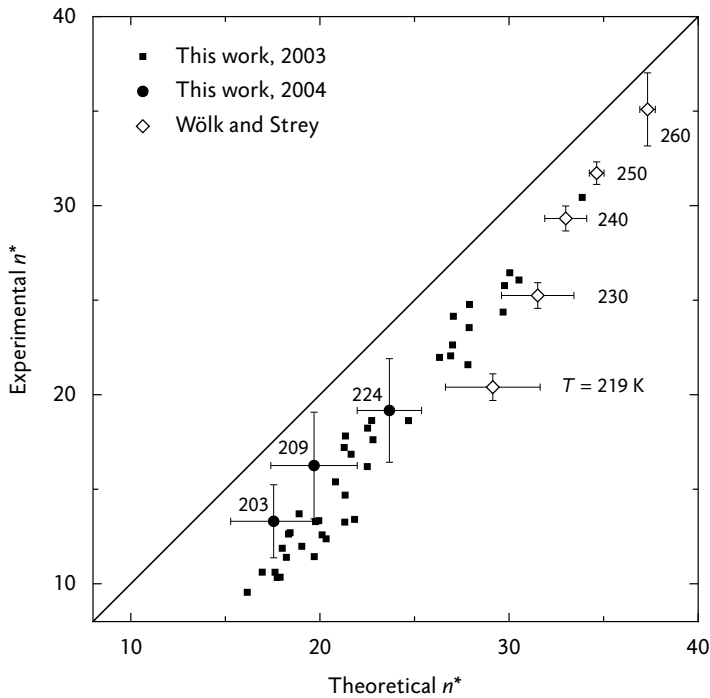


Figure 5.5: Experimental critical size found with the nucleation theorem of Eq. 2.101 as a function of the theoretical critical size of Eq. 2.21. All experimental points lie below the line of slope unity that indicates perfect agreement. The vertical error bars indicate the 90% confidence intervals representing the uncertainty of fitting in the $\ln J$ – $\ln S$ plot. The horizontal error bars indicate the effect of possible systematic errors in the physical properties; these errors increase with decreasing temperature.

In Figure 5.5, the experimental critical sizes n_{exp}^* , obtained with the nucleation theorem, are plotted as a function of the theoretical critical sizes n_{cl}^* from Eq. 2.21. In all cases the experimental value lies below the CNT prediction. The vertical error bars shown are 90% confidence intervals. Our n_{exp}^* values have larger vertical error bars than Wölk and Strey's because our isotherms have more scatter and consist of fewer experimental points.

Contrary to our findings, Wölk and Strey¹⁹ concluded that their experimental critical sizes did agree with the n_{cl}^* predictions. There are three reasons for this difference. First, we fitted lines to the isotherms by minimizing horizontal – instead of vertical – residuals in the $\ln J$ – $\ln S$ plot. Second, Wölk and Strey used the nucleation theorem in the form $n^* = (\partial \ln J / \partial \ln S)$, ignoring the supersaturation dependence of the prefactor K from the nucleation rate expression (Eq. 2.96). Our expression has $(\partial \ln J / \partial \ln S) - 1$ at the right-hand side, so that we find n_{exp}^* values that are 1 lower than theirs. The largest difference is caused by our model for the surface tension, which gives up to

4.5% higher values than the Wölk and Strey fit (see Figure 1.24 on page 50). As a result, our n_{cl}^* values are higher than those found by Wölk and Strey.

5.6 Hale's scaled model

Hale²²⁴ noted that experimental supersaturations can be scaled in a model-independent way, such that data sets from different temperatures collapse into one line in a J - S plot. The scaled supersaturation S_{sc} is computed from

$$\ln[S_{sc}(T)] = \left[\frac{(T_c/T_{ref}) - 1}{(T_c/T) - 1} \right]^{3/2} \ln S, \quad (5.11)$$

where T_c is the critical temperature of the vapour and T_{ref} is a reference temperature that can be freely chosen. In Figure 5.6, the scaling has been applied to the 2003 dataset and the measurements of Wölk and Strey. As also observed by Hale, all five isotherms of Wölk and Strey collapse into one line. This line is extended by the 2003 dataset from this work, which agrees with the Wölk and Strey data in the range of overlap. The dependence of the nucleation rate on the scaled supersaturation is also well reproduced by the temperature- and supersaturation-corrected theory of Eq. 5.8, which is plotted as a line.

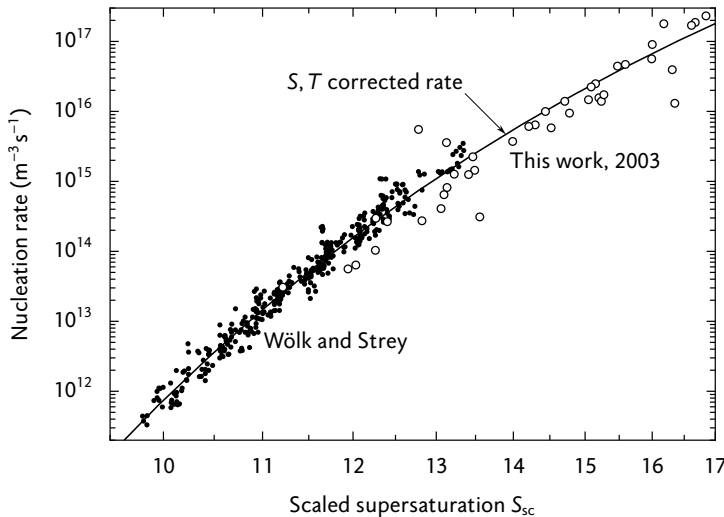


Figure 5.6: Application of Hale's scaled nucleation model. Nucleation rates of this work and Wölk and Strey¹⁹ as a function of the scaled supersaturation S_{sc} from Eq. 5.11 with $T_{ref} = 240$ K. The line is the temperature- and supersaturation-corrected theory from Eq. 5.8.

5.7 Conclusion

Homogeneous nucleation rate measurements of water in helium in the range 200–240 K have been presented. In the temperature range where a comparison with the Wölk and Strey results is possible (220–240 K) a good agreement of nucleation rates is found, and the supersaturation dependence also agrees. The supersaturation dependence of both our rates and those of Wölk and Strey is lower than classical theory predicts, which means that the number of molecules in a critical cluster is also smaller than the CNT value. The difference in supersaturation dependence is most pronounced at low temperature and high supersaturation. It must be realized, though, that the predictions of classical theory below 233 K are affected by the uncertain properties of supercooled water.

Because of the discrepancy in the supersaturation dependence, scaling the classical nucleation theory with a temperature-dependent factor is insufficient to correct it. On the other hand, a scaling with a temperature- and supersaturation-dependent factor does result in an accurate empirical correction of the classical theory. The current empirical formula of Wölk et al.²¹⁷ contains only a temperature-dependent correction factor; future empirical correlations should include a supersaturation correction for better accuracy.

Water nucleation in methane and carbon dioxide

6

In contrast to the nucleation in helium, non-idealities play a significant role in the high-pressure nucleation of water in methane and carbon dioxide. The experimental results in this chapter will be analysed with the equation of state that has been obtained in chapter 1.

6.1 Nucleation rates

Figure 6.1 shows nucleation rates as a function of the supersaturation in the nucleation pulse. The supersaturation has been computed using Eq. 1.29 or Eq. 1.31, taking into account the effect of methane and carbon dioxide on the equilibrium vapour fraction and surface tension of water. All data was obtained at approximately 235 K and 10 bar, with standard deviations of ± 0.7 K and ± 0.1 bar. Experiments were performed in pure methane and in mixtures of methane and carbon dioxide, with carbon dioxide molar fractions of 3%

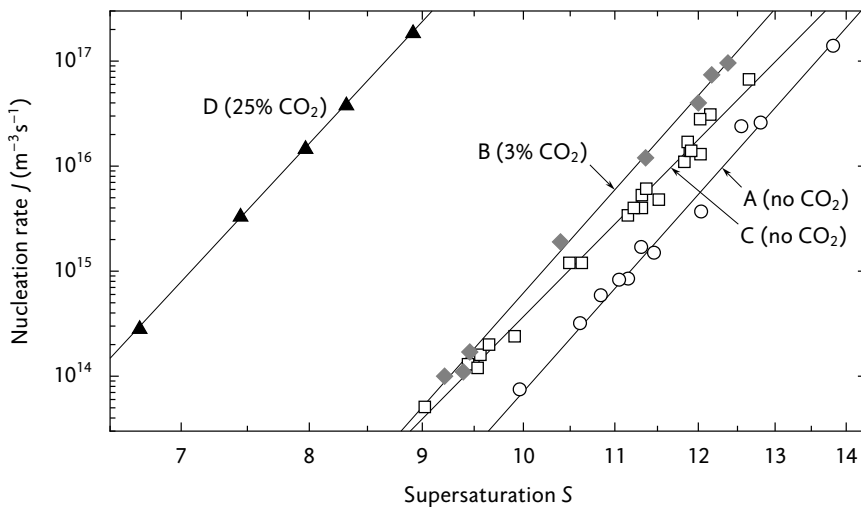


Figure 6.1: Nucleation rate of water in methane and carbon dioxide at 10 bar and 235 K, as a function of the supersaturation.

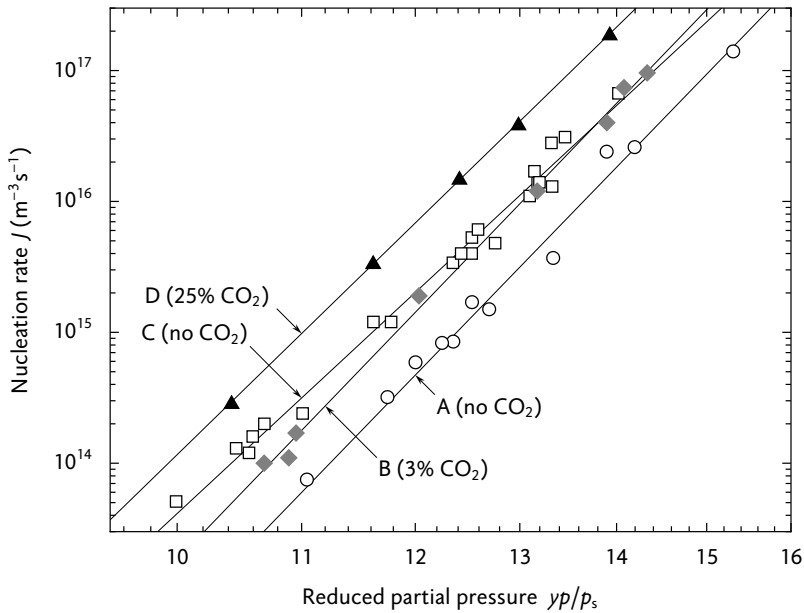


Figure 6.2: Nucleation rate of water in methane and carbon dioxide at 10 bar and 235 K, as a function of the reduced partial pressure of water.

and 25%. The set without carbon dioxide was repeated, which gave a different result. Consequently, four distinct measurement sets can be distinguished in Figure 6.1; these sets are labelled A to D.

At first glance, the effect of 3% carbon dioxide is unclear because of the discrepancy between the two series without carbon dioxide. A full discussion of this discrepancy is postponed to section 6.4; here it is important to know that series B was performed immediately after series A. To assess the effect of 3% carbon dioxide, therefore, series A and B should be compared. It is observed that 3% carbon dioxide results in an increase of the nucleation rate by a factor of about ten, at equal supersaturation.

The influence of 25% carbon dioxide on the nucleation rate is quite large. To evaluate the effect, series C and D should be compared because these were performed consecutively. Because of the large gap between these series, the only supersaturation common to both is $S \approx 9$. At that supersaturation, the 25% carbon dioxide increases the nucleation rate by about four orders of magnitude.

In Figure 6.2, the nucleation rate is plotted versus the reduced partial pressure, which is the ratio of the partial pressure of water and the saturated vapour pressure. The reduced partial pressure is equal to the supersaturation if the enhancement factor were not taken into account. In Figure 6.2, the effect of carbon dioxide appears smaller than in Figure 6.1.

Like the water–helium data, the results were corrected for small deviations of the temperature, assuming that CNT predicts the correct changes in nucleation rate for small changes in temperature and supersaturation. For each experiment, we estimate the supersaturation S_{corr} that is obtained when the temperature is made equal to the mean isotherm temperature \bar{T} , while keeping the nucleation rate constant. Then, in a first-order approximation, $S_{\text{corr}} - S = (\bar{T} - T)(\partial S/\partial T)_J$, with S and T the actual supersaturation and temperature. As in Luijten's work,¹¹³ the derivative $(\partial S/\partial T)_J$ was evaluated from the classical nucleation rate expression, Eq. 2.75, ignoring the temperature and supersaturation dependence of the prefactor. Luijten did not include the temperature dependence of the liquid density $\rho(T)$; here it is taken into account. The correlation that has been used for the density is described in appendix A.2. The corrected supersaturation becomes

$$S_{\text{corr}} = S + (\bar{T} - T) \frac{S \ln S}{2} \left[\frac{3\sigma'(T)}{\sigma(T)} - \frac{2\rho'(T)}{\rho(T)} - \frac{3}{T} \right], \quad (6.1)$$

where the prime denotes differentiation with respect to T , and σ is the surface tension of water. Deviations in the nucleation pressure can also be taken into account, using the pressure dependence of the surface tension, as done by Labetski.¹⁰ For our experiments, the correction for pressure deviations is much smaller than the temperature correction, so it was not applied.

6.2 Critical cluster composition

The number of water molecules in the critical cluster, n_w^* , can be obtained from experimental J - S data using the nucleation theorem of Eq. 2.101,

$$n_w^* = \left(\frac{\partial \ln J}{\partial \ln S} \right) - 1. \quad (6.2)$$

As can be seen in the double-logarithmic plot of Figure 6.1, all four experimental series have nearly the same slope, so the critical cluster size is also similar. Indeed, application of Eq. 6.2 yields sizes of about 22 molecules; see Table 6.1. Only the second series without carbon dioxide has a slightly lower slope. Equation 2.21 gives a theoretical prediction of the critical cluster size. A comparison of the theoretical and experimental values (Table 6.1) shows that Eq. 2.21 overpredicts the critical size by 10 to 18 molecules.

The amount of carrier gas molecules in the critical cluster n_g^* can be obtained with the pressure version of the nucleation theorem, derived in section 2.9. The Luijten et al.⁶ or S form (Eq. 2.108) applied to the water–methane

Table 6.1: Summary of nucleation results

| y_c | \bar{T} (K) | \bar{p} (bar) | \bar{S} | $n_w^*(\text{exp})$ | $n_w^*(\text{theo})$ | σ (mN/m) | f_e |
|-------|---------------|-----------------|-----------|---------------------|----------------------|-----------------|-------|
| 0 | 235.0 | 10.09 | 11.77 | 22 ± 2 | 32 ± 3 | 80.00 | 1.11 |
| 0 | 235.5 | 10.11 | 10.91 | 20 ± 1 | 34 ± 4 | 79.92 | 1.11 |
| 0.03 | 235.4 | 10.07 | 10.70 | 22 ± 1 | 34 ± 4 | 78.92 | 1.16 |
| 0.25 | 235.5 | 10.12 | 7.80 | 22 ± 1 | 40 ± 9 | 72.35 | 1.56 |

The uncertainty of the experimental n_w^* is the 90% confidence interval; the uncertainty of the theoretical n_w^* is a standard deviation, taking into account the uncertainties of the surface tension σ and the enhancement factor f_e . The average of S is calculated from the mean of $\ln S$, that is, $\bar{S} \equiv e^{(\ln S)}$.

system reads

$$\left(\frac{\partial \ln J}{\partial \ln p} \right)_{S,T} = \left(\frac{pv_w^l}{kT} - x_m^{\text{eq}} \right) n_w^* + Z_m \Delta n_m^* + 2 \ln f_e, \quad (6.3)$$

where v_w^l is the molecular volume of liquid water, x_m^{eq} is the equilibrium molar fraction of dissolved methane in the liquid, Z_m is the compressibility factor of methane, and f_e is the enhancement factor in equilibrium. Furthermore, Δn_m^* is the excess number of methane molecules; that is, the number of methane molecules in the cluster minus the number of methane molecules in one critical cluster volume in the gas phase.

The Kalikmanov and Labetski¹¹ form or y form (Eq. 2.114) is given by

$$\left(\frac{\partial \ln y}{\partial \ln p} \right)_{J,T} = - \frac{1}{n_w^* + 1} \left(\frac{p\bar{V}_w^{\text{gas}}}{RT} \Delta n_w^* + Z_m \Delta n_m^* + \ln f_e + 1 \right), \quad (6.4)$$

where \bar{V}_w^{gas} is the partial molar volume of water vapour in the gas phase.

To apply Eq. 6.3 or Eq. 6.4, measurements of the nucleation rate at different pressures are required. In Figure 6.3, a collection of water nucleation rates at 235 K and several pressures is presented. Peeters et al.⁸ obtained nucleation rates at 10 bar – as in this work – and at 25 bar. At lower pressures, our 1 bar water–helium data is shown, as well as the water–argon measurements of Wölk and Strey¹⁹ at about 0.6 bar. Of course, the pressure nucleation theorem is intended to be used for measurements with the same carrier gas, but at low total pressures (1 bar or less) the effect of the carrier gas is expected to be small. For the following analysis, the data with helium or argon will therefore be treated as measurements in methane at 1 bar.

For the data of Peeters et al., the supersaturation has been corrected for temperature deviations in the same way as described before (Eq. 6.1). The enhancement factor from the CPA model from this work was used to calculate

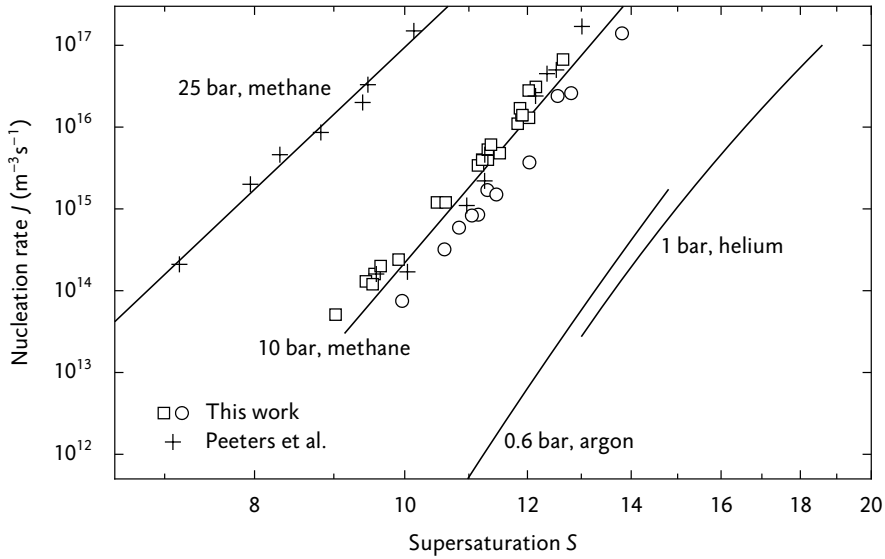


Figure 6.3: Effect of carrier gas pressure on the nucleation rate of water at 235 K. For water in methane, the two measurement series at 10.1 bar from this work are shown, as well as the data of Peeters et al.⁸ at 10 bar and 25 bar. For low carrier gas pressures, fits to the data from this work and Wölk and Strey¹⁹ are given.

S , whereas Peeters et al. used their own model. Consequently, the supersaturations differ somewhat (at most 2%) from those obtained by Peeters et al.

To determine the methane content of the critical cluster with the S form of the pressure nucleation theorem at 10 bar, the nucleation rate at a supersaturation of $S = 11.25$ was taken, for all three available pressures. The value of $S = 11.25$ corresponds to the middle of the 10 bar data. In Figure 6.4a, the resulting nucleation rates are plotted as a function of the methane pressure. A quadratic interpolation through the points was used to obtain the derivative $(\partial \ln J / \partial \ln p)_{S,T} = 5 \pm 1$ at $S = 11.25$, which was substituted in Eq. 6.3. The remaining quantities x_g^{eq} and f_e were computed with the CPA EOS. Finally, the excess number of methane molecules in the critical cluster was found to be $\Delta n_m^* = 5 \pm 1$.

To apply the y form (Eq. 6.4), supersaturations were taken at a nucleation rate of $3 \times 10^{15} \text{ m}^{-3} \text{ s}^{-1}$, which lies in the middle of our measurement range. The supersaturation values were then converted to vapour fractions with the help of Eq. 1.29, that is, $y = S f_e p_s / p$. For the argon and helium data, an enhancement factor of $f_e = 1$ was taken. The vapour fractions were plotted versus the pressure (Figure 6.4b), and a quadratic interpolation was employed again to find the derivative $(\partial \ln y / \partial \ln p)_{J,T} = -1.1 \pm 0.1$. The partial molar volume of water vapour in methane was calculated using the GERG EOS^{61,62} and the relation $\bar{V} = V + (\partial V / \partial y)_{T,p}$, with \bar{V} the partial molar volume and

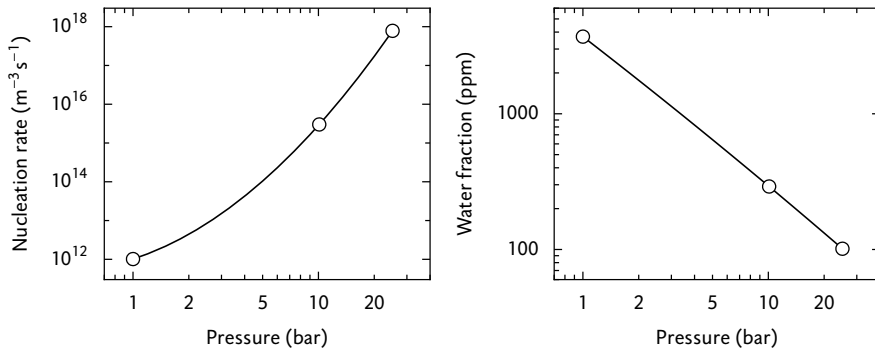


Figure 6.4: Effect of carrier gas pressure on water nucleation at 235 K. *Left:* Nucleation rate as a function of methane pressure, for a constant supersaturation of 11.25. *Right:* Water vapour fraction as a function of methane pressure, for a constant nucleation rate of $3 \times 10^{15} \text{ m}^{-3} \text{ s}^{-1}$.

V the molar volume, valid for $y \ll 1$. Finally, the excess number of methane molecules in the critical cluster was found to be $\Delta n_m^* = 6 \pm 2$, which agrees with the result obtained by the S form, Eq. 6.3.

The actual number of methane molecules in the cluster is the sum of the excess number of methane molecules and the number of methane molecules in the gas phase that occupy a cluster volume. For our conditions (10 bar and 235 K) the actual number is about 0.3 molecules higher than the excess number. Taking into account the uncertainties of ± 1 and ± 2 in the results for the excess number, the absolute number of methane molecules can be taken equal to the excess number. This means that at the mentioned conditions and a supersaturation of about 11, the critical cluster consists of approximately 22 water molecules and 5 methane molecules. Accordingly, the liquid fraction of methane is about 0.2, whereas the equilibrium methane fraction is 2×10^{-3} , a hundred times smaller (see Figure 1.12 on page 37).

6.3 Comparison with theory

In chapter 1, the effect of methane and carbon dioxide on the enhancement factor and surface tension of water has been quantified. To calculate the theoretical influence on the nucleation rate, the classical nucleation rate expression of Eq. 2.75 was evaluated at the experimental nucleation conditions, with the surface tension and enhancement factor values from chapter 1. In Figure 6.5, the experimental results are compared with the theoretical nucleation rates. There is a large discrepancy, of about four orders of magnitude, between the nucleation rates experiments and theory. On the other hand, the shift in supersaturation resulting from the carbon dioxide addition is pre-

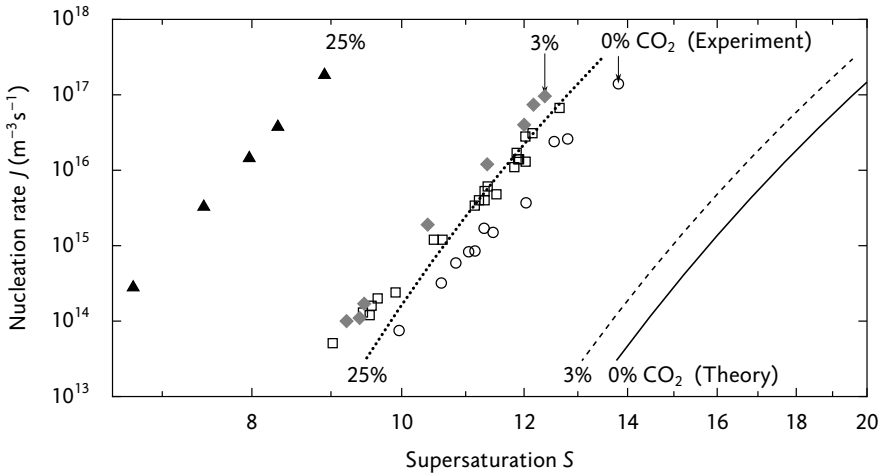


Figure 6.5: Comparison of experiment and theory: nucleation rates of water in methane and carbon dioxide at 10 bar and 235 K. The points are the supersaturation-corrected measurements, the lines represent the theoretical nucleation rate from Eq. 2.75.

dicted fairly well.

For illustrative purposes, it is possible to adjust the theoretical rate to match the experiments. For example, the corrected rate

$$J_{\text{CNT}}^{\text{corr}}(T, S) = 100 \times J_{\text{CNT}}(T, S + 2), \quad (6.5)$$

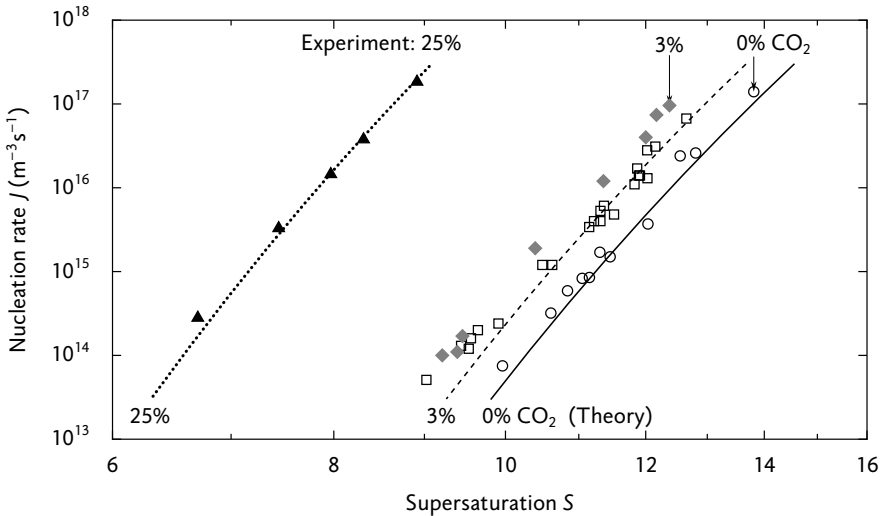


Figure 6.6: The classical nucleation theory values have been corrected to agree with the experimental data (Eq. 6.5). The points are the measurements, the lines represent the corrected theoretical nucleation rate.

with J_{CNT} the original classical nucleation rate, agrees fairly well with the experimental rates (Figure 6.6).

For the water–methane system, Peeters⁶⁹ also calculated the theoretical nucleation rate from Eq. 2.75, but obtained rates of about three orders of magnitude higher than the rates from this work. This discrepancy is caused by Peeters’s surface tension model,⁸ which yields a 7% lower surface tension at 235 K and 10 bar. The shift brings Peeters’s theoretical rates closer to the experiments, but that does not imply that his surface tension model is more plausible than the current model. In fact, the relatively low value of the Peeters surface tension is the result of a singularity at 227 K, where the surface tension goes to minus infinity.

6.4 Possible sources of error

The two series of experiments without carbon dioxide clearly disagree. To identify possible causes of the discrepancy, this section provides a chronological overview of the experimental sequence. Individual experiments will be indicated by their number, which is shown in Figure 6.7. After that, it is discussed whether inaccuracies in measurements can explain the deviation.

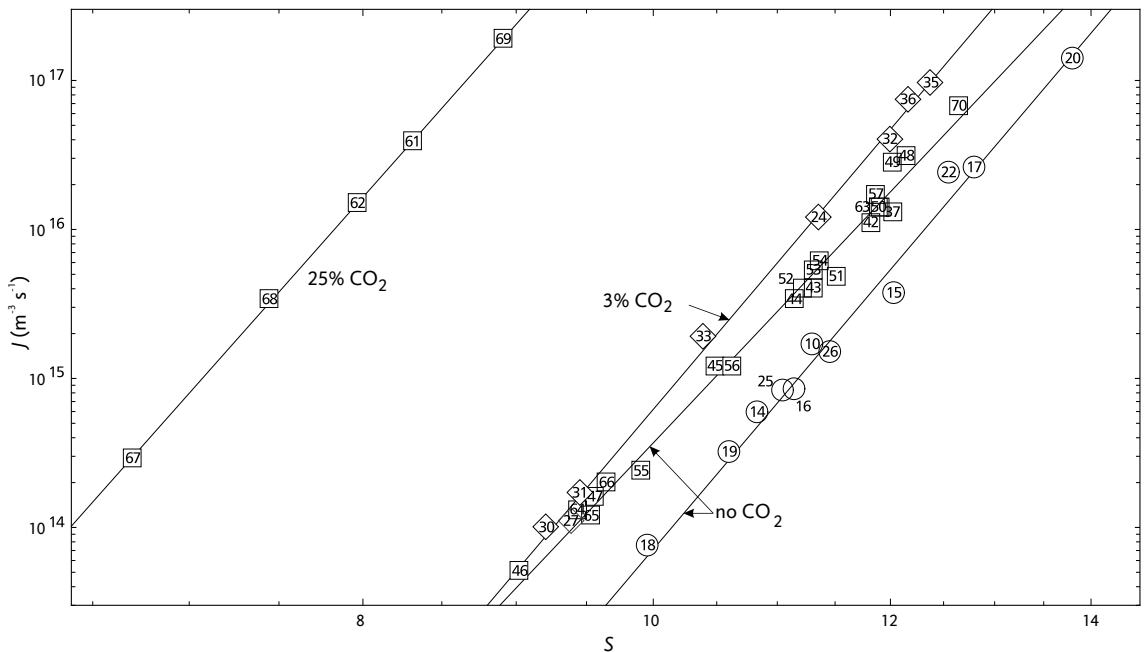


Figure 6.7: Order in which the experiments were performed. Each data point is labelled with the identification number of that experiment. Note that not all numbers occur because some experiments failed.

The first series, without carbon dioxide, consists of experiments 10 to 20. During this series, the water content of the gas mixture was measured with the Karl Fischer coulometer. Results from these measurements are shown in Figure 1.10 on page 32.

After the series without carbon dioxide, the mixture preparation device (MPD) was moved for calibration of the mass flow controller for the carbon dioxide–methane mixture. Following the return of the MPD, an experiment without carbon dioxide was repeated (22) to confirm the setup could still reproduce earlier results; that was the case. Then, the first experiment with 3% CO₂ was done (24), after which two experiments (25 and 26) without CO₂ were done as checks. When these proved to agree, the rest of the 3% CO₂ series was performed (27–35). The setup was then unused for some time during the summer holidays.

After this break, an experiment with 3% CO₂ was repeated (36); the result agreed with earlier experiments. Subsequently, the MPD was moved again to the calibration room, to prepare for the 25% CO₂ measurements. One MFC was calibrated for the first time with pure CO₂. In addition, a lower pressure upstream of the mass flow controllers (MFCs) was chosen, which necessitated a recalibration of the other MFCs. The MPD was returned, and an experiment without CO₂ was performed (37) to check the reproducibility. This experiment deviated more from the other experiments than expected; the nucleation rate was too high, or the supersaturation was too low. Therefore, the calibration of the pressure transducers in the high-pressure section was checked; it was found to be consistent. A second experiment (42) without CO₂ again deviated from the older measurements. It was suspected that the modified MFC upstream pressure had influenced the results, so experiments (43–46) with the original high MFC pressure were performed; this did not change the deviation. Next, a series of tests of the mixture composition were done. The vapour fraction was measured again with the Karl Fischer coulometer. The vapour fraction was found to be about 2% lower than during the first series. This difference could not explain the discrepancy; on the contrary, a 7% *higher* vapour fraction is needed to explain the increased nucleation rates.

To exclude the possibility of liquid water in the MPD outside the saturators, the MPD was evacuated with the saturators disconnected, and the pipes exiting the saturators were heated. The experiments that followed, 50 and 51, deviated less, so it was believed that this procedure had solved part of the problem. The next experiments, however, deviated more.

Finally, the measurement of the HPS temperature was checked, by exchanging the sensor. Furthermore, the temperature distribution in the HPS could be monitored after installing three additional thermocouples at different positions. Temperature differences existed across the HPS, but they were

not large enough to explain deviations in the results.

Because the discrepancy of the new experiments could not be explained, the 25% CO₂ series was started (61 and 62). Several experiments without CO₂ were then performed (63-66), after which the three last 25% CO₂ experiments were done (67-69). A final measurement (70) without CO₂ concluded the experiments.

Because of the deviation, the absolute *J*, *S* positions of all series are somewhat uncertain. Expressed in nucleation rate, the uncertainty is a factor of four; expressed in supersaturation, it is seven percent. However, the relative shifts between several series are more accurate. In two cases, experiments of different series were alternated in a short time period (several days). This was done between the first series without CO₂ and the series with 3% CO₂ (experiments 22-27). The offset between those series is therefore reliable. Experiments were also alternated between the second series without CO₂ and the series with 25% CO₂ (57-70).

Assuming that a single phenomenon or instrument error is responsible for the deviation of the second series, we can calculate how large the error should be, and if it can be excluded.

Vapour fraction

An increase of the vapour fraction by 7% for the second series would explain its deviations. Such an increase has been excluded by three independent checks. First, the Humicap humidity measurement in the HPS flushing loop shows that the vapour fraction is at most 1.5% higher. Second, the coulometer indicates that the vapour fraction is not higher at all, but 2% lower. Third, a plot of growth rates versus vapour fraction (Figure 6.8) shows no significant differences between the two series; because of the scatter, the maximum possible deviation is a 2% lower vapour fraction for the second series.

Pressure

An error of 0.4 bar in the initial HPS pressure is required to account for the difference. The calibration of the pressure transducer was checked several times during the first and second series; the output of this instrument was always consistent within 0.01 bar.

The pressure difference of about 15 bar between the initial state and the state after the expansion was measured by the piezoresistive transducer. An error of 0.2 bar, which corresponds to a relative error of 1.3% in the sensitivity, would explain the deviation. However, during the entire experimental programme, the sensitivity varied less than 0.08%.

Temperature

In the case of the initial temperature measurement, an error of 1 K is required to account for the deviation. The sensor was verified to be accurate to 0.01 K. In the measurement region near the end wall, temperature differences of at most 0.05 K were observed. Furthermore, the time between isolation of the HPS (that is, the end of the flushing process) and the start of the experiment (the breaking of the diaphragm) was varied between one and ten minutes, to study the possible thermal equalization between the gas mixture and the tube. No effect was found.

Nucleation rate

Nucleation rates are three to five times as high. It is unlikely that the measurement of the nucleation rate, or droplet number density, is incorrect. The calculation of the droplet density only depends on fixed parameters, like the extinction length and the refractive index of the droplets. During the experiment, only relative light intensities are important; the intensity measurement does not need to be calibrated.

If the measured nucleation rate is correct, the nucleation rate itself could have been influenced. For example, a polluting substance may have been present somewhere in the setup.

Summary

To summarize, the measured nucleation rate has changed significantly between the first and second series of water nucleation in methane. Expressed in supersaturation, the relative change is seven percent, and expressed in nucleation rate it is a factor of four. This change cannot be explained by errors or inaccuracies of instruments in the setup. There is more certainty about the effect of adding carbon dioxide because experiments with and without carbon dioxide were alternated, with consistent results. The addition of three percent carbon dioxide increased the nucleation rate by a factor of ten; twenty-five percent carbon dioxide increased the rate by four orders of magnitude.

6.5 Droplet growth rates

Besides nucleation rates, droplet growth rates are measured in our experiments. A useful quantity is the initial growth rate of the squared radius, dr^2/dt , which is approximately constant in time at the beginning of the observed growth. In the optical signal analysis, a three-parameter growth model was fitted to the experimental growth curve (Eq. 4.19, p. 136). The c parameter in that model is the initial growth rate of the squared radius, precisely the quantity of interest.

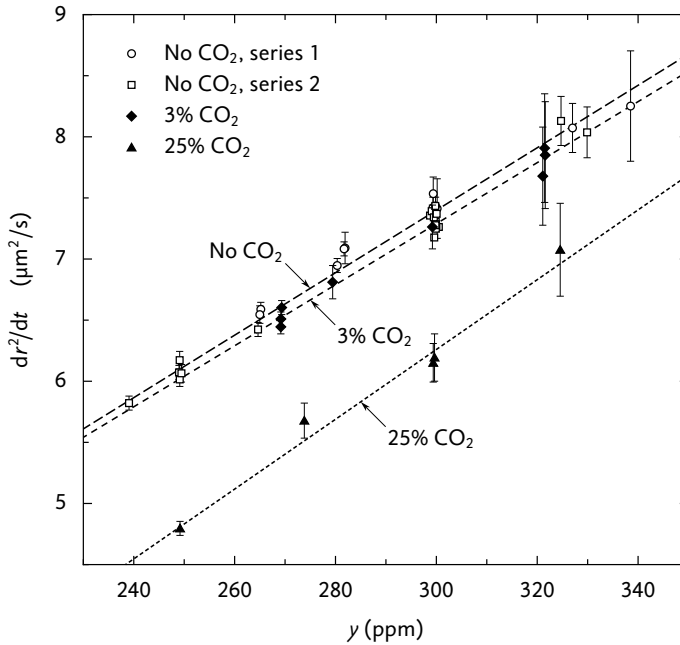


Figure 6.8: Initial growth rate of the squared droplet radius versus the initial water vapour fraction, at approximately 243 K and 11.5 bar, in methane and methane–carbon dioxide mixtures. The lines are least-squares fits which are *not* forced through the equilibrium vapour fraction y_{eq} at $dr^2/dt = 0$.

Before discussing the experimental growth rates, let us review the expected dependence on the vapour fraction. At the beginning of the droplet growth, depletion is negligible, and the growth rate of the squared radius is given by Eq. 2.139,

$$\frac{dr^2}{dt} = \frac{2\rho_g D}{x\rho_l} (y - y_{\text{eq}}), \quad (6.6)$$

where ρ_g and ρ_l are molar densities of the gas mixture and the liquid, respectively, D is the diffusion coefficient of water in the gas mixture, x is the water liquid fraction, y is the water vapour fraction, and y_{eq} is the equilibrium vapour fraction of water at the droplet growth conditions. According to Eq. 6.6, the growth rates of different experiments are a linear function of the water vapour fraction in the experiments, as long as the other quantities are held constant.

In Figure 6.8, the growth rates of individual experiments are plotted as a function of the vapour fraction y . As expected, a linear trend is observed for experiments with the same carbon dioxide fraction. The presence of 25% carbon dioxide clearly decreases the growth rate. It is more difficult to see

Table 6.2: Droplet growth conditions

| y_c | T (K) | p (bar) | D (mm ² /s) | | ρ_g (mol/m ³) | x_m (%) | x_c (%) | $\Delta\rho_l$ (%) | y_{eq} (ppm) |
|-------|---------|-----------|--------------------------|-----------|-----------------------------------|--------------|--------------|-----------------------|-------------------|
| | | | exp. | Fuller | | | | | |
| 0 | 243.3 | 11.53 | 1.37 ± 0.02 | 1.5 ± 0.2 | 594.0 | 0.15 | – | –0.2 | 49.7 |
| 0.03 | 242.9 | 11.41 | 1.37 ± 0.03 | 1.5 ± 0.2 | 589.4 | 0.15 | 0.17 | –0.3 | 50.2 |
| 0.25 | 241.7 | 11.23 | 1.14 ± 0.04 | 1.4 ± 0.2 | 589.4 | 0.13 | 1.41 | –1.4 | 58.6 |

Note: $\Delta\rho_l = (\rho_l/\rho_w) - 1$, with ρ_l the molar density of the liquid and ρ_w the molar density of pure water at the same temperature and pressure. The values x_m and x_c are the molar liquid fractions of methane and carbon dioxide, respectively.

that the growth rates of the experiments with 3% carbon dioxide are also slightly lower, since the effect is small compared to the scatter. A remarkable result is the agreement of the growth rates of the two series without carbon dioxide, series A and B. This agreement implies that the vapour fractions of both series are consistent, so the discrepancy in nucleation rates between the series cannot be due to an incorrect vapour fraction.

It is seen in Figure 6.8 that the uncertainty of the growth rate is larger for experiments with a higher water fraction. In those experiments, depletion is important, and the strong decrease of the growth rate in time results in a less accurate value for the initial growth rate. Conversely, most experiments with water fractions below 280 ppm have negligible depletion, so their growth curve can be analysed with the two-parameter model $r^2 = c(t - t_0)$, which leads to accurate values of the initial growth rate c .

While the measurements of the droplet growth rate in methane and carbon dioxide are new, growth rates in the methane–water system have been measured earlier by Peeters et al.²⁰⁰ Their measurements agree with the values from this work to within the experimental uncertainties.

From the experimental growth rates, the diffusion coefficients were determined in the manner described by Peeters et al.,²⁰⁰ which proceeds as follows. A straight line is fitted to measurements in Figure 6.8 with a constant carbon dioxide fraction. According to Eq. 6.6, the slope of the line is equal to $2\rho_g D/(x\rho_l)$, so D can be obtained when ρ_g , ρ_l and x are known or estimated. If the equilibrium water vapour fraction y_{eq} is also known, the accuracy of the fit can be improved by forcing the line through the y_{eq} on the horizontal axis, at which the growth rate is zero (Eq. 6.6). In our case, y_{eq} was computed with the CPA EOS. Other quantities from Eq. 6.6, listed in Table 6.2, were obtained as follows. The molar density of pure methane was taken from the NIST webbook⁷³ and the density of the methane–carbon dioxide mixture from the GERG EOS.⁶² The liquid fractions of methane, carbon dioxide and water were computed with the CPA EOS. The density of the liquid could not be taken di-

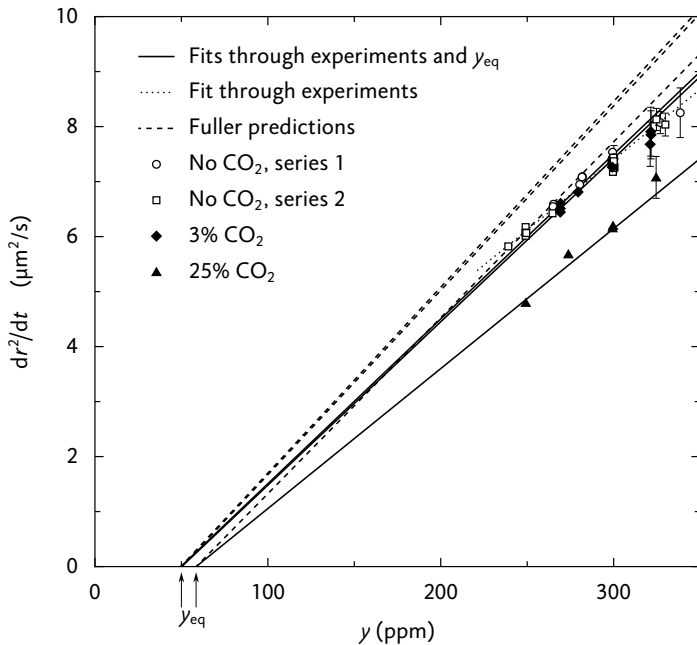


Figure 6.9: Growth rate of the squared droplet radius versus the initial water vapour fraction, at approximately 243 K and 11.5 bar, for different carbon dioxide fractions. Error bars smaller than $\pm 0.2 \mu\text{m}^2/\text{s}$ are not shown. The solid lines are least-squares fits which are forced through the equilibrium vapour fraction y_{eq} at $dr^2/dt = 0$. Because of the enhancement effect, y_{eq} increases with increasing carbon dioxide fraction. The dashed lines are predictions, with slopes given by the Fuller correlation (Eqs. 6.6 and 6.7). The dotted line is fitted to the no- CO_2 data, without constraining it to equilibrium (it is the fit also shown in Figure 6.8).

rectly from the CPA model because its density predictions are inaccurate, as shown in section 1.4. The CPA can, however, be used to approximate the relative density change caused by the solution of methane and carbon dioxide into water. This value was combined with the IAPWS¹⁴ density of pure water to obtain the density of the mixture.

The resulting fits are given as solid lines in Figure 6.9, and the diffusion constants are listed in Table 6.2. The fits through y_{eq} agree with the experiments fairly well, although for the experiments without carbon dioxide the slope deviates somewhat; the slope of the constrained fit is 17% higher than the slope of the unconstrained fit. In fact, the slope of the unconstrained fit is so low that extrapolation down to $dr^2/dt = 0$ yields $y_{\text{eq}} = 10 \pm 7$. Such a value corresponds to an enhancement factor of about 0.2, which is impossible, given the known behaviour of the methane–water system. In view of this inaccuracy, it is clear that a fit through y_{eq} results in a more reliable value for the diffusion constant.

Comparison with Fuller correlation

The Fuller correlation²⁵ provides reliable estimates of binary diffusion coefficients. Here, the version modified by Lujtjen¹¹³ is used, which reads

$$D_{AB} = \frac{0.0143T^{0.75}}{[(\Sigma_v)_A^{1/3} + (\Sigma_v)_B^{1/3}]^2} \left(\frac{1/M_A + 1/M_B}{2 \times 10^3} \right)^{1/2} \frac{M_A}{\rho_A R}, \quad (6.7)$$

with Σ_v the diffusion volume of a component (listed in Ref. 25), M the molar mass in kg/mol, ρ the mass density of the gas in kg/m³, R the gas constant in J mol⁻¹ K⁻¹, and subscripts A and B referring to the carrier gas and the condensing component, respectively.

The Fuller correlation can only be used for binary mixtures, such as the water–methane system. For diffusion of water in a homogeneous mixture of methane and carbon dioxide, the effective diffusion coefficient can be approximated with Blanc's law,²⁵

$$D_w = \left(\frac{y_c}{D_{cw}} + \frac{1 - y_c}{D_{mw}} \right)^{-1}, \quad (6.8)$$

where D_{cw} and D_{mw} are the diffusion coefficients of water in pure carbon dioxide and methane, respectively, evaluated at the same pressure and temperature as the mixture.

The resulting diffusion constants are listed in Table 6.2. In addition, purely theoretical growth rate lines are shown dashed in Figure 6.9. These lines intersect the computed equilibrium point and have a slope given by Eq. 6.6 with the Fuller/Blanc diffusion constant. Clearly, the Fuller approximation overpredicts the experimental values. In the case of 25% carbon dioxide, the deviation is 26%, which is larger than the expected uncertainty of about 10% of the Fuller method.²⁵ On the other hand, the qualitative behaviour of lower growth rates with increasing carbon dioxide fraction is reproduced.

6.6 Conclusion

The two series of nucleation experiments in pure methane do not have consistent nucleation rates; specifically, the difference in rate is a factor of four, and the difference in supersaturation (at equal nucleation rate) is seven percent. Possible causes of the discrepancy were extensively investigated, but no explanation was found. The growth rates of the two series agree; therefore, the difference in nucleation rates is not caused by an error in the vapour fraction. The earlier water–methane rates by Peeters et al.⁸ lie between the two series of this work.

Because experiments with and without carbon dioxide were alternated, the effect of carbon dioxide is unambiguous. Three percent of carbon dioxide increases the nucleation rate by a factor of ten; twenty-five percent carbon dioxide increases the rate by four orders of magnitude. The slope of the nucleation isotherms in the J - S diagram is unaffected by carbon dioxide; therefore, the number of water molecules in the critical cluster is also independent of the carbon dioxide concentration. In the case of nucleation in pure methane, the critical cluster contains 22 water molecules and 5 methane molecules, as an application of the pressure nucleation theorem shows. Remarkably, the methane fraction in the critical cluster is a hundred times as large as it is in the water-methane system in equilibrium.

Nucleation theory reproduces the influence of carbon dioxide qualitatively. The increase in nucleation rate is explained by the reduction in the water surface tension by carbon dioxide. It is estimated that in the mixture with 25% carbon dioxide, the surface tension is 13% lower than the pure-water value; conversely, in pure methane at our conditions, it is 3.5% lower than the pure-water value.

The influence of carbon dioxide is not only visible in the nucleation rates, but also in the growth rates. At equal temperature, pressure and water vapour fraction, the growth rate of the squared droplet radius is about 20% lower in the mixture with 25% carbon dioxide than in pure methane. Since the molar densities of liquid and gas are nearly independent of the carbon dioxide concentration, the lower growth rate is mainly caused by a smaller diffusion coefficient in the mixture with carbon dioxide. The decrease of the diffusion coefficient with increasing carbon dioxide concentration is qualitatively reproduced by the Fuller correlation in combination with Blanc's law. Quantitatively, the experimental diffusion coefficient in the mixture with 25% carbon dioxide is 20% lower than the Fuller prediction.

Conclusion

The research in this thesis is divided into three topics: (1) the nucleation of water in methane and carbon dioxide, including a description of the equilibrium in the ternary system water–methane–carbon dioxide; (2) the nucleation rate of water without carrier gas influence: the water–helium experiments, and (3) a theoretical analysis of the nucleation pulse method with two equations that describe nucleation and droplet growth.

Both the experimental and the theoretical research relates to our experimental setup, the expansion wave tube. This setup has been improved in collaboration with Labetski,¹⁰ resulting in better pressure measurements and a simpler, but more accurate, optical setup. For this work, the data analysis of pressure signals and optical signals was enhanced, which led to more accurate nucleation pressures, nucleation temperatures and growth rates. Despite the improvements, it was not always possible to reproduce nucleation rates from previous experiments. A deviation of a factor of four between measurements of nucleation rates obtained in June and October 2007 was observed. Within each series of experiments, the reproducibility was better than a factor of two. An extensive investigation did not reveal the cause, so the issue remains unresolved.

Nucleation in methane and carbon dioxide

In spite of the uncertainties in the nucleation rates, the influence of methane and carbon dioxide on the water nucleation rate could be quantified. The nucleation rate in methane at 235 K and 10 bar was found to be about three orders of magnitude higher than the nucleation rate of water in helium or argon at about 1 bar, at equal temperature and supersaturation. The increase is likely caused by the reduction of the water surface tension by methane; at 235 K and 10 bar, the relative decrease of surface tension is estimated at 3.5%.

The presence of carbon dioxide beside methane increases the nucleation rate even more. At 235 K and 10 bar, 3% carbon dioxide increases the rate by one order of magnitude, and 25% carbon dioxide increases it by four orders of magnitude, compared to the rate in pure methane. This effect is also explained by a decrease in surface tension. At our conditions with 25% carbon

dioxide, the estimated relative decrease of the surface tension is 13%, compared to the pure-water surface tension.

The effects of methane and carbon dioxide can only be evaluated when the enhancement factor of water is taken into account in the supersaturation. When this is not done, and nucleation rates are plotted as functions of the partial water pressure, the carrier gas effects diminish. These compensating influences of enhancement factor and surface tension are also seen in other systems, such as water–nitrogen and nonane–methane.^{6,113}

To precisely determine the influence of the carrier gas, the enhancement factors that are used to compute the supersaturations must be accurately known. Understandably, there are no measurements of the enhancement factor involving deeply supercooled water, so the use of an equation of state is inevitable. The CPA EOS, used in this work, can be no more accurate than the experimental data to which it was fitted. Unfortunately, existing literature data on enhancement factors is not accurate enough for our purposes. At our nucleation conditions, the relative uncertainty in the predicted enhancement factor is 5% to 15%. Still, the effect of 25% carbon dioxide on the nucleation rate is so large that it remains significant, even if the enhancement factor has an error of 15%.

In view of the large uncertainties in the enhancement factor and the surface tension, a direct, quantitative comparison between experimental and theoretical nucleation rates in our systems is of limited value. The effect of carbon dioxide on the nucleation rate is qualitatively reproduced by classical theory, however. Nucleation theory should also take into account the large number of methane molecules in the critical cluster. From an application of the nucleation theorem to our experimental data, it was found that at 235 K and 10 bar the molar fraction of methane in the critical cluster is 0.2, which is a hundred times as large as the equilibrium fraction at those conditions.

Besides nucleation rates, growth rates of water droplets were measured in methane and in methane–carbon dioxide mixtures. At equal temperature, pressure and water vapour fraction, the growth rate of the squared droplet radius is about 20% lower in the mixture with 25% carbon dioxide than in pure methane. The lower growth rate is caused by a smaller diffusion coefficient in the mixture with carbon dioxide; the difference in the diffusion coefficient is qualitatively predicted by the Fuller correlation. The two sets of experiments in pure methane, whose nucleation rates do not agree, do have consistent growth rates. This implies that the water vapour fractions of both series are reliable.

Nucleation in helium

The description of the nucleation of water in helium at atmospheric pressure is less complicated than the nucleation in methane, as helium behaves as an ideal gas. Our nucleation rates agree with those measured by Wölk and Strey¹⁹ in the temperature and nucleation rate range of overlap. The results provide a plausible extension of nucleation rate measurements to high supersaturations and low temperatures. Classical nucleation theory predicts an incorrect temperature dependence of the nucleation rate, as is well known.²¹⁷ Our results demonstrate that the supersaturation dependence of the classical rate is also incorrect, contrary to what is usually assumed.¹⁹

Nucleation pulse analysis

The droplet size distribution that results from the nucleation pulse method was analysed with the kinetic equation and the general dynamic equation (GDE). The GDE was found to be inaccurate for droplet sizes near the critical size and smaller. This inaccuracy is inherent in the GDE and cannot be avoided. In contrast, the number density of larger droplets in the GDE can be made to agree with the kinetic equation by adjusting the initial droplet radius in the GDE.

For short nucleation pulses, a considerable fraction of the droplets that are formed during the pulse will evaporate after the end of the pulse. This violates the assumption of the nucleation pulse method that all droplets that are formed will be detected. Our experimental pulses, however, are long enough; the number of droplets that evaporate after the pulse is negligible. For long nucleation pulses, depletion of the vapour may become important, which can violate the assumption of a constant nucleation rate during the pulse. The effects of depletion were not computed in this work; in a future analysis, it should be analysed how long the pulse can be made before depletion becomes significant.

* * *

The present work has demonstrated that there remains much to study about the nucleation of water. A comparison of theoretical and experimental nucleation rates is only meaningful if the physical properties of water are precisely known at the nucleation conditions. This is the case for nucleation above 273 K in a low-pressure ideal carrier gas, such as helium. In that system, the nucleation rates of the different research groups show a large amount of scatter,^{217,218} so the temperature and supersaturation dependence of the nucleation rate is uncertain at some conditions. The empirical rate expression of Wölk et al.²¹⁷ is a promising development, but it may be inaccurate for high supersaturations and low temperatures, as our measurements indicate.

In the case of water nucleation in natural-gas-like mixtures, the equilibrium properties are poorly known. New, accurate measurements of the enhancement factor in methane and carbon dioxide are needed. However, since these measurements are likely impossible when water is supercooled, the problem of extrapolation to the nucleation temperature remains. Another difficulty in the description of nucleation is the large number of methane molecules that enter the critical cluster, something that is not predicted by the equilibrium data at all. Only experiments can reveal peculiarities as these, and, in the end, the true nature of water nucleation.

Properties of supercooled water



Water is a continuous source of fascination because of its peculiar behaviour and tremendous importance in all branches of science. Continuous research efforts are dedicated to answering questions about the physical properties of water, such as the question whether water possesses a second critical point. This liquid–liquid critical point, located around 220 K and 100 MPa,²²⁵ could account for the anomalous behaviour of water, such as the apparent singularities in many of its properties. Indeed, in the so-called supercooled state of liquid water, its thermophysical properties exhibit a pronounced temperature dependence.^{108,226} Several of these properties – such as the coefficient of thermal expansion, the isothermal compressibility and the constant-pressure specific heat – tend to diverge at a temperature of 228 K, only slightly below the lowest temperature that has been reached in conventional experiments on supercooled water. In these experiments, a small amount of water is cooled down to several tens of degrees below the freezing point, after which measurements are performed. The limit of supercooling (that is, the temperature at which the water sample freezes) depends on the homogeneous ice nucleation rate, which strongly increases with decreasing temperature. The time delay for crystallization decreases by more than a factor of ten when water is cooled by one degree.²²³ Using conventional cooling techniques, it has therefore not been possible to supercool liquid water below temperatures of 233 ± 2 K, the *homogeneous ice nucleation limit*. The temperature regime below this limit is called a ‘no man’s land’.²²⁵

The majority of our water–helium nucleation experiments take place in the no man’s land, where liquid water with unknown properties is formed. To evaluate the supersaturation and the theoretical nucleation rate, however, properties such as vapour pressure and density must be known or extrapolated. This appendix describes how the values of those quantities have been estimated. The surface tension of supercooled water is discussed in section 1.9.

A.1 Vapour pressure

The vapour pressure of supercooled water is known to within 0.2% down to 235 K, but the impossibility of taking measurements below that temperature results in a large uncertainty at lower temperature. Most correlations are not fitted to measurements of the vapour pressure itself, but are derived from heat capacity data, using the Clausius–Clapeyron equation.⁶⁷ This approach was followed by Muijens and Looijmans²²⁷ in 1990, assuming a temperature-independent heat capacity. Their resulting correlation, valid down to 255 K, has been used by many authors,^{9,113,228} with Peeters⁶⁹ using it down to 200 K.

Another equation that is frequently used in nucleation work (for example by Wölk and Strey¹⁹ and Heath et al.²²⁹) was first published in 1981 by Preining et al.,²³⁰ who probably also developed it. The equation is a fit to Landolt–Börnstein²³¹ vapour pressure data from 273 K to 373 K, but it has been used¹⁹ down to 220 K. A third fit, from the same Landolt–Börnstein²³¹ book of 1960, is also still used, for example by Brus et al.²¹⁸ in 2008. That equation is valid down to 273 K, but some workers^{195,232} have used it below 220 K.

After these fits had been developed, heat capacity measurements down to 236 K were published,²³³ showing a pronounced increase at low temperature. In 2005, Murphy and Koop⁶⁷ reviewed several vapour pressure parameterizations and found that none agreed with the new heat capacity measurements. Therefore, they created a new correlation, which is also used in this work,

$$\begin{aligned} \ln(p_s/\text{Pa}) = & 54.842763 - 6763.22/T - 4.210 \ln(T) + 0.000367T \\ & + \tanh[0.0415(T - 218.8)](53.878 - 1331.22/T \\ & - 9.44523 \ln(T) + 0.014025T), \end{aligned} \quad (\text{A.1})$$

valid between 123 and 332 K. The uncertainty of the fit rapidly increases below 230 K, and is larger than $\pm 5\%$ at 200 K.

From Figure A.1 it can be seen that down to about 235 K, all fits agree with each other to within 0.2%. At lower temperatures, the **Murphy and Koop** fit predicts significantly lower vapour pressures than the three other fits. This is a result of the anomalous behaviour of the heat capacity, which cannot be reproduced by extrapolation of the higher-temperature values. The figure also shows the deviation of the vapour pressure from the IAPWS-95 model, which is valid down to 273 K but can be evaluated down to 233.6 K, and agrees well with the **Murphy and Koop** fit.

For the experiments where the CPA EOS is used to compute phase equilibrium, the choice of vapour pressure parametrization has no influence on

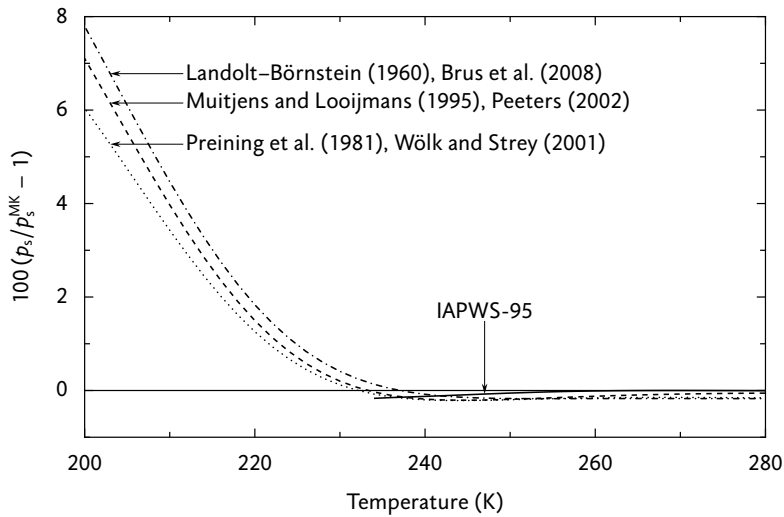


Figure A.1: Vapour pressure of supercooled water; deviations of several fits (Refs. 19, 69, 218, 227, 230, 231) from the Murphy and Koop⁶⁷ fit (Eq. A.1). All equations are plotted here below their stated validity range because they have been used there by other authors. The solid line represents the IAPWS-95 equation of state.¹⁴

the calculated supersaturations. That is, the supersaturation follows from $S = y/y_{\text{eq}}$ (Eq. 1.29 or Eq. 1.31), where y_{eq} is predicted by the CPA model.

A.2 Density

The density of liquid water between 0 and 100 °C has been measured countless times. Its well-known maximum at 4 °C was used until 1964 to define the millilitre.²³⁴ The experimental data is currently best reproduced by the IAPWS-95 formulation,^{14,15} or the simpler correlation for use at atmospheric pressure.²³⁵

Below the freezing point, measurements of the density of supercooled water are more difficult. Even so, already at the beginning of the 20th century, the density was known down to about -10 °C.^{236,248} Freezing of the water could be prevented by using pure water in a capillary. The smaller the capillary diameter (and the amount of water), the further it could be cooled down without freezing. In the 1960s, several workers^{238,239} had successfully measured densities down to -34 °C in capillaries with an inside diameter of 4 μm. However, in the 1980s, it became clear that surface effects were so important in these thin capillaries that the density measurements were affected by them.²⁴⁹ Therefore, Hare and Sorensen²⁴³ made considerable efforts to perform measurements in 300 μm capillaries, and succeeded in keeping their water samples liquid down to -33 °C. Today, their 1987 measurements are

Table A.1: Measurements of the density of supercooled water

| Author ^a | Year | Method ^b | Sample diameter | Lowest T (°C) |
|--|------|------------------------------|-----------------------|-----------------|
| Mohler ²³⁶ | 1912 | capillary | 188–380 μm | –13 |
| Schufle ²³⁷ | 1965 | capillary | 133 μm | –21 |
| Schufle and Venugopalan ²³⁸ | 1967 | capillary | 4, 10 μm | –40 |
| Zheleznyi ²³⁹ | 1969 | capillary | 4–18 μm | –34 |
| Rasmussen and MacKenzie ²⁴⁰ | 1973 | emulsion | 3.5 μm | –36 |
| Sorensen ²⁴¹ | 1983 | capillary | 60–90 μm | –25 |
| Hare and Sorensen ²⁴² | 1986 | capillary | 25 μm | –34 |
| Hare and Sorensen ²⁴³ | 1987 | capillary | 300 μm | –33 |
| Liu et al. ²⁴⁴ | 2007 | nanopore / SANS ^c | 1.5 nm | –113 |
| Mallamace et al. ²⁴⁵ | 2007 | nanopore / R&F | 1.4 nm | –90 |
| Liu et al. ²⁴⁶ | 2008 | nanopore / SANS ^c | 1.5, 1.9 nm | –133 |
| Zhang et al. ²⁴⁷ | 2009 | nanopore / SANS | 1.4 nm | –143 |

a Additional references to older literature are given by Kell,²³⁴ Angell,²²⁶ and Debenedetti.¹⁰⁸

b Methods: nanopore = 1D cylindrical nanopores, SANS = small angle neutron scattering, R&F = Raman and Fourier spectroscopy

c Measurement of D₂O density

still regarded as the most accurate; in fact, no newer measurements in capillaries exist.

With the capillary method pushed to the limit, another way was needed to reach deeper supercooling. Recently, it has become possible to keep water liquid below the homogeneous ice nucleation temperature by confining it to nanopores, tiny cylindrical channels in silica with diameters of about 1.5 nm. Confined to these pores, the water molecules cannot form a long-range crystalline structure,²⁴⁵ which inhibits ice nucleation. Using this method, it was found that the density of water has a minimum near 203 K.²⁴⁵ Of course, it cannot be expected that the density of water in nanopores is equal to the bulk density. Indeed, for heavy water (D₂O) the density in confinement is 8% higher than the bulk density.²⁴⁶ However, the clusters that are important during the nucleation process are as small as the nanopores – our critical clusters have a diameter of 1 nm. Therefore, use of the nanopore density data is appropriate for our experiments.

Several models or correlations for the density of supercooled water exist. The IAPWS model was fitted¹⁴ to the correlation of Kell²⁵⁰ down to 236 K, which is unfortunate since Kell's correlation is not valid for supercooled water. Kell evaluated his correlation below the freezing point, but warned that 'values below 0 °C were obtained by extrapolation, and no claim is made for their accuracy.'²⁵⁰ In spite of the questionable fit, the IAPWS-95 model agrees well with the measurements of Hare and Sorensen. The IAPWS equation of

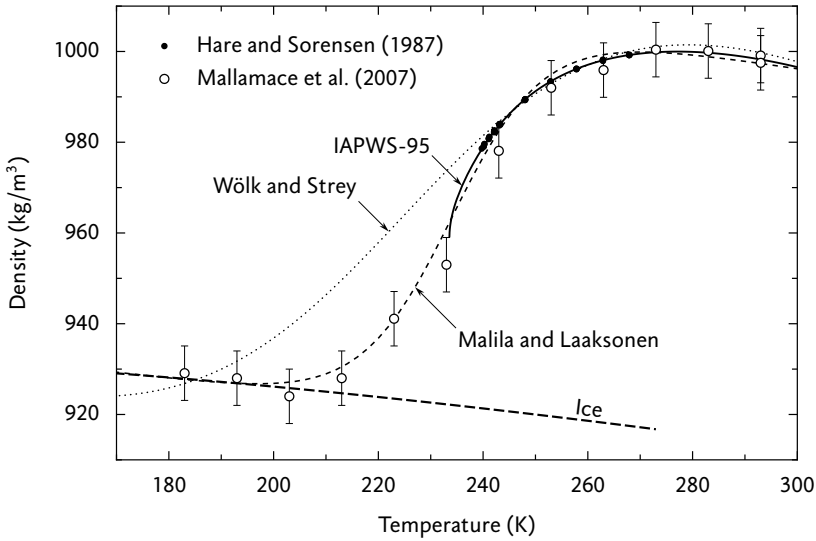


Figure A.2: Density of supercooled water: measurements in capillaries by Hare and Sorensen²⁴³ and in nanopores by Mallamace et al.²⁴⁵ Also several correlations are plotted.^{15,19,251} For comparison, the density of ice²⁵² is shown as well.

state can be evaluated down to 233.56 K, where it predicts a spinodal. At that point, the temperature derivative of the density is infinitely large.

Assuming that the spinodal is just an artifact of the IAPWS model, we expect the structure of supercooled water to become more ice-like as the temperature decreases. This assumption is supported by the Mallamace et al.²⁴⁵ nanopore densities (Figure A.2), which approach the ice density at 200 K and below. Based on the structural transition, Wölk and Strey¹⁹ developed a correlation in 2001 that shows a smoothly decreasing density with decreasing temperature. As the nanopore measurements did not exist yet, their correlation could not be based on experimental data below 240 K. Recently, Malila and Laaksonen²⁵¹ made a correlation based on the Mallamace et al. measurements,

$$\rho(T) = 43.51 \tanh\left(\frac{T - 234.08 \text{ K}}{17.65 \text{ K}}\right) + 345.54 \left(\frac{T_c - T}{T_c}\right)^{0.2} + 647.66, \quad (\text{A.2})$$

where T_c is the critical temperature (647.096 K), and the density is obtained in kg/m^3 . Their result is used in this work.

A.3 Refractive index

Knowledge of the index of refraction is required to calculate theoretical light scattering and extinction by water droplets, which are used to determine the

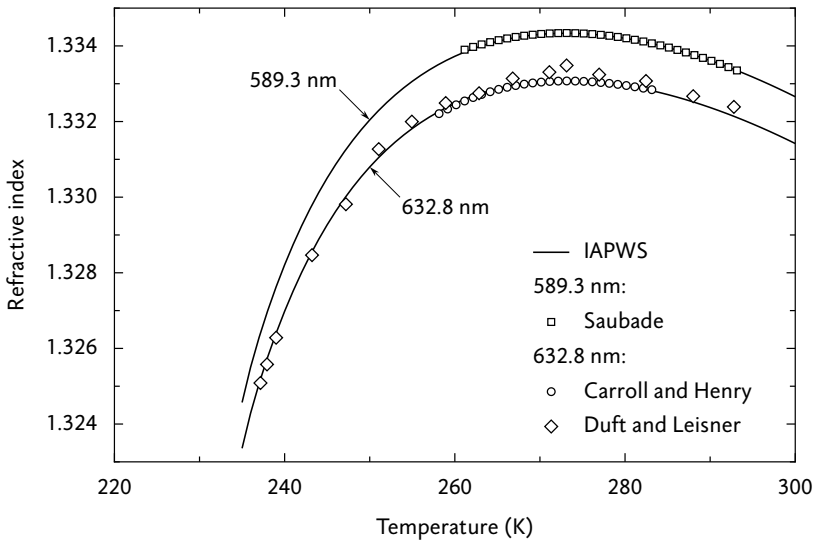


Figure A.3: Refractive index of supercooled water, relative to vacuum, at 1 bar. Measurements are by Saubade,²⁵⁶ Carroll and Henry,²⁵⁷ and Duft and Leisner.²⁵⁸ The lines represent the IAPWS correlation,²⁵⁴ which is valid down to 261 K but has been extrapolated here.

size and number density of the droplets in our experiments. Since the refractive index has never been measured at some of our experimental temperatures, this quantity must be extrapolated. For wavelengths around 500 nm, the imaginary part of the complex refractive index is very small²⁵³ (about 10^{-9}). Hence, absorption can be neglected.

The IAPWS published a release^{254,255} in 1997 that gives the refractive index as a function of temperature and density, valid down to -12°C . To include the dependence of density on temperature and pressure, it must be used in combination with the density values of the IAPWS-95 formulation.¹⁵ By extrapolation of the IAPWS refractive index correlation, the refractive index can be determined from the density (described in the previous section) also below -12°C . To test the validity of this approach, the extrapolated IAPWS refractive index values are compared with several experimental data sets in Figure A.3.

The temperature dependence of the refractive index is similar to that of the density (Figure A.2), including the steep decrease at low temperatures. The maximum of the refractive index occurs at approximately 0°C . The IAPWS correlation agrees quite well with the experiments, so that the extrapolation is justified at least down to 237 K.

With some confidence in the extrapolation of the IAPWS correlation, we proceed to extrapolate it at our laser wavelength (532 nm) down to even lower temperatures. The result is plotted in Figure A.4. Below 235 K, the Malila

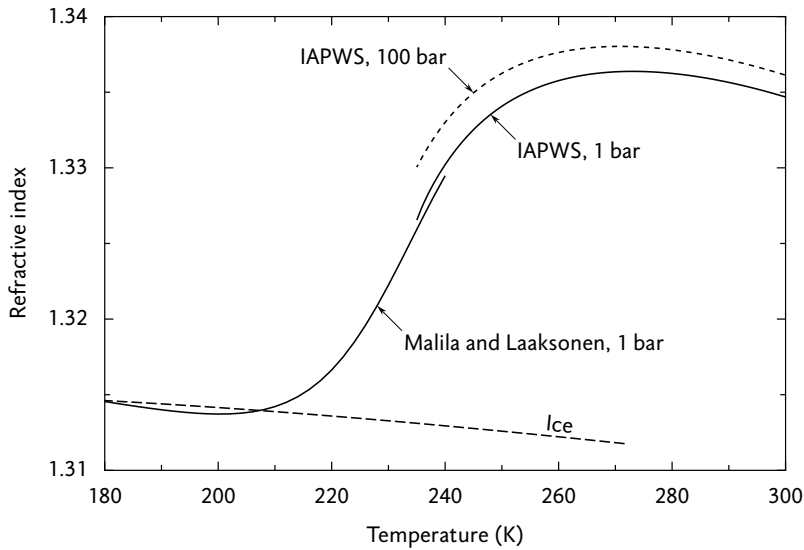


Figure A.4: Refractive index of supercooled water, relative to vacuum, at 532 nm, computed with the IAPWS correlation²⁵⁴ using densities from IAPWS-95¹⁵ and Malila and Laaksonen.²⁵¹ For comparison, the refractive index of ice²⁵⁹ is shown as well.

density (Eq. A.2) was used as input for the IAPWS refractive index correlation.

For the analysis of our experiments, the relative refractive index (the ratio of the indexes of water and the carrier gas) is needed, since that quantity determines scattering and extinction.²⁰⁴ As the relative refractive index depends on the type of carrier gas and its pressure, both the helium and methane experiments will be discussed.

Experiments in helium

Our nucleation experiments in helium were performed between 200 and 240 K at a pressure of 1.0 ± 0.1 bar. During droplet growth, the temperature was between 215 and 250 K and the pressure was 1.1 ± 0.1 bar. The wavelength of the laser was 514 nm, which results in a refractive index that is negligibly (7×10^{-4}) higher than the values plotted in Figure A.4 for 532 nm. The refractive index of the helium itself is estimated at 1.000 05.²⁶⁰ Therefore, the relative refractive index is not significantly different from the water refractive index. It varies from 1.315 at 215 K to 1.334 at 250 K. For simplicity, all helium experiments were analysed using a refractive index of 1.33, which corresponds to the high-temperature experiments. Below 220 K, however, the droplets remain smaller than $\alpha \approx 7$ and the effect of the refractive index is small for those droplet sizes (Figure 4.8 on page 134).

Experiments in methane

Droplet growth in the methane experiments takes place at about 243 K and 11.5 bar (Table 6.2). To illustrate the effect of pressure on the refractive index of water, it is plotted in Figure A.4 for 1 bar and 100 bar. The effect of our carrier gas pressure of 11.5 bar is sufficiently small to be neglected. The refractive index of the carrier gas, however, must be taken into account; it is estimated at 1.0058, independent of the carbon dioxide concentration.^{10,260,261} At 243 K, the water refractive index is 1.332 (Figure A.4), so the relative refractive index is 1.324. For historical reasons, the experiments were analysed with an index of 1.33, like the helium experiments. This difference is not expected to significantly affect the analysis.

Water–methane composition fits

B

B.1 Water vapour fraction

The molar vapour fraction of water in the methane–water system is expressed by the enhancement factor f_e of water in methane. Two fits of f_e are given here. The first one is a fit to the Duan and Mao⁹⁰ model (p. 30), which is used as input for fitting the CPA model. The second fit represents the result of the CPA model and is used to analyse experiments.

The fit to the Duan and Mao model is a polynomial fit that is quadratic in the pressure p and cubic in the temperature T . The fit is valid for T in the range of 273 to 375 K and for $p \leq 200$ bar, and is given by

$$f_e = 1 + (a_0 + a_1\tau + a_2\tau^2 + a_3\tau^3)p_r + (b_0 + b_1\tau + b_2\tau^2 + b_3\tau^3)p_r^2, \quad (\text{B.1})$$

with

$$\tau = \frac{T}{320 \text{ K}} \quad \text{and} \quad p_r = \frac{p - p_s(T)}{100 \text{ bar}}, \quad (\text{B.2})$$

and coefficients

$$\begin{aligned} a_0 &= 2.278127, & a_1 &= -3.448200, & a_2 &= 1.804727, & a_3 &= -0.2787907, \\ b_0 &= 3.015240, & b_1 &= -7.704825, & b_2 &= 6.648207, & b_3 &= -1.937428. \end{aligned}$$

The form of Eq. B.1 enforces the limit $f_e \rightarrow 1$ for $p \rightarrow p_s(T)$. To compute an equilibrium water vapour fraction y_{eq} using the fit of Eq. B.1 and the relation $y_{\text{eq}} = f_e p_s / p$ (see Eq. 1.26), the IAPWS vapour pressure¹⁴ $p_s(T)$ must be used.

The second fit, which describes the result of the CPA model, can be used at lower temperatures (230–300 K) than the previous fit. The pressure range, however, is limited to pressures that occur in our experimental setup (9–25 bar). Because the IAPWS vapour pressure cannot be computed below 234 K, the Wölk and Strey¹⁹ vapour pressure was chosen as reference, and must therefore be used when computing an equilibrium water vapour fraction using the following fit,

$$f_e = 1 + (a_0 + a_1\tau + a_2\tau^2 + a_3\tau^3)p_r + (b_0 + b_1\tau + b_2\tau^2 + b_3\tau^3)p_r^2, \quad (\text{B.3})$$

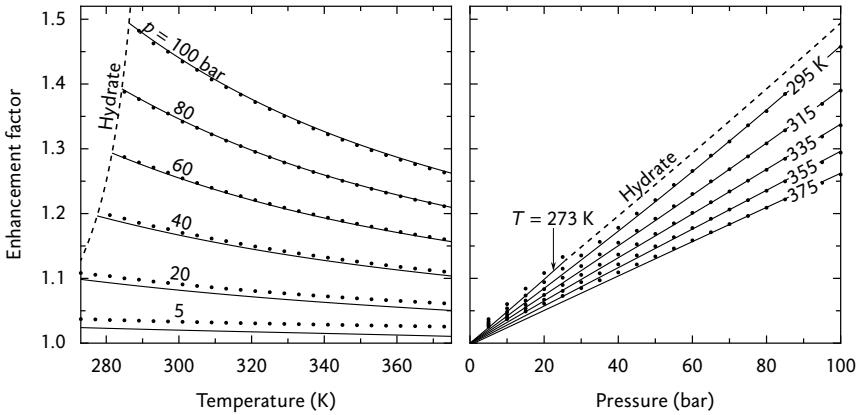


Figure B.1: Enhancement factor of water in methane as a function of temperature and pressure. The curves are calculated with the fit of Eq. B.1, and the points are from the Duan and Mao model.⁹⁰

with

$$\tau = \frac{T}{260 \text{ K}} \quad \text{and} \quad p_r = \frac{p - p_s(T)}{20 \text{ bar}}, \quad (\text{B.4})$$

and coefficients

$$\begin{aligned} a_0 &= 3.45384, & a_1 &= -7.73395, & a_2 &= 6.01149, & a_3 &= -1.59443, \\ b_0 &= 2.91334, & b_1 &= -7.62979, & b_2 &= 6.73142, & b_3 &= -2.00099. \end{aligned}$$

The fit of Eq. B.3 reproduces the f_e values of the CPA model with a relative error of less than 0.1%, in the given temperature and pressure ranges.

B.2 Methane solubility in water

The molar liquid fraction of methane in the methane–water system x_m was also obtained by a fit to the Duan and Mao model, but this fit is fourth order in p and ninth order in T . The high number of terms was required to reproduce all digits given by the Duan and Mao computer program. The fit is valid from 273 to 375 K and for $p \leq 100$ bar, and is given by

$$x_m = \sum_{n=1}^4 p_r^n \sum_{m=0}^9 c_{nm} \tau^m, \quad (\text{B.5})$$

with τ and p_r defined by Eq. B.2, and coefficients c_{nm} given below.

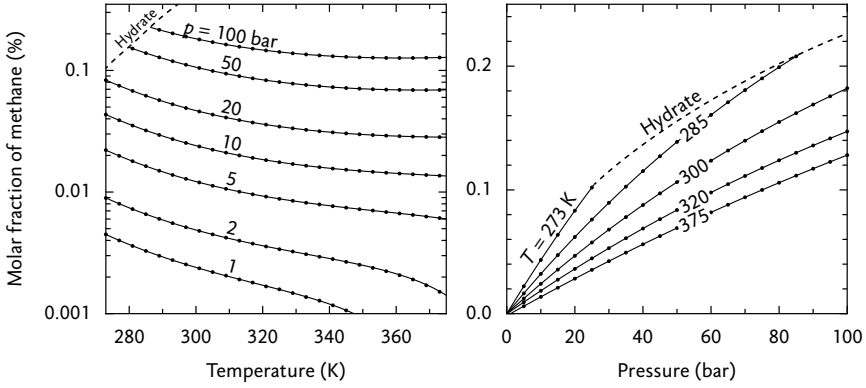


Figure B.2: Solubility of methane in water as a function of temperature and pressure. The curves are calculated with the fit of Eq. B.5, and the points are from the Duan and Mao model.⁹⁰

| m | c_{1m} | c_{2m} | c_{3m} | c_{4m} |
|-----|-----------|-----------|-----------|-----------|
| 0 | 158.6133 | 52.73272 | -74.29270 | -30.41917 |
| 1 | -1305.244 | -492.9723 | 545.2282 | 353.0406 |
| 2 | 4788.393 | 2000.596 | -1682.678 | -1720.642 |
| 3 | -10273.14 | -4647.372 | 2761.896 | 4711.401 |
| 4 | 14199.24 | 6829.327 | -2405.881 | -8072.647 |
| 5 | -13108.30 | -6594.469 | 689.7624 | 9034.704 |
| 6 | 8080.797 | 4187.770 | 663.4206 | -6632.963 |
| 7 | -3207.179 | -1686.911 | -754.0776 | 3089.548 |
| 8 | 743.5341 | 390.9910 | 302.4264 | -830.2570 |
| 9 | -76.70888 | -39.69269 | -45.80451 | 98.23323 |

The form of Eq. B.5 enforces the limit $x_m \rightarrow 0$ for $p \rightarrow p_s(T)$.

Numerical solution of the kinetic equation



C.1 Numerical integration

The equations describing the kinetics of cluster formation are (Eq. 2.31)

$$\frac{df_n}{dt} = C_{n-1}f_{n-1} - (C_n + E_n)f_n + E_{n+1}f_{n+1}. \quad (\text{C.1})$$

To solve the set of equations numerically, each equation must be discretized in time. The time t is divided into steps of size Δt ,

$$t_k = k\Delta t, \quad k = 0, 1, 2, \dots \quad (\text{C.2})$$

Although we have a set of ordinary differential equations, we will benefit from numerical methods developed for partial differential equations. This is so because the right-hand side of Eq. C.1 is similar to the finite difference equivalent of a second derivative in space. Indeed, in section 3.2, Eq. C.1 was converted to a partial differential equation. Now, we apply a simple finite difference method, called forward differencing, to the time derivative.

$$\frac{df_n}{dt} \approx \frac{f_n^{k+1} - f_n^k}{\Delta t}, \quad (\text{C.3})$$

which, when substituted in Eq. C.1, leads to

$$f_n^{k+1} = \Delta t C_{n-1}f_{n-1}^k + [1 - \Delta t (C_n + E_n)]f_n^k + \Delta t E_{n+1}f_{n+1}^k. \quad (\text{C.4})$$

In the case of partial differential equations, this finite difference method is called *forward time, centred space* (FTCS), and is first-order accurate in time. It is also explicit, which means that the new value f_n^{k+1} can be computed explicitly from known quantities at timestep k . The FTCS scheme turns out to be unsuitable for the current problem because it requires a very small Δt for stability. Applying the von Neumann stability analysis¹⁸⁹ to Eq. C.4 gives the condition $\Delta t < 1/(C_n + E_n)$. For large n , C_n and E_n keep increasing with increasing n (see Figure 2.3 on page 71). The differential equation is called stiff, which means that a very small Δt is required for stability.

To avoid problems related with Δt values, we examine a scheme which is stable for any Δt . We take the same time differencing of Eq. C.3, but evaluate the right-hand side of Eq. C.1 at timestep $k + 1$, instead of k , giving

$$-\Delta t C_{n-1} f_{n-1}^{k+1} + [1 + \Delta t (C_n + E_n)] f_n^{k+1} - \Delta t E_{n+1} f_{n+1}^{k+1} = f_n^k. \quad (\text{C.5})$$

This method, known as *backward time, centred space* (BTCS), is implicit, and the f_n^{k+1} values have to be found by solving the set of linear equations that Eq. C.5 represents. Fortunately, the system is tridiagonal and can be solved by a simple algorithm.¹⁸⁹

An even better method, which is second-order accurate in time, can be obtained by taking the average of the FTCS and BTCS methods.

$$\frac{f_n^{k+1} - f_n^k}{\Delta t} = \frac{1}{2} (C_{n-1} f_{n-1}^k + D_n f_n^k + E_{n+1} f_{n+1}^k + C_{n-1} f_{n-1}^{k+1} + D_n f_n^{k+1} + E_{n+1} f_{n+1}^{k+1}) \quad (\text{C.6})$$

with $D_n = -(C_n + E_n)$, leading to

$$-\frac{\Delta t}{2} C_{n-1} f_{n-1}^{k+1} + (1 - \frac{\Delta t}{2} D_n) f_n^{k+1} - \frac{\Delta t}{2} E_{n+1} f_{n+1}^{k+1} = \frac{\Delta t}{2} C_{n-1} f_{n-1}^k + (1 + \frac{\Delta t}{2} D_n) f_n^k + \frac{\Delta t}{2} E_{n+1} f_{n+1}^k. \quad (\text{C.7})$$

This method is called *Crank–Nicolson*,¹⁸⁹ and it consists again of a tridiagonal set of equations. In practice, a Crank–Nicolson step corresponds to the FTCS and BTCS methods applied in sequence: an explicit step with step size $\Delta t/2$, followed by an implicit step with step size $\Delta t/2$. Like the BTCS method, the Crank–Nicolson method is stable for any Δt .

C.2 Bins in size space

Although the timestep can be taken larger with the Crank–Nicolson scheme, the number of equations (from i to M) is still excessively large, and so is the computational time. The size of the system can be reduced by decreasing the number of points in size space where f_n needs to be known. Size space is therefore divided into a series of intervals, or bins.

Bins are numbered by index $N = 1, 2, 3, \dots$, begin at b_1, b_2, \dots and end at e_1, e_2, \dots . Of course, a new bin starts next to the bin before, so $b_{N+1} = e_N + 1$. The length of a bin is denoted by $l_N = b_{N+1} - b_N$. To find the evolution of f in bin N , we sum Eq. C.1 over all included n , that is, from b_N to e_N . On the right-hand side, many terms cancel, and we finally obtain

$$\begin{aligned} \sum_{n=b_N}^{e_N} \frac{df_n}{dt} &= C_{b_N-1} f_{b_N-1} - E_{b_N} f_{b_N} - C_{e_N} f_{e_N} + E_{e_N+1} f_{e_N+1} \\ &= J_{b_N-1} - J_{e_N}. \end{aligned} \quad (\text{C.8})$$

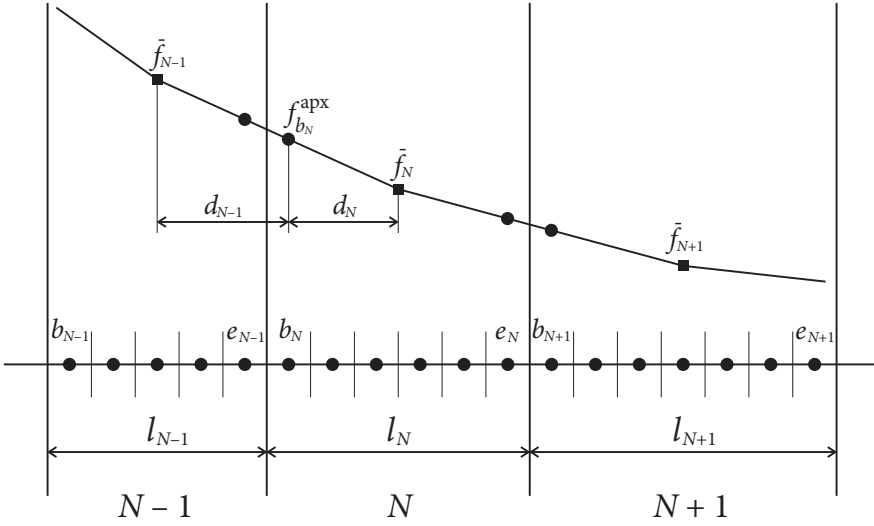


Figure C.1: Division of size space into bins. In this example, bins $N - 1$, N and $N + 1$ have respective sizes of 5, 6 and 7 units.

We introduce the notation F_N for the total f that a bin contains, that is,

$$F_N = \sum_{n=b_N}^{e_N} f_n. \quad (\text{C.9})$$

By swapping the derivative and summation in Eq. C.8, we obtain

$$\frac{dF_N}{dt} = J_{b_{N-1}} - J_{e_N}. \quad (\text{C.10})$$

This equation states that the change of the contents of a bin only depends on the fluxes at its boundaries.

The original set of equations of Eq. C.1 has now been reduced to the smaller set of Eq. C.10, which contains only one equation for each bin. This small set will be used on its own to solve the entire problem, with F_N as unknowns, so that the individual f_n values in a bin never need to be computed. However, to calculate the fluxes at the bin boundaries, we do need the values of f at those positions. They will be approximated by a linear interpolation, as follows. First, we define \bar{f} as a notation for the average f in a bin, which is the total f divided by the bin length:

$$\bar{f}_N = \frac{1}{l_N} \sum_{n=b_N}^{e_N} f_n = \frac{F_N}{l_N}. \quad (\text{C.11})$$

The f distribution is assumed to take the value \bar{f} at the exact centre of a bin. We now introduce the quantity f_n^{apx} , which is the linear approximation of f

at a point n somewhere between the centres of bins $N - 1$ and N . It is given by

$$f_n^{\text{apx}} = \frac{d_N \bar{f}_{N-1} + d_{N-1} \bar{f}_N}{d_{N-1} + d_N}, \quad (\text{C.12})$$

with d_{N-1} the distance from n to the centre of bin $N - 1$, and d_N the distance from n to the centre of bin N . For the point b_N , for instance, the distances are $d_{N-1} = \frac{1}{2}l_{N-1} + \frac{1}{2}$ and $d_N = \frac{1}{2}l_N - \frac{1}{2}$. The approximation at b_N becomes

$$f_{b_N}^{\text{apx}} = \frac{(\frac{1}{2}l_N - \frac{1}{2})\bar{f}_{N-1} + (\frac{1}{2}l_{N-1} + \frac{1}{2})\bar{f}_N}{\frac{1}{2}l_{N-1} + \frac{1}{2}l_N} = \frac{(l_N - 1)\bar{f}_{N-1} + (l_{N-1} + 1)\bar{f}_N}{l_{N-1} + l_N}. \quad (\text{C.13})$$

Note that in the case of bins of unit size ($N = n$, $b_N = e_N = n$, $l_N = 1$), Eq. C.13 correctly reduces to $f_n^{\text{apx}} = f_n$. Similar approximations are made at $b_N - 1$, e_N , and $e_N + 1$. Equation C.10 becomes

$$\frac{dF_N}{dt} = C_{b_N-1} f_{b_N-1}^{\text{apx}} - E_{b_N} f_{b_N}^{\text{apx}} - C_{e_N} f_{e_N}^{\text{apx}} + E_{e_N+1} f_{e_N+1}^{\text{apx}}. \quad (\text{C.14})$$

We now perform several steps to arrive at the final result. First, we divide through by l_N , so that F_N at the left-hand side becomes \bar{f}_N . Then, we collect together all terms that involve \bar{f}_{N-1} , \bar{f}_N , and \bar{f}_{N+1} .

$$\frac{d\bar{f}_N}{dt} = U_{N-1} \bar{f}_{N-1} + V_N \bar{f}_N + W_{N+1} \bar{f}_{N+1}. \quad (\text{C.15})$$

This equation is the equivalent of Eq. C.1 in the case of bins. U , V and W are constants that only depend on C_n , E_n and l_N . For example, U is given by

$$U_{N-1} = \frac{1}{l_N} \frac{(l_N + 1)C_{b_N-1} - (l_N - 1)E_{b_N}}{l_{N-1} + l_N}. \quad (\text{C.16})$$

Experimental data



Table D.1: Water nucleation data in methane

| Exp. | p_0 (bar) | T_0 (K) | p (bar) | T (K) | y_w (ppm) | Δt (ms) | S | S_{corr} | J ($\text{m}^{-3}\text{s}^{-1}$) |
|------|-------------|-----------|-----------|---------|-------------|-----------------|-------|-------------------|--------------------------------------|
| 10 | 24.946 | 294.08 | 10.105 | 234.77 | 281.9 | 0.26 | 11.49 | 11.31 | 1.7×10^{15} |
| 14 | 24.946 | 295.21 | 10.025 | 235.26 | 281.7 | 0.26 | 10.85 | 10.84 | 5.9×10^{14} |
| 15 | 24.946 | 294.25 | 10.066 | 234.68 | 299.4 | 0.26 | 12.27 | 12.03 | 3.7×10^{15} |
| 16 | 24.946 | 294.59 | 10.037 | 234.80 | 280.3 | 0.26 | 11.32 | 11.15 | 8.5×10^{14} |
| 17 | 24.946 | 294.34 | 10.130 | 235.14 | 327.0 | 0.27 | 12.87 | 12.81 | 2.6×10^{16} |
| 18 | 24.946 | 294.66 | 10.198 | 235.81 | 265.2 | 0.27 | 9.82 | 9.96 | 7.5×10^{13} |
| 19 | 24.946 | 294.69 | 10.000 | 234.67 | 265.0 | 0.25 | 10.81 | 10.61 | 3.2×10^{14} |
| 20 | 24.946 | 293.90 | 10.078 | 234.46 | 338.5 | 0.26 | 14.20 | 13.81 | 1.4×10^{17} |
| 22 | 24.946 | 294.33 | 9.924 | 233.91 | 300.2 | 0.24 | 13.13 | 12.55 | 2.4×10^{16} |
| 25 | 24.946 | 294.94 | 10.202 | 236.07 | 299.3 | 0.40 | 10.81 | 11.05 | 8.3×10^{14} |
| 26 | 24.946 | 294.73 | 10.136 | 235.50 | 299.8 | 0.29 | 11.39 | 11.46 | 1.5×10^{15} |
| 37 | 24.946 | 294.37 | 10.056 | 234.73 | 300.5 | 0.28 | 12.24 | 12.03 | 1.3×10^{16} |
| 42 | 24.946 | 294.77 | 10.029 | 234.91 | 299.9 | 0.27 | 11.97 | 11.83 | 1.1×10^{16} |
| 43 | 24.946 | 295.25 | 10.067 | 235.54 | 298.7 | 0.27 | 11.23 | 11.31 | 4.0×10^{15} |
| 44 | 24.946 | 295.31 | 10.105 | 235.81 | 299.1 | 0.26 | 10.99 | 11.15 | 3.4×10^{15} |
| 45 | 24.946 | 294.59 | 10.048 | 234.87 | 264.6 | 0.28 | 10.62 | 10.49 | 1.2×10^{15} |
| 46 | 24.946 | 295.33 | 10.061 | 235.57 | 239.1 | 0.32 | 8.96 | 9.02 | 5.1×10^{13} |
| 47 | 24.946 | 294.75 | 10.118 | 235.41 | 249.1 | 0.27 | 9.53 | 9.56 | 1.6×10^{14} |
| 48 | 24.946 | 295.48 | 10.112 | 236.00 | 329.9 | 0.28 | 11.90 | 12.15 | 3.1×10^{16} |
| 49 | 24.946 | 294.45 | 10.039 | 234.69 | 300.0 | 0.29 | 12.25 | 12.02 | 2.8×10^{16} |
| 50 | 24.946 | 294.47 | 10.065 | 234.86 | 299.6 | 0.27 | 12.06 | 11.89 | 1.4×10^{16} |
| 51 | 24.946 | 294.96 | 10.077 | 235.35 | 299.8 | 0.28 | 11.50 | 11.52 | 4.8×10^{15} |
| 52 | 24.946 | 295.21 | 10.111 | 235.76 | 299.7 | 0.29 | 11.07 | 11.22 | 4.0×10^{15} |
| 53 | 24.946 | 295.21 | 10.086 | 235.62 | 299.9 | 0.27 | 11.21 | 11.31 | 5.3×10^{15} |
| 54 | 24.946 | 295.11 | 10.091 | 235.56 | 299.9 | 0.26 | 11.28 | 11.37 | 6.1×10^{15} |
| 55 | 24.946 | 294.82 | 10.553 | 237.99 | 299.8 | 0.30 | 9.24 | 9.91 | 2.4×10^{14} |
| 56 | 24.946 | 295.39 | 10.241 | 236.68 | 299.8 | 0.25 | 10.23 | 10.63 | 1.2×10^{15} |
| 57 | 24.946 | 294.62 | 10.043 | 234.86 | 299.5 | 0.26 | 12.03 | 11.87 | 1.7×10^{16} |
| 63 | 24.946 | 294.48 | 10.063 | 234.86 | 300.1 | 0.29 | 12.07 | 11.91 | 1.4×10^{16} |
| 64 | 24.946 | 294.77 | 10.152 | 235.63 | 249.1 | 0.23 | 9.35 | 9.44 | 1.3×10^{14} |
| 65 | 24.940 | 294.73 | 10.124 | 235.45 | 249.0 | 0.26 | 9.49 | 9.53 | 1.2×10^{14} |
| 66 | 24.946 | 294.73 | 10.098 | 235.28 | 249.5 | 0.24 | 9.65 | 9.65 | 2.0×10^{14} |
| 70 | 24.946 | 294.58 | 10.103 | 235.18 | 324.7 | 0.17 | 12.70 | 12.65 | 6.7×10^{16} |

Note: p_0 and T_0 are the pressure and temperature before the expansion, and p and T are those during the pulse, which has a duration of Δt . The quantity S_{corr} is the corrected supersaturation (Eq. 6.1) with $\bar{T} = 235.3$ K.

Table D.2: Water–methane mixture preparation

| Exp. | T_{sat} (K) | p_{sat} (bar) | f_e | y_w^s (ppm) | Q_m (L/min) | Q_0 (L/min) | y_w (ppm) |
|------|----------------------|------------------------|-------|---------------|---------------|---------------|-------------|
| 10 | 290.99 | 70.00 | 1.270 | 370.7 | 1.852 | 0.584 | 281.9 |
| 14 | 290.99 | 70.00 | 1.270 | 370.7 | 1.752 | 0.554 | 281.7 |
| 15 | 291.00 | 25.34 | 1.111 | 896.2 | 0.725 | 1.446 | 299.4 |
| 16 | 291.00 | 25.34 | 1.111 | 896.2 | 0.716 | 1.573 | 280.3 |
| 17 | 291.01 | 25.34 | 1.111 | 896.6 | 0.743 | 1.296 | 327.0 |
| 18 | 291.02 | 25.34 | 1.111 | 897.0 | 0.572 | 1.365 | 265.2 |
| 19 | 291.01 | 25.34 | 1.111 | 896.7 | 0.610 | 1.456 | 265.0 |
| 20 | 291.01 | 25.34 | 1.111 | 896.4 | 0.725 | 1.196 | 338.5 |
| 22 | 291.02 | 25.34 | 1.111 | 897.1 | 0.636 | 1.267 | 300.2 |
| 25 | 291.00 | 25.34 | 1.111 | 896.3 | 0.732 | 1.461 | 299.3 |
| 26 | 291.01 | 25.34 | 1.111 | 896.3 | 0.667 | 1.329 | 299.8 |
| 37 | 291.03 | 25.34 | 1.111 | 897.8 | 0.764 | 1.519 | 300.5 |
| 42 | 291.01 | 25.34 | 1.111 | 896.6 | 0.578 | 1.151 | 299.9 |
| 43 | 291.02 | 25.34 | 1.111 | 896.9 | 0.591 | 1.184 | 298.7 |
| 44 | 291.02 | 25.34 | 1.111 | 896.9 | 0.742 | 1.485 | 299.1 |
| 45 | 291.00 | 25.34 | 1.111 | 896.3 | 0.612 | 1.463 | 264.6 |
| 46 | 291.00 | 25.34 | 1.111 | 896.0 | 0.553 | 1.521 | 239.1 |
| 47 | 291.01 | 25.34 | 1.111 | 896.5 | 0.580 | 1.509 | 249.1 |
| 48 | 291.01 | 25.34 | 1.111 | 896.6 | 0.764 | 1.313 | 329.9 |
| 49 | 291.01 | 25.34 | 1.111 | 896.3 | 0.604 | 1.202 | 300.0 |
| 50 | 291.00 | 25.34 | 1.111 | 896.2 | 0.600 | 1.195 | 299.6 |
| 51 | 291.01 | 25.34 | 1.111 | 896.8 | 0.600 | 1.195 | 299.8 |
| 52 | 291.01 | 25.34 | 1.111 | 896.6 | 0.600 | 1.195 | 299.7 |
| 53 | 291.01 | 25.34 | 1.111 | 896.6 | 0.626 | 1.247 | 299.9 |
| 54 | 291.01 | 25.34 | 1.111 | 896.3 | 0.619 | 1.232 | 299.9 |
| 55 | 291.00 | 25.34 | 1.111 | 896.0 | 0.619 | 1.232 | 299.8 |
| 56 | 291.00 | 25.34 | 1.111 | 896.3 | 0.625 | 1.244 | 299.8 |
| 57 | 291.00 | 25.34 | 1.111 | 896.2 | 0.612 | 1.220 | 299.5 |
| 63 | 291.01 | 25.34 | 1.111 | 896.6 | 0.609 | 1.212 | 300.1 |
| 64 | 291.01 | 25.34 | 1.111 | 896.5 | 0.464 | 1.207 | 249.1 |
| 65 | 291.01 | 25.34 | 1.111 | 896.6 | 0.475 | 1.237 | 249.0 |
| 66 | 291.01 | 25.34 | 1.111 | 896.5 | 0.481 | 1.249 | 249.5 |
| 70 | 291.00 | 25.34 | 1.111 | 896.1 | 0.719 | 1.266 | 324.7 |

Note: T_{sat} and p_{sat} are the conditions in the saturators. For flow definitions see Figure 4.12.

Table D.3: Water nucleation data in methane and 3% carbon dioxide ($y_c = 0.0305$)

| Exp. | p_0 (bar) | T_0 (K) | p (bar) | T (K) | y_w (ppm) | Δt (ms) | S | S_{corr} | J ($\text{m}^{-3}\text{s}^{-1}$) |
|------|-------------|-----------|-----------|---------|-------------|-----------------|-------|-------------------|--------------------------------------|
| 24 | 24.946 | 294.43 | 10.067 | 234.85 | 299.2 | 0.26 | 11.51 | 11.36 | 1.2×10^{16} |
| 27 | 24.946 | 294.81 | 10.256 | 236.28 | 269.2 | 0.38 | 9.15 | 9.39 | 1.1×10^{14} |
| 30 | 24.946 | 294.56 | 10.361 | 236.68 | 269.3 | 0.28 | 8.88 | 9.21 | 1.0×10^{14} |
| 31 | 24.946 | 295.29 | 10.148 | 236.06 | 269.2 | 0.43 | 9.26 | 9.46 | 1.7×10^{14} |
| 32 | 24.946 | 295.25 | 9.966 | 234.95 | 321.1 | 0.35 | 12.13 | 12.00 | 4.0×10^{16} |
| 33 | 24.946 | 295.33 | 9.968 | 235.03 | 279.4 | 0.27 | 10.48 | 10.39 | 1.9×10^{15} |
| 35 | 24.946 | 295.07 | 9.902 | 234.42 | 321.5 | 0.33 | 12.73 | 12.38 | 9.6×10^{16} |
| 36 | 24.946 | 295.52 | 9.877 | 234.65 | 321.6 | 0.29 | 12.42 | 12.17 | 7.4×10^{16} |

Table D.4: Water nucleation data in methane and 25% carbon dioxide ($y_c = 0.250$)

| Exp. | p_0 (bar) | T_0 (K) | p (bar) | T (K) | y_w (ppm) | Δt (ms) | S | S_{corr} | I ($m^{-3}s^{-1}$) |
|------|-------------|-----------|-----------|---------|-------------|-----------------|------|------------|------------------------|
| 61 | 24.946 | 294.69 | 10.056 | 235.06 | 299.6 | 0.22 | 8.37 | 8.32 | 3.9×10^{16} |
| 62 | 24.946 | 294.72 | 10.189 | 235.87 | 299.4 | 0.39 | 7.86 | 7.97 | 1.5×10^{16} |
| 67 | 24.946 | 295.11 | 10.085 | 235.59 | 249.2 | 0.19 | 6.66 | 6.70 | 2.9×10^{14} |
| 68 | 24.946 | 294.65 | 10.129 | 235.46 | 273.8 | 0.22 | 7.42 | 7.45 | 3.4×10^{15} |
| 69 | 24.946 | 294.53 | 10.118 | 235.29 | 324.6 | 0.21 | 8.92 | 8.91 | 1.9×10^{17} |

Table D.5: Water–methane–carbon dioxide mixture preparation

| Exp. | T_{sat} (K) | p_{sat} (bar) | f_e | y_w^s (ppm) | Normal vol. flows (L/min) | | | y_w (ppm) |
|------|---------------|-----------------|-------|---------------|---------------------------|-------|-------|-------------|
| | | | | | Q_m | Q_0 | Q_1 | |
| 24 | 291.02 | 25.34 | 1.111 | 897.1 | 0.545 | 0.108 | 0.982 | 299.2 |
| 27 | 291.00 | 25.34 | 1.111 | 896.3 | 0.481 | 0.159 | 0.962 | 269.2 |
| 30 | 291.01 | 25.34 | 1.111 | 896.4 | 0.511 | 0.169 | 1.021 | 269.3 |
| 31 | 291.01 | 25.34 | 1.111 | 896.7 | 0.508 | 0.168 | 1.018 | 269.2 |
| 32 | 291.01 | 25.34 | 1.111 | 896.5 | 0.604 | 0.070 | 1.014 | 321.1 |
| 33 | 291.01 | 25.34 | 1.111 | 896.8 | 0.523 | 0.148 | 1.009 | 279.4 |
| 35 | 291.01 | 25.34 | 1.111 | 896.7 | 0.601 | 0.070 | 1.007 | 321.5 |
| 36 | 291.01 | 25.34 | 1.111 | 896.8 | 0.589 | 0.068 | 0.987 | 321.6 |

Note: $y_c^0 = 0.0508$ and $y_c = 0.0305$.

Table D.6: Water–methane–carbon dioxide mixture preparation

| Exp. | T_{sat} (K) | p_{sat} (bar) | f_e | y_w^s (ppm) | Normal vol. flows (L/min) | | | y_w (ppm) |
|------|---------------|-----------------|-------|---------------|---------------------------|-------|-------|-------------|
| | | | | | Q_m | Q_0 | Q_1 | |
| 61 | 291.01 | 25.34 | 1.111 | 896.5 | 0.699 | 0.871 | 0.522 | 299.6 |
| 62 | 291.01 | 25.34 | 1.111 | 896.6 | 0.694 | 0.866 | 0.519 | 299.4 |
| 67 | 291.00 | 25.34 | 1.111 | 896.3 | 0.546 | 0.928 | 0.493 | 249.2 |
| 68 | 291.00 | 25.34 | 1.111 | 896.2 | 0.620 | 0.903 | 0.508 | 273.8 |
| 69 | 291.00 | 25.34 | 1.111 | 896.3 | 0.735 | 0.788 | 0.508 | 324.6 |

Note: Q_1 refers to a pure carbon dioxide flow, and $y_c = 0.2499 \pm 0.006$.

Table D.7: Droplet growth in methane and 3% carbon dioxide ($y_c = 0.0305$)

| Exp. | p (bar) | T (K) | y_w (ppm) | n (m^{-3}) | dr^2/dt ($\mu m^2/s$) | r_m (μm) |
|------|-----------|---------|-------------|----------------------|---------------------------|-------------------|
| 24 | 11.506 | 242.89 | 299.2 | 3.5×10^{12} | 7.26 ± 0.18 | 0.574 |
| 27 | 11.551 | 243.46 | 269.2 | 4.6×10^{10} | 6.45 0.06 | – |
| 30 | 11.526 | 243.11 | 269.3 | 3.2×10^{10} | 6.60 0.06 | – |
| 31 | 11.417 | 243.16 | 269.2 | 7.7×10^{10} | 6.51 0.06 | – |
| 32 | 11.350 | 242.76 | 321.1 | 1.5×10^{13} | 7.68 0.40 | 0.372 |
| 33 | 11.373 | 242.96 | 279.4 | 5.7×10^{11} | 6.81 0.14 | 1.452 |
| 35 | 11.275 | 242.21 | 321.5 | 3.5×10^{13} | 7.91 0.44 | 0.270 |
| 36 | 11.308 | 242.90 | 321.6 | 2.3×10^{13} | 7.85 0.44 | 0.305 |

Table D.8: Droplet growth in methane

| Exp. | p (bar) | T (K) | y_w (ppm) | n (m^{-3}) | dr^2/dt ($\mu m^2/s$) | r_m (μm) |
|------|-----------|---------|-------------|----------------------|---------------------------|-------------------|
| 10 | 11.555 | 242.84 | 281.9 | 4.9×10^{11} | 7.09 ± 0.13 | 1.434 |
| 14 | 11.506 | 243.57 | 281.7 | 1.7×10^{11} | 7.08 0.06 | – |
| 15 | 11.522 | 242.81 | 299.4 | 1.1×10^{12} | 7.53 0.14 | 0.911 |
| 16 | 11.478 | 242.88 | 280.3 | 2.4×10^{11} | 6.95 0.06 | – |
| 17 | 11.529 | 242.93 | 327.0 | 7.5×10^{12} | 8.07 0.20 | 0.454 |
| 18 | 11.666 | 243.93 | 265.2 | 2.2×10^{10} | 6.59 0.06 | – |
| 19 | 11.454 | 242.84 | 265.0 | 8.9×10^{10} | 6.55 0.07 | – |
| 20 | 11.544 | 242.63 | 338.5 | 4.1×10^{13} | 8.25 0.45 | 0.260 |
| 22 | 11.409 | 242.28 | 300.2 | 6.3×10^{12} | 7.41 0.24 | 0.461 |
| 25 | 11.620 | 243.94 | 299.3 | 3.6×10^{11} | 7.42 0.09 | – |
| 26 | 11.556 | 243.41 | 299.8 | 4.6×10^{11} | 7.43 0.07 | – |
| 37 | 11.539 | 243.01 | 300.5 | 4.0×10^{12} | 7.26 0.18 | 0.564 |
| 42 | 11.558 | 243.46 | 299.9 | 3.2×10^{12} | 7.31 0.17 | 0.624 |
| 43 | 11.530 | 243.73 | 298.7 | 1.2×10^{12} | 7.36 0.14 | 0.871 |
| 44 | 11.500 | 243.62 | 299.1 | 9.4×10^{11} | 7.39 0.14 | 1.002 |
| 45 | 11.547 | 243.25 | 264.6 | 3.6×10^{11} | 6.42 0.06 | – |
| 46 | 11.520 | 243.75 | 239.1 | 1.8×10^{10} | 5.82 0.06 | – |
| 47 | 11.448 | 242.86 | 249.1 | 4.9×10^{10} | 6.17 0.07 | – |
| 48 | 11.507 | 243.81 | 329.9 | 9.7×10^{12} | 8.04 0.21 | 0.409 |
| 49 | 11.529 | 243.02 | 300.0 | 8.8×10^{12} | 7.26 0.20 | 0.414 |
| 50 | 11.541 | 243.10 | 299.6 | 4.2×10^{12} | 7.18 0.16 | 0.563 |
| 51 | 11.474 | 243.18 | 299.8 | 1.4×10^{12} | 7.28 0.15 | 0.855 |
| 52 | 11.516 | 243.62 | 299.7 | 1.3×10^{12} | 7.27 0.15 | 0.968 |
| 53 | 11.534 | 243.72 | 299.9 | 1.6×10^{12} | 7.28 0.15 | 0.839 |
| 54 | 11.547 | 243.70 | 299.9 | 1.7×10^{12} | 7.25 0.15 | 0.800 |
| 55 | 11.828 | 244.92 | 299.8 | 7.7×10^{10} | 7.43 0.06 | – |
| 56 | 11.562 | 244.02 | 299.8 | 3.2×10^{11} | 7.28 0.06 | – |
| 57 | 11.497 | 243.00 | 299.5 | 4.9×10^{12} | 7.34 0.15 | 0.503 |
| 63 | 11.552 | 243.17 | 300.1 | 4.5×10^{12} | 7.37 0.17 | 0.525 |
| 64 | 11.486 | 243.08 | 249.1 | 3.3×10^{10} | 6.01 0.06 | – |
| 65 | 11.501 | 243.14 | 249.0 | 3.4×10^{10} | 6.07 0.06 | – |
| 66 | 11.492 | 243.08 | 249.5 | 5.3×10^{10} | 6.07 0.07 | – |
| 70 | 11.529 | 243.14 | 324.7 | 1.3×10^{13} | 8.13 0.20 | 0.375 |

Note: n is the droplet density after the pulse, which is about 10% higher than during the pulse. The value dr^2/dt is the c parameter of Eq. 4.19; it is the growth rate of the squared radius at the beginning of the droplet growth, found from a fit of the growth curve. The value r_m is the expected maximum droplet radius found from the growth curve fit. If r_m is not specified, depletion is negligible and the dr^2/dt value is taken constant for the observed duration of droplet growth.

Table D.9: Droplet growth in methane and 25% carbon dioxide ($y_c = 0.250$)

| Exp. | p (bar) | T (K) | y_w (ppm) | n (m^{-3}) | dr^2/dt ($\mu m^2/s$) | r_m (μm) |
|------|-----------|---------|-------------|----------------------|---------------------------|-------------------|
| 61 | 11.189 | 241.44 | 299.6 | 9.4×10^{12} | 6.19 ± 0.19 | 0.419 |
| 62 | 11.218 | 241.59 | 299.4 | 6.1×10^{12} | 6.15 0.16 | 0.454 |
| 67 | 11.229 | 241.99 | 249.2 | 6.0×10^{10} | 4.80 0.06 | – |
| 68 | 11.280 | 241.87 | 273.8 | 8.1×10^{11} | 5.68 0.14 | 0.792 |
| 69 | 11.223 | 241.45 | 324.6 | 4.4×10^{13} | 7.08 0.38 | 0.246 |

Table D.10: Water nucleation data in helium: 2003 data

| Exp. | p_0 (bar) | T_0 (K) | p (bar) | T (K) | y_w (ppm) | S | n (m^{-3}) | J ($\text{m}^{-3}\text{s}^{-1}$) |
|------|-------------|-----------|-----------|---------|-------------|-------|-------------------------|--------------------------------------|
| 25 | 1.775 | 296.75 | 0.987 | 234.77 | 3415 | 15.08 | 1.38×10^{11} | 8.2×10^{14} |
| 27 | 1.775 | 296.45 | 0.970 | 232.92 | 3519 | 18.50 | 4.67×10^{12} | 2.5×10^{16} |
| 28 | 1.775 | 296.55 | 0.958 | 231.81 | 3479 | 20.28 | 1.70×10^{13} | 9.0×10^{16} |
| 29 | 1.775 | 296.95 | 0.992 | 235.44 | 3482 | 14.44 | 3.56×10^{10} | 2.7×10^{14} |
| 30 | 1.775 | 296.75 | 0.957 | 231.90 | 3316 | 19.13 | 2.96×10^{12} | 1.6×10^{16} |
| 31 | 1.775 | 297.25 | 0.965 | 233.06 | 2793 | 14.39 | 1.10×10^{10} | 6.4×10^{13} |
| 32 | 1.775 | 297.25 | 0.964 | 232.92 | 3021 | 15.77 | 7.06×10^{10} | 4.1×10^{14} |
| 35 | 1.663 | 296.75 | 0.941 | 236.42 | 3670 | 13.07 | 9.30×10^9 | 5.6×10^{13} |
| 39 | 1.613 | 296.35 | 0.943 | 239.19 | 4621 | 12.51 | 1.76×10^{10} | 1.0×10^{14} |
| 42 | 1.713 | 296.95 | 1.017 | 241.17 | 4525 | 10.91 | 6.21×10^9 | 3.1×10^{13} |
| 43 | 1.853 | 296.65 | 1.089 | 239.96 | 4518 | 13.11 | 1.14×10^{11} | 6.5×10^{14} |
| 44 | 1.853 | 296.75 | 1.094 | 240.50 | 4812 | 13.32 | 2.62×10^{11} | 1.4×10^{15} |
| 45 | 1.893 | 296.75 | 1.049 | 234.45 | 3207 | 15.55 | 2.20×10^{11} | 1.3×10^{15} |
| 46 | 1.913 | 296.85 | 1.096 | 237.65 | 3552 | 13.01 | 5.90×10^{10} | 3.0×10^{14} |
| 47 | 1.903 | 296.85 | 1.053 | 234.44 | 3890 | 18.97 | 3.42×10^{13} | 1.8×10^{17} |
| 48 | 1.955 | 296.85 | 1.017 | 228.67 | 2484 | 21.52 | 8.20×10^{12} | 4.4×10^{16} |
| 49 | 1.955 | 296.95 | 1.010 | 228.05 | 2252 | 20.72 | 2.43×10^{12} | 1.4×10^{16} |
| 50 | 1.955 | 296.95 | 1.013 | 228.39 | 1902 | 16.93 | 4.36×10^{10} | 2.7×10^{14} |
| 51 | 2.015 | 296.75 | 1.001 | 224.34 | 1806 | 24.93 | 6.16×10^{12} | 4.7×10^{16} |
| 52 | 2.013 | 296.85 | 0.980 | 222.67 | 1763 | 28.91 | 3.56×10^{13} | 2.3×10^{17} |
| 53 | 2.015 | 297.05 | 0.973 | 222.05 | 1386 | 24.26 | 1.12×10^{12} | 6.4×10^{15} |
| 54 | 2.095 | 296.65 | 0.970 | 218.10 | 1199 | 33.58 | 3.33×10^{13} | 1.9×10^{17} |
| 55 | 2.095 | 296.85 | 0.944 | 215.84 | 903 | 32.53 | 2.46×10^{12} | 1.4×10^{16} |
| 58 | 2.095 | 296.75 | 0.970 | 218.18 | 1202 | 33.34 | 3.18×10^{13} | 1.7×10^{17} |
| 59 | 2.095 | 296.25 | 0.974 | 218.08 | 1004 | 28.27 | 9.14×10^{11} | 5.8×10^{15} |
| 60 | 2.095 | 296.05 | 0.945 | 215.37 | 852 | 32.57 | 2.60×10^{12} | 1.5×10^{16} |
| 62 | 2.407 | 296.25 | 1.005 | 208.92 | 400 | 37.62 | 4.97×10^{11} | 3.7×10^{15} |
| 66 | 2.407 | 295.85 | 1.015 | 209.48 | 450 | 39.68 | 1.52×10^{12} | 9.5×10^{15} |
| 67 | 2.407 | 295.75 | 1.003 | 208.36 | 351 | 35.56 | 1.96×10^{11} | 1.3×10^{15} |
| 68 | 2.639 | 295.85 | 1.056 | 205.10 | 291 | 48.74 | 3.74×10^{12} | 2.2×10^{16} |
| 69 | 2.639 | 296.35 | 1.077 | 207.06 | 274 | 35.63 | 9.19×10^{11} | 5.5×10^{15} |
| 70 | 2.639 | 296.25 | 1.067 | 206.22 | 274 | 39.61 | 3.93×10^{11} | 2.2×10^{15} |
| 73 | 2.659 | 296.45 | 1.017 | 201.83 | 204 | 52.48 | 1.61×10^{12} | 1.0×10^{16} |
| 74 | 2.659 | 296.35 | 1.014 | 201.52 | 172 | 46.15 | 5.93×10^{11} | 3.6×10^{15} |
| 75 | 2.659 | 296.20 | 1.010 | 201.13 | 187 | 52.79 | 1.05×10^{12} | 6.1×10^{15} |
| 77 | 2.106 | 297.25 | 0.926 | 214.05 | 857 | 37.97 | 6.34×10^{12} | 3.9×10^{16} |
| 82 | 2.617 | 296.65 | 1.017 | 203.29 | 275 | 57.26 | 8.62×10^{12} | 5.6×10^{16} |
| 83 | 2.403 | 296.85 | 0.998 | 208.87 | 452 | 42.52 | 2.47×10^{12} | 1.7×10^{16} |
| 84 | 2.400 | 296.85 | 0.998 | 209.00 | 502 | 46.47 | 1.94×10^{12} | 1.3×10^{16} |
| 87 | 1.939 | 296.05 | 0.988 | 226.11 | 1794 | 20.04 | 5.41×10^{10} | 3.1×10^{14} |

Table D.11: Water–helium mixture 2003

| Exp. | T_{sat} (K) | p_{sat} (bar) | f_e | γ_w^s (ppm) | Q_m (L/min) | Q_0 (L/min) | y_w (ppm) |
|------|----------------------|------------------------|--------|--------------------|---------------|---------------|-------------|
| 25 | 290.53 | 5.199 | 1.0039 | 3831 | 3.915 | 0.479 | 3415 |
| 27 | 295.82 | 5.199 | 1.0038 | 5318 | 3.802 | 1.953 | 3519 |
| 28 | 295.83 | 5.199 | 1.0038 | 5319 | 4.199 | 2.231 | 3479 |
| 29 | 295.82 | 5.199 | 1.0038 | 5318 | 3.373 | 1.788 | 3482 |
| 30 | 295.36 | 5.199 | 1.0038 | 5171 | 3.198 | 1.798 | 3316 |
| 31 | 295.82 | 5.199 | 1.0038 | 5318 | 2.589 | 2.353 | 2793 |
| 32 | 295.82 | 5.199 | 1.0038 | 5318 | 2.829 | 2.163 | 3021 |
| 35 | 292.15 | 5.199 | 1.0039 | 4241 | 4.313 | 0.674 | 3670 |
| 39 | 290.68 | 4.350 | 1.0032 | 4621 | 2.792 | 0.000 | 4621 |
| 42 | 290.68 | 3.980 | 1.0030 | 5050 | 3.418 | 0.399 | 4525 |
| 43 | 290.67 | 3.980 | 1.0030 | 5044 | 3.045 | 0.356 | 4518 |
| 44 | 290.67 | 3.980 | 1.0030 | 5045 | 3.601 | 0.175 | 4812 |
| 45 | 290.68 | 3.980 | 1.0030 | 5048 | 2.185 | 1.261 | 3207 |
| 46 | 290.68 | 3.980 | 1.0030 | 5049 | 2.404 | 1.018 | 3552 |
| 47 | 290.68 | 4.000 | 1.0030 | 5024 | 2.648 | 0.775 | 3891 |
| 48 | 290.69 | 5.039 | 1.0038 | 3992 | 2.389 | 1.456 | 2484 |
| 49 | 290.68 | 4.999 | 1.0037 | 4023 | 1.921 | 1.517 | 2252 |
| 50 | 290.69 | 5.998 | 1.0045 | 3356 | 1.722 | 1.321 | 1902 |
| 51 | 290.68 | 5.998 | 1.0045 | 3355 | 1.804 | 1.553 | 1806 |
| 52 | 290.68 | 5.998 | 1.0045 | 3356 | 1.768 | 1.603 | 1763 |
| 53 | 290.69 | 5.998 | 1.0045 | 3356 | 1.396 | 1.990 | 1386 |
| 54 | 290.68 | 5.998 | 1.0045 | 3355 | 1.202 | 2.168 | 1199 |
| 55 | 290.69 | 5.998 | 1.0045 | 3356 | 0.856 | 2.332 | 903 |
| 58 | 290.67 | 5.998 | 1.0045 | 3352 | 1.187 | 2.131 | 1202 |
| 59 | 290.67 | 5.998 | 1.0045 | 3352 | 1.016 | 2.385 | 1004 |
| 60 | 290.67 | 5.998 | 1.0045 | 3352 | 0.875 | 2.578 | 852 |
| 62 | 290.68 | 7.997 | 1.0060 | 2521 | 0.535 | 2.850 | 400 |
| 66 | 290.68 | 14.091 | 1.0106 | 1437 | 1.187 | 2.611 | 450 |
| 67 | 290.68 | 14.091 | 1.0106 | 1437 | 0.774 | 2.396 | 351 |
| 68 | 290.69 | 14.091 | 1.0106 | 1438 | 0.626 | 2.465 | 291 |
| 69 | 290.68 | 14.091 | 1.0106 | 1437 | 0.457 | 1.943 | 274 |
| 70 | 290.68 | 14.091 | 1.0106 | 1436 | 0.439 | 1.863 | 274 |
| 73 | 290.68 | 14.091 | 1.0106 | 1437 | 0.328 | 1.985 | 204 |
| 74 | 290.68 | 14.091 | 1.0106 | 1437 | 0.277 | 2.037 | 172 |
| 75 | 290.67 | 14.091 | 1.0106 | 1436 | 0.300 | 2.011 | 187 |
| 77 | 290.68 | 5.998 | 1.0045 | 3354 | 0.688 | 2.011 | 857 |
| 82 | 290.67 | 14.191 | 1.0106 | 1426 | 0.526 | 2.205 | 275 |
| 83 | 290.67 | 14.191 | 1.0106 | 1426 | 0.784 | 1.690 | 452 |
| 84 | 290.67 | 14.171 | 1.0106 | 1428 | 0.880 | 1.624 | 502 |
| 87 | 290.68 | 6.018 | 1.0045 | 3343 | 1.001 | 0.867 | 1794 |

Table D.12: Water nucleation data in helium: 2004 data

| Exp. | p_0 (bar) | T_0 (K) | p (bar) | T (K) | y_w (ppm) | S | S_{corr} | n (m^{-3}) | J ($\text{m}^{-3}\text{s}^{-1}$) |
|---------|-------------|-----------|-----------|---------|-------------|-------|-------------------|-------------------------|--------------------------------------|
| 08-3, 1 | 1.921 | 294.25 | 0.966 | 223.55 | 1345 | 19.64 | 19.25 | 6.74×10^{10} | 3.9×10^{14} |
| 08-3, 2 | 1.921 | 295.05 | 0.981 | 225.53 | 1585 | 18.75 | 19.44 | 9.33×10^{10} | 5.2×10^{14} |
| 08-3, 3 | 1.921 | 295.45 | 0.969 | 224.75 | 1829 | 23.35 | 23.73 | 5.11×10^{12} | 2.8×10^{16} |
| 08-3, 4 | 1.919 | 295.55 | 0.965 | 224.59 | 1716 | 22.24 | 22.49 | 1.21×10^{12} | 7.4×10^{15} |
| 09-3, 1 | 1.923 | 294.45 | 0.968 | 223.84 | 1651 | 23.37 | 23.06 | 3.56×10^{12} | 2.0×10^{16} |
| 09-3, 2 | 1.921 | 295.05 | 0.965 | 224.10 | 1626 | 22.27 | 22.18 | 7.76×10^{11} | 4.4×10^{15} |
| 10-3, 1 | 1.921 | 293.95 | 0.966 | 223.35 | 1596 | 23.85 | 23.15 | 2.10×10^{12} | 1.2×10^{16} |
| 11-3, 1 | 2.330 | 294.35 | 0.984 | 208.52 | 416 | 40.49 | 40.06 | 1.08×10^{12} | 7.0×10^{15} |
| 11-3, 2 | 2.331 | 295.05 | 0.980 | 208.64 | 403 | 38.45 | 38.19 | 4.23×10^{11} | 2.9×10^{15} |
| 11-3, 4 | 2.329 | 295.45 | 0.980 | 209.02 | 397 | 35.95 | 36.20 | 1.53×10^{11} | 9.6×10^{14} |
| 12-3, 1 | 2.330 | 294.25 | 0.985 | 208.55 | 439 | 42.57 | 42.15 | 2.10×10^{12} | 1.3×10^{16} |
| 12-3, 3 | 2.330 | 295.55 | 0.984 | 209.35 | 419 | 36.45 | 37.15 | 2.75×10^{11} | 1.7×10^{15} |
| 13-3, 1 | 2.562 | 294.35 | 1.025 | 204.04 | 304 | 57.33 | 59.67 | 4.88×10^{12} | 3.0×10^{16} |
| 13-3, 3 | 2.561 | 295.15 | 0.988 | 201.64 | 235 | 60.32 | – | 1.23×10^{12} | 8.3×10^{15} |
| 16-3, 1 | 2.564 | 294.55 | 1.004 | 202.43 | 216 | 50.17 | 48.86 | 1.97×10^{11} | 1.2×10^{15} |
| 16-3, 4 | 2.562 | 295.95 | 1.010 | 203.99 | 224 | 41.98 | 43.40 | 6.63×10^{10} | 3.8×10^{14} |
| 16-3, 5 | 2.563 | 296.05 | 0.994 | 202.66 | 225 | 50.20 | 49.35 | 3.09×10^{11} | 2.0×10^{15} |
| 16-3, 6 | 2.563 | 296.05 | 1.008 | 203.82 | 252 | 48.23 | 49.64 | 3.30×10^{11} | 2.3×10^{15} |
| 17-3, 2 | 2.565 | 295.75 | 0.993 | 202.39 | 252 | 58.27 | 56.56 | 1.94×10^{12} | 1.2×10^{16} |
| 17-3, 3 | 2.563 | 295.85 | 1.017 | 204.39 | 243 | 43.17 | 45.29 | 4.98×10^{10} | 4.5×10^{14} |
| 18-3, 1 | 2.564 | 295.65 | 0.991 | 202.15 | 243 | 58.12 | 55.85 | 7.26×10^{11} | 4.6×10^{15} |
| 18-3, 2 | 2.564 | 296.25 | 1.000 | 203.29 | 262 | 53.63 | 54.11 | 9.48×10^{11} | 6.5×10^{15} |
| 18-3, 3 | 2.564 | 296.55 | 1.022 | 205.28 | 262 | 41.33 | – | 1.35×10^{11} | 9.2×10^{14} |
| 18-3, 4 | 2.563 | 296.65 | 0.986 | 202.47 | 262 | 59.42 | 57.88 | 3.32×10^{12} | 2.1×10^{16} |
| 19-3, 1 | 2.563 | 295.75 | 0.994 | 202.50 | 216 | 49.16 | 48.06 | 2.45×10^{11} | 1.6×10^{15} |
| 19-3, 2 | 2.563 | 296.25 | 0.995 | 202.88 | 243 | 52.43 | 52.01 | 9.04×10^{11} | 5.7×10^{15} |

Table D.13: Water–helium mixture 2004

| Exp. | T_{sat} (K) | p_{sat} (bar) | f_e | y_w^s (ppm) | Q_m (L/min) | Q_0 (L/min) | y_w (ppm) |
|---------|----------------------|------------------------|--------|---------------|---------------|---------------|-------------|
| 08-3, 1 | 290.68 | 10.004 | 1.0075 | 2017 | 1.682 | 0.843 | 1345 |
| 08-3, 2 | 290.67 | 10.004 | 1.0075 | 2017 | 1.720 | 0.469 | 1585 |
| 08-3, 3 | 290.68 | 10.004 | 1.0075 | 2017 | 2.232 | 0.230 | 1829 |
| 08-3, 4 | 290.67 | 10.011 | 1.0075 | 2015 | 1.951 | 0.341 | 1716 |
| 09-3, 1 | 290.68 | 10.011 | 1.0075 | 2016 | 1.849 | 0.410 | 1651 |
| 09-3, 2 | 290.68 | 10.004 | 1.0075 | 2017 | 1.702 | 0.410 | 1626 |
| 10-3, 1 | 290.68 | 10.004 | 1.0075 | 2017 | 1.516 | 0.401 | 1596 |
| 11-3, 1 | 290.68 | 10.004 | 1.0075 | 2017 | 0.438 | 1.689 | 416 |
| 11-3, 2 | 290.68 | 10.004 | 1.0075 | 2018 | 0.461 | 1.850 | 403 |
| 11-3, 4 | 290.68 | 10.004 | 1.0075 | 2017 | 0.460 | 1.883 | 397 |
| 12-3, 1 | 290.68 | 9.997 | 1.0075 | 2019 | 0.482 | 1.739 | 439 |
| 12-3, 3 | 290.67 | 10.004 | 1.0075 | 2017 | 0.429 | 1.638 | 419 |
| 13-3, 1 | 290.68 | 11.005 | 1.0082 | 1835 | 0.364 | 1.835 | 304 |
| 13-3, 3 | 290.68 | 18.016 | 1.0135 | 1127 | 0.320 | 1.213 | 235 |
| 16-3, 1 | 290.68 | 18.016 | 1.0135 | 1127 | 0.364 | 1.538 | 216 |
| 16-3, 4 | 290.68 | 18.016 | 1.0135 | 1127 | 0.375 | 1.513 | 224 |
| 16-3, 5 | 290.68 | 18.016 | 1.0135 | 1127 | 0.375 | 1.503 | 226 |
| 16-3, 6 | 290.68 | 18.016 | 1.0135 | 1127 | 0.424 | 1.473 | 252 |
| 17-3, 2 | 290.68 | 18.016 | 1.0135 | 1127 | 0.464 | 1.613 | 252 |
| 17-3, 3 | 290.68 | 18.016 | 1.0135 | 1127 | 0.447 | 1.633 | 243 |
| 18-3, 1 | 290.68 | 18.016 | 1.0135 | 1127 | 0.468 | 1.704 | 243 |
| 18-3, 2 | 290.68 | 18.009 | 1.0135 | 1127 | 0.505 | 1.671 | 262 |
| 18-3, 3 | 290.68 | 18.009 | 1.0135 | 1128 | 0.505 | 1.673 | 262 |
| 18-3, 4 | 290.68 | 18.009 | 1.0135 | 1127 | 0.505 | 1.673 | 262 |
| 19-3, 1 | 290.68 | 18.016 | 1.0135 | 1127 | 0.422 | 1.784 | 216 |
| 19-3, 2 | 290.68 | 18.016 | 1.0135 | 1127 | 0.473 | 1.724 | 243 |

Summary

Water nucleation: wave tube experiments and theoretical considerations

This work is an experimental and theoretical study of the condensation of water. Condensation consists of nucleation – the formation of droplets – and the subsequent growth of those droplets. In our expansion tube setup, these processes are separated in time with the nucleation pulse principle, in the following manner. First, a mixture of water vapour and a carrier gas is cooled down by means of an adiabatic expansion. Nucleation then takes place during a period of constant pressure, temperature, and supersaturation; this period is called the nucleation pulse. At the end of the pulse, the gas is slightly recompressed, which ends the formation of new droplets. A state of supersaturation is maintained, so that the existing droplets grow until they become large enough to be detected. The number density of droplets is inferred from the extinction of a laser beam and the scattered light from the droplets. The ratio of the number density of detected droplets and the pulse duration yields the nucleation rate: the number of macroscopic droplets that are formed per unit of space and time.

The fraction of droplets that is detected after use of the nucleation pulse method has been analysed theoretically by two condensation models. The first is based on the kinetic master equation, which describes the growth of molecular clusters of arbitrary size by collisions with monomers. The second model is based on the general dynamic equation (GDE), which is often used in aerosol science. It was found that the GDE is inaccurate for small droplets, whereas it agrees with the kinetic equation for large droplets. The nucleation pulse analysis shows that after short pulses, a significant number of droplets evaporate, resulting in a systematic underestimation of the nucleation rate. In contrast, for our experimental pulse length, the number of droplets that evaporate after the pulse is negligible.

The nucleation rates of water have been measured with helium as a carrier gas, at a nucleation pressure of 1 bar and nucleation temperatures between 200 and 240 K. Our nucleation rates agree with accurate measurements by Wölk and Strey in the temperature and nucleation rate range of

overlap. The results provide an extension of nucleation rate measurements to high supersaturations and low temperatures. Classical nucleation theory predicts an incorrect temperature dependence of the nucleation rate; this is well known. Contrary to what is usually assumed, our results demonstrate that the supersaturation dependence of the classical rate is incorrect as well. As the temperature dependence of the experimental rates is smooth, we assume that down to 200 K water condenses as supercooled liquid drops, which remain liquid during our measurement time (15 ms). Supercooled water does not normally exist below 233 K and its properties there are unknown, which makes the theoretical predictions more uncertain.

Water nucleation has also been studied in a mixture of methane and carbon dioxide, a system that is important for the natural gas industry. To model nucleation, a description of the equilibrium composition in the water–methane–carbon dioxide system was required. Therefore, a suitable ‘cubic plus association’ (CPA) equation of state was selected and fitted to experimental data. For that purpose, literature data on phase equilibrium in the three binary systems water–methane, water–carbon dioxide, and methane–carbon dioxide was summarized and reviewed. The literature data on water vapour fractions in the two binary systems with water is inaccurate and inconsistent, and the CPA prediction is accurate to 5%, at best. On the other hand, the solubility of methane or carbon dioxide in water is reproduced well. The validity range of the CPA equation of state from this work is 220–340 K and 0–50 bar.

Another quantity that is required for the prediction of the nucleation rate is the surface tension of water. For natural-gas-like systems, the influence of methane and carbon dioxide on the surface tension should be known. Therefore, literature data were collected and are summarized by empirical fits that are accurate to 0.5% in the range of experimental data. The fits can be extrapolated down to 235 K, but the relative uncertainty of the surface tension is then about 5%, which strongly affects the prediction of nucleation rates.

Water nucleation rates were measured at 235 K and 10 bar in pure methane, and also in two mixtures of methane and carbon dioxide. The nucleation rate in methane was found to be about three orders of magnitude higher than the nucleation rate of water in helium at 1 bar, at equal temperature and supersaturation. The increase is likely caused by the reduction of the water surface tension by methane; the relative decrease of surface tension is estimated at 3.5%.

In our measurements with carbon dioxide we encountered problems in reproducing measurements on the long term. Within a measurement series, carried out in a few months, reproducibility of the nucleation rate was better than a factor of two, but we observed differences of a factor of four between series performed in June and October 2007. The relative effect of car-

bon dioxide, however, is clear because experiments with and without carbon dioxide were performed consecutively. This allows drawing the following conclusions: The presence of 3% carbon dioxide beside methane increases the nucleation rate by one order of magnitude, compared to the rate in pure methane. Furthermore, 25% carbon dioxide increases the rate by four orders of magnitude, compared to pure methane. This effect is also explained by a decrease in surface tension. For 25% carbon dioxide, the estimated relative decrease of the surface tension is 13%, compared to the pure-water surface tension.

In view of the large uncertainties at 235 K in the predictions of the CPA equation of state and in the surface tension, a direct, quantitative comparison between experimental and theoretical nucleation rates in our systems is of limited value. The effect of carbon dioxide on the nucleation rate is qualitatively reproduced by the classical nucleation theory, however.

The so-called nucleation theorem provides a way to deduce the properties of the critical cluster – the smallest stable molecular cluster – from experimental nucleation rate data. For water nucleation in methane at 235 K and 10 bar, the critical cluster consists of 22 water molecules and 5 methane molecules. The fraction of methane molecules in the cluster is a hundred times larger than the equilibrium fraction at those conditions, which indicates that the properties of small clusters strongly deviate from the macroscopic properties.

Besides nucleation rates, growth rates of water droplets were measured in methane and in methane–carbon dioxide mixtures. At equal temperature, pressure and water vapour fraction, the growth rate of the squared droplet radius is about 20% lower in the mixture with 25% carbon dioxide than in pure methane. The lower growth rate is caused by a smaller diffusion coefficient of water in the mixture with carbon dioxide; the difference of the diffusion coefficients is qualitatively reproduced by the empirical Fuller correlation.

References

- 1 Evolution – the key to sustainable innovation, *EP Technology magazine* **2008**(4), 14 (2008), published by Shell International Exploration and Production.
- 2 R.J.E. van Wissen, *Centrifugal separation for cleaning well gas streams: from concept to prototype*, Ph.D. thesis, Technische Universiteit Eindhoven (2006).
- 3 G.P. Willems, *Condensed rotational cleaning of natural gas*, Ph.D. thesis, Technische Universiteit Eindhoven (2009).
- 4 K.N.H. Looijmans and M.E.H. van Dongen, A pulse–expansion wave tube for nucleation studies at high pressures, *Exp. Fluids* **23**, 54 (1997).
- 5 C.C.M. Luijten, K.J. Bosschaart, and M.E.H. van Dongen, High pressure nucleation in water/nitrogen systems, *J. Chem. Phys.* **106**, 8116 (1997).
- 6 C.C.M. Luijten, P. Peeters, and M.E.H. van Dongen, Nucleation at high pressure. II. Wave tube data and analysis, *J. Chem. Phys.* **111**, 8535 (1999).
- 7 D.G. Labetski, V. Holten, and M.E.H. van Dongen, Comment on ‘The nucleation behavior of supercooled water vapor in helium’ [J. Chem. Phys. **117**, 5647 (2002)], *J. Chem. Phys.* **120**, 6314 (2004).
- 8 P. Peeters, J. Hrubý, and M.E.H. van Dongen, High pressure nucleation experiments in binary and ternary mixtures, *J. Phys. Chem. B* **105**, 11763 (2001).
- 9 K.N.H. Looijmans, *Homogeneous nucleation and droplet growth in the coexistence region of n-alkane/methane mixtures at high pressures*, Ph.D. thesis, Technische Universiteit Eindhoven (1995).
- 10 D. Labetski, *Nucleation of n-nonane in mixtures of methane, propane, and carbon dioxide*, Ph.D. thesis, Technische Universiteit Eindhoven (2007).
- 11 V.I. Kalikmanov and D.G. Labetski, Theory of anomalous critical-cluster content in high-pressure binary nucleation, *Phys. Rev. Lett.* **98**, 085701 (2007).
- 12 C.C.M. Luijten, R.G.P. van Hooy, J.W.F. Janssen, and M.E.H. van Dongen, Multicomponent nucleation and droplet growth in natural gas, *J. Chem. Phys.* **109**, 3553 (1998).
- 13 C.C.M. Luijten and M.E.H. van Dongen, Nucleation at high pressure. I. Theoretical considerations, *J. Chem. Phys.* **111**, 8524 (1999).
- 14 W. Wagner and A. Pruß, The IAPWS formulation 1995 for the thermodynamic properties of ordinary water substance for general and scientific use, *J. Phys. Chem. Ref. Data* **31**, 387 (2002), see also the IAPWS release (ref. 15).
- 15 *Release on the IAPWS Formulation 1995 for the Thermodynamic Properties of Ordinary Water Substance for General and Scientific Use*, IAPWS (1996).
• <http://www.iapws.org/relguide/IAPWS95.pdf>
- 16 C.T.R. Wilson, Condensation of water vapour in the presence of dust-free air and other gases, *Philos. Trans. R. Soc. London, Ser. A* **189**, 265 (1897).
- 17 R.H. Heist and H. Reiss, Investigation of the homogeneous nucleation of water vapor using a diffusion cloud chamber, *J. Chem. Phys.* **59**, 665 (1973).
- 18 R.C. Miller, R.J. Anderson, J.L. Kassner, and D.E. Hagen, Homogeneous nucleation rate measurements for water over a wide range of

- temperature and nucleation rate, *J. Chem. Phys.* **78**, 3204 (1983).
- 19 J. Wölk and R. Strey, Homogeneous nucleation of H₂O and D₂O in comparison: The isotope effect, *J. Phys. Chem. B* **105**, 11683 (2001).
 - 20 E. A. Boucher, Nucleation in the atmosphere, in *Nucleation*, edited by A. C. Zettlemoyer (Marcel Dekker, New York, 1969), chapter 10, pp. 528, 535.
 - 21 F. F. Abraham, *Homogeneous Nucleation Theory: The Pretransition Theory of Vapor Condensation* (Academic, New York, 1974).
 - 22 D. Kashchiev, *Nucleation: Basic Theory with Applications* (Butterworth-Heinemann, Oxford, 2000).
 - 23 H. Vehkamäki, *Classical Nucleation Theory in Multicomponent Systems* (Springer, Berlin, 2006).
 - 24 R. G. Van Name and W. R. Longley (editors), *The Collected Works of J. Willard Gibbs* (Longmans, London, 1928).
 - 25 B. E. Poling, J. M. Prausnitz, and J. P. O'Connell, *The Properties of Gases and Liquids* (McGraw-Hill, New York, 2001), fifth edition.
 - 26 K. Stephan and F. Mayinger, *Mehrstoffsysteme und chemische Reaktionen*, volume 2 of *Thermodynamik: Grundlagen und technische Anwendungen* (Springer, Berlin, 1988), twelfth edition.
 - 27 P. W. Atkins, *Physical Chemistry* (Oxford University Press, 1998), sixth edition.
 - 28 G. Soave, Equilibrium constants from a modified Redlich-Kwong equation of state, *Chem. Eng. Sci.* **27**, 1197 (1972).
 - 29 O. Redlich and J. N. S. Kwong, On the thermodynamics of solutions. V. An equation of state. Fugacities of gaseous solutions, *Chem. Rev.* **44**, 233 (1949).
 - 30 D.-Y. Peng and D. B. Robinson, A new two-constant equation of state, *Ind. Eng. Chem. Fundam.* **15**, 59 (1976).
 - 31 F. Dolezalek, Theory of binary mixtures and concentrated solutions, *Z. Phys. Chem.* **64**, 727 (1908).
 - 32 R. A. Heidemann and J. M. Prausnitz, A van der Waals type equation of state for fluids of associating molecules, *Proc. Natl. Acad. Sci. U.S.A.* **73**, 1773 (1976).
 - 33 M. S. Wertheim, Fluids with highly directional attractive forces. I. Statistical thermodynamics, *J. Stat. Phys.* **35**, 19 (1984).
 - 34 W. G. Chapman, K. E. Gubbins, G. Jackson, and M. Radosz, New reference equation of state for associating liquids, *Ind. Eng. Chem. Res.* **29**, 1709 (1990).
 - 35 S. H. Huang and M. Radosz, Equation of state for small, large, polydisperse, and associating molecules, *Ind. Eng. Chem. Res.* **29**, 2284 (1990).
 - 36 S. H. Huang and M. Radosz, Equation of state for small, large, polydisperse, and associating molecules: Extension to fluid mixtures, *Ind. Eng. Chem. Res.* **30**, 1994 (1991).
 - 37 E. A. Müller and K. E. Gubbins, Molecular-based equations of state for associating fluids: A review of SAFT and related approaches, *Ind. Eng. Chem. Res.* **40**, 2193 (2001).
 - 38 J. M. Prausnitz, R. N. Lichtenthaler, and E. Gomes de Azevedo, *Molecular Thermodynamics of Fluid-Phase Equilibria* (Prentice Hall PTR, 1999), third edition.
 - 39 G. M. Kontogeorgis, E. C. Voutsas, I. V. Yakoumis, and D. P. Tassios, An equation of state for associating fluids, *Ind. Eng. Chem. Res.* **35**, 4310 (1996).
 - 40 G. M. Kontogeorgis, M. L. Michelsen, G. K. Folas, S. Derawi, N. von Solms, and E. H. Stenby, Ten years with the CPA (cubic-plus-association) equation of state. Part 1. Pure compounds and self-associating systems, *Ind. Eng. Chem. Res.* **45**, 4855 (2006).
 - 41 G. M. Kontogeorgis, M. L. Michelsen, G. K. Folas, S. Derawi, N. von Solms, and E. H. Stenby, Ten years with the CPA (cubic-plus-association) equation of state. Part 2. Cross-associating and multicomponent systems, *Ind. Eng. Chem. Res.* **45**, 4869 (2006).
 - 42 M. L. Michelsen and E. M. Hendriks, Physical properties from association models, *Fluid Phase Equilib.* **180**, 165 (2001).
 - 43 D. Chandler, *Introduction to Modern Statistical Mechanics* (Oxford University Press, 1987).
 - 44 G. A. Mansoori, N. F. Carnahan, K. E. Starling, and T. W. Leland, Jr., Equilibrium

- thermodynamic properties of the mixture of hard spheres, *J. Chem. Phys.* **54**, 1523 (1971).
- 45 I. V. Yakoumis, G. M. Kontogeorgis, E. C. Voutsas, and D. P. Tassios, Vapor-liquid equilibria for alcohol/hydrocarbon systems using the CPA equation of state, *Fluid Phase Equilib.* **130**, 31 (1997).
- 46 G. M. Kontogeorgis, I. V. Yakoumis, H. Meijer, E. Hendriks, and T. Moorwood, Multicomponent phase equilibrium calculations for water-methanol-alkane mixtures, *Fluid Phase Equilib.* **158-160**, 201 (1999).
- 47 O. Pfohl, A. Pagel, and G. Brunner, Phase equilibria in systems containing o-cresol, p-cresol, carbon dioxide, and ethanol at 323.15-473.15 K and 10-35 MPa, *Fluid Phase Equilib.* **157**, 53 (1999).
- 48 S. J. Suresh and J. R. Elliott, Jr., Multiphase equilibrium analysis via a generalized equation of state for associating mixtures, *Ind. Eng. Chem. Res.* **31**, 2783 (1992).
- 49 E. C. Voutsas, I. V. Yakoumis, and D. P. Tassios, Prediction of phase equilibria in water-alcohol-alkane systems, *Fluid Phase Equilib.* **158-160**, 151 (1999).
- 50 C. Perakis, E. Voutsas, K. Magoulas, and D. Tassios, Thermodynamic modeling of the vapor-liquid equilibrium of the water/ethanol/CO₂ system, *Fluid Phase Equilib.* **243**, 142 (2006).
- 51 C. A. Perakis, E. C. Voutsas, K. G. Magoulas, and D. P. Tassios, Thermodynamic modeling of the water + acetic acid + CO₂ system: The importance of the number of association sites of water and of the nonassociation contribution for the CPA and SAFT-type models, *Ind. Eng. Chem. Res.* **46**, 932 (2007).
- 52 E. Voutsas, C. Perakis, G. Pappa, and D. Tassios, An evaluation of the performance of the cubic-plus-association equation of state in mixtures of non-polar, polar and associating compounds: Towards a single model for non-polymeric systems, *Fluid Phase Equilib.* **261**, 343 (2007).
- 53 G. K. Folas, G. M. Kontogeorgis, M. L. Michelsen, and E. H. Stenby, Application of the cubic-plus-association (CPA) equation of state to complex mixtures with aromatic hydrocarbons, *Ind. Eng. Chem. Res.* **45**, 1527 (2006).
- 54 G. K. Folas, E. W. Froyna, J. Lovland, G. M. Kontogeorgis, and E. Solbraa, Data and prediction of water content of high pressure nitrogen, methane and natural gas, *Fluid Phase Equilib.* **252**, 162 (2007).
- 55 O. Pfohl, T. Giese, R. Dohrn, and G. Brunner, 1. Comparison of 12 equations of state with respect to gas-extraction processes: Reproduction of pure-component properties when enforcing the correct critical temperature and pressure, *Ind. Eng. Chem. Res.* **37**, 2957 (1998).
- 56 K. S. Pitzer, D. Z. Lippmann, R. F. Curl, C. M. Huggins, and D. E. Petersen, The volumetric and thermodynamic properties of fluids. II. Compressibility factor, vapor pressure and entropy of vaporization, *J. Am. Chem. Soc.* **77**, 3433 (1955).
- 57 P. M. Mathias, A versatile phase equilibrium equation of state, *Ind. Eng. Chem. Process Des. Dev.* **22**, 385 (1983).
- 58 O. Pfohl, S. Petkov, and G. Brunner, "PE" quickly makes available the newest equations of state via the internet, *Ind. Eng. Chem. Res.* **39**, 4439 (2000).
- 59 PE 2000 for Windows (2002), version 2.99a.
• <http://www.tuhh.de/vt2/pe2000/>
- 60 M. L. Huber, *NIST Thermophysical Properties of Hydrocarbon Mixtures Database (SUPERTRAPP), version 3.1*, U.S. Department of Commerce, National Institute of Standards and Technology, Gaithersburg, MD (2003).
- 61 O. Kunz, R. Klimeck, W. Wagner, and M. Jaeschke, *The GERG-2004 Wide-Range Equation of State for Natural Gases and Other Mixtures, GERG Technical Monograph 15*, volume 557 of *Fortschritt-Berichte VDI Energieerzeugung* (VDI Verlag, Düsseldorf, 2007).
• http://www.gerg.info/publications/tm/tm15_04.pdf
- 62 W. Wagner, *Software package for the Calculation of Thermodynamic Properties from the GERG-2004 Wide-Range Reference Equation of State for Natural Gases and Other Mixtures*, Ruhr-Universität Bochum, Fakultät für Maschinenbau, Lehrstuhl für

- Thermodynamik, Bochum (2007), version 11.05.2007.
- 63 C. Jarne, S. T. Blanco, M. A. Gallardo, E. Rauzy, S. Otín, and I. Velasco, Dew points of ternary methane (or ethane) + carbon dioxide + water mixtures: Measurement and correlation, *Energy Fuels* **18**, 396 (2004).
- 64 C. Jarne, S. T. Blanco, M. Artal, E. Rauzy, S. Otín, and I. Velasco, Dew points of binary carbon dioxide + water and ternary carbon dioxide + water + methanol mixtures: Measurement and modelling, *Fluid Phase Equilib.* **216**, 85 (2004).
- 65 L. W. Diamond and N. N. Akinfiev, Solubility of CO₂ in water from -1.5 to 100 °C and from 0.1 to 100 MPa: evaluation of literature data and thermodynamic modelling, *Fluid Phase Equilib.* **208**, 265 (2003).
- 66 *Revised Release on the Pressure along the Melting and Sublimation Curves of Ordinary Water Substance*, IAPWS (2008).
• <http://www.iapws.org/relguide/meltsub.pdf>
- 67 D. M. Murphy and T. Koop, Review of the vapour pressures of ice and supercooled water for atmospheric applications, *Q. J. R. Meteorol. Soc.* **131**, 1539 (2005).
- 68 S. Aparicio-Martínez and K. R. Hall, Phase equilibria in water containing binary systems from molecular based equations of state, *Fluid Phase Equilib.* **254**, 112 (2007).
- 69 P. Peeters, *Nucleation and Condensation in Gas-Vapor mixtures of Alkanes and Water*, Ph.D. thesis, Technische Universiteit Eindhoven (2002).
- 70 C. Lundstrøm, M. L. Michelsen, G. M. Kontogeorgis, K. S. Pedersen, and H. Sørensen, Comparison of the SRK and CPA equations of state for physical properties of water and methanol, *Fluid Phase Equilib.* **247**, 149 (2006).
- 71 U. Setzmann and W. Wagner, A new equation of state and tables of thermodynamic properties for methane covering the range from the melting line to 625 K at pressures up to 1000 MPa, *J. Phys. Chem. Ref. Data* **20**, 1061 (1991).
- 72 R. Span and W. Wagner, A new equation of state for carbon dioxide covering the fluid region from the triple-point temperature to 1100 K at pressures up to 800 MPa, *J. Phys. Chem. Ref. Data* **25**, 1509 (1996).
- 73 E. W. Lemmon, M. O. McLinden, and D. G. Friend, Thermophysical properties of fluid systems, in *NIST Chemistry WebBook, NIST Standard Reference Database Number 69*, edited by P. J. Linstrom and W. G. Mallard (National Institute of Standards and Technology, Gaithersburg MD, 2009).
• <http://webbook.nist.gov/chemistry/fluid>
- 74 E. D. Sloan, Jr, *Clathrate Hydrates of Natural Gases* (Marcel Dekker, New York, 1998), second edition.
- 75 T. Y. Makogon and E. D. Sloan, Jr, Phase equilibrium for methane hydrate from 190 to 262 K, *J. Chem. Eng. Data* **40**, 344 (1995).
- 76 R. Sun and Z. Duan, Prediction of CH₄ and CO₂ hydrate phase equilibrium and cage occupancy from ab initio intermolecular potentials, *Geochim. Cosmochim. Acta* **69**, 4411 (2005).
- 77 A. H. Mohammadi, A. Chapoy, D. Richon, and B. Tohidi, Experimental measurement and thermodynamic modeling of water content in methane and ethane systems, *Ind. Eng. Chem. Res.* **43**, 7148 (2004).
- 78 A. Chapoy, *Phase Behaviour in Water/Hydrocarbon Mixtures Involved in Gas Production Systems*, Ph.D. thesis, École des Mines de Paris (2004).
• http://pastel.paristech.org/1202/01/These_Antonin_2_0.pdf
- 79 R. H. Olds, B. H. Sage, and W. N. Lacey, Composition of the dew-point gas of the methane-water system, *Ind. Eng. Chem. Res.* **34**, 1223 (1942).
- 80 K. Althaus, *Messung und Berechnung von Wassergehalten kohlenwasserstoffhaltiger Gasgemische*, volume 590 of *Fortschritt-Berichte VDI Verfahrenstechnik* (VDI Verlag, Düsseldorf, 1999), experimental data in Chapoy,⁷⁸ see also Ref. 81.
- 81 L. R. Oellrich and K. Althaus, *GERG - Water Correlation (GERG Technical Monograph TM 14): Relationship Between Water Content and Water Dew Point Keeping in Consideration the Gas Composition in the Field of Natural Gas*, volume 679 of *Fortschritt-Berichte VDI Verfahrenstechnik* (VDI Verlag, Düsseldorf, 2001).

- 82 M. Rigby and J.M. Prausnitz, Solubility of water in compressed nitrogen, argon, and methane, *J. Phys. Chem.* **72**, 330 (1968).
- 83 A. Chapoy, C. Coquelet, and D. Richon, Solubility measurement and modeling of water in the gas phase of the methane/water binary system at temperatures from 283.08 to 318.12 K and pressures up to 34.5 MPa, *Fluid Phase Equilib.* **214**, 101 (2003).
- 84 N.E. Kosyakov, B.I. Ivchenko, and P.P. Krishtopa, Solubility of moisture in compressed gases at low temperatures (in Russian), *Vopr. Khim. Khim. Tekhnol.* **68**, 33 (1982), citation and experimental data in Chapoy⁷⁸.
- 85 P.C. Gillespie and G.M. Wilson, *Vapor-Liquid and Liquid-Liquid Equilibria: Water-Methane, Water-Carbon Dioxide, Water-Hydrogen Sulfide, Water-n-Pentane, Water-Methane-n-Pentane*, Research Report RR-48, Gas Processors Association, Tulsa, Okla. (1982).
- 86 A. Chapoy, C. Coquelet, and D. Richon, Corrigendum to "Revised solubility data and modeling of water in the gas phase of the methane/water binary system at temperatures from 283.08 to 318.12 K and pressures up to 34.5 MPa", *Fluid Phase Equilib.* **230**, 210 (2005).
- 87 N.L. Yarym-Agaev, R.P. Sinyavskaya, I.I. Koliushko, and L. Ya. Levinton, Phase equilibria in the water-methane and methanol-methane binary systems under high pressures, *Zhurnal Prikladnoi Khimii* **58**, 165 (1985), English translation published by Plenum Publishing Corp.
- 88 A. Chapoy, A.H. Mohammadi, B. Tohidi, and D. Richon, Estimation of water content for methane + water and methane + ethane + n-butane + water systems using a new sampling device, *J. Chem. Eng. Data* **50**, 1157 (2005).
- 89 C. Yokoyama, S. Wakana, G.-I. Kaminishi, and S. Takahashi, Vapor-liquid equilibria in the methane-diethylene glycol-water system at 298.15 and 323.15 K, *J. Chem. Eng. Data* **33**, 274 (1988).
- 90 Z. Duan and S. Mao, A thermodynamic model for calculating methane solubility, density and gas phase composition of methane-bearing aqueous fluids from 273 to 523 K and from 1 to 2000 bar, *Geochim. Cosmochim. Acta* **70**, 3369 (2006).
- 91 A. Chapoy, A.H. Mohammadi, D. Richon, and B. Tohidi, Gas solubility measurement and modeling for methane-water and methane-ethane-n-butane-water systems at low temperature conditions, *Fluid Phase Equilib.* **220**, 113 (2004).
- 92 M. Wendland, H. Hasse, and G. Maurer, Experimental pressure-temperature data on three- and four-phase equilibria of fluid, hydrate, and ice phases in the system carbon dioxide-water, *J. Chem. Eng. Data* **44**, 901 (1999).
- 93 J. Longhi, Phase equilibria in the system CO₂-H₂O I: New equilibrium relations at low temperatures, *Geochim. Cosmochim. Acta* **69**, 529 (2005).
- 94 L. W. Diamond, Review of the systematics of CO₂-H₂O fluid inclusions, *Lithos* **55**, 69 (2001).
- 95 H.-J. Ng and D.B. Robinson, Hydrate formation in systems containing methane, ethane, propane, carbon dioxide or hydrogen sulfide in the presence of methanol, *Fluid Phase Equilib.* **21**, 145 (1985).
- 96 D. Li and Z. Duan, The speciation equilibrium coupling with phase equilibrium in the H₂O-CO₂-NaCl system from 0 to 250 °C, from 0 to 1000 bar, and from 0 to 5 molality of NaCl, *Chem. Geol.* **244**, 730 (2007).
- 97 N. Spycher, K. Pruess, and J. Ennis-King, CO₂-H₂O mixtures in the geological sequestration of CO₂. I. Assessment and calculation of mutual solubilities from 12 to 100 °C and up to 600 bar, *Geochim. Cosmochim. Acta* **67**, 3015 (2003).
- 98 Z. Duan, R. Sun, C. Zhu, and I.-M. Chou, An improved model for the calculation of CO₂ solubility in aqueous solutions containing Na⁺, K⁺, Ca²⁺, Mg²⁺, Cl⁻, and SO₄²⁻, *Mar. Chem.* **98**, 131 (2006).
- 99 R. Wiebe and V.L. Gaddy, Vapor phase composition of carbon dioxide-water mixtures at various temperatures and at pressures to 700 atmospheres, *J. Am. Chem. Soc.* **63**, 475 (1941).
- 100 C.R. Coan and A.D. King, Jr, Solubility of water in compressed carbon dioxide, nitrous

- oxide, and ethane. Evidence for hydration of carbon dioxide and nitrous oxide in the gas phase, *J. Am. Chem. Soc.* **93**, 1857 (1971).
- 101** A. Austegard, E. Solbraa, G. de Koeijer, and M.J. Mølnvik, Thermodynamic models for calculating mutual solubilities in H₂O–CO₂–CH₄ mixtures, *Chem. Eng. Res. Des.* **84**, 781 (2006).
- 102** X. Ji, S.P. Tan, H. Adidharma, and M. Radosz, SAFT1-RPM approximation extended to phase equilibria and densities of CO₂–H₂O and CO₂–H₂O–NaCl systems, *Ind. Eng. Chem. Res.* **44**, 8419 (2005).
- 103** T. Kihara, Self-crystallizing molecular models. II, *Acta Cryst.* **21**, 877 (1966).
- 104** J. Davalos, W.R. Anderson, R.E. Phelps, and A.J. Kidnay, Liquid–vapor equilibria at 250.00K for systems containing methane, ethane, and carbon dioxide, *J. Chem. Eng. Data* **21**, 81 (1976).
- 105** M.S.-W. Wei, T.S. Brown, A.J. Kidnay, and E.D. Sloan, Vapor + liquid equilibria for the ternary system methane + ethane + carbon dioxide at 230 K and its constituent binaries at temperatures from 207 to 270 K, *J. Chem. Eng. Data* **40**, 726 (1995).
- 106** J. Qin, R.J. Rosenbauer, and Z. Duan, Experimental measurements of vapor–liquid equilibria of the H₂O + CO₂ + CH₄ ternary system, *J. Chem. Eng. Data* **53**, 1246 (2008).
- 107** *IAPWS Release on Surface Tension of Ordinary Water Substance*, IAPWS (1994).
• <http://www.iapws.org/relguide/surf.pdf>
- 108** P.G. Debenedetti, Supercooled and glassy water, *J. Phys.: Condens. Matter* **15**, R1669 (2003).
- 109** P.T. Hacker, *Experimental values of the surface tension of supercooled water*, Technical Note 2510, National Advisory Committee for Aeronautics (1951).
• <http://naca.central.cranfield.ac.uk/reports/1951/naca-tn-2510.pdf>
- 110** M.A. Floriano and C.A. Angell, Surface tension and molar surface free energy and entropy of water to –27.2 °C, *J. Phys. Chem.* **94**, 4199 (1990).
- 111** E.H. Trinh and K. Ohsaka, Measurement of density, sound velocity, surface tension, and viscosity of freely suspended supercooled liquids, *Int. J. Thermophys.* **16**, 545 (1995).
- 112** Y.J. Lü and B. Wei, Second inflection point of water surface tension, *Appl. Phys. Lett.* **89**, 164106 (2006).
- 113** C.C.M. Luijten, *Nucleation and Droplet Growth at High Pressure*, Ph.D. thesis, Technische Universiteit Eindhoven (1998).
- 114** J. Hrubý, Nucleation and a new thermodynamic model of supercooled water, in *Nucleation and Atmospheric Aerosols 2004: 16th International Conference*, edited by M. Kasahara and M. Kulmala (Kyoto University Press, 2004), pp. 135–138.
- 115** V. Holten, D.G. Labetski, and M.E.H. van Dongen, Homogeneous nucleation of water between 200 and 240 K: New wave tube data and estimation of the Tolman length, *J. Chem. Phys.* **123**, 104505 (2005).
- 116** N.B. Vargaftik, B.N. Volkov, and L.D. Voljak, International tables of the surface tension of water, *J. Phys. Chem. Ref. Data* **12**, 817 (1983).
- 117** J.C. Eriksson, On the thermodynamic theory for the effect of pressure on surface tension, *Acta Chem. Scand.* **16**, 2199 (1962).
- 118** A. Hebach, A. Oberhof, N. Dahmen, A. Kögel, H. Ederer, and E. Dinjus, Interfacial tension at elevated pressures – measurements and correlations in the water + carbon dioxide system, *J. Chem. Eng. Data* **47**, 1540 (2002).
- 119** P. Chiquet, J.-L. Daridon, D. Broseta, and S. Thibeau, CO₂/water interfacial tensions under pressure and temperature conditions of CO₂ geological storage, *Energy Conversion and Management* **48**, 736 (2007).
- 120** B.-S. Chun and G.T. Wilkinson, Interfacial tension in high-pressure carbon dioxide mixtures, *Ind. Eng. Chem. Res.* **34**, 4371 (1995).
- 121** J.A. Barbero, L.G. Hepler, K.G. McCurdy, and P.R. Tremaine, Thermodynamics of aqueous carbon dioxide and sulfur dioxide: heat capacities, volumes, and the temperature dependence of ionization, *Can. J. Chem.* **61**, 2509 (1983).
- 122** Z. Duan, J. Hu, D. Li, and S. Mao, Densities of the CO₂–H₂O and CO₂–H₂O–NaCl systems up to 647 K and 100 MPa, *Energy Fuels* **22**, 1666 (2008).
- 123** W. Sachs and V. Meyn, Surface tension in the system methane/water: A glance at numeric and precision of the experimental method “pendent-drop” and precise experimental

- results in comparison with literature, *Erdöl Erdgas Kohle* **111**, 119 (1995).
- 124** K.A.G. Schmidt, G.K. Folas, and B. Kvamme, Calculation of the interfacial tension of the methane–water system with the linear gradient theory, *Fluid Phase Equilib.* **261**, 230 (2007).
- 125** W. Sachs and V. Meyn, Pressure and temperature dependence of the surface tension in the system natural gas/water: Principles of investigation and the first precise experimental data for pure methane/water at 25 °C up to 46.8 MPa, *Colloids Surf. A* **94**, 291 (1995).
- 126** C. Jho, D. Nealon, S. Shogbola, and A.D. King, Jr., Effect of pressure on the surface tension of water: Adsorption of hydrocarbon gases and carbon dioxide on water at temperatures between 0 and 50 °C, *J. Colloid Interface Sci.* **65**, 141 (1978).
- 127** Q.-Y. Ren, G.-J. Chen, W. Yan, and T.-M. Guo, Interfacial tension of (CO₂ + CH₄) + water from 298 K to 373 K and pressures up to 30 MPa, *J. Chem. Eng. Data* **45**, 610 (2000).
- 128** G. Koglbauer and M. Wendland, Water vapor concentration enhancement in compressed humid nitrogen, argon, and carbon dioxide measured by fourier transform infrared spectroscopy, *J. Chem. Eng. Data* **53**, 77 (2008).
- 129** J. Wedekind, A.-P. Hyvärinen, D. Brus, and D. Reguera, Unraveling the “pressure effect” in nucleation, *Phys. Rev. Lett.* **101**, 125703 (2008).
- 130** G. Wilemski, The Kelvin equation and self-consistent nucleation theory, *J. Chem. Phys.* **103**, 1119 (1995).
- 131** J. Frenkel, A general theory of heterophase fluctuations and pretransition phenomena, *J. Chem. Phys.* **7**, 538 (1939).
- 132** J. Frenkel, *Kinetic Theory of Liquids* (Dover, New York, 1955).
- 133** W.G. Courtney, Remarks on homogeneous nucleation, *J. Chem. Phys.* **35**, 2249 (1961).
- 134** S.L. Girshick and C.-P. Chiu, Kinetic nucleation theory: A new expression for the rate of homogeneous nucleation from an ideal supersaturated vapor, *J. Chem. Phys.* **93**, 1273 (1990).
- 135** L. Farkas, Keimbildungsgeschwindigkeit in übersättigten Dämpfen, *Z. Phys. Chem.* **125**, 236 (1927), in this article Farkas credits L. Szilard as the creator of the kinetic model of nucleation.
- 136** J.L. Katz and M.D. Donohue, A kinetic approach to homogeneous nucleation theory, in *Advances in Chemical Physics*, volume 40, edited by I. Prigogine and S.A. Rice (John Wiley, 1979), pp. 137–155.
- 137** W.G. Courtney, Non-steady-state nucleation, *J. Chem. Phys.* **36**, 2009 (1962).
- 138** Y. Okada and Y. Hara, Calculation of the sticking probability of a water molecule to a water cluster, *Earozoru Kenkyu (J. Aerosol Res. Japan)* **22**, 147 (2007).
- 139** D. Tabor, *Gases, liquids and solids* (Cambridge University Press, Cambridge, 1979), second edition.
- 140** J.C. Maxwell, Letter to Peter Guthrie Tait, 11 December 1867, in *The Scientific Letters and Papers of James Clerk Maxwell*, volume II, edited by P.M. Hardman (Cambridge University Press, Cambridge, UK, 1995), pp. 331–332.
- 141** W. Thomson, The kinetic theory of the dissipation of energy, in *Maxwell's Demon: Entropy, Information, Computing*, edited by H.S. Leff and A.F. Rex (Adam Hilger, Bristol, 1990), pp. 34–36.
- 142** J.L. Katz and H. Wiedersich, Nucleation theory without Maxwell demons, *J. Colloid Interface Sci.* **61**, 351 (1977).
- 143** J.E. McDonald, Homogeneous nucleation of vapor condensation. II. Kinetic aspects, *Amer. J. Phys.* **31**, 31 (1963), reprinted in Ref. 21 on pp 238–256.
- 144** B.E. Wyslouzil and G. Wilemski, Binary nucleation kinetics. III. Transient behavior and time lags, *J. Chem. Phys.* **105**, 1090 (1996).
- 145** E.N. Chesnokov and L.N. Krasnoperov, Complete thermodynamically consistent kinetic model of particle nucleation and growth: Numerical study of the applicability of the classical theory of homogeneous nucleation, *J. Chem. Phys.* **126**, 144504 (2007).
- 146** Ya.B. Zeldovich, On the theory of new phase formation: Cavitation, *Zh. Eksp. Teor. Fiz.* **12**, 525 (1942).
Ya.B. Zeldovich, On the theory of new phase formation: Cavitation, in *Chemical Physics*

- and *Hydrodynamics*, volume I of *Selected Works of Yakov Borisovich Zeldovich*, edited by J. P. Ostriker, G. I. Barenblatt, and R. A. Sunyaev (Princeton University Press, Princeton, 1992).
- 147 R. Malek-Madani, *Advanced Engineering Mathematics with Mathematica and MATLAB*, volume 1 (Addison-Wesley, Reading, Massachusetts, 1998).
- 148 D. Zwillinger, *Handbook of Differential Equations* (Academic, San Diego, 1989).
- 149 F. F. Abraham, Multistate kinetics in nonsteady-state nucleation: A numerical solution, *J. Chem. Phys.* **51**, 1632 (1969).
- 150 V. A. Shneidman, Transient nucleation distributions and fluxes at intermediate times and sizes, *J. Chem. Phys.* **115**, 8141 (2001).
- 151 D. Kashchiev, On the relation between nucleation work, nucleus size, and nucleation rate, *J. Chem. Phys.* **76**, 5098 (1982).
- 152 D. W. Oxtoby and D. Kashchiev, A general relation between the nucleation work and the size of the nucleus in multicomponent nucleation, *J. Chem. Phys.* **100**, 7665 (1994).
- 153 P. R. ten Wolde, *Numerical Study of Pathways for Homogeneous Nucleation*, Ph.D. thesis, Universiteit van Amsterdam (1998).
- 154 D. W. Oxtoby and A. Laaksonen, Some consequences of the nucleation theorem for binary fluids, *J. Chem. Phys.* **102**, 6846 (1995).
- 155 C. L. Weakliem and H. Reiss, The factor $1/S$ in the classical theory of nucleation, *J. Phys. Chem.* **98**, 6408 (1994).
- 156 D. Kashchiev, Thermodynamically consistent description of the work to form a nucleus of any size, *J. Chem. Phys.* **118**, 1837 (2003).
D. Kashchiev, Multicomponent nucleation: Thermodynamically consistent description of the nucleation work, *J. Chem. Phys.* **120**, 3749 (2004).
- 157 J. W. P. Schmelzer and V. G. Baidakov, On different possibilities of a thermodynamically consistent determination of the work of critical cluster formation in nucleation theory, *J. Chem. Phys.* **119**, 10759 (2003).
J. W. P. Schmelzer and V. G. Baidakov, Comment on "Multicomponent nucleation: Thermodynamically consistent description of the nucleation work" [*J. Chem. Phys.* **120**, 3749 (2004)], *J. Chem. Phys.* **121**, 1644 (2004).
- 158 V. I. Kalikmanov, Crossover model for the work of critical cluster formation in nucleation theory, *J. Chem. Phys.* **121**, 8916 (2004).
- 159 G. Wilemski and J.-S. Li, Nucleation near the spinodal: Limitations of mean field density functional theory, *J. Chem. Phys.* **121**, 7821 (2004).
- 160 V. I. Kalikmanov, Mean-field kinetic nucleation theory, *J. Chem. Phys.* **124**, 124505 (2006).
- 161 V. I. Kalikmanov, J. Wölk, and T. Kraska, Argon nucleation: Bringing together theory, simulations, and experiment, *J. Chem. Phys.* **128**, 124506 (2008).
- 162 D. Reguera, R. K. Bowles, Y. Djikaev, and H. Reiss, Phase transitions in systems small enough to be clusters, *J. Chem. Phys.* **118**, 340 (2003).
- 163 D. Reguera and H. Reiss, Fusion of the extended modified liquid drop model for nucleation and dynamical nucleation theory, *Phys. Rev. Lett.* **93**, 165701 (2004).
- 164 D. Reguera and H. Reiss, Extended modified liquid drop–dynamical nucleation theory (EMLD–DNT) approach to nucleation: A new theory, *J. Phys. Chem. B* **108**, 19831 (2004).
- 165 J. W. Cahn and J. E. Hilliard, Free energy of a nonuniform system. I. Interfacial free energy, *J. Chem. Phys.* **28**, 258 (1958).
- 166 J. Hrubý, D. G. Labetski, and M. E. H. van Dongen, Gradient theory computation of the radius-dependent surface tension and nucleation rate for n -nonane clusters, *J. Chem. Phys.* **127**, 164720 (2007).
- 167 P. Peeters, C. C. M. Luijten, and M. E. H. van Dongen, Transitional droplet growth and diffusion coefficients, *Int. J. Heat Mass Transfer* **44**, 181 (2001).
- 168 H. Hertz, Ueber die Verdunstung der Flüssigkeiten, insbesondere des Quecksilbers, im luftleeren Raume, *Ann. Phys.* **253**, 177 (1882).
- 169 M. Knudsen, Die maximale Verdampfungsgeschwindigkeit des Quecksilbers, *Ann. Phys.* **352**, 697 (1915).
- 170 P. Peeters, G. Pieterse, and M. E. H. van Dongen, Multi-component droplet growth. II. A theoretical model, *Phys. Fluids* **16**, 2575 (2004).

- 171 X. Luo, B. Prast, M.E.H. van Dongen, H.W.M. Hoeijmakers, and J. Yang, On phase transition in compressible flows: modelling and validation, *J. Fluid Mech.* **548**, 403 (2006).
- 172 M.J.E.H. Muijtens, V.I. Kalikmanov, M.E.H. van Dongen, and A. Hirschberg, On mist formation in natural gas, *Revue de l'Institut Français du Pétrole* **49**, 63 (1994).
- 173 V. Holten and M.E.H. van Dongen, Comparison between solutions of the general dynamic equation and the kinetic equation for nucleation and droplet growth, *J. Chem. Phys.* **130**, 014102 (2009), included in this thesis as Chapter 3.
- 174 T.W. Peterson, F. Gelbard, and J.H. Seinfeld, Dynamics of source-reinforced, coagulating, and condensing aerosols, *J. Colloid Interface Sci.* **63**, 426 (1978).
- 175 J.H. Seinfeld and S.N. Pandis, *Atmospheric Chemistry and Physics: From Air Pollution to Climate Change* (Wiley, New York, 1998).
- 176 M.M.R. Williams and S.K. Loyalka, *Aerosol Science: Theory and Practice* (Pergamon, Oxford, 1991).
- 177 Z. Kožíšek, K. Sato, P. Demo, and A.M. Sveshnikov, Homogeneous nucleation of droplets from supersaturated vapor in a closed system, *J. Chem. Phys.* **120**, 6660 (2004).
- 178 F. Gelbard and J.H. Seinfeld, The general dynamic equation for aerosols: Theory and application to aerosol formation and growth, *J. Colloid Interface Sci.* **68**, 363 (1979).
- 179 R. Hagmeijer, R.H.A. IJzermans, and F. Put, Solution of the general dynamic equation along approximate fluid trajectories generated by the method of moments, *Phys. Fluids* **17**, 056101 (2005).
- 180 V.A. Shneidman, Size distribution of new-phase particles during transient condensation of a supercooled gas, *Sov. Phys. Tech. Phys.* **32**, 76 (1987).
- 181 V.A. Shneidman, Establishment of a steady-state nucleation regime. Theory and comparison with experimental data for glasses, *Sov. Phys. Tech. Phys.* **33**, 1338 (1988).
- 182 V.A. Shneidman, Universal distributions generated in a nucleation pulse, *Phys. Rev. Lett.* **101**, 205702 (2008).
- 183 H. Risken, *The Fokker-Planck Equation: Methods of Solution and Applications* (Springer, 1989), second edition.
- 184 J.R. Brock, New aspects of aerosol growth processes, *Aerosol Sci. Technol.* **2**, 109 (1982).
- 185 R. Hagmeijer, Equivalence of two different integral representations of droplet distribution moments in condensing flow, *Phys. Fluids* **16**, 176 (2004).
- 186 S.K. Loyalka and J.W. Park, Aerosol growth by condensation: A generalization of Mason's formula, *J. Colloid Interface Sci.* **125**, 712 (1988).
- 187 F. Gelbard, Y. Tambour, and J.H. Seinfeld, Sectional representations for simulating aerosol dynamics, *J. Colloid Interface Sci.* **76**, 541 (1980).
- 188 J.D. Landgrebe and S.E. Pratsinis, A discrete-sectional model for particulate production by gas-phase chemical reaction and aerosol coagulation in the free-molecular regime, *J. Colloid Interface Sci.* **139**, 63 (1990).
- 189 W.H. Press, S.A. Teukolsky, W.T. Vetterling, and B.P. Flannery, *Numerical Recipes in C: The Art of Scientific Computing* (Cambridge University Press, Cambridge, 1992), second edition.
- 190 V.A. Shneidman, pers. comm. (2009).
- 191 T.E. Ramabhadran, T.W. Peterson, and J.H. Seinfeld, Dynamics of aerosol coagulation and condensation, *AIChE J.* **22**, 840 (1976).
- 192 R. Strey, P.E. Wagner, and Y. Viisanen, The problem of measuring homogeneous nucleation rates and the molecular contents of nuclei: Progress in the form of nucleation pulse measurements, *J. Phys. Chem.* **98**, 7748 (1994).
- 193 E.F. Allard and J.L. Kassner, Jr., New cloud-chamber method for the determination of homogeneous nucleation rates, *J. Chem. Phys.* **42**, 1401 (1965).
- 194 P.E. Wagner and R. Strey, Homogeneous nucleation rates of water vapor measured in a two-piston expansion chamber, *J. Phys. Chem.* **85**, 2694 (1981).
- 195 Y. Viisanen, R. Strey, and H. Reiss, Homogeneous nucleation rates for water, *J. Chem. Phys.* **99**, 4680 (1993).
- 196 F. Peters, A new method to measure

- homogeneous nucleation rates in shock tubes, *Exp. Fluids* **1**, 143 (1983).
- 197 K.N.H. Looijmans, P.C. Kriesels, and M.E.H. van Dongen, Gasdynamic aspects of a modified expansion-shock tube for nucleation and condensation studies, *Exp. Fluids* **15**, 61 (1993).
- 198 K.N.H. Looijmans, C.C.M. Luijten, and M.E.H. van Dongen, Binary nucleation rate measurements of *n*-nonane/methane at high pressures, *J. Chem. Phys.* **103**, 1714 (1995).
- 199 C.C.M. Luijten, O.D.E. Baas, and M.E.H. van Dongen, Homogeneous nucleation rates for *n*-pentanol from expansion wave tube experiments, *J. Chem. Phys.* **106**, 4152 (1997).
- 200 P. Peeters, G. Pieterse, J. Hrubý, and M.E.H. van Dongen, Multi-component droplet growth. I. Experiments with supersaturated *n*-nonane vapor and water vapor in methane, *Phys. Fluids* **16**, 2567 (2004).
- 201 V.V. Sychev, A.A. Vasserman, V.A. Zagoruchenko, A.D. Kozlov, G.A. Spiridonov, and V.A. Tsymarny, *Thermodynamic Properties of Methane* (Hemisphere, Washington, 1987).
- 202 J. Wölk, *Homogene Keimbildung von H₂O und D₂O*, Ph.D. thesis, Universität zu Köln (2001).
- 203 J.L. Schmitt, J. Whitten, G.W. Adams, and R.A. Zalabsky, Binary nucleation of ethanol and water, *J. Chem. Phys.* **92**, 3693 (1990).
- 204 H.C. van de Hulst, *Light Scattering by Small Particles* (Dover, New York, 1981), reprint of 1957 edition published by Wiley, New York.
- 205 G. Mie, Beiträge zur Optik trüber Medien, speziell kolloidaler Metallösungen, *Ann. Phys.* **330**, 377 (1908).
- 206 C.F. Bohren and D.R. Huffman, *Absorption and Scattering of Light by Small Particles* (Wiley, New York, 1983).
- 207 N.L. Swanson, B.D. Billard, and T.L. Gennaro, Limits of optical transmission measurements with application to particle sizing techniques, *Appl. Opt.* **38**, 5887 (1999).
- 208 V. Holten, *From supersaturated water vapour to supercooled liquid water: analysis and experiments*, Master's thesis, Technische Universiteit Eindhoven (2004).
- 209 J. Hrubý, *New mixture-preparation device for investigation of nucleation and droplet growth in natural gas-like systems*, Internal report R-1489-D, Technische Universiteit Eindhoven (1999).
- 210 R.G. Wylie and R.S. Fisher, Molecular interaction of water vapor and air, *J. Chem. Eng. Data* **41**, 133 (1996).
- 211 R.W. Hyland and A. Wexler, The enhancement of water vapor in carbon dioxide-free air at 30, 40 and 50 °C, *Journal of Research of the National Bureau of Standards* **77A**, 115 (1973).
- 212 *General mass flow controller calibration procedure*, Document no. 834-P-064, Brooks Instrument B.V., Ede, Netherlands (2000).
- 213 P. Bruttel and R. Schlink, *Water Determination by Karl Fischer Titration* (Metrohm Ltd., Herisau, Switzerland, 2003), published as Metrohm monograph 8.026.5003 or 8.026.5013.
- 214 Tips and tricks for determining the water content in gases according to ISO 10101-3, *Metrohm Information* **35**(2), 11 (2006).
• http://www.metrohm.com/com/Metrohm_Info/eng
- 215 *Natural gas – Determination of water by the Karl Fischer method*, ISO 10101, International Organization for Standardization, Geneva, Switzerland (1993).
- 216 R. Massoudi and A.D. King, Jr., Effect of pressure on the surface tension of water. Adsorption of low molecular weight gases on water at 25°, *J. Phys. Chem.* **78**, 2262 (1974).
- 217 J. Wölk, R. Strey, C.H. Heath, and B.E. Wyslouzil, Empirical function for homogeneous water nucleation rates, *J. Chem. Phys.* **117**, 4954 (2002).
- 218 D. Brus, V. Ždimal, and J. Smolík, Homogeneous nucleation rate measurements in supersaturated water vapor, *J. Chem. Phys.* **129**, 174501 (2008).
- 219 P. Peeters, J.J.H. Gielis, and M.E.H. van Dongen, The nucleation behavior of supercooled water vapor in helium, *J. Chem. Phys.* **117**, 5647 (2002).
- 220 X. Luo, H. Olivier, H.W.M. Hoeijmakers, and M.E.H. van Dongen, Wave induced thermal boundary layers in a compressible fluid: analysis and numerical simulations, *Shock Waves* **16**, 339 (2007).
- 221 C.-H. Hung, M.J. Krasnopoler, and J.L. Katz,

- Condensation of a supersaturated vapor. VIII. The homogeneous nucleation of *n*-nonane, *J. Chem. Phys.* **90**, 1856 (1989).
- 222** R. Strey, P.E. Wagner, and T. Schmeling, Homogeneous nucleation rates for *n*-alcohol vapors measured in a two-piston expansion chamber, *J. Chem. Phys.* **84**, 2325 (1986).
- 223** T. Koop, Homogeneous ice nucleation in water and aqueous solutions, *Z. Phys. Chem* **218**, 1231 (2004).
- 224** B.N. Hale, Temperature dependence of homogeneous nucleation rates for water: Near equivalence of the empirical fit of Wölk and Strey, and the scaled nucleation model, *J. Chem. Phys.* **122**, 204509 (2005).
- 225** O. Mishima and H.E. Stanley, The relationship between liquid, supercooled and glassy water, *Nature* **396**, 329 (1998).
- 226** C.A. Angell, Supercooled water, *Ann. Rev. Phys. Chem.* **34**, 593 (1983).
- 227** M. Muijtens and K. Looijmans, *Temperatuurafhankelijkheid van enkele grootheden van water, pentaan, nonaan*, Internal report R-1070-D, Technische Universiteit Eindhoven (1990).
- 228** G. Lamanna, *On Nucleation and Droplet Growth in Condensing Nozzle Flows*, Ph.D. thesis, Technische Universiteit Eindhoven (2000).
- 229** C.H. Heath, K. Streletzky, B.E. Wyslouzil, J. Wölk, and R. Strey, H₂O–D₂O condensation in a supersonic nozzle, *J. Chem. Phys.* **117**, 6176 (2002).
- 230** O. Preining, P.E. Wagner, F.G. Pohl, and W. Szymanski, *Heterogeneous Nucleation and Droplet Growth: Measurements with a Process Controlled Fast Expansion Chamber, the Size Analyzing Nuclei Counter SANC*, volume III of *Aerosolforschung am Institut für Experimentalphysik der Universität Wien* (Institute for Experimental Physics of the University of Vienna, Vienna, Austria, 1981).
- 231** K. Schäfer and E. Lax (editors), *Eigenschaften der Materie in ihren Aggregatzuständen* (Springer, Berlin, 1960), volume II, part 2a of *Landolt–Börnstein Zahlenwerte und Funktionen aus Physik-Chemie-Astronomie-Geophysik und Technik*, pp. 32, 61.
- 232** V.B. Mikheev, P.M. Irving, N.S. Laulainen, S.E. Barlow, and V.V. Pervukhin, Laboratory measurement of water nucleation using a laminar flow tube reactor, *J. Chem. Phys.* **116**, 10772 (2002).
- 233** D.G. Archer and R.W. Carter, Thermodynamic properties of the NaCl + H₂O system. 4. Heat capacities of H₂O and NaCl(aq) in cold-stable and supercooled states, *J. Phys. Chem. B* **104**, 8563 (2000).
- 234** G.S. Kell, Precise representation of volume properties of water at one atmosphere, *J. Chem. Eng. Data* **12**, 66 (1967).
- 235** J. Pátek, J. Hrubý, J. Klomfar, and M. Součková, Reference correlations for thermophysical properties of liquid water at 0.1 MPa, *J. Phys. Chem. Ref. Data* **38**, 21 (2009).
- 236** J.F. Mohler, The expansion of water below zero degree centigrade, *Phys. Rev. (Series I)* **35**, 236 (1912), part of an article that starts at p. 233.
- 237** J.A. Schuffle, The specific gravity of supercooled water in a capillary, *Chem. Ind.* **16**, 690 (1965).
- 238** J.A. Schuffle and M. Venugopalan, Specific volume of liquid water to –40 °C, *J. Geophys. Res.* **72**, 3271 (1967).
- 239** B.V. Zheleznyi, The density of supercooled water, *Russ. J. Phys. Chem.* **43**, 1311 (1969).
- 240** D.H. Rasmussen and A.P. MacKenzie, Clustering in supercooled water, *J. Chem. Phys.* **59**, 5003 (1973).
- 241** C.M. Sorensen, Densities and partial molar volumes of supercooled aqueous solutions, *J. Chem. Phys.* **79**, 1455 (1983).
- 242** D.E. Hare and C.M. Sorensen, Densities of supercooled H₂O and D₂O in 25 μ glass capillaries, *J. Chem. Phys.* **84**, 5085 (1986).
- 243** D.E. Hare and C.M. Sorensen, The density of supercooled water. II. Bulk samples cooled to the homogeneous nucleation limit, *J. Chem. Phys.* **87**, 4840 (1987).
- 244** D. Liu, Y. Zhang, C.-C. Chen, C.-Y. Mou, P.H. Poole, and S.-H. Chen, Observation of the density minimum in deeply supercooled confined water, *Proc. Natl. Acad. Sci. U.S.A.* **104**, 9570 (2007).
- 245** F. Mallamace, C. Branca, M. Broccio, C. Corsaro, C.-Y. Mou, and S.-H. Chen, The anomalous behavior of the density of water in

- the range $30\text{ K} < T < 373\text{ K}$, *Proc. Natl. Acad. Sci. U.S.A.* **104**, 18387 (2007).
- 246** D. Liu, Y. Zhang, Y. Liu, J. Wu, C.-C. Chen, C.-Y. Mou, and S.-H. Chen, Density measurement of 1-D confined water by small angle neutron scattering method: Pore size and hydration level dependences, *J. Phys. Chem. B* **112**, 4309 (2008).
- 247** Y. Zhang, K.-H. Liu, M. Lagi, D. Liu, K. C. Littrell, C.-Y. Mou, and S.-H. Chen, Absence of the density minimum of supercooled water in hydrophobic confinement, *J. Phys. Chem. B* **113**, 5007 (2009).
- 248** A. Winkelmann (editor), *Handbuch der Physik*, volume 2, part 2 (Eduard Trewendt, Breslau, 1896), the density data cited on p. 92 and tabulated on p. 93 dates from 1866.
• <http://www.archive.org/details/handbuchderphys01auergoog>
- 249** J. V. Leyendekkers and R. Hunter, Thermodynamic properties of water in the subcooled region. II, *J. Chem. Phys.* **82**, 1447 (1985).
- 250** G. S. Kell, Density, thermal expansivity, and compressibility of liquid water from 0° to 150°C : Correlations and tables for atmospheric pressure and saturation reviewed and expressed on 1968 temperature scale, *J. Chem. Eng. Data* **20**, 97 (1975).
- 251** J. Malila and A. Laaksonen, Properties of supercooled water clusters from nucleation rate data with the effect of non-ideal vapour phase, in *Proceedings of the 15th International Conference on the Properties of Water and Steam*, edited by R. Span and I. Weber (VDI, Düsseldorf, 2008).
• <http://www.icpws15.de/proceedings.htm>
- 252** R. Feistel, W. Wagner, V. Tchijov, and C. Guder, Numerical implementation and oceanographic application of the Gibbs potential of ice, *Ocean Sci.* **1**, 29 (2005).
- 253** G. M. Hale and M. R. Query, Optical constants of water in the 200-nm to 200- μm wavelength region, *Appl. Opt.* **12**, 555 (1973).
- 254** *Release on the Refractive Index of Ordinary Water Substance as a Function of Wavelength, Temperature and Pressure*, IAPWS (1997).
• <http://www.iapws.org/relguide/rindex.pdf>
- 255** A. H. Harvey, J. S. Gallagher, and J. M. H. Levelt Sengers, Revised formulation for the refractive index of water and steam as a function of wavelength, temperature and density, *J. Phys. Chem. Ref. Data* **27**, 761 (1998).
- 256** Ch. Saubade, Indice de réfraction de l'eau pure aux basses températures, pour la longueur d'onde de 5893 Å, *J. Phys. (France)* **42**, 359 (1981).
- 257** L. Carroll and M. Henry, Autocompensating interferometer for measuring the changes in refractive index of supercooled water as a function of temperature at 632.8 nm, *Appl. Opt.* **41**, 1330 (2002).
- 258** D. Duft and T. Leisner, The index of refraction of supercooled solutions determined by the analysis of optical rainbow scattering from levitated droplets, *Int. J. Mass Spectrom.* **233**, 61 (2004).
- 259** A. Ehringhaus, Beiträge zur Kenntnis der Dispersion der Doppelbrechung einiger Kristalle, in *Neues Jahrbuch für Mineralogie, Geologie und Paläontologie*, volume Beilage-Band 41, edited by M. Bauer, Fr. Frech, and Th. Liebisch (E. Schweizerbart, Stuttgart, 1917), pp. 342–419, the data on ice is on pp. 362–371 and p. 391.
- 260** Elasto-optic, electro-optic, and magneto-optic constants, in Ref. 262.
- 261** T. M. Miller, Atomic and molecular polarizabilities, in Ref. 262.
- 262** D. R. Lide (editor), *CRC Handbook of Chemistry and Physics* (CRC, 2004), 84th edition.

Curriculum vitae

- 25 February 1982** Born in Eindhoven, The Netherlands
- 1992–1998** VWO student
Stedelijk College Eindhoven
- 1998–2004** Student of Applied Physics (diploma cum laude)
Eindhoven University of Technology
Master's thesis: *From supersaturated water vapour
to supercooled liquid water*
- 2004–2009** PhD candidate
Group of Gasdynamics and Aeroacoustics (2004–2007)
Group of Mesoscopic Transport Phenomena (2008–2009)
Eindhoven University of Technology
- November 2004–
February 2005** Stay at the Institute of Thermomechanics of the
Academy of Sciences of the Czech Republic
Prague, Czech Republic

Colophon

Typeset by L^AT_EX

Typefaces: Minion Pro, designed by Robert Slimbach, and Cavitates, designed by the author

Graphs produced by PyX